DEPARTMENT OF ELECTRONIC & ELECTRICAL ENGINEERING

University of Strathclyde Engineering

Driving Power Grid Resilience and Capacity Expansion with Distributed Sensing and Data Analytics

Himanshi Singh

Department of Electronic and Electrical Engineering
University of Strathclyde, Glasgow
United Kingdom.

A thesis submitted for the degree of
Doctor of Philosophy

June 2026

Copyright Declaration

This thesis is the result of the author's original research. It has been composed by the author and has not been previously submitted for examination, which has led to the award of a degree.

The copyright of this thesis belongs to the author under the terms of the United Kingdom Copyright Acts as qualified by the University of Strathclyde Regulation 3.50. Due acknowledgement must always be made of the use of any material contained in, or derived from, this thesis.

Signed:

Singh

Himanshi Singh.

Date: Thursday 11th June, 2026

Abstract

Ensuring the reliability and longevity of overhead power transmission lines is fundamental to the stability and efficiency of modern electrical grids. As global energy demand rises and the transition towards smart grid infrastructure accelerates, the need for advanced real-time monitoring technologies has become increasingly critical, particularly those capable of operating accurately under challenging environmental conditions. This thesis presents the development, implementation, and experimental validation of fibre Bragg grating (FBG) sensors for structural health monitoring (SHM) of overhead line (OHL) conductors.

FBG sensors offer several advantages over conventional electrical sensing techniques, including immunity to electromagnetic interference, multiplexing capability, compact size, and suitability for remote sensing over long distances. This work exploits these advantages by developing an FBG-based monitoring approach for key mechanical and thermal parameters, including conductor sag, strain, temperature, and vibration, under varying mechanical loading and thermal cycling conditions.

The novel contributions of this PhD thesis include the design and optimisation of a mechanically robust FBG-based sag sensor mounting assembly for OHL conductors; the laboratory characterisation of the sensor response to force and temperature over operating conditions relevant to power networks; the assessment of measurement uncertainty associated with force, temperature, wavelength, and sag estimation; the field deployment and validation of the sensor system on an OHL test span at the Power Network Demonstration Centre (PNDC); and the development of a fatigue-assessment methodology using FBG sensor data, rainflow counting, Miner's rule, and stress-life analysis to estimate the operational durability of both the sensor and conductor.

Experimental results confirm that FBG sensors are capable of reliably detecting structural variations in OHL conductors, enabling early identification of changes associated with sag, thermal loading, and vibration. The findings demonstrate the potential for integrating FBG-based SHM systems into future smart grid infrastructure, providing a lightweight, scalable, and high-fidelity solution for continuous condition monitoring and predictive maintenance in power transmission networks.

Acknowledgements

I would like to extend my deepest gratitude to my supervisors, Professor Pawel Niewczas, Dr. Grzegorz Fusiek, and Dr. Valerie Livina, for their continuous support, insightful guidance, and encouragement throughout the course of my PhD. Their expertise and mentorship have played a pivotal role in shaping both my research and personal development.

I am also sincerely thankful to the University of Strathclyde for awarding me the John Anderson Research Award (JARA) Studentship and for fostering an outstanding academic environment that enabled the successful completion of my research. My appreciation also goes to the National Physical Laboratory (NPL) for their collaboration and support during this work.

A special thanks to my colleagues at the Advanced Sensor Laboratory at Strathclyde. I am particularly grateful to Jack and Alfred for their friendship and for creating a motivating and collaborative atmosphere in the lab.

I would also like to take this opportunity to thank the people whose support has been unwavering throughout this journey. My heartfelt appreciation goes to my parents, Mr. M. P. Singh and Mrs. Santosh Singh, and my sister, Upasna Singh, whose love, patience, and faith in me have been constant sources of strength. I am also thankful to Dr. Gaurav Gautam for his steadfast support, encouragement, and belief in my potential. His presence has been a guiding light throughout this journey.

Lastly, I am grateful to my grandparents, uncles, aunts, and my dear friend Parinita Saini for their continued kindness, encouragement, and moral support. Their presence has made this journey all the more meaningful.

Contents

List of Figures

List of Tables

Nomenclature

$\mathbf{3D}$: Three Dimensional

$\mathbf{\Delta}\lambda_{\mathbf{BS}}$: Wavelength Shifts due to Applied Longitudinal Strain

ϵ : Strain

λ : Wavelength

$\lambda_{\mathbf{B}}$: Bragg Wavelength

ϕ : Phase Angle Between Force and Velocity

ρ_{α} : Fibre's Photoelastic Coefficient

$\sigma_{\mathbf{a}}$: Stress Amplitude

$\sigma_{\mathbf{PS}}$: Stress Amplitude (Zero-to-Peak)

$\mathbf{AAAC}$: All Aluminium Alloy Conductor

$\mathbf{AAC}$: All Aluminium Conductor

$\mathbf{AACSR}$: Aluminium Alloy Conductor Steel-Reinforced

$\mathbf{AC}$: Alternating Current

$\mathbf{ACAR}$: Aluminium- Conductor Alloy- Reinforced

ACSR : Aluminium Conductor Steel-Reinforced

Al : Aluminium

AMRL : Advanced Material Research Laboratory

ASL : Applied Sensor Laboratory

ASTM : American Society for Testing Materials

AWM : Aircraft Warning Markers

C : Capacitance

CFBG : Chirped Fibre Bragg Grating

CIGRE : Conseil International des Grands Réseaux Électriques

$\mathbf{CO_2}$: Carbon Dioxide

CTE : Coefficient of Thermal Expansion

D : Sag

DAQ : Data Acquisition

DC : Direct Current

DLR : Dynamic Line Rating

DOFS : Distributed Optical Fibre Sensing

E : Young's Modulus

EBM : Energy Balance Model

EDT : Everyday Tension

EHV : Extra High Voltage

ELEDs : Edge-Emitting Light-Emitting Diodes

EPRI : Electric Power Research Institute

F : Force

$\mathbf{F_c}$: Force at the Damper Clamp

FBG : Fibre Bragg Grating

FEA : Finite Element Analysis

FEM : Finite Element Modelling

FFT : Fast Fourier Transform

FP : Fabry-Perot Interferometric Sensors

FRP : Fiber Reinforced Plastic

FSR : Free Spectral Range

FWHM : Full Width at Half Maximum

GPRS : General Packet Radio Service

GPS : Global Positioning System

GUM : Guide to the Expression of Uncertainty in Measurement

H : Horizontal Tension

$\mathbf{H_2}$: Hydrogen

$\mathbf{H_2S}$: Hydrogen Sulphide

HDC : Hard Drawn Copper

HILDA : High Line Data Acquisition System

HTLS : High Temperature Low Sag

HVDC : High Voltage Direct Current

I : Current

IEEE : Institute of Electrical and Electronics Engineers

IoT : Internet of Things

IR : Infrared

ISWR : Inverse Standing Wave Ratio

K : Poffenberger Constant

$\mathbf{K}_{\epsilon}$: Strain Sensitivity Coefficient

$\mathbf{K_F}$: Force Sensitivity Coefficient

$\mathbf{K_T}$: Temperature Sensitivity Coefficient

L : Inductance

LIDAR : Light Detection and Ranging

LV : Low Voltage

m : Mass per Unit Length

MPE : Maximum Permissible Error

MV : Medium Voltage

$\mathbf{N_i}$: Number of Cycles to Failure

NCI : Non-Ceramic Insulators

OH : Hydroxyl

OHL : Overhead Line

OHLCD : Overhead Line Corrosion Detector

OLS : Ordinary Least Squares

OPD : Optical Path Difference

OTLM : Overhead Transmission Line Monitoring

P : Pressure

$\mathbf{P_d}$: Power Dissipated by the Damper

$\mathbf{P_j}$: Joule Heating

$\mathbf{P_m}$: Magnetic Heating

PLC : Power Line Carrier

PM : Polarimetric Fibre Optic Sensors

PMU : Phasor Measurement Unit

PNDC : Power Network Demonstration Centre

PRT : Platinum Resistance Thermocouple

PS : Poffenberger-Swart

PT : Pico Technology

PXI : PCI extensions for Instrumentation

PZT : Piezoelectric

R : Resistance

RF : Radio Frequency

RFID : Radio Frequency Identification

RSS : Root-Sum-of-Squares

S − N Curve : Stress-Life Curves

S1 : Sensor 1

S2 : Sensor 2

S : Span Length

SFSs : Super-Fluorescent Fibre Sources

SHM : Structural Health Monitoring

SI : Scanned Interferometer

SLDs : Super-Luminescent Diodes

SLR : Static Line Rating

SS : Stainless Steel

T : Temperature

T : Tension

TFLs : Tunable Fibre Lasers

TM : Two-Mode Fibre Optic Sensors

TMD : Tuned Mass Damper

ToF : Time of Flight

TP : Twisted Pair

TW : Trapezoidal Shape

UAV : Unmanned Aerial Vehicle

UHV : Ultra-High Voltage

UTS : Ultimate Tensile Strength

UV : Ultraviolet

$\mathbf{v_c}$: Clamp Velocity

$\mathbf{v_w}$: Maximum Wind Velocity

$\mathbf{w}$: Conductor Weight per Unit Length

$\mathbf{Y_b}$: Bending Amplitude

YTS : Yield Tensile Strength

$\mathbf{Z_d}(\omega)$: Mechanical Impedance of the Damper

1

Introduction

1.1 Motivation, justification for, and introduction to research

Society heavily relies on electrical power, and the continuously increasing demand substantially strains the current electrical grid. Utilities are challenged to meet these demands by upgrading or replacing existing infrastructure. This involves substantial investment and strategic planning to enhance the grid's capacity, efficiency, and resilience. In 2024, the world experienced a notable acceleration in energy demand, as shown in Figure 1.1, with global consumption rising by approximately 2.2 %, a significant increase compared to the 1.3 % average annual growth seen over the previous decade. This uptick was partly driven by unusually warm weather conditions, which added an estimated 0.3 % points to overall energy use. Despite this, energy consumption expanded at a slower pace than the global economy, which grew by around 3.2 % in the same period [1].

Among all sectors, electricity demand grew most rapidly, increasing by 4.3 %, outpacing both total energy growth and GDP growth. This surge reflects structural shifts, including broader access to electricity-intensive devices like air conditioners, rising use of electric vehicles, and the expanding role of data centres and artificial intelligence technologies. Altogether, electricity accounted for approximately 60 % of the total growth in energy consumption [1].

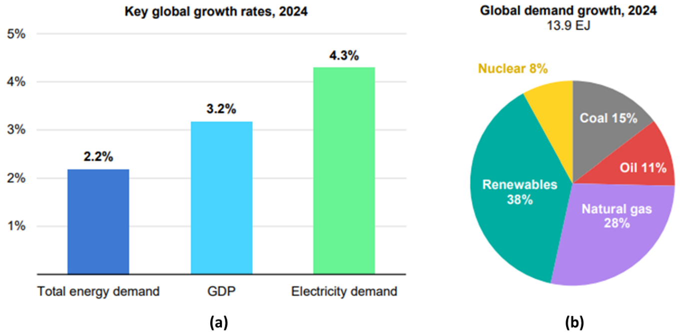

Figure 1.1: (a) Key global growth rates in 2024, highlighting electricity demand rising by 4.3 %, surpassing GDP growth (3.2 %) and total energy demand (2.2 %). (b) Distribution of global energy demand growth by source, with renewables contributing the largest share (38 %), followed by natural gas (28 %), coal (15 %), oil (11 %), and nuclear (8 %) [1].

The increase in global energy supply in 2024 was primarily driven by renewable energy, which accounted for approximately 38 % of the growth. This was followed by natural gas (28 %), coal (15 %), oil (11 %), and nuclear power (8 %). All major energy sources expanded in 2024, with natural gas seeing a 2.7 % increase, setting a new global record in usage, especially in fast-developing Asian markets like China and India [1].

Oil demand increased by just 0.8 %, a slowdown compared to 2023, as post-pandemic travel growth tapered off and electric mobility alternatives gained ground. Demand was mostly flat in high-income countries and grew modestly in emerging markets. Coal consumption rose by just over 1 %, also reaching an all-time high, although growth was concentrated in developing Asian economies, particularly China, while advanced economies saw a continued decline [1].

Among non-fossil energy sources, renewables grew by nearly 6 %, driven by significant expansions in solar and wind capacity. Hydropower output rebounded with a 4.4 % increase, recovering from drought-related declines in 2023. Nuclear energy also saw growth of about 4 % globally [1].

The year 2024 was the warmest on record, surpassing the previous high set in 2023. As a result, cooling needs increased substantially, with global cooling degree days up by 6 % from the previous year and 20 % above the long-term average (2000–2020). This led to heightened electricity demand, especially in countries like China, India, and the United States, Figure 1.2

[1].

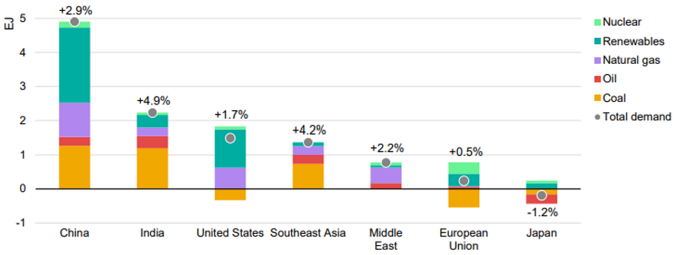

Figure 1.2: Breakdown of energy demand growth by fuel type (coal, oil, natural gas, renewables, nuclear) across major regions. The grey dots indicate total energy demand growth in exajoules (EJ) and percentage terms. Developing economies, particularly China and India, drove most global demand growth, while Japan experienced a decline [1].

Weather-related effects are estimated to have contributed to 15 % of the total growth in global energy demand in 2024. The impact was particularly strong in the electricity, natural gas, and coal sectors, as these fuels were used to meet higher cooling demands. Approximately 20 % of the growth in both electricity and gas consumption, and most of the increase in coal demand, is attributed to temperature effects. For CO_2 emissions, weather was responsible for nearly half of the increase recorded in 2024, as shown in Figure 1.3 and 1.4 [1].

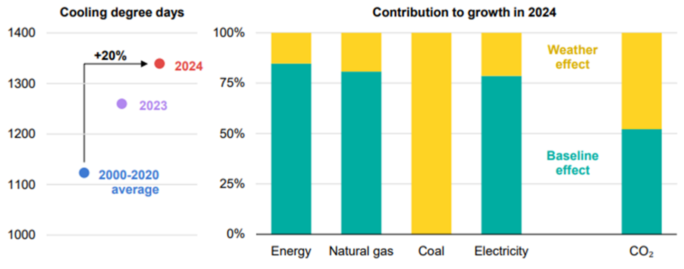

(a) (b)

Figure 1.3: (a) Cooling degree days in 2024 rose by 20 % above the 2000–2020 average, indicating increased cooling demand. (b) Weather-related effects accounted for a substantial portion of growth in energy, gas, coal, electricity, and CO_2 emissions in 2024, particularly dominating the increase in coal and electricity consumption [1].

These trends reinforce the increasing operational pressure on power systems, especially during temperature extremes, when demand peaks and network assets may simultaneously experience reduced thermal headroom. As a result, transmission operators are increasingly interested in uprating overhead lines (OHLs), i.e., increasing permissible power transfer,

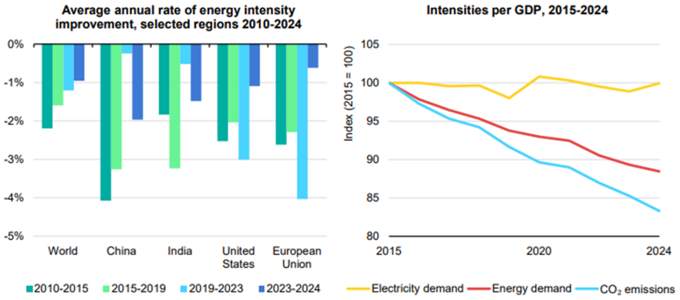

(a) (b)

Figure 1.4: (a) Average annual rates of energy intensity improvement by region and period. Notable slowdowns are seen across regions in 2023–2024 compared to earlier years. (b) Indexed trends (2015 = 100) of electricity demand, total energy demand, and CO_2 *emissions per unit of GDP from 2015 to 2024, indicating declining carbon and energy intensity, while electricity intensity remains relatively flat [1].*

through a combination of analytical reassessment, targeted modifications, and (where necessary) major asset upgrades. In the literature and in utility practice, OHL uprating approaches can be grouped into three broad categories, ranging from low-cost analytical changes to more disruptive physical interventions [2]. The following categories provide a structured framework for discussing these methods and their applicability.

Category 1: Re-evaluation of line rating assumptions and safety factors

Category 1 encompasses the most commonly used approaches, which involve reevaluating the line rating assumptions and safety factors applied during the initial design of the OHL structure. Techniques in this category often include allowing for higher maximum conductor operating temperatures or using less conservative weather conditions. These methods primarily require precise calculations and historical weather data related to the structure. They are particularly beneficial for older OHL structures designed with conservative assumptions due to the lack of accurate weather data during construction. These upgrades are cost-effective; therefore, they do not require structural modifications, which makes them highly preferred by utilities. However, they may not always be feasible due to environmental changes and global warming. Newer structures, built after the deregulation of electrical utilities, generally use less conservative designs to reduce costs, limiting the applicability of these methods [2].

Category 2: Modifications of critical span in the structure

The second category includes techniques for increasing the power rating of an OHL through minor, selective modifications at specific weak points, referred to as critical spans. Modifications might involve raising the height of conductor attachment points or installing additional monitoring equipment [2]. These monitors enable dynamic line rating by measuring variables like conductor temperature, ambient temperature, and wind speed, effectively increasing power transfer capacity.

Category 3: Replacing conductors, reinforcing structures, reconstructing

Category 3 methods, generally more expensive and disruptive, are often necessary after the simpler and cheaper techniques of Categories 1 and 2 have been exhausted. This category includes major modifications such as reconductoring, reinforcing, and rebuilding existing structures to support higher current flow and/or voltage levels. Due to the high cost of rebuilding, the most common methods for increasing power capacity, which directly relates to enhancing the current rating of the conductor (ampacity), are retensioning and reconductorisation as explained in category 2 [2].

Retensioning is typically applied to older lines where conductor sag limits thermal rating increases or lines subjected to severe weather and electrical loads beyond the design specifications. Sag prediction errors, often due to misinterpreting the conversion of conductor plastic elongation to thermal elongation, may also necessitate retensioning [2].

Reconductorisation involves replacing existing conductors with larger or alternative materials and technologies, such as advanced composite conductors [2]. This reduces conductor resistance and/or sag, thereby increasing power transfer capacity. High-temperature Low-Sag (HTLS) conductors, which maintain mechanical strength at elevated temperatures, are particularly effective [2]. However, the weight of these conductors affects system stresses and may require structural reinforcement, increasing upgrading costs. Thus, it is crucial to consider the weather loading and the properties of the OHL structure, rather than simply comparing the properties of the conductors, when evaluating increases in thermal rating [2].

The increase in electric current in OHL conductors leads to an increase in the conductor's temperature, which affects the distribution of the tensile load within the conductor. The uneven thermal expansion between the core and the outer strands results in an imbalanced distribution of tensile stress, with the core and the outer layers bearing different portions of the total load. This imbalance can affect the mechanical performance and long-term reliability of the conductor. The temperature of these conductors significantly influences their thermal rating, mechanical behaviour (including susceptibility to vibration), and ageing processes such as creep. All of these factors collectively affect the overall performance and longevity of the conductors.

For instance, higher temperatures can lead to increased thermal expansion, influencing the conductor's tension and sag. Over time, these thermal and mechanical stresses can accelerate ageing, reducing the conductor's effectiveness and lifespan. The impact of the temperature-tension effect on the OHL conductor system is influenced by the differing technologies like the conductor's geometry, thermal rating, material properties of the conductor and the components of the line [2]. Additionally, the performance and durability of the line are affected by other elements of the transmission system, such as:

- Supporting structures (like towers or poles) that support the conductors must be robust and well-maintained to prevent structural failure that could affect the line's integrity [2].
- Insulators, which prevent electrical faults by isolating the conductors from the supporting structures, must be resistant to environmental conditions like pollution, moisture, and temperature changes. Degraded insulators can lead to electrical leaks or faults [2].
- Connectors and fittings used to connect and secure the conductors must be durable and able to withstand mechanical stresses and environmental factors. Corrosion or mechanical wear can weaken these components, impacting the overall reliability of the transmission line [2].
- Protection systems, including circuit breakers and surge protectors, are crucial for

protecting the line from faults and surges. Their reliability ensures the transmission line can handle unexpected electrical disturbances without sustaining damage [2].

- Environmental factors (such as wind, ice, and extreme temperatures) can impose additional mechanical loads on the conductors and supporting structures. Proper design and maintenance are necessary to mitigate these effects and ensure long-term durability [2].
- Maintenance practices like regular inspections and maintenance are essential to identify and address issues before they lead to significant failures. Preventive maintenance helps maintain the performance and extends the lifespan of the transmission system [2].

Understanding these factors is crucial for optimising the performance and extending the life of the conductors in high-demand scenarios [2].

A significant concern when installing and tensioning overhead line conductors is the risk of aeolian vibrations, which can cause long-term damage through metal fatigue. Current standard practices for evaluating the installation, vibration and ageing performance of OHLs typically use simplified conductor models that assume homogeneous properties. These models need to be re-assessed to accommodate the substantial variations in the sizes, materials, and geometries of composite conductors. Although the impact of conductor vibrations under extreme operational conditions, particularly for HTLS conductors, has been adequately studied or modelled in recent years, there is still a need for more comprehensive models. These advanced conductors operate under higher temperatures and different stress conditions, making it crucial to develop models that accurately predict their behaviour and longevity under real-world conditions. Standards such as CIGRE [3] and IEEE [4, 5] provide acceptable results for vibration-induced fatigue. Ensuring the reliability and durability of OHL systems in increasingly demanding environments is essential.

This thesis focuses on monitoring OHLs and developing methodologies for power line failure detection and prediction using novel photonic sag sensors [6]. In this context, failure detection refers to identifying measurable precursors to conductor degradation, including excessive sag, abnormal strain, temperature rise, increased vibration levels, and sudden changes in mechanical loading. The photonic sag sensors measure strain, temperature, and vibration-induced wavelength shifts, which can be converted into conductor tension, sag variation, and cyclic stress histories. These data can then be used to detect abnormal operating conditions and to estimate accumulated fatigue damage, thereby supporting early warning and prediction of possible conductor or fitting failure before mechanical breakdown occurs.

The thesis aims at improved design of the prototype optical sag sensors for monitoring sag, temperature, and vibration previously developed in the Applied Sensor Laboratory (ASL). The sag sensor was characterised experimentally in laboratory conditions to verify the finite element analysis performed using COMSOL Multiphysics. The methodology was developed to predict the lifetime of the proposed sag sensor and OHL conductor using data from a trial carried out at the PNDC (Power Network Demonstration Centre). It seeks to assess the low-frequency variability caused by wind, which provides insights into the impact of strain on the overhead line and the conductor's lifetime.

1.2 Aims, objectives, and outcomes of the research

The thesis aims to develop and test novel photonic sag sensors for overhead power lines and develop methodologies for power line failure detection and prediction. The research presented here focused on designing and evaluating an overhead line sensor based on a fibre Bragg grating (FBG) photonic strain and temperature transducers. The goal was to monitor critical parameters such as sag, temperature, and vibration to create a comprehensive system for power grid monitoring, control, and protection [6].

Fibre-optic sensors are a promising option since optical fibre is already incorporated into transmission lines. Wang et al. [7] demonstrated tension-based sag measurement using a fibre Bragg grating load sensor positioned between the tower and the insulator supporting the transmission line. More FBG-based sag sensors were described in [8, 9]. These designs utilised a chirped FBG to measure both strain and temperature for determining line tension. However, these solutions do not support sag monitoring at high temperatures.

To provide a comprehensive measurement system for monitoring both electrical and mechanical parameters of OHL, a variety of optical sensors were previously proposed [10–12]. These included optical voltage and current sensors, as well as optical sensors for monitoring sag, temperature, and vibration of standard low-temperature OHLs, which could be integrated with sensors measuring electrical parameters [6, 13]. FBGs were chosen for their high sensitivity, accuracy, and compatibility with similar sensors, making them ideal for this application.

The sensors were subjected to laboratory testing before their installation for a field trial. The study also focused on failure and lifetime monitoring, devising methodologies to predict potential events on the line, such as excessive sagging, line breakage, overheating, or mechanical wear. These events can impact the reliability and safety of the transmission lines, making early detection and prediction crucial for maintaining optimal performance and preventing outages. This involved specifying OHL measurement requirements, developing and evaluating the OHL sensor, and making iterative design modifications as needed. A data algorithm was implemented for detecting and predicting power line failures. This process included analysing strain and temperature data recorded by a sensor prototype at the PNDC at the University of Strathclyde and performing stochastic modelling of time series in various high-voltage line scenarios observed in the energy industry. The results of this analysis can be applied to real-time data analytics of strain sensors, enhancing the reliability and effectiveness of power grid monitoring systems.

The research objectives of this work can be summarised as follows:

- To improve the design of the existing FBG-based sag sensors for OHL failure prediction and detection.

- To characterise novel FBG-based optical sag sensors for overhead power line monitoring, prototyped in the Advanced Sensor Laboratory (ASL) at the University of Strathclyde [6].

- To identify the most promising techniques to monitor OHL critical parameters such as sag, temperature, and vibration and to create a comprehensive system for power grid monitoring, control, and protection.

- To propose real-time data analytics of sag FBG-based sensors, enhancing the reliability and effectiveness of power grid monitoring systems.

1.2.1 Contribution to the research

The main contribution of the research described in this thesis can be listed as follows:

- Improved design of the prototype optical sag sensor previously developed by the Advanced Sensors Team [6]. The improvement was achieved by redesigning the sensor mounting assembly and evaluating alternative mounting-plate geometries to obtain a more suitable strain-transfer response between the conductor and the FBG transducer. Finite element analysis was used to assess the stress distribution and mechanical response of the proposed geometries, while laboratory force and temperature characterisation were used to verify the sensor response experimentally. The revised design improves mechanical robustness by providing a more secure attachment to the conductor and reducing localised stress concentrations in the mounting structure. It also improves measurement reliability by enabling repeatable strain transfer to the FBG transducer under cyclic loading and temperature variation. In addition, the use of integrated strain and temperature FBGs allows sag-related strain, temperature, and vibration-induced dynamic strain to be monitored within the same sensor assembly. These improvements support more reliable real-time condition monitoring of OHL conductors in field environments.
- Finite Element Analysis (FEA) of the expected sensor performance and the related sensor design optimisation. This involved COMSOL Multiphysics simulations to estimate the expected sensor response when installed on a conductor and its sensitivity to strain and temperature at a load up to 5 kN and temperatures between -20 °C to 200 °C.
- The verification of the FEA results by detailed experimental strain and temperature characterisation of the proposed FBG-based sensors at loads up to 3 kN within the

temperature range from 20 °C to 180 °C, and with no load applied within temperatures between -20 °C to 20 °C.

- The development of methodologies for the lifetime prediction of the proposed sag sensor using the measurement data from the field trial at the PNDC.
- The outcomes of OHL sag and vibration measurements were utilised to evaluate the sag sensor's longevity. Two different stainless-steel plates were analysed, and the fatigue life was estimated using a finite element model of the OHL sensors. Development and application of a lifetime-estimation methodology for the considered OHL conductors using simulated field environmental data derived from the PNDC field trial at the University of Strathclyde, UK. This contribution enabled the assessment of conductor fatigue behaviour under representative operating conditions and supported the prediction of long-term mechanical performance.
- The implementation of the rainflow counting algorithm and Miner's rule for estimation of the cumulative damage in the conductor.

1.3 Thesis overview

The remainder of this thesis has been divided into the following chapters:

Chapter 2 provides a concise introduction to high-voltage overhead line technology. It begins by defining the concept of overhead lines and classifying different types of overhead lines. Furthermore, it explores the different types of conductors, fixtures, dampers, etc, and states key issues and trends in OHLs.

Chapter 3 outlines the practical motivation and objectives of this study. It begins by introducing the applications of conductors in OHL systems, followed by an analysis of the challenges associated with operating OHLs under continuous electrical loading over extended periods. The chapter then explores the potential of HTLS conductors as a solution to these challenges. Various types of OHL conductors and techniques used for dynamic line rating (DLR) are presented, along with a discussion of their key characteristics and limitations.

Chapter 4 focuses on the design and laboratory characterisation of the fibre Bragg grating OHL sensor. In addition, this research provides a compact solution for using FBG sensors for OHL dynamic monitoring, allowing early warning signals to engineers about any changes in the operation of OHLs with changes in vibration, galloping, ice load, storms, and heat waves.

Chapter 5 presents a fatigue assessment of OHLs using an FBG sensor. The PNDC data have been utilised to develop the lifetime estimation methodology for the OHL sensor and the conductor based on the rainflow counting algorithm and Miner's rule with the S-N curve of the considered materials. Moreover, the calculation of fatigue on an example OHL conductor was done using the Poffenberger-Swart formula to estimate its lifetime.

Chapter 6 provides a comprehensive summary of the research findings, integrating the various lines of inquiry and examining their implications. The chapter concludes by offering recommendations that can guide future research in this area.

1.4 Associated Publications

The following publications have arisen from the work presented in this thesis:

1.4.1 Journal Publications

1. **Himanshi Singh**, Grzegorz Fusiek and Pawel Niewczas, "Methodological Framework for Conductor Lifetime Estimation Using Optical Sag Sensors," in IEEE Sensors Letters, 2024, doi: 10.1109/LSENS.2024.3415430.

2. **Himanshi Singh**, Grzegorz Fusiek and Pawel Niewczas, "Extended characterization of an optical sag sensor for high-temperature low-sag lines," IEEE Sensors Letters, 2023, doi: 10.1109/LSENS.2023.3300810.

1.4.2 Conference Publications

1. **Himanshi Singh**, Grzegorz Fusiek, Pawel Niewczas, and Valerie Livina, "Estimation of the Fatigue Life of a Fiber Bragg Grating Overhead Line Sag Sensor," IEEE Interna-

tional Instrumentation and Measurement Technology Conference (I2MTC), Glasgow, May 2024.

2. Grzegorz Fusiek, **Himanshi Singh** and Pawel Niewczas, “Temperature and force characterization of an optical sag sensor for overhead line monitoring,” in 2023 IEEE International Instrumentation and Measurement Technology Conference (I2MTC), Malaysia, May 2023.

References

[1] International Energy Agency. Global Energy Review 2025. Technical report, International Energy Agency, 2025.

[2] Konstantinos Kopsidas and Simon M. Rowland. Evaluation of potentially effective ways for increasing power capacity of existing overhead lines. In *2009 International Conference on Sustainable Power Generation and Supply*, pages 1–7. IEEE, 2009.

[3] CIGRÉ Task Force B2.11.04. Overhead conductor safe design tension with respect to aeolian vibrations. Technical Brochure 273, CIGRÉ, June 2005.

[4] IEEE Power Engineering Society, Transmission and Distribution Committee. IEEE guide on conductor self-damping measurements. IEEE Standard IEEE Std 563-1978, Institute of Electrical and Electronics Engineers, 1978.

[5] IEEE Power Engineering Society, Transmission and Distribution Committee. IEEE guide for laboratory measurement of the power dissipation characteristics of aeolian vibration dampers for single conductors. IEEE Standard IEEE Std 664-1993, Institute of Electrical and Electronics Engineers, 1993.

[6] Grzegorz Fusiek and Pawel Niewczas. Design of an optical sensor with varied sensitivities for overhead line sag, temperature and vibration monitoring. In *2022 IEEE*

International Instrumentation and Measurement Technology Conference (I2MTC), pages 1–6. IEEE, 2022.

[7] Heng Wang, Shijia Han, Li-Jun Lv, and Li-Jun Jin. Transmission line sag measurement based on single aerial image. In *2017 24th International Conference on Mechatronics and Machine Vision in Practice (M2VIP)*, pages 1–5. IEEE, 2017.

[8] Michał Wydra, Piotr Kisała, Damian Harasim, and Piotr Kacejko. Overhead transmission line sag estimation using a simple optomechanical system with chirped fiber bragg gratings. part 1: Preliminary measurements. *Sensors*, 18(1):309, 2018.

[9] Krzysztof Skorupski, Damian Harasim, Patryk Panas, Sławomir Cieszczyk, Piotr Kisała, Piotr Kacejko, Janusz Mroczka, and Michał Wydra. Overhead transmission line sag estimation using the simple opto-mechanical system with fiber bragg gratings—part 2: Interrogation system. *Sensors*, 20(9):2652, 2020.

[10] John Nelson, Grzegorz Fusiek, Lloyd Clayburn, Paweł Niewczas, Campbell Booth, Philip Orr, and Neil Gordon. Development and testing of optically-interrogated current sensors. In *2016 IEEE International Workshop on Applied Measurements for Power Systems (AMPS)*, pages 1–5. IEEE, 2016.

[11] Grzegorz Fusiek, John Nelson, Pawel Niewczas, Jussi Havunen, Esa-Pekka Suomalainen, and Jari Hällström. Optical voltage sensor for MV networks. In *2017 IEEE SENSORS*, pages 1–3. IEEE, 2017.

[12] Grzegorz Fusiek, Pawel Niewczas, Neil Gordon, Philip Orr, and Paul Clarkson. 132 kV optical voltage sensor for wide area monitoring, protection and control applications. In *2020 IEEE International Instrumentation and Measurement Technology Conference (I2MTC)*, pages 1–5. IEEE, 2020.

[13] Himanshi Singh, Grzegorz Fusiek, and Pawel Niewczas. Extended characterization of an optical sag sensor for high-temperature low-sag lines. *IEEE Sensors Letters*, 7(9):1–4, 2023.

2

High Voltage Overhead Line Technology

2.1 Introduction

Overhead lines have a long history, beginning with the first AC transmission in 1891 at 15 kV as shown in Figure 2.1.

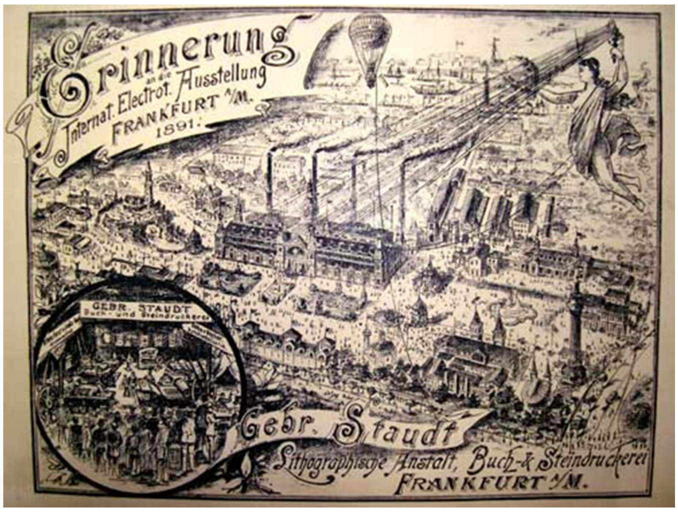

Figure 2.1: Postcard of first AC transmission line between Lauffen/Neckar to Frankfurt in 1891 [1].

Since then, technology has progressed, resulting in AC lines that can transmit voltages as high as 1000 kV and 1200 kV today, as shown in Figure 2.2.

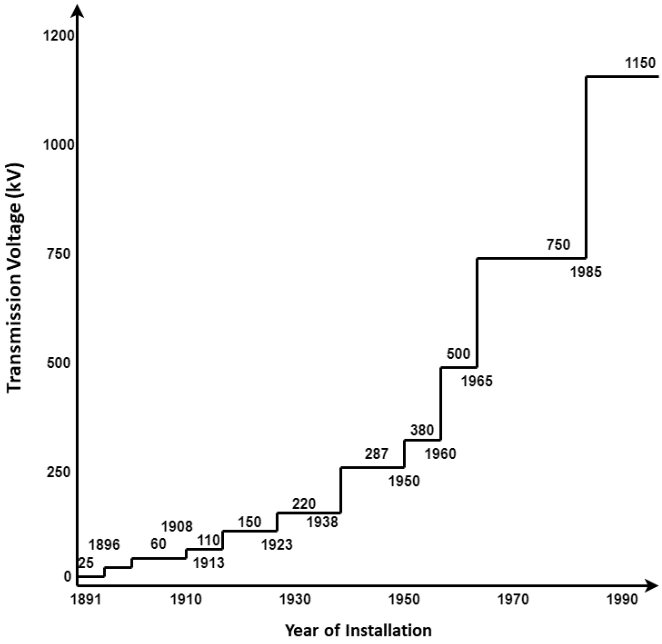

Figure 2.2: Development of overhead lines transmission voltage over the years.

This progression highlights the continuous advances in electrical engineering and the increasing demand for efficient high-capacity power transmission systems to meet the growing energy needs of modern society.

An overhead transmission line is a highly complex structure that often extends for thousands of kilometres, traversing various weather zones and enduring significant electrical, mechanical, and environmental stresses. Due to these factors, it is crucial to recognise the line as an integrated system from conception to decommissioning. Effective management practices must ensure that no aspect of the life cycle is compromised [2].

Reliable electric power transmission is essential for both current and future power grids. Over many decades, the system has been adapted to meet local constraints and preferences. In the coming years, a substantial increase [3]. This growing demand, combined with the integration of additional wind and solar energy production, is likely to cause congestion on numerous OHL [4, 5]. To address this issue, additional capacity can be achieved by improving operations, upgrading existing OHLs, or constructing new ones. The first two options are generally preferred due to the increasing opposition to building new OHL, particularly in densely populated areas.

Several methods are available to increase the capacity of OHL [6–8]. An approach, as described in [9], is to improve ampacity by using higher quality conductors or optimising operational procedures. Another strategy is to raise the voltage in transmission lines. In addition, more complex measures, such as converting alternating current (AC) overhead lines to direct current (DC), can significantly increase capacity.

The other options require substantial investments due to the requirement for different equipment and adherence to additional regulatory compliance. As a result, power-based solutions are often favoured since they can effectively increase capacity at potentially lower costs. These solutions can be divided into conductor and operation-based options.

Conductor-based solutions involve the installation of higher ampacity conductors where the supporting structures do not need significant reinforcement. However, this approach can be expensive due to the cost of new conductors and the prolonged line outage period required for installation. In rare cases, additional conductors or complete three-phase systems can be installed on existing structures. Re-tensioning existing conductors is a potential solution when the conductor is thermally rated for higher currents, but the resulting increase in sag at elevated temperatures would otherwise violate ground clearance requirements. By increasing the mechanical tension, sag can be reduced, thereby maintaining safe clearances while allowing for higher current carrying capacity.

To maintain proper sag and ground clearance, overhead lines are designed to operate at a maximum temperature. The conductor must withstand this maximum temperature without annealing and must not exceed a tolerable creep rate, such as HTLS conductors [8, 10]. The highest acceptable electric current for a specific overhead line is known as its thermal rating. The conductor's temperature is influenced by current and ambient conditions. Higher currents cause Ohmic heating, raising the conductor temperature, which can also be increased by solar radiation. Wind, ambient temperature, and heat emission help cool the conductor. Considering these ambient conditions, operation-based solutions can improve the capacity of overhead lines.

Traditionally, the worst-case scenario of high solar radiation, low wind, and high ambient air temperature is assumed when limiting the current to the maximum design temperature [11, 12]. Depending on regional conditions, this assumption may vary seasonally. The rating of an overhead line must be determined according to the area with the highest risk of overheating the conductor. However, this assumption is typically kept constant for each season or even longer periods, leading to what is known as static thermal line rating (SLR). While SLR simplifies current limitations over long periods, it has the disadvantage of unused capacity when worst-case conditions are not met. Conversely, if assumptions are not restrictive enough, the thermal rating can be exceeded under worst-case conditions, posing a risk [11].

Thermal dynamic line rating (DLR) adapts the thermal rating for shorter periods based on real-time or forecasted weather conditions [11]. This method is generally more accurate than SLR since worst-case conditions occur infrequently, allowing the full capacity of the overhead line to be utilised up to the maximum allowable conductor temperature.

DLR can also be used for load scheduling based on weather forecasts. However, the uncertainty in weather predictions, especially wind conditions, presents risks. Wind speeds significantly influence conductor temperatures but are difficult to predict and can vary along an overhead line. Real-time local weather conditions can help adjust the predicted DLR for better accuracy [11].

Various monitoring techniques can improve DLR accuracy. Weather data can be obtained from nearby weather stations or additional measurement equipment installed near the overhead lines. The real-time conductor temperature can be monitored directly on the conductor or by measuring the sag, regardless of weather conditions [11].

In general, increasing capacity through operation-based solutions results in higher conductor temperatures. However, if applied carefully, these methods ensure the maximum allowable temperature is not exceeded.

2.2 Classification of Overhead lines

From an electrical perspective, a transmission line is characterised by three distributed parameters: resistance (R), inductance (L), and capacitance (C), which are continuously spread along its length. These parameters govern the line's ability to transmit voltage and current and are central to power flow, voltage regulation, and loss calculations. Resistance and inductance constitute the series impedance, while capacitance, which exists between conductors in a single-phase line or from a conductor to neutral in a three-phase line, forms a shunt path along the line, as shown in Figure 2.3.

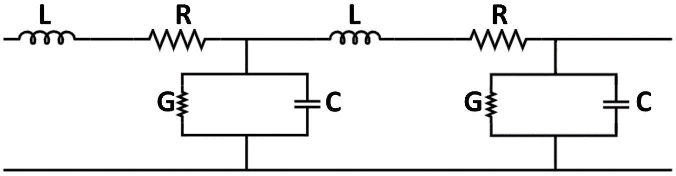

Figure 2.3: Voltage distribution connection of overhead lines.

These capacitance effects add complexity to transmission line calculations. However, when assessing the real-world performance and longevity of overhead lines, it is also essential to consider mechanical characteristics such as conductor tension, sag, span length, weight, and susceptibility to dynamic loads like wind-induced vibration. These mechanical factors are critical in evaluating structural reliability and fatigue life, particularly at attachment points such as suspension clamps, which are addressed in detail in later chapters.

The majority of insulation for overhead lines is provided by air, making it the most cost-effective method for transmitting large amounts of electric power. The supporting towers for these lines can be constructed from various materials, including wood, steel, concrete, aluminium, and occasionally reinforced plastics. The wire conductors are generally made of aluminium, either plain or reinforced with steel or sometimes composite materials like copper. Some copper wires are also used, particularly in medium-voltage distribution and low-voltage connections to customer premises, as illustrated in Figure 2.4. The comparison of overhead transmission lines has been shown in Table 2.1.

Table 2.1: Comparison of overhead transmission lines.

Transmission Line	**Voltage**	**Length**	**Effect of R, L, C**
Short Transmission Line	Below 20 kV	Up to 50 km	R & L
Medium Transmission Line	20 kV to 100 kV	50 km to 150 km	R, L, C
Long Transmission Line	More than 100 kV	More than 150 km	R, L, C

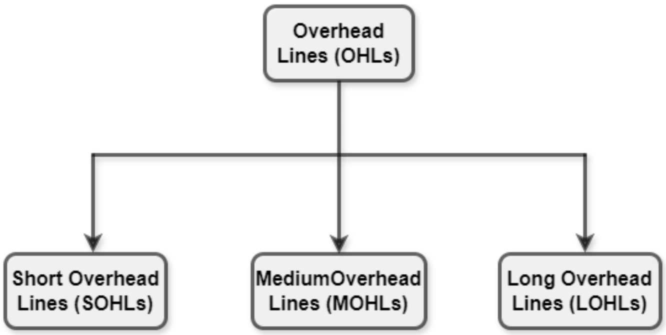

Figure 2.4: Classification of Overhead lines (OHLs).

2.2.1 Short transmission lines

In short transmission lines, typically less than 50 km in length and operating at voltages below approximately 20 kV, the effects of line capacitance are minimal. As a result, in the electrical modelling of such lines, capacitance is generally neglected. The simplified equivalent circuit includes only the series parameters, resistance and inductance, which have a more significant impact on voltage drop and power flow under these conditions.

2.2.2 Medium transmission lines

In medium transmission lines, the length of the overhead line ranges from approximately 50 to 150 km, and the line voltage is between 20 kV and 100 kV. Due to the sufficient length and voltage of the line, capacitance effects must be considered. To simplify calculations, the capacitance is divided and represented as condensers shunted across the line at one or more points.

2.2.3 Long transmission lines

When the length of an overhead line exceeds 150 km, and the line voltage is above 100 kV, it is classified as a long transmission line. In such cases, the line constants are assumed to be uniformly distributed along the entire length of the line.

2.3 Conductors, insulators, clamps, dampers

2.3.1 Conductors

A transmission line exhibits capacitive behaviour because it consists of conductors separated by air, which acts as a dielectric medium. The potential difference between conductors results in charge accumulation, making the line behave similarly to a distributed capacitor. The total line capacitance increases with the conductor length and decreases with greater spacing between conductors and distance to ground.

For short lines (typically <80 km), line capacitance is negligible and often omitted in simplified models. For medium-length lines (80- 250 km), capacitive charging current becomes noticeable, and for long lines (>250 km), especially high voltages (e.g., 400 kV and above), it becomes a dominant factor. In such cases, charging currents can reach 10-20 % of the total line current, reducing the line's active power transfer capability and affecting voltage regulation [13].

When multiple conductors are arranged in proximity, such as in bundled conductors or multi-circuit towers, mutual capacitance increases due to electric field coupling. This can elevate charging currents and introduce unbalanced voltages if the geometry is asymmetric. These effects are typically mitigated through conductor transposition, where phases are periodically swapped among physical positions on the tower (e.g., top, middle, and bottom) to equalise the average capacitance and impedance experienced by each phase. This improves voltage balance and reduces system losses [14].

It should be noted that increasing the height of conductors above ground may marginally reduce line-to-ground capacitance; however, it does not directly influence line tension. Line tension is a mechanical parameter determined by conductor span, weight, temperature, wind loading, and sag. Sag is intentionally introduced to control tension and prevent mechanical overstress of the conductors [15].

Therefore, the interaction between electrical and mechanical design parameters must be treated distinctly: capacitance affects electrical performance (current, voltage, losses), while tension and sag relate to structural integrity and mechanical safety.

OHL conductors play a crucial role in power transmission networks, carrying voltage and current waves along transmission lines. The choice of conductor type, dimensions, and electrical and mechanical properties significantly impacts the design of the transmission line. Bare conductors are classified into homogeneous and nonhomogeneous types [16]. Homogeneous conductors consist of the same strand material, whereas nonhomogeneous conductors (or composite conductors) are made of mixed materials to enhance mechanical and electrical properties. Transmission lines use two main types of overhead conductors: conventional and modified. Modified conductors are designed for specific applications and requirements and can operate at higher temperatures than conventional conductors. An efficient conductor should transmit electric power effectively, taking into account both implementation costs and electrical properties. The key characteristics of a good conductor include [16]:

- **Low thermal expansion:** Materials with a low thermal coefficient of expansion can withstand high temperatures with minimal sag.
- **Low electrical resistance:** Low electrical resistance (a result of both material conductivity and conductor geometry) reduces power losses and enables higher current ratings. This is often achieved by using materials with high electrical conductivity, such as copper or aluminium, and optimising conductor dimensions.

- **High strength:** Strong materials ensure the conductor can endure high operating temperatures and extreme weather conditions.

Conventional Conductors

Conventional conductors are made from various materials, featuring a round wire strand composed of multiple strands combined into a single conductor, as shown in Figure 2.5.

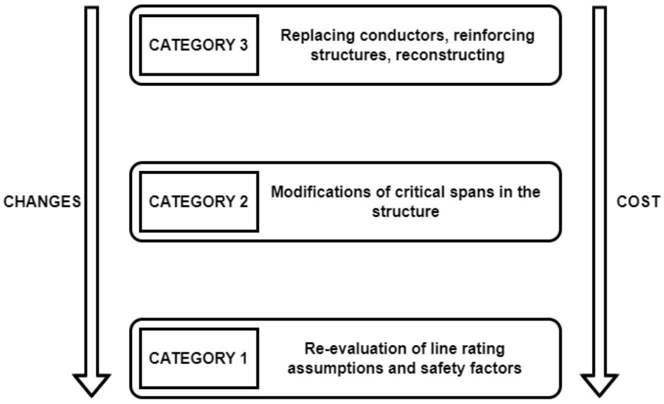

Figure 2.5: Classification of overhead line uprating methods according to the extent of physical modification and associated cost [17].

Common types of conventional conductors include all-aluminium conductor (AAC), all-aluminium alloy conductor (AAAC), aluminium-conductor alloy-reinforced (ACAR), aluminium conductor steel-reinforced (ACSR), and aluminium alloy conductor steel-reinforced (AACSR) [16, 18].

Typically, conventional conductors use all-aluminium alloy strands, with the aluminium core often replaced by materials like steel or alloy (e.g., in ACSR and AACSR) to enhance their electrical and mechanical properties. Aluminium wires have a high thermal expansion coefficient, causing faster expansion under high temperatures, and are prone to creep over time. In contrast, steel cores strengthen the conductor, bearing tensile loads and exhibiting low thermal elongation. Consequently, ACSR conductors are commonly used for bare overhead transmission lines due to several advantages [18]:

- The steel core in ACSR reduces elongation, minimising sag during operation.

- ACSR offers good conductivity and high tensile strength, making it suitable for icy and windy conditions.
- ACSR is more durable, with a fatigue life five times greater than AAAC, reducing the risk of breakage from falling tree limbs.

These benefits make ACSR a prevalent choice for overhead transmission lines. The standard operating temperature for conventional conductors ranges from 50 °C to 75 °C, depending on their size [19, 20]. However, some conductors can operate at higher temperatures due to uprating capabilities. For instance, the maximum continuous operating temperature for ACSR DRAKE 795 kcal (26/7) is 93 °C, with an emergency rating of 127 °C [21]. Nevertheless, to prevent annealing, the maximum operating temperature for conventional conductors should not exceed 75 °C. At elevated temperatures above 94 °C to 100 °C, aluminium strands begin to anneal, leading to a permanent reduction in mechanical strength due to microstructural changes caused by thermal stress.

According to the CIGRE technical brochure [22], the maximum allowable conductor temperature is set at 95 °C, provided the electrical clearance is not compromised. This condition can increase the thermal rating by 20 % to 40 % without replacing the conductor in overhead lines. However, continuous exposure to high temperatures may degrade the tensile strength of OHLs. Jakl et al. [23] suggest that non-homogeneous conductors possess better mechanical properties than homogeneous ones, allowing for higher operating temperatures without negative effects [15].

Selecting the appropriate conductor for installation is crucial, as it must withstand wind and weather loading and be suitable for the local terrain. For example, conductors near the coast face severe corrosion issues, making AAAC a preferable choice due to its superior anti-corrosion properties. AACSR conductors are ideal for extra-long spans, such as across rivers, due to their combination of high-tensile aluminium alloy and steel, providing higher tensile strength and moderate conductivity for electric current transmission.

Table 2.2 compares common conventional conductors and their applications in overhead lines.

Table 2.2: Comparison of common conventional conductors.

Conductor	**Material**	**Properties**	**Advantages**	**Disadvantages**
AAC	Outer and core: Al	Short span lengths, usually in urban areas.	Good corrosion resistance; conductivity is better than AAAC; lighter than ACSR.	Poor strength.
AAAC	Outer and core: Al alloy	Usually used in seacoast areas; more suitable for overhead distribution than ACSR.	Corrosion resistance is excellent; tensile strength is higher than AAC; resistance is lower than equivalent ACSR.	Conductivity and resistance to bending are moderate; prone to fatigue; expensive due to aluminium alloy.
ACAR	Outer: Al; core: Al alloy	Used for wide transmission lines.	Excellent corrosion resistance; higher strength; can be considered as a replacement for conventional ACSR.	Corrosion resistance is lower than AAAC.
ACSR	Outer: Al; core: galvanised steel	Used in rural distribution areas, long spans, river crossings, and ice and wind loading areas.	Low sag and excellent strength; good conductivity; higher durability than AAAC under bending stress.	Maximum operating temperature is 93 °C; limited for heavy-load operation; lower conductivity compared with ACAR.

High Temperature Conductors

The enhancement of conductor performance has been extensively studied in [16, 19, 24–32]. Conventional conductors have been modified to improve power transmission capabilities under specific conditions. These modifications include using different types of corrosion-resistant coatings, altering strand shapes, and changing the geometric configuration of conductors to optimise performance. These enhancements improve transmission lines' electrical and mechanical properties, enabling them to better resist strong winds (galloping), low wind speeds (aeolian vibration), ice loading, and high temperatures. Table 2.3 lists various high-temperature conductors and their categories.

Table 2.3: Different types of high-temperature conductors.

Group of conductors	**Conductors**	**Properties**	**Advantages**	**Disadvantages**
TW	ACSR, AAC, AAAC, ACSS	Reduced wind and ice loading effects.	Improves the mechanical and electrical properties of conventional conductors; lighter than equivalent conventional conductors; current-carrying capacity increases due to changes in conductor geometry; restricts creep over service life.	Used up to 16 kV lines; small conductors may be prone to corona; special equipment is required for manufacturing and geometric design during wire stranding, which can be prone to breaking.

Continued on next page

Table 2.3: Different types of high-temperature conductors continued.

Group of conductors	**Conductors**	**Properties**	**Advantages**	**Disadvantages**
TP	ACSR, AAC, ACAR	Anti-galloping behaviour and aeolian-vibration resistance.	Designed to prevent ice formation and reduce power losses.	Limited use for other applications; lower operating-temperature conductor; expensive installation and hardware.
HTLS	ZTACIR, GZTACSR, TACSR, ACSS, ACCR, ACCC, HDC	Used in high-load operation, windy areas, aeolian-vibration conditions, river crossings, and long-distance spans.	High conductivity, high-temperature operability, low sag, lighter weight, suitability for extreme weather, and reduced fatigue issues.	Expensive installation.

Altering the geometry of aluminium wires to a trapezoidal shape (TW) can reduce the outer diameter by 10 % compared to conventional round conductors [16]. This compactness allows more aluminium conductors to be added, increasing strength to endure icy and wind loads. TW conductors offer improved current-carrying capacity and reduced sag, making them ideal for high-temperature operations [18]. For example, ACSS/TW conductors have a reduced diameter and an increased operating temperature range from 200 °C to 250 °C without compromising mechanical properties [29]. TW conductors are also used in self-damping conductors like ASCR/SD to minimise size and enhance temperature gradient, resistance, and vibration resistance [25].

Motion-resistant conductors, featuring twisted-pair (TP) or oval arrangements, are designed to withstand extreme wind loads, addressing aeolian vibration and galloping issues. These conductors prevent fatigue, structural damage, and flashovers caused by high wind speeds. Motion-resistant conductors can include AAC, AAAC, ACAR, ACSR, ACSR/TW, and AAC/TW types, tailored to thermal and mechanical strength requirements [16]. The CIGRE WG 22.11.04 recommends safe design tension at average temperatures using specific conductors to mitigate aeolian vibration [33].

High-temperature low-sag (HTLS) conductors have gained popularity due to their high performance. Research on HTLS conductors covers performance [34–37], durability [24, 38, 39], economic cost [19, 40–42], ampacity increase [43, 44], and material properties [45–47]. HTLS conductors are designed to mitigate vibration and galloping effects while increasing current-carrying capacity to meet rising electricity demand. Although rated for high-temperature operation between 150 °C and 250 °C [48], they are fully capable of performing efficiently at lower temperatures under standard loading conditions. Table 2.4 shows the operating temperatures of various HTLS conductors, demonstrating their superior high-temperature capabilities compared to conventional conductors.

HTLS conductors are ideal for upgrading existing transmission lines due to their lighter weight, lower sag, and higher strength, even at the same diameter as ACSR. They also carry more current than conventional conductors. Recent studies on composite-core ACCC conductors indicate lower sag compared to ACSR when exceeding knee-point temperatures of 90 °C and 70 °C, respectively, due to ACCC's mechanical properties [36]. A detailed comparison between HTLS and ACSR conductors is discussed in [49].

HTLS conductors are engineered to withstand elevated operating temperatures while exhibiting minimal thermal expansion, thereby maintaining lower sag compared to conventional conductors. Their geometric and material design helps preserve ground clearance at higher temperatures, contributing to reduced structural loads and lower installation costs [49]. HTLS conductors are also manufactured using materials with high electrical conductivity and low resistivity, which helps minimise electrical resistance along the length of the conductor. This

Table 2.4: Configuration of HTLS conductors [16, 22, 50].

Type of conductors	**Material properties**	**Operating temperatures**
TACSR	Outer: thermal-resistant aluminium zirconium alloy and Core: galvanised steel reinforced	150 °C (continuous) and 180 °C (emergency)
TACIR	Outer: thermal-resistant zirconium aluminium alloy and core: aluminium-clad invar alloy/ zinc-coated invar alloy	210 °C (continuous)
HDC	Outer and inner: hard- drawn copper	180 °C (continuous) and 200 °C (emergency)

combination enhances their current-carrying capacity and overall transmission efficiency. HTLS conductors are the best solution for upgrading power lines from ACSR and for new high-voltage transmission lines. Reconducting existing lines with HTLS is more practical for improving power line capacity. The economic cost of reconductoring has driven new studies. The cost of reconductoring with HTLS is significantly lower than building new ACSR lines. A study on uprating a 220 kV double circuit to 1260 A compared several HTLS conductors with similar diameters to ACSR, finding that AC offers the lowest power losses due to its low resistance.

2.3.2 Insulators

According to [51], an insulator is defined as a “device intended for electrical insulation and mechanical fixation of equipment or conductors subjected to electric potential differences.”

In overhead lines, insulators primarily separate the system potential at the conductor from the earth potential at the support. The term ”insulator” comes from the Latin word ”insula,” meaning island, which itself derives from the Greek word ”níssos,” implying a piece of land separated by water from the mainland [52].

Insulators must handle electrical insulation under system voltage and overvoltages from lightning and switching operations. They also transfer mechanical loads from the conductor to the support, enduring adverse environmental conditions. A power flashover can occur under all three voltage scenarios, prompting the use of insulator protection fittings. Atmospheric pollution influences the shape of insulators, particularly their shed profile, which combats leakage currents due to surface contamination. While hydrophilic insulators rely on their shape for leakage current suppression, hydrophobic insulators use water repellency as their primary mechanism [52].

A 3 m column of air provides adequate insulation for a 400 kV AC conductor, but surfaces prone to outdoor contamination must offer at least three times that path length [53], adhering to required creepage distances based on local conditions. Mechanical integrity is crucial for the proper functioning of a line, as failure can lead to power loss and severe damage or injuries [52].

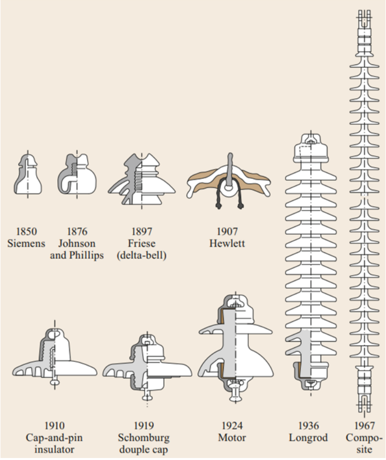

Figure 2.6: Historic high-voltage AC overhead line arrangement showing the geometry of early overhead line construction [52].

Insulators originated in telegraph-line applications and later evolved for DC and AC overhead line systems. Figure 2.6 shows an example of an early high-voltage AC overhead line arrangement, illustrating the historic geometry of overhead line construction rather than the detailed evolution of insulator designs [52].

Different types of insulators are defined in table 2.5.

Table 2.5: Summary of overhead line insulator types and typical applications.

Type	**Description**	**Application**
Porcelain insulator	Ceramic insulator commonly manufactured as cap-and-pin or long-rod units. It provides good electrical insulation and high mechanical strength [52].	Widely used in transmission and distribution lines. Long-rod porcelain insulators are suitable for polluted environments because of their aerodynamic profile [52].
Glass insulator	Usually manufactured as toughened glass discs or cap-and-pin units. Damaged units are often visually identifiable, since severely damaged units tend to shatter [52].	Commonly used in suspension strings where visual detection of failed units is useful during inspection [52].
Composite/polymeric insulator	Non-ceramic insulator consisting of a fibre-reinforced plastic rod, metallic end fittings, and polymer housing, commonly silicone rubber [?].	Used for compact lines, voltage uprating, polluted environments, and long-distance high-power transmission because of low weight, flexibility, and good pollution performance [52].

Continued on next page

Table 2.5: Summary of overhead line insulator types and typical applications continued.

Type	**Description**	**Application**
Bell-type insulator	Early porcelain insulator design used historically in overhead line and telegraph applications [52].	Largely replaced by cap-and-pin and long-rod designs for higher-voltage and higher-strength overhead line applications [52].
Cap-and-pin insulator	Modular disc-type insulator in which individual units are connected in series to form an insulator string [52, 54, 55].	Used in suspension and tension strings, particularly where modularity and replacement of individual units are required [52, 54, 55].
Long-rod insulator	Single-piece elongated insulator body fitted with metallic end connections. It may be made from porcelain or composite material [52].	Used where improved pollution performance and reduced puncture risk are required [52].
Post insulator	Rigid insulator designed to support conductors or fittings while resisting bending or compression loads [52].	Used in substations, compact line arrangements, insulating cross-arms, and support applications where bending loads are significant [52].
Tie insulator	Functional class of insulator loaded mainly in tension, such as suspension or dead-end insulators [52].	Used to suspend or terminate conductors and transfer tensile loads to the supporting structure [52].

Continued on next page

Table 2.5: Summary of overhead line insulator types and typical applications continued.

Type	**Description**	**Application**
Strut insulator	Functional class of insulator loaded mainly in compression, such as insulators used in insulating cross-arm systems [52].	Used where the insulator acts as a compression member within the support arrangement [52].
Beam insulator	Functional class of insulator loaded mainly in bending, such as vertical or horizontal post insulators [52].	Used where conductor loading produces bending stress in the insulator body [52].
Arcing distance	Shortest distance through air between the metallic end fittings of an insulator [52, 53].	Important for flashover performance under power-frequency, switching, and lightning overvoltage conditions [52, 53].
Creepage distance	Shortest path along the insulator surface between the end fittings [52, 53].	Critical for pollution performance because surface contamination and moisture can increase leakage current [52, 53].

2.3.3 Fittings

Overhead line fittings, also referred to as line hardware or accessories, provide the mechanical attachment, electrical connection, and protection required for conductors, insulators, and supporting structures. They may be used as individual components or as part of larger assemblies, such as suspension sets, tension sets, insulator strings, and conductor-connection systems [52].

Fittings are required to withstand mechanical, electrical, thermal, chemical, and environmental stresses during installation, operation, and maintenance. Their design must prevent damage to conductors, maintain adequate mechanical strength, minimise electrical losses and corona activity, resist corrosion and ageing, and allow safe installation and live-line maintenance where required [52]. In addition, compression fittings must be protected from contamination before installation, while non-metallic materials, such as elastomers, should be resistant to service temperature, ozone, ultraviolet radiation, pollution, and ageing [52].

The main types of fittings used in overhead line systems are summarised in Table 2.6.

Table 2.6: Summary of common overhead line fittings and their functions.

Fitting type	**Function**	**Examples**
Conductor fittings	Directly attached to conductors to suspend, terminate, join, protect, or space them.	Suspension clamps, dead-end clamps, connectors, branch-off clamps, vibration-protection fittings, bundle spacers, and repair sleeves [52].
Insulator set fittings	Connect suspension or tension insulators to the supporting structure and to conductor fittings. They also connect individual insulator units within a string.	Yoke plates, shackles, links, corona rings, grading rings, and arcing horns [52].
Suspension clamps	Support the conductor at suspension points while limiting conductor damage and fatigue near the clamp exit.	Require suitable curvature, rounded profiles, corrosion resistance, low contact resistance, and allowance for conductor movement under unbalanced loading [52, 56, 57].

Continued on next page

Table 2.6: Summary of common overhead line fittings and their functions continued.

Fitting type	**Function**	**Examples**
Tension or dead-end clamps	Terminate conductors at locations where the full mechanical tension of the span must be sustained.	Compression clamps, wedge clamps, helical terminations, and bolted clamps. Compression clamps are widely used, while wedge and bolted clamps allow sag correction by shifting the clamp position [58, 59].
Connectors and joints	Join sections of the same phase conductor or earth wire while maintaining electrical continuity and, where required, mechanical strength.	Full-tension compression joints and non-tension connectors such as parallel-groove clamps for jumpers [59].
Repair sleeves	Restore mechanical strength and electrical performance in damaged conductor sections.	Usually installed by compression and formed from interlocking elements [52].
HTLS conductor fittings	Provide suitable attachment and connection for high-temperature low-sag conductors.	Bolted clamps over armour rods, compression dead-ends, and spacers. Their performance is critical for long-term reliability at elevated operating temperatures [60].
Aircraft warning markers	Improve the visibility of overhead lines to low-flying aircraft.	Warning spheres and, in some regions, illuminated night warning devices [61].
Distribution-line fittings	Used for low-voltage and medium-voltage overhead distribution lines.	Shackles, post-insulators, soft wire bindings, stirrup-type bindings, and preformed wire wraps [62].

Continued on next page

Table 2.6: Summary of common overhead line fittings and their functions continued.

Fitting type	**Function**	**Examples**
Insulator protection fittings	Protect insulators against power arcs caused by overvoltages or pollution flashovers.	Arcing horns and rings transfer arcs away from insulator surfaces to reduce thermal overstress and preserve mechanical integrity [63, 64].

Among these components, suspension clamps and tension clamps are particularly important because they directly influence conductor stress distribution. Suspension clamps must support the conductor without introducing excessive local bending or strand damage, especially under vibration and changing mechanical load conditions. A typical suspension clamp used for overhead line conductor support is shown in Figure 2.7. Their geometry, including the body profile, keeper profile, exit angle, and turning angle, therefore plays an important role in reducing local stress concentration and fatigue risk, as shown in Figure 2.8 [52].

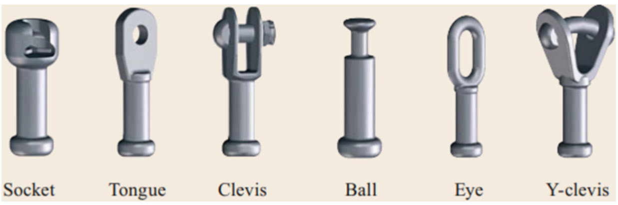

Figure 2.7: Suspension clamp used for overhead line conductor support [52].

Tension clamps, also known as dead-end clamps, are used where the conductor must be terminated and the full span tension transferred to the support. The main types are compression clamps, wedge clamps, helical terminations, and bolted clamps. Compression clamps are commonly used for transmission lines, whereas wedge and bolted clamps may allow sag correction by repositioning the clamp. Helical terminations use preformed rods to distribute gripping forces over a longer conductor length [58, 59].

Connectors, joints, and repair sleeves are used to maintain the electrical and mechanical continuity of conductors. Full-tension joints must sustain specified tensile loads while

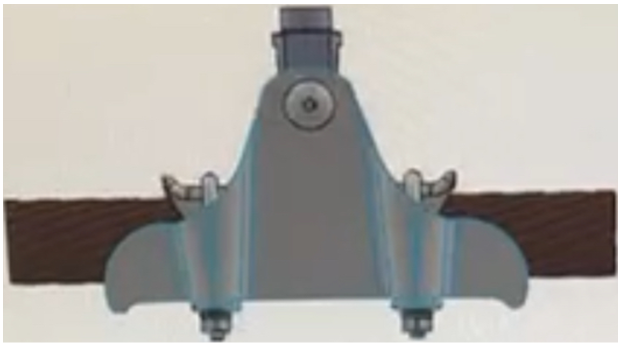

Figure 2.8: Mechanical configuration and angular parameters of a suspension clamp, including the exit angle, maximum exit angle, turning angle, and maximum turning angle [52].

maintaining acceptable temperature rise and voltage drop. Non-tension connectors, such as parallel-groove clamps, are commonly used for jumpers and branch connections. Repair sleeves are used where local conductor damage must be restored without replacing the entire spa [52, 59].

Protection fittings, including arcing horns, grading rings, and corona-control fittings, are used to control electric-field distribution and protect insulators from flashover-related damage. For composite insulators, direct attachment of power-arc protection devices to the end fitting is generally avoided where possible, since short-circuit current passing through the fitting can cause overheating, expansion, and loss of mechanical integrity [52, 63, 64].

Overall, overhead line fittings are essential for maintaining the mechanical and electrical integrity of transmission and distribution lines. Their selection and installation directly affect conductor reliability, insulator performance, vibration behaviour, corrosion resistance, and the long-term service life of overhead line assets.

2.3.4 Vibration Dampers

Wind-induced conductor vibration has been a long-standing concern in overhead transmission lines because repeated cyclic bending can lead to strand fatigue, damage near clamps, and, in severe cases, conductor failure. Vibration dampers are therefore installed to reduce aeolian vibration and to improve the mechanical reliability and service life of the line [52].

The most widely used device is the Stockbridge damper, originally patented by George H.

Stockbridge in 1928 [65]. It operates as a tuned mass damper, in which the damper weights act as secondary masses and the messenger cable provides elastic support. Vibrational energy from the conductor is transferred to the damper and dissipated mainly through friction between the strands of the messenger cable [52]. A simplified representation of the Stockbridge damper as a mass–spring mechanical system is shown in Figure 2.9.

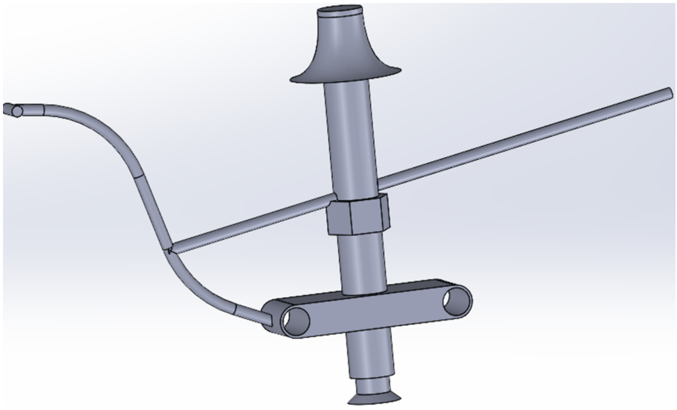

Figure 2.9: Stockbridge damper represented as a mass–spring mechanical system [52].

The damping performance depends on the damper mass, messenger-cable stiffness, geometry, moment of inertia, and the location of installation relative to the suspension clamp. The mechanical impedance of the damper should be suitably matched to the conductor wave impedance so that vibration energy is effectively absorbed rather than reflected [52, 66]. Damper placement is also important, as the damper must be positioned close enough to the support point to reduce bending stress at the clamp while remaining effective over the expected aeolian vibration frequency range.

The main damper types and their relevance to overhead line applications are summarised in Table 2.7.

Table 2.7: Summary of vibration dampers and related devices used in overhead lines.

Device	**Operating principle**	**Typical application**
Stockbridge damper	Acts as a tuned mass damper. The damper weights and messenger cable absorb conductor vibration energy, which is dissipated mainly through inter-strand friction in the messenger cable.	Most commonly used damper for reducing aeolian vibration and fatigue damage near conductor support points [52, 67].
Messenger cable and damper weights	The messenger cable provides flexibility and damping, while the attached masses determine the resonant behaviour of the damper.	Modern designs commonly use multi-strand messenger cables and damper weights made from zinc-aluminium alloys, cast iron, or forged steel [52].
Damper clamp	Connects the damper to the conductor and transfers vibration energy from the conductor to the damper.	Must provide secure attachment without causing conductor damage, corrosion, or excessive local stress concentration [52].
Alternative dampers	Includes Elgra, Haro, festoon, and torsional dampers.	Used in specific applications or countries, but they have not generally replaced the Stockbridge damper in widespread overhead line practice [52].
Spacer dampers	Maintain spacing between sub-conductors in bundled lines while also providing vibration damping.	Used in bundle-conductor systems to reduce sub-span oscillation, conductor clashing, and vibration-induced damage [52].

Dynamic testing is required to verify damper performance and fatigue resistance. Common test methods include the inverse standing wave ratio test, power test, decay test, and forced-response or shaker test [68]. The shaker test is widely used to evaluate the dynamic characteristics and long-term fatigue performance of dampers, as illustrated in Figure 2.10.

Figure 2.10: Shaker test setup for evaluating the dynamic performance of a Stockbridge damper [52].

In bundled conductor systems, spacers and spacer dampers are used to maintain conductor geometry and prevent conductor clashing during oscillations. Modern spacer dampers often incorporate elastomeric components to provide damping while maintaining axial and torsional grip on the sub-conductors [52]. Overall, vibration dampers are essential for limiting wind-induced vibration, reducing fatigue damage, and improving the long-term reliability of overhead line conductors.

2.4 Key issues and trends

Overhead lines are exposed to mechanical, electrical, thermal, and environmental stresses throughout their service life. These stresses can lead to degradation of conductors, fittings, joints, dampers, insulators, and supporting hardware. Reliable condition assessment is therefore essential for maintaining line safety, preventing forced outages, and supporting asset-life extension. The main issues and commonly used inspection methods are summarised in Table 2.8.

Among the degradation mechanisms affecting overhead lines, wind-induced vibration is particularly important because it links conductor dynamics with long-term mechanical damage. Wind-induced damage may result from aeolian vibration, subconductor oscillation, galloping, or related conductor motion, producing cyclic bending, local wear, fretting fatigue, strand breakage, and damage or displacement of dampers, clamps, spacers, insulator strings, and other line hardware. Identifying vulnerable spans and attachment points is therefore important for targeted inspection, maintenance planning, and fatigue-risk reduction [2, 69, 70].

Table 2.8: Summary of key degradation issues and inspection methods for overhead line components.

Component	**Typical problem**	**Inspection or mitigation method**
Corrosion	Steel corrosion is commonly caused by industrial or salt pollution in the presence of moisture. Aluminium corrosion may occur as pitting, bulging, or discolouration of conductor strands.	Steel corrosion may be detected using an overhead line corrosion detector (OHLCD), which applies eddy-current principles. Aluminium corrosion is commonly identified by visual inspection of the outer strands [52].

Continued on next page

Table 2.8: Summary of key degradation issues and inspection methods for overhead line components continued.

Component	**Typical problem**	**Inspection or mitigation method**
Wind-induced vibration damage	Wind-induced conductor motion, including aeolian vibration, subconductor oscillation, and galloping, can cause cyclic bending, fretting fatigue, broken strands, displaced or missing dampers, missing nuts, displaced corona rings, damaged insulator strings, shifted aircraft warning markers, and loose tower members.	Inspection may be carried out from the ground or by helicopter using visual assessment, stabilised video, corona measurements, or X-ray methods for detecting internal strand breaks [52, 70].
Conductor joints	Poor compression or incorrect installation of joints can increase electrical resistance, produce local overheating, and reduce mechanical integrity. In ACSR conductors, overheating of the steel core may increase the risk of rupture.	Joint condition is commonly assessed using electrical resistance measurement, infrared thermography, and temperature-difference methods for classifying fault severity [52, 71].
Aged fittings	Fittings in long-term service may suffer from corrosion, wear, reduced mechanical strength, or loss of residual life. This is particularly relevant for fittings that have been in service for more than 30 years.	Representative fittings may be removed from service and tested to assess residual strength and determine whether replacement is necessary [52, 72].

Continued on next page

Table 2.8: Summary of key degradation issues and inspection methods for overhead line components continued.

Component	**Typical problem**	**Inspection or mitigation method**
In-span work carts	In-span access can introduce additional mechanical loading on aged conductors, increasing the risk of conductor damage or failure during maintenance.	Conductor integrity should be assessed before work-cart use. Alternative access methods include bucket trucks, cranes, helicopters, and robotic inspection systems [52, 73].
Porcelain insulators	Failures may arise from vandalism, manufacturing defects, or corrosion of the steel pin, which can generate expansive corrosion products and radial cracking.	Inspection methods include visual inspection, voltage-drop measurement, electric-field measurement, infrared thermography, ultraviolet detection, and radio-frequency or microwave emission detection [52, 74].
Glass insulators	Glass units may shatter due to surface damage, discharge activity, or imbalance of internal stresses.	Visual inspection is often effective because damaged glass units are usually clearly identifiable. Additional electrical or thermal inspection may be used where required [52, 75].
Composite insulators	Composite insulators may degrade because of premature ageing, housing damage, moisture ingress, partial discharge, or internal manufacturing defects. These defects may be difficult to detect visually.	Inspection may include combined infrared and ultraviolet measurements, directional wireless acoustic emission, electric-field methods, and high-frequency high-voltage diagnostic tools [52, 74].

Overall, the degradation mechanisms summarised in Table 2.8 show that overhead line reliability depends on both electrical and mechanical condition. Corrosion, vibration fatigue, joint overheating, fitting ageing, and insulator degradation can all reduce asset performance and service life. Consequently, condition monitoring and targeted inspection are essential for safe operation, maintenance planning, and future uprating of overhead line systems.

2.4.1 Uprating and Upgrading

Ageing transmission infrastructure, increasing electricity demand, and the difficulty of obtaining approval for new overhead line routes have increased the need to maximise the use of existing overhead line assets. In many countries, a large proportion of transmission infrastructure was constructed during the 1950s and 1960s and is now approaching or exceeding its original design life. Consequently, utilities are required to extend asset life while also increasing power-transfer capability and maintaining acceptable levels of reliability and safety [52].

In this context, a distinction is made between *uprating* and *upgrading*. Uprating refers to increasing the electrical transfer capability of an existing line, usually by increasing current, voltage, or both. In practice, increasing ampacity is more common than increasing voltage because it can often be achieved within the existing line corridor [52, 76]. Upgrading, by contrast, focuses on improving the structural or electrical performance of the line to increase reliability and reduce the probability of failure, for example by strengthening components or designing for higher wind and ice loading conditions [2, 77].

The main drivers, definitions, and technical considerations associated with uprating and upgrading are summarised in Table 2.9.

Table 2.9: Summary of uprating and upgrading considerations for overhead lines.

Aspect	**Description**	**Key considerations**
Drivers	The need for uprating and upgrading is driven by ageing infrastructure, assets exceeding their design life, increasing power-transfer requirements, and difficulties in obtaining approval for new overhead line routes [52].	Life extension, capacity enhancement, asset condition assessment, and continued safe operation.
Uprating	Increases the electrical capability of an existing overhead line, usually by increasing current, voltage, or both. Increasing current capacity is generally more common than increasing voltage [52, 76].	Higher ampacity, increased conductor temperature, increased losses if resistance is unchanged, and greater dependence on conductor and fitting condition.
Upgrading	Improves the original structural strength or electrical performance of line components to increase reliability and reduce failure probability [52].	Structural reinforcement, improved component strength, increased reliability under wind and ice loading, and mitigation of ageing-related degradation.
Ampacity increase	Allows more current to be transmitted through the existing line corridor.	Requires assessment of conductor condition, clamp performance, actual design temperature, thermal limits, sag clearance, and additional power losses [52].

Continued on next page

Table 2.9: Summary of uprating and upgrading considerations for overhead lines continued.

Aspect	**Description**	**Key considerations**
Reliability improvement	Aims to increase line availability and reduce failure risk under mechanical and environmental loading.	May involve designing for higher return periods of wind or ice loads, reducing climatic load effects, or increasing characteristic strengths of line components [2, 77].

Overall, uprating and upgrading provide complementary approaches for improving the performance of existing overhead line networks. Uprating mainly addresses the need for increased power transfer, whereas upgrading focuses on reliability, safety, and structural resilience. Both approaches require accurate knowledge of conductor condition, fittings, thermal behaviour, mechanical loading, and remaining asset life.

2.5 Conclusion

This chapter has provided an overview of the history, design, materials, and applications of overhead transmission lines, which have been fundamental to electric power systems since their inception. Despite being a traditionally conservative industry, overhead lines and their components have seen significant innovations in recent decades. These include the introduction of composite insulators, high-temperature conductors, composite poles, and advanced erection and maintenance techniques supported by robotics. The industry has also embraced digitalisation, incorporating GPS-based geoinformation systems and asset management applications.

Overhead lines face acceptance issues in many countries, primarily due to their appearance and concerns about electromagnetic field health hazards. The industry has responded with aesthetic support structures and extensive research into health impacts. There is also a growing trend to place lines underground, weighing the pros and cons of overhead versus underground technologies.

Despite these challenges, the demand for new transmission corridors, especially in developing countries, and the need to replace ageing lines in Europe and North America, mean that overhead transmission will continue to dominate. There will be a shift towards extra high voltage (EHV), ultra-high voltage (UHV), and HVDC systems.

References

[1] Edison Tech Center. Lauffen to Frankfurt 1891: The Beginning of Modern Electric Power in the World, 2013. Image caption: “Erinnerung Internat. Electrot. Ausstellung Frankfurt A/M 1891. A keepsake postcard showing the electric lithography machines displayed at the event. Notice the lady proving electricity from afar.” Historical photos provided by the Historisches Museum, Frankfurt, Germany. Accessed: 2026-05-11.

[2] Konstantin O Papailiou. *Overhead lines*. Springer, 2021.

[3] ENTSO-E Regional Investment Plan. Continental central east. Technical report, 2018.

[4] Wilhelm Winter. European wind integration study (ewis). Towards a successful integration of large scale wind power into european electricity grids. final report. Technical report, 2010.

[5] Wilhelm Winter. European wind integration study (ewis). In *14. Kasseler Symposium Energie-Systemtechnik*, page 25, 2010.

[6] Sanna Uski-Joutsenvuo, Riku Pasonen, and S Rissanen. Maximising power line transmission capability by employing dynamic line ratings–technical survey and applicability in Finland. Technical report, 2013.

[7] R Stephen. Description and evaluation of options relating to uprating of overhead transmission lines. *Electra*, 2:1–7, 2004.

[8] CIGRE Working Group B2. 12. Guide for selection of weather parameters for bare overhead conductor ratings. Technical report, 2006.

[9] S. Guerard M. Norton R. Puffer A. Sorensen G. Aanhaanen M. Weibel P. Pramayon, P. Catchpole and K. Bakic. Increasing capacities of overhead lines needs and solutions. Technical report, CIGRE Session, 42(B2-108), 2008.

[10] CIGRE Working Group B2.42. Guide to the Operation of Conventional Conductor Systems Above 100 °C. Technical Brochure 643, CIGRE, 2015.

[11] S. Guerard M. Norton R. Puffer A. Sorensen G. Aanhaanen M. Weibel P. Pramayon, P. Catchpole and K. Bakic. Increasing capacities of overhead lines needs and solutions. Technical report, CIGRE Session, 42(B2-108), 2008.

[12] CIGRE Working Group B2.43. Guide for Thermal Rating Calculations of Overhead Lines. Technical Brochure 601, CIGRE, 2014.

[13] RK Rajput. *Power system engineering*. Firewall Media, 2006.

[14] Babar Noor, M Zulqarnain Abbasi, Shahryar Shafique Qureshi, and Sanaullah Ahmed. Temperature and wind impacts on sag and tension of AAAC overhead transmission line. *Int. J. Adv. Appl. Sci.*, 5(2):14–18, 2018.

[15] N Mohd Zainuddin, MS Abd Rahman, MZA Ab Kadir, NH Nik Ali, Zaipatimah Ali, Miszaina Osman, Muhamad Mansor, A Mohd Ariffin, M Syahmi Abd Rahman, Shamsul Fahmi Mohd Nor, et al. Review of thermal stress and condition monitoring technologies for overhead transmission lines: Issues and challenges. *IEEE Access*, 8:120053–120081, 2020.

[16] Southwire Company. Southwire Company Conductor Manual. Technical report, Southwire Company, Carrollton, GA, USA, 2018.

[17] Konstantinos Kopsidas and Simon M. Rowland. Evaluation of potentially effective

ways for increasing power capacity of existing overhead lines. In *2009 International Conference on Sustainable Power Generation and Supply*, pages 1–7. IEEE, 2009.

[18] Jerry M Hesterlee, Eugene T Sanders, and Frank R Thrash. Bare overhead transmission and distribution conductor design overview. *IEEE Transactions on Industry Applications*, 32(3):709–713, 1996.

[19] Somboon Nuchprayoon and Artitaya Chaichana. Cost evaluation of current uprating of overhead transmission lines using ACSR and HTLS conductors. In *2017 IEEE International Conference on Environment and Electrical Engineering and 2017 IEEE Industrial and Commercial Power Systems Europe (EEEIC/I&CPS Europe)*, pages 1–5. IEEE, 2017.

[20] VT Morgan. The thermal rating of overhead-line conductors part i. the steady-state thermal model. *Electric power systems research*, 5(2):119–139, 1982.

[21] Ibrahim Hathout, Karen Callery, Jessica Trac, and Tariq Hathout. Impact of thermal stresses on the end of life of overhead transmission conductors. In *2018 IEEE Power & Energy Society General Meeting (PESGM)*, pages 1–5. IEEE, 2018.

[22] CIGRE Working Group B2.12. Conductors for the Uprating of Existing Overhead Lines. Technical report, CIGRE, Paris, France, 2004.

[23] Franc Jakl and Andrej Jakl. Effect of elevated temperatures on mechanical properties of overhead conductors under steady state and short-circuit conditions. *IEEE Transactions on Power Delivery*, 15(1):242–246, 2000.

[24] Christian Kühnel, Richard Bardl, Dominik Stengel, Wilhelm Kiewitt, and Steffen Grossmann. Investigations on the mechanical and electrical behaviour of HTLS conductors by accelerated ageing tests. *CIRED-Open Access Proceedings Journal*, 2017(1):273–277, 2017.

[25] K Munaswamy and Asim Haldar. Self-damping measurements of conductors with circular and trapezoidal wires. *IEEE Transactions on Power Delivery*, 15(2):604–609, 2000.

[26] Gordon C Baker. ACSR twisted pair overhead conductors. In *2000 Rural Electric Power Conference. Papers Presented at the 44th Annual Conference (Cat. No. 00CH37071)*, pages B4–1. IEEE, 2000.

[27] Ahmad Alawar, Eric J Bosze, and Steven R Nutt. A composite core conductor for low sag at high temperatures. *IEEE transactions on power delivery*, 20(3):2193–2199, 2005.

[28] Konstantinos Kopsidas, Boudjemaa Boumecid, and Ian P Cooper. Overhead line design considerations for conductor creep mitigation. *IET Generation, Transmission & Distribution*, 10(10):2424–2432, 2016.

[29] FR Thrash. ACSS/TW-An improved high temperature conductor for upgrading existing lines or new construction. In *2001 Power Engineering Society Summer Meeting. Conference Proceedings (Cat. No. 01CH37262)*, volume 1, pages 182–185. IEEE, 2001.

[30] Michèle Gaudry, Francis Chore, Claude Hardy, and Elias Ghannoum. Increasing the ampacity of overhead lines using homogeneous compact conductors. *CIGRE 1998 session documentation. Report CIGRE 22*, 201, 1998.

[31] FR Thrash. ACSS/TW-An improved conductor for upgrading existing lines or new construction. In *1999 IEEE Transmission and Distribution Conference (Cat. No. 99CH36333)*, volume 2, pages 852–857. IEEE, 1999.

[32] K Kopsidas and SM Rowland. Evaluating opportunities for increasing power capacity of existing overhead line systems. *IET generation, transmission & distribution*, 5(1):1–10, 2011.

[33] CIGRE Working Group. Permanent Elongation of Conductors: Prediction Equation and Evaluation Methods. Technical Report 75, Electra, 1981.

[34] Somboon Nuchprayoon and Artitaya Chaichana. Performance comparison of using ACSR and HTLS conductors for current uprating of 230-kV overhead transmission lines. In *2018 IEEE International Conference on Environment and Electrical Engineering and 2018 IEEE Industrial and Commercial Power Systems Europe (EEEIC/I&CPS Europe)*, pages 1–5. IEEE, 2018.

[35] Igor Albizu, Elvira Fernández, Rafael Alberdi, Miren Terese Bedialauneta, and Angel Javier Mazón. Adaptive static line rating for systems with HTLS conductors. *IEEE Transactions on Power Delivery*, 33(6):2849–2855, 2018.

[36] Kun Qiao, Anping Zhu, Baoming Wang, Chengrui Di, Junwei Yu, and Bo Zhu. Characteristics of heat resistant aluminum alloy composite core conductor used in overhead power transmission lines. *Materials*, 13(7):1592, 2020.

[37] GS Shivashankar et al. Overview of different overhead transmission line conductors. *Materials Today: Proceedings*, 4(10):11318–11324, 2017.

[38] B Burks, DL Armentrout, and M Kumosa. Failure prediction analysis of an accc conductor subjected to thermal and mechanical stresses. *IEEE Transactions on Dielectrics and Electrical Insulation*, 17(2):588–596, 2010.

[39] Guoqi Zhao, Jiayi Wang, Wenfeng Hao, Ying Luo, and Guangping Guo. Creep life evaluation of aluminum conductor composite core utilized in high voltage electric transmission. *Polymer Testing*, 63:573–581, 2017.

[40] Ajay Kumar Jha and Saroj Shrestha. Application of high capacity conductors for uprating of existing transmission lines in nepal. *JournalNX*, 4(08):32–37, 2018.

[41] Semir Hadžimuratović. Financial impacts of replacing old transmission lines with aluminum composite core conductors. In *Advanced Technologies, Systems, and Applications III: Proceedings of the International Symposium on Innovative and Interdisciplinary Applications of Advanced Technologies (IAT), Volume 1*, pages 187–197. Springer, 2019.

[42] E Mateescu, D Marginean, G Florea, St IA Gal, and C Matea. Reconductoring using HTLS conductors. Case study for a 220 kV double circuit transmission line in Romania. In *2011 IEEE PES 12th International Conference on Transmission and Distribution Construction, Operation and Live-Line Maintenance (ESMO)*, pages 1–7. IEEE, 2011.

[43] S Favuzza, MG Ippolito, F Massaro, G Paterno, A Puccio, and G Filippone. A new approach to increase the integration of RES in a mediterranean island by using HTLS conductors. In *2015 IEEE 5th International Conference on Power Engineering, Energy and Electrical Drives (POWERENG)*, pages 272–277. IEEE, 2015.

[44] Aniket V Kenge, Sagar V Dusane, and Joydeep Sarkar. Statistical analysis & comparison of HTLS conductor with conventional ACSR conductor. In *2016 International Conference on Electrical, Electronics, and Optimization Techniques (ICEEOT)*, pages 2955–2959. IEEE, 2016.

[45] HE Dève. Importance of materials in composite conductors. *Electric Power Systems Research*, 172:290–295, 2019.

[46] Jacques Lobry and Daniel Guery. Theoretical study of dielectric breakdown in a new composite core HTLS conductor. *IEEE Transactions on Power Delivery*, 27(4):1862–1867, 2012.

[47] Miren T Bedialauneta, Igor Albizu, Elvira Fernandez, and A Javier Mazon. Uncertainties in the testing of the coefficient of thermal expansion of overhead conductors. *Energies*, 13(2):411, 2020.

[48] CIGRE. Guide for Qualifying High-Temperature Conductors for Use on Overhead Transmission Lines. Technical report, CIGRE, Paris, France, 2010.

[49] Manish Kumar and R Rahangdale. Comparative analysis of ACSR and HTLS conductor. *Int. J. Futur. Revolut. Comput. Sci. Commun. Eng*, 4(5):29–35, 2018.

[50] Ilie Ardelean, Marius Oltean, George Florea, Elena Mateescu, Daniel Mărginean, Ştefan Kilyeni, and Constantin Bărbulescu. Case study on increasing the transport capacity of

220 kV DC OHL Iernut-Baia Mare by reconductoring using LM technologies. In *2011 IEEE PES 12th International Conference on Transmission and Distribution Construction, Operation and Live-Line Maintenance (ESMO)*, pages 1–7. IEEE, 2011.

[51] International Electrotechnical Commission. International Electrotechnical Vocabulary (IEV) – Part 471: Insulators. Technical report, IEC, Geneva, Switzerland, 2007.

[52] Konstantin O Papailiou. *Springer Handbook of Power Systems*. Springer Nature, 2021.

[53] John ST Looms. *Insulators for high voltages*. Number 7. IET, 1988.

[54] International Electrotechnical Commission. Insulators for Overhead Lines with a Nominal Voltage Above 1000 V – Part 2: Insulator Strings and Insulator Sets for A.C. Systems – Definitions, Test Methods and Acceptance Criteria. Technical report, IEC, 1993.

[55] M. Ammann, K. O. Papailiou, P. Dallèves, M. Leva, and S. Villa. A New 400 kV Line with Compact Towers and Composite Insulated Cross-Arms. In *CIGRE Session*, Paris, France, 1998.

[56] CIGRE SC22 WG01. Guide on the use of bolted suspension clamps. in: Electra, vol. 123 (CIGRE, Paris 1989). Technical report, CIGRE Paris, 1989.

[57] CIGRE TB 174. Load control devices on overhead transmission lines (CIGRE, Paris 2000). Technical report, CIGRE Paris, 2000.

[58] Christian Hildmann. *Zum elektrischen Kontakt-und Langzeitverhalten von Pressverbindungen mit konventionellen und Hochtemperatur-Leiterseilen mit geringem Durchhang*. PhD thesis, Dissertation, Dresden, Technische Universität Dresden, 2016, 2017.

[59] CIGRE TB 216. Joints on transmission line conductors – field testing and replacement criteria (CIGRE, Paris 2002). Technical report, CIGRE Paris, 2002.

[60] CIGRE TB 341. Considerations relating to the use of high temperature conductors (CIGRE, Paris 2007). Technical report, CIGRE Paris, 2007.

[61] CIGRE TF B2.11.03. State of the art survey on aircraft warning markers. in: Electra, vol. 224 (CIGRE, Paris 2006). Technical report, CIGRE Paris, 2006.

[62] J. McCombe and F. R. Haigh. *Overhead Line Practice*. Macdonald, London, UK, 1966.

[63] CIGRE Working Group 22.03. Use of Stress Control Rings on Composite Insulators. Electra 143, CIGRE, Paris, France, 1992.

[64] CIGRE TB 365. On the use of power arc protection devices for composite insulators on transmission lines (CIGRE, Paris 2008). Technical report, CIGRE Paris, 2008.

[65] George H. Stockbridge. Overcoming vibration in transmission lines, July 1928.

[66] O Nigol, RC Heics, and HJ Houston. Aeolian vibration of single conductors and its control. *IEEE transactions on power apparatus and systems*, (11):3245–3254, 1985.

[67] George H. Stockbridge. Overcoming vibration in transmission lines. *Electrical World*, 86:1304–1305, 1925.

[68] International Electrotechnical Commission. Overhead Lines – Requirements and Tests for Stockbridge Type Aeolian Vibration Dampers. Technical report, IEC, 1998.

[69] CIGRE Task Force B2.11.04. Overhead conductor safe design tension with respect to aeolian vibrations. Technical Brochure 273, CIGRE, Paris, France, June 2005.

[70] N. Pouliot, G. Rousseau, A. Leblond, and S. Montambault. Portable x-ray system for in situ detection of broken ACSR strands at suspension clamps: Field results and introduction onto line scout roboting technology. In *CIGRE Session*, number B2-106, Paris, France, 2016. CIGRE.

[71] Yi Hu and Kai Liu. *Inspection and monitoring technologies of transmission lines with remote sensing*. Academic Press, 2017.

[72] CIGRE TB 477. Evaluation of Aged Fittings (CIGRE, Paris 2011). Technical report, CIGRE Paris, 2011.

[73] CIGRE TB 471. Working Safely While Supported on Aged Overhead Conductors(CIGRE, Paris 2011). Technical report, CIGRE Paris, 2011.

[74] CIGRE TB 481. Guide for the Assessment of Composite Insulators in the Laboratory After Their Removal from Service (CIGRE, Paris 2011). Technical report, CIGRE Paris, 2011.

[75] CIGRE TB 306. Guide for the Assessment of Old Cap and Pin and Longrod Transmission Line Insulators Made of Porcelain or Glass: What to Do and When to Replace (CIGRE, Paris 2006). Technical report, CIGRE Paris, 2006.

[76] CIGRE TB 294. How Overhead Lines are Redesigned for Uprating/Upgrading - Analysis of the Replies to the Questionnaire (CIGRE, Paris 2006). Technical report, CIGRE Paris, 2006.

[77] CIGRE TB 353. Guidelines for Increased Utilization of Existing Overhead Transmission Lines (CIGRE, Paris 2008). Technical report, CIGRE Paris, 2008.

3

State of the art in monitoring overhead line conductors for sag, dynamic rating, and structural health assessment

3.1 Introduction

Transmission lines are critical components of power grids because they connect generation sources to consumers and enable long-distance power transfer. The transition to a low-carbon energy system, increasing electricity demand, and the integration of bulk renewable generation require higher utilisation of existing transmission corridors, since constructing new overhead lines is often costly, time-consuming, and constrained by planning approval [1]. Increasing the transferred power normally increases conductor current, which raises conductor temperature and sag and may reduce ground clearance, particularly under variable wind, ice, snow, solar radiation, and ambient-temperature conditions [2]. In the UK, transmission lines mainly operate at 400 kV and 275 kV, while distribution levels include 132 kV, 33 kV, 11 kV, and 230 V; maintaining safe ground clearance is therefore essential during operation [3].

Overhead line sag is the vertical distance between the straight line joining two supports and the lowest point of the conductor. It is directly related to electrical clearance and is influenced by conductor tension, current, temperature, span length, weather loading, and creep [2, 4]. Dynamic line rating (DLR) has been developed to increase current-carrying capacity by using real-time or forecast information from weather stations, conductor-mounted sensors, and line-monitoring systems rather than relying only on conservative static ratings [5–9]. However, higher utilisation also requires closer monitoring of sag, conductors, towers, insulators, spacers, clamps, and fittings to maintain safety margins [9]. This chapter reviews methods for monitoring sag, applying DLR, and assessing structural health in overhead line conductors.

3.2 Sag Measurement

Sag occurs because a suspended conductor hangs below the level of its supports. Although sag reduces excessive conductor tension, excessive sag can compromise ground clearance and operational safety. Conductor elongation is controlled by elastic strain, thermal strain, and long-term creep, while wind and ice loads further modify the sag–tension state [4].

3.2.1 Sag Monitoring Techniques

Sag-monitoring methods are commonly grouped into direct and indirect approaches. Direct approaches measure the conductor shape or position using image, laser, LIDAR, GPS, or robotic systems. Indirect approaches infer sag from related mechanical, thermal, electrical, magnetic, or optical quantities, such as tension, temperature, tilt, vibration frequency, magnetic field, space potential, PMU data, RF path loss, carrier-signal behaviour, or optical strain response [3]. Table 3.1 summarises the main sag-monitoring approaches considered in this chapter.

Table 3.1: Summary of sag-monitoring methods for overhead lines.

Method	**Principle**	**Advantages**	**Limitations**
Aerial imaging and LIDAR	UAVs or helicopters acquire images, videos, or point clouds from which conductor position and clearance are extracted.	Non-contact and suitable for corridor inspection over long spans.	Provides measurements only during inspection and can be expensive for frequent monitoring [10–15].
Terrestrial optical and laser methods	Ground-based cameras, laser scanners, or infrared laser systems measure conductor position, clearance, or angular displacement.	Non-contact, relatively direct, and potentially accurate with good calibration.	Limited by access, line-of-sight, weather, vegetation, and installation geometry [16–20].
Line robots	Mobile devices installed on the conductor measure sag, inclination, temperature, current, or conductor geometry.	Can provide local real-time data from the line.	Contact-based, costly, and may require outage access or affect conductor loading [21, 22].
GPS	Differential or multiple GPS receivers estimate the conductor position and sag.	Suitable for remote spans and less affected by visibility constraints.	Usually contact-based and can require expensive receivers or signal processing [23–27].
Tension and temperature	Sag is calculated from catenary, parabolic, state-change, or sag–tension relationships using tension, temperature, loading, and span data.	Established engineering basis and compatible with line design calculations.	Accuracy depends on conductor model, installation history, creep, temperature, and loading assumptions [28–31].

Continued on next page

Table 3.1: Summary of sag-monitoring methods for overhead lines continued.

Method	**Principle**	**Advantages**	**Limitations**
Tilt, air pressure, and vibration	Sag is inferred from inclination, altitude difference, swing period, or vibration frequency.	Can be simple and suitable for line-mounted monitoring.	Usually contact-based and sensitive to span geometry, motion amplitude, and calibration [32–36].
Magnetic field and space potential	Electromagnetic field measurements are used to reconstruct conductor position or infer sag.	Non-contact methods can be useful where physical access is difficult.	Accuracy depends strongly on sensor placement, line geometry, current/voltage knowledge, and electromagnetic interference [37–41].
RF, PMU, and carrier-signal methods	Sag is inferred from RF path loss, PMU-derived resistance/temperature, or power-line carrier signal changes.	Can reuse communication or power-system measurement infrastructure.	Accuracy depends on propagation models, signal quality, line configuration, and calibration [42–46].
Optical methods	Fibre-optic sensors measure strain, temperature, phase, or backscatter changes related to sag.	High sensitivity, multiplexing capability, dielectric sensing medium, and suitability for high-voltage environments.	Requires fibre installation, interrogation equipment, calibration, and mechanical strain transfer [29, 47–49].

3.2.2 Direct Methods: Aerial, Terrestrial, Line-Robot, and GPS Approaches

Aerial methods use UAVs or helicopters to acquire images, videos, or LIDAR point clouds for conductor reconstruction and clearance assessment. Reported examples include UAV photogrammetry with image processing and random sample consensus, helicopter LIDAR for line–vegetation distance measurement, point-cloud classification, and UAV-based LIDAR or camera systems with reported errors ranging from sub-percent values to tens of centimetres depending on equipment and processing method [10–15, 50, 51]. These methods are valuable for inspection but normally provide sag only at the time and location of the flight, and repeated monitoring can be expensive [3].

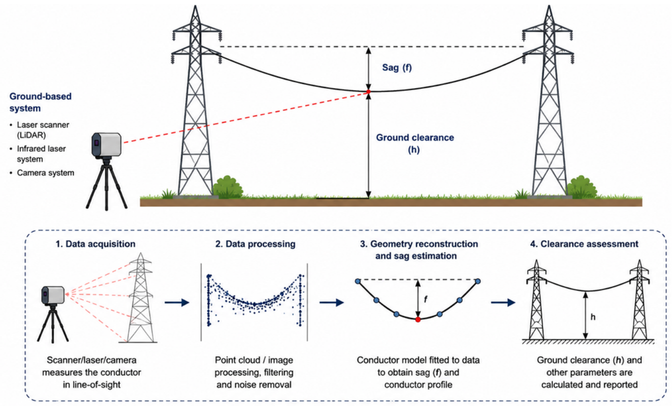

Figure 3.1: Schematic representation of a terrestrial method for overhead line sag and clearance assessment. A ground-based scanner, laser, or camera acquires line-of-sight measurements of the conductor, which are processed to reconstruct the conductor geometry and estimate sag and ground clearance [52].

Terrestrial methods use ground-based laser scanners, infrared laser systems, or cameras to estimate conductor geometry and sag, as shown in Figure 3.1. Infrared laser systems operating around 1550 nm have been used for sag, clearance, defect, and ice monitoring, while terrestrial laser scanning and camera-based systems have reported centimetre- to millimetre-scale laboratory or field accuracies depending on the setup [16–20, 53–60]. These systems are generally simpler than aerial surveys but can be affected by line-of-sight restrictions, weather, vegetation, and access to remote spans [3].

Line robots and GPS systems provide contact-based sag information. Inspection robots can move along a conductor and carry sensors for sag, temperature, current, inclination, or imaging, but their deployment is costly and may require outage access [21, 22]. GPS-based methods use one or more receivers mounted on the conductor, often combined with differential correction, least-squares estimation, wavelet processing, Kalman filtering, or bad-data rejection; reported accuracies range from centimetres to metres depending on the configuration and processing method [23–27, 61–65]. GPS methods can be useful for critical spans but are usually contact-based and require reliable communications and power [3].

3.2.3 Indirect Sag Estimation from Tension and Strain Measurements

Tension and strain-based sag estimation is an indirect measurement approach. In these methods, sag is not measured directly from the conductor profile or ground clearance; instead, it is inferred from conductor state variables such as horizontal tension, strain, temperature, conductor length, weight per unit length, and span length. The accuracy of the estimated sag, therefore, depends on the accuracy of the measured input quantities and the validity of the mechanical span model used.

Sag-tension calculations are commonly based on the catenary equation or its parabolic approximation. For a level span, the sag depends mainly on conductor weight per unit length, horizontal tension, and span length, and the parabolic approximation is sufficiently accurate when the sag is small relative to the span length [28, 29, 66]. The conductor profile and mid-span sag can be expressed as:

$$y(x) = \frac{H}{w}\left[\cosh\left(\frac{wx}{H}\right) - 1\right] \approx \frac{wx^2}{2H} \tag{3.1}$$

$$D = \frac{H}{w}\left[\cosh\left(\frac{wS}{2H}\right) - 1\right] \approx \frac{wS^2}{8H} \tag{3.2}$$

where D is sag, H is horizontal tension, w is conductor weight per unit length, S is span length, and x is the horizontal distance from the lowest point of the conductor. The conductor length may be approximated as:

$$L \approx S\left(1 + \frac{S^2w^2}{24H^2}\right) \tag{3.3}$$

or, in terms of sag,

$$L \approx S + \frac{8D^2}{3S}, \qquad D = \sqrt{\frac{3S(L-S)}{8}}. \tag{3.4}$$

Temperature and stress changes alter conductor length and therefore sag. A commonly used form is:

$$L_2 = L_1\left[1 + \alpha(T_2 - T_1) + \beta(\sigma_2 - \sigma_1)\right], \tag{3.5}$$

where subscripts 1 and 2 denote initial and final states, α is the thermal expansion coefficient, β is the elastic elongation coefficient, T is conductor temperature, and σ is conductor stress [28, 29]. Figure 3.2 illustrates the catenary geometry, while Figure 3.3 summarises the indirect sag-estimation process based on conductor state variables.

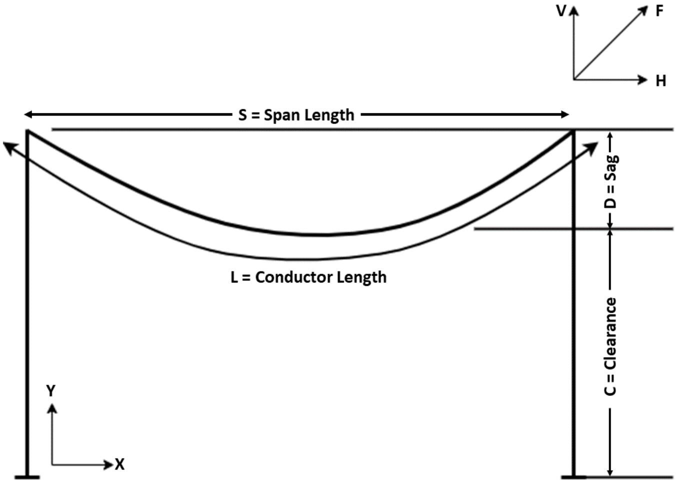

Figure 3.2: Catenary curve of a conductor suspended between two supports.

Strain-based sag estimation can be obtained by measuring conductor elongation between two sensor clamps. If the sensor is installed before tensioning and strain transfer is complete, sag may be estimated as:

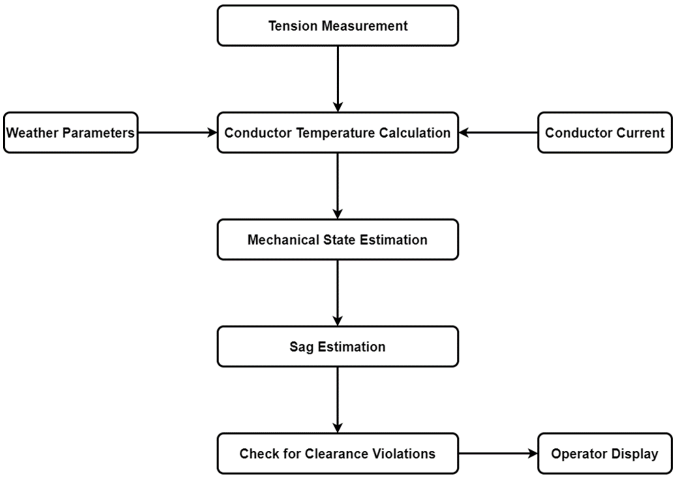

Figure 3.3: Sag estimation process based on conductor state variables [28, 29].

$$D = \sqrt{\frac{3S\left(L_c(1+\epsilon) - S\right)}{8}}, \tag{3.6}$$

where L_c is the initial distance between sensor clamps and ϵ is the measured strain. If the sensor is installed after the conductor is already tensioned, only changes in sag can be obtained unless the initial sag, tension, and conductor length are known.

3.2.4 Other Indirect Sag-Monitoring Methods

Temperature–current methods are indirect sag estimate approaches in which the conductor temperature is estimated from line current and thermal models, and then sag is calculated using sag–tension relationships. Real-time ampacity models have been used to predict conductor sag at elevated temperatures, while holistic models for HTLS conductors include structural, conductor, weather, electrical, mechanical, and ageing data [67–71]. Span-length and tilt methods are closely related to catenary-based geometry; they use span position, inclination, or tower/suspension angle to infer sag [32, 33, 72–75]. Air-pressure methods use two barometers to estimate the altitude difference between the conductor and support, but their accuracy depends strongly on barometer sensitivity because sag corresponds to a relatively small pressure difference [3, 34].

Magnetic-field methods use the field produced by a line current to estimate conductor position. The underlying relationship is commonly based on the Biot–Savart law,

$$\mathbf{B}_0 = \frac{\mu_0}{4\pi} \int \frac{I(\mathbf{l})\, d\mathbf{l} \times \mathbf{a}_0(\mathbf{l})}{|\mathbf{r}_0(\mathbf{l})|^2}, \tag{3.7}$$

which reduces for an ideal long straight conductor to:

$$B = \frac{\mu_0 I}{2\pi r}, \tag{3.8}$$

where $\mathbf{B}_0$ or B is magnetic flux density, I is current, r is distance from the conductor, μ_0 is permeability of free space, and $\mathbf{r}_0$ is the vector between the source and observation point. Magnetic field sensors have been used for non-contact clearance, current, ampacity, and sag estimation, including ground-based and support-mounted configurations [37, 39, 76–83]. Sun et al. used magnetoresistive sensors to measure the magnetic field at ground level and estimate conductor position and current through inverse electromagnetic calculation. The method was evaluated using a computational simulation of a 500 kV transmission-line configuration, and the calculated conductor positions were reported to have an average error of 6 cm, corresponding to 0.246 $\%$ [38].

RF, space-potential, PMU, and carrier-signal methods infer sag from electrical or communication quantities affected by conductor geometry. RF methods relate sag to changes in propagation path length, path loss, phase, or angle of arrival caused by changes in conductor position. However, their sensitivity depends strongly on the operating frequency, antenna geometry, propagation distance, and the magnitude of the sag-induced displacement relative to the total link distance. In free space, the received RF power decreases according to the free-space path loss relationship, while practical measurements are also affected by multipath propagation, atmospheric attenuation, rain, humidity, antenna alignment, and electromagnetic interference. Therefore, RF-based sag estimation requires site-specific calibration, reference measurements, and environmental compensation to distinguish sag-related variations from propagation and noise effects. Space-potential methods use electric-field coupling or induced currents, PMU methods estimate conductor temperature from resistance and then calculate sag, and power-line carrier methods use changes in modal propagation to infer conductor height [41–46, 84–93]. These methods are attractive because they may reuse existing electrical or communication infrastructure, but they require careful calibration and are sensitive to line geometry, signal quality, environmental conditions, and interference.

3.2.5 Optical Sag Monitoring

Sag and tension change the mechanical state of an overhead line conductor and can be monitored using fibre-optic sensors attached to, or integrated with, the conductor. In fibre Bragg grating (FBG) sensors, strain and temperature changes are transferred to the optical fibre, producing measurable Bragg wavelength shifts from which sag or tension can be inferred using suitable calibration.

Compared with RF, magnetic-field, space-potential, PMU, and carrier-signal methods, fibre-optic sensors provide strong practical immunity to electromagnetic interference because the signal is transmitted optically through a dielectric medium. This is particularly important for overhead line (OHL) monitoring, where sensors operate in the presence of high electric and magnetic fields. However, this immunity should be understood in a practical instrumentation sense rather than as an absolute absence of field interaction, since fused silica has a finite Verdet constant. In conventional FBG strain and temperature sensing, such magneto-optic effects are typically negligible unless deliberately exploited for magnetic-field or current measurement.

Chirped FBG and standard FBG systems have been used to measure conductor strain and infer sag, while distributed optical fibre sensors have also been investigated for photoelectric composite conductors and optical-fibre-integrated line structures [29, 47–49, 94]. For phase-sensitive optical time-domain reflectometry, sag has been related to optical phase change as:

$$S = \frac{\sqrt{3}\lambda L}{32\pi n}\Delta\theta + S_0^2, \tag{3.9}$$

where $\Delta\theta$ is the phase change, S_0 is the initial sag, L is the span length, n is the fibre-core refractive index, and λ is the optical wavelength [48].

Different types of sag-monitoring methods for OHLs have been discussed in Table 3.1. The FBG-based approach was therefore selected in this thesis because it directly addresses the requirements of OHL condition monitoring in high-voltage environments. It provides a dielectric sensing solution with practical immunity to electromagnetic interference, supports multiplexing and remote interrogation, and enables strain, temperature, and vibration-induced dynamic strain to be measured using a common optical platform. In addition, the proposed sensor is compatible with the wider FBG-based optical monitoring architecture developed by the Advanced Sensors Team at Strathclyde, allowing mechanical parameters such as sag and vibration to be integrated with optical voltage, current, and temperature measurements. The main research challenge is therefore not simply the use of FBGs, but the development of a mechanically robust, temperature-characterised, and field-deployable FBG sag sensor capable of providing reliable data for real-time condition monitoring and fatigue assessment.

3.2.6 Sag Prediction, Standards, and Industrial Devices

Sag prediction should be distinguished from sag estimation. Sag estimation determines the present conductor sag from current measurements, line geometry, conductor temperature, tension, or environmental conditions. Sag prediction, in contrast, forecasts future sag using present and historical measurements together with a predictive model. The methods reported in the literature include both deterministic thermal–mechanical calculation programs and data-driven forecasting models. For example, Bush et al. [95] experimentally verified a real-time program for determining conductor temperature and sag from line and environmental data, which is better described as real-time sag calculation rather than purely historical-data prediction. Tension-derived sag time series and applied chaos-theory-based phase-space reconstruction with singular value decomposition for short-term sag prediction were used in [96]. Predicted conductor sag within a dynamic line rating framework using conductor thermal behaviour and operating conditions in [97]. More recent data-driven approaches include support-vector-machine models optimised using particle swarm optimisation, such as the PSO–SVM method reported by [98]. Although sag prediction remains less mature than sag estimation, it is important for dynamic line rating, operational planning, and predictive maintenance.

Table 3.2: Summary of modelling approaches used for overhead line sag estimation and prediction.

Method	**Comment**
Real-time thermal–mechanical calculation program	Determines conductor temperature and sag from line data and environmental/loading conditions; better classified as real-time sag calculation rather than data-driven prediction [95].
Chaos-theory-based time-series prediction	Uses measured tension to calculate sag, reconstructs the sag time-series phase space using the C–C method, and applies singular value decomposition for short-term sag prediction [96].
Dynamic line rating-based sag prediction model	Predicts conductor sag using conductor thermal behaviour and DLR operating conditions [97].
PSO–SVM model	Uses a support-vector-machine regression model with parameters optimised by particle swarm optimisation for sag prediction [99].

Industrial devices and standards provide practical routes for sag monitoring and line operation. The EPRI video sagometer used cameras, conductor reference markers, and weather sensors for real-time sag monitoring, while modern systems increasingly integrate weather stations, conductor sensors, fibre optics, communications, and analytics platforms [100–104]. The Overhead Transmission Line Monitor (OTLM) developed by C&G Ljubljana measures temperature, wind speed, inclination, current, and humidity, transmits data using cellular, LoRa, WiFi, or satellite communications, and has been deployed on 110 kV transmission lines in Slovenia [3]. Other industrial systems include Ampacimon, Power Doughnut, SAGSEC, CAT-1, and Sagmeter, while IEEE Std 524-2016 and CIGRE Task Force B2.12.3 provide guidance for conductor installation and sag–tension calculations [105–112].

3.3 Dynamic Line Rating

Dynamic line rating adjusts the permissible loading of an overhead line using real-time or forecast information about conductor and environmental conditions, while maintaining safety margins [113, 114]. DLR is particularly valuable for renewable-rich systems because wind conditions that increase wind generation can also increase convective cooling of conductors, thereby increasing available ampacity [115–117]. Reviews have classified DLR methods by monitored variables, including weather, conductor temperature, sag, clearance, and tension, and have highlighted both implementation and operational challenges [5, 118–124].

The relevance of DLR to this thesis is through the mechanical-state monitoring route rather than through the development of a complete DLR forecasting algorithm. Weather-based and thermal-state DLR methods estimate allowable current mainly from environmental data and conductor heat-balance models, whereas this work focuses on direct optical measurement of conductor mechanical behaviour [116, 119, 122]. The FBG-based sag sensor developed in this thesis measures strain, temperature, and vibration-induced dynamic strain, which can be related to sag, conductor tension, and fatigue-relevant cyclic loading [125–127]. These measured quantities provide additional information for assessing whether increased loading leads to excessive sag, abnormal mechanical stress, or vibration-related damage. Therefore, the sensor system can complement DLR by providing field measurements for validation, condition monitoring, and operational confidence in real-time line-rating decisions [117, 123].

DLR methods can be grouped into ambient-state, thermal-state, and mechanical-state approaches. Ambient-state methods use weather variables such as wind speed, wind direction, solar radiation, and ambient temperature to calculate conductor temperature from heat-balance models. Thermal-state methods measure conductor temperature directly but may represent only local conditions. Mechanical-state methods use sag, clearance, tension, or vibration to infer the thermal and mechanical state of the line over a span [116, 119, 122]. DLR can reduce congestion, improve renewable integration, defer reinforcement, and increase operational flexibility, but its adoption depends on measurement reliability, modelling accuracy, operator confidence, protection coordination, and clear economic benefits [5, 117]. DLR is increasingly recognised as a viable option for enhancing power-system flexibility and transitioning to a smart grid [117].

DLR is increasingly recognised as a viable option for enhancing power-system flexibility and supporting the transition towards smart grid operation [117]. In this context, the FBG-based sensor developed in this thesis contributes to the mechanical-state monitoring aspect of DLR by providing direct measurements of strain, temperature, sag-related tension changes, and vibration under operating conditions.

3.3.1 Dynamic Line Rating of Overhead Lines

Dynamic line rating of overhead lines is based on conductor heat balance, which relates heat gains from electrical current and solar radiation to heat losses through convection and radiation [128–130]. In IEEE Std 738, the steady-state heat balance for a bare overhead conductor is commonly written as:

$$P_j + P_s = P_c + P_r, \tag{3.10}$$

where P_j is Joule heating, P_s is solar heating, P_c is convective cooling, and P_r is radiative cooling [6]. The CIGRE formulation may also include magnetic heating, corona heating, and evaporative cooling:

$$P_j + P_m + P_s + P_i = P_c + P_r + P_w, \tag{3.11}$$

where P_m is magnetic heating, P_i is corona heating, and P_w is evaporative cooling [128, 131]. The allowable current can then be estimated from the balance between heating and cooling terms, with conductor resistance evaluated at conductor temperature [113, 132–134].

The forced-convection heat loss, q_c, varies with wind speed and wind direction. IEEE Std 738 therefore provides two forced-convection correlations, corresponding to low- and high-wind-speed regimes as shown in Equations 3.12 and 3.13, respectively. As no fixed transition wind speed is specified, both correlations are evaluated, and the larger heat-loss value is selected [6, 114, 135].

$$q_c \approx K_{\text{angle}} \left[1.01 + 1.35 N_{Re}^{0.52}\right] k_f (T_s - T_a), \tag{3.12}$$

$$q_c \approx K_{\text{angle}}\, 0.647 N_{Re}^{0.6} k_f (T_s - T_a), \tag{3.13}$$

where K_{angle} is the wind-direction coefficient, N_{Re} is the Reynolds number, k_f is the thermal conductivity of air at the film temperature, T_s is the conductor surface temperature, and T_a is ambient temperature [6]. The wind-direction coefficient is given by:

$$K_{\text{angle}} = 1.194 - \cos\theta + 0.194\cos(2\theta) + 0.386\sin(2\theta), \tag{3.14}$$

where θ is the angle between the wind direction and conductor axis [6].

3.4 Structural Health Monitoring

Structural health monitoring (SHM) of power networks aims to detect degradation, support maintenance planning, and reduce the likelihood of forced outages. Power-grid components experience electrical, thermal, mechanical, and environmental stresses, including transformer heating and gas generation, tower deformation, foundation movement, galloping, icing, wind loading, and conductor temperature changes [136, 137]. Overhead transmission lines are particularly exposed because they operate over long distances and across varying terrain and weather conditions.

Overhead line conductors experience several forms of wind-induced motion. Aeolian vibrations are caused by vortex shedding and can occur on most overhead transmission lines under steady low-to-moderate wind speeds, typically about 1-7 m/s (2 mph to 16 mph). Small vertical oscillation amplitudes characterise them, usually of the order of the conductor diameter, and relatively high frequencies, commonly in the range of 3-120 Hz. Wind speed, conductor diameter, span length, and tension influence the vibration response. Prolonged aeolian vibration can cause fatigue damage near suspension clamps and fittings, and may also affect attached devices such as aircraft warning markers [138]. Galloping generally occurs under moderate-to-strong winds, typically above about 7 m/s (16 mph), when ice or wet snow accretion changes the conductor cross-section and produces aerodynamic instability. It is characterised by low-frequency, large-amplitude oscillations, often with amplitudes much larger than the conductor diameter. Although galloping events are less frequent and may last only a few hours, they can cause reduced phase clearances, flashover, conductor clashing, mechanical damage, outages, and, in severe cases, conductor or support failure [138]. Wake-induced or subspan oscillations occur mainly in bundled conductors, while turbulent buffeting is associated with strong-wind, low-frequency horizontal motion [138].

3.4.1 Condition Analysis of Overhead Lines

Transmission lines are inspected regularly to maintain information on asset condition and the surrounding environment. Inspections may be performed from aircraft, vehicles, foot patrols, climbing inspections, or specialised monitoring systems, and they support decisions on refurbishment, maintenance, and replacement of ageing assets [139, 140]. The main conductor, fitting, insulator, and support issues relevant to this thesis are summarised in Table 3.3.

Table 3.3: Summary of structural health issues in overhead line components.

Component / issue	**Typical degradation mechanism**	**Relevance to monitoring**
Conductor corrosion	Internal or external corrosion caused by salt, industrial pollution, moisture, zinc loss, steel exposure, or galvanic effects.	Can reduce mechanical strength and electrical conductivity; severe cases may cause overheating or tensile failure [140].

Continued on next page

Table 3.3: Summary of structural health issues in overhead line components continued.

Component / issue	**Typical degradation mechanism**	**Relevance to monitoring**
Wind-induced damage	Repeated conductor motion can produce fretting, fatigue damage, broken strands, displaced dampers, loosened hardware, and clearance reduction.	Important for fatigue assessment near suspension clamps, spacers, dampers, and other constrained locations [140, 141].
Lightning damage	Severe lightning strikes can cause pitting, melting, and strand breakage.	Reduces conductor cross-section and mechanical strength even when ground wires are installed [140].
Conductor joints and fittings	Incorrect compression, poor installation, corrosion, contact degradation, and AC corrosion can increase resistance and overheating.	Requires inspection and testing to determine whether fittings remain fit for service [102, 103, 140].
Porcelain and glass insulators	Porcelain can crack due to steel-pin corrosion, while glass units may shatter after surface damage or stress imbalance.	Failed units can reduce insulation strength and increase flashover risk [140].
Steel supports	Weather, altitude, pollution, surface protection, and delayed painting can accelerate corrosion.	Support degradation affects mechanical integrity and long-term line reliability [140].

Wind-induced damage in overhead line conductors is mainly caused by repeated conductor motion under wind loading. Aeolian vibration produces small-amplitude, high-cycle bending, particularly near suspension clamps and other attachment points, where it can lead to fretting, fatigue damage, broken strands, and eventual conductor failure. Galloping and subconductor oscillation generally involve larger-amplitude motion and can result in conductor clashing, reduced electrical clearances, displaced hardware, and increased mechanical loading. The severity of wind-induced damage depends on wind conditions, conductor tension, span length, conductor construction, clamp geometry, and damping performance [140, 141].

3.4.2 Fretting Fatigue and Conductor Fatigue

The fatigue endurance of conductor–clamp systems is a critical consideration during the design phase of transmission lines and remains a key factor in evaluating their remaining service life. The fatigue behaviour of stranded conductors is particularly complex and often manifests at locations where conductor movement is constrained, such as suspension clamps [3, 103, 137]. Since then, significant advancements have been made in the understanding, testing, and modelling of conductor fatigue [104].

Fretting fatigue occurs when small-amplitude oscillatory motion produces microslip at contact interfaces. In stranded conductors, this occurs between adjacent wires and between external wires and clamps, spacers, dampers, or other fittings. The process combines wear, oxidation, cyclic local stress, crack initiation, and crack propagation, making conductor fatigue more complex than conventional material fatigue [104]. Experimental testing remains important because conductor–clamp fatigue cannot yet be predicted reliably using only the material properties of individual wires [104, 142].

Fretting fatigue generally develops through a sequence of contact, crack-initiation, and crack-propagation stages. In the initial stage, small-amplitude relative motion between contacting wires disrupts the surface oxide layer and produces local adhesion, abrasion, and oxidation. This generates fretting debris and local surface damage. If the slip amplitude is sufficiently large, newly formed surface microcracks may be removed by wear before they propagate significantly; this corresponds mainly to a fretting-wear regime. However, when microcracks penetrate below the oxide layer and extend into the bulk material, the mechanism shifts towards fretting fatigue. In this stage, the contact stresses promote crack initiation, while the applied cyclic bending or tensile stresses drive crack growth. As the crack becomes deeper, the influence of the local contact stresses decreases, and the bulk cyclic stresses dominate the propagation process. The final stage is complete fatigue failure, which may occur once the remaining cross-section can no longer sustain the applied mechanical loading. Figure 3.4 illustrates these phases of fretting fatigue [104].

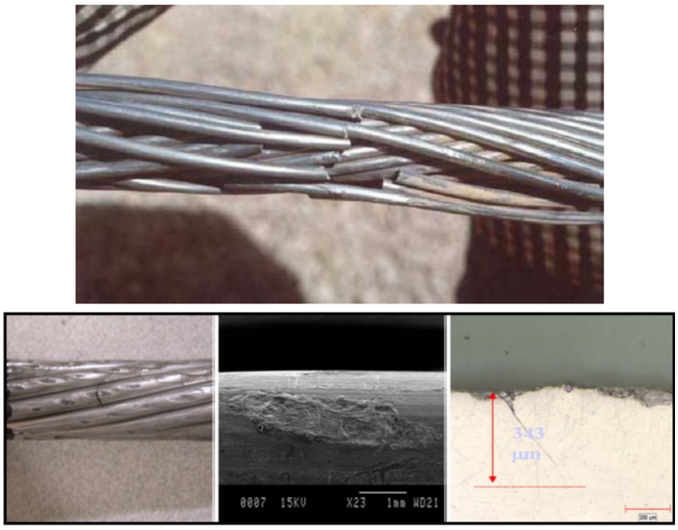

Figure 3.4: Schematic representation of the main phases of fretting fatigue, including surface damage and debris formation, microcrack initiation, crack propagation into the bulk material, and final fatigue failure [104].

Early studies identified fretting marks as crack-initiation sites in overhead conductor failures and showed that frictional corrosion significantly influences fatigue resistance [143–145]. Guidance on endurance testing has shown that fretting can occur between adjacent wire layers and between external wires and line accessories, while black aluminium oxide debris may indicate vibration-related fatigue activity within the conductor [104, 146]. The Poffenberger–Swart (P–S) formula relates measured bending amplitude at a specified distance from the clamp to dynamic bending stress in the outer strand, but this stress is not an exact representation of the local fracture process because fretting at inter-wire contacts also contributes to wire failure [147–150]. The bending amplitude Y_b is therefore often used as a practical indicator of vibration severity and micro-slip at critical conductor–clamp locations [151].

3.4.3 OHL Conductor Mechanics

Aeolian vibration contributes to conductor fatigue by producing repeated bending near suspension clamps and other attachment points. This process is closely associated with fretting fatigue, a chemo-mechanical damage mechanism involving cyclic contact, micro-slip, wear, oxidation, crack initiation, and crack propagation. The main factors influencing fretting fatigue, including contact pressure, slip amplitude, cyclic stress, material condition, environment, and conductor-clamp geometry, are summarised in Figure 3.5 [104, 152].

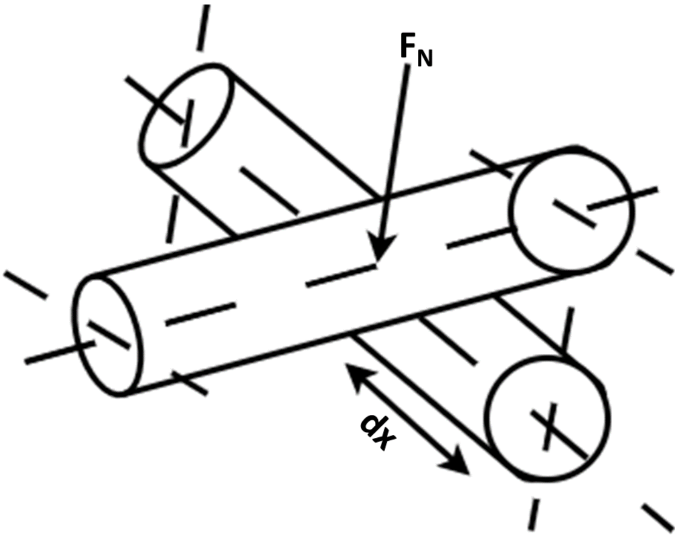

Figure 3.5: Wires in two adjacent layers experiencing a normal load F_N and relative displacement dx.

In stranded overhead conductors, fretting fatigue is governed by the interaction between global conductor loading and local wire-to-wire contact conditions. The most important mechanical factors are the macroscopic, or bulk, stresses in the individual wires; the relative movement, or micro-slip, between adjacent wires; and the normal forces between wires, which generate local contact stresses at crossing points [104].

In Figure 3.6, X_b denotes the distance from the last point of contact between the conductor and the suspension clamp to the point where the bending amplitude Y_b is measured. In the Poffenberger–Swart approach, this distance is standardised as X_b = 89 mm, equivalent to 3.5 in. The measured bending amplitude Y_b is then used to estimate the dynamic bending

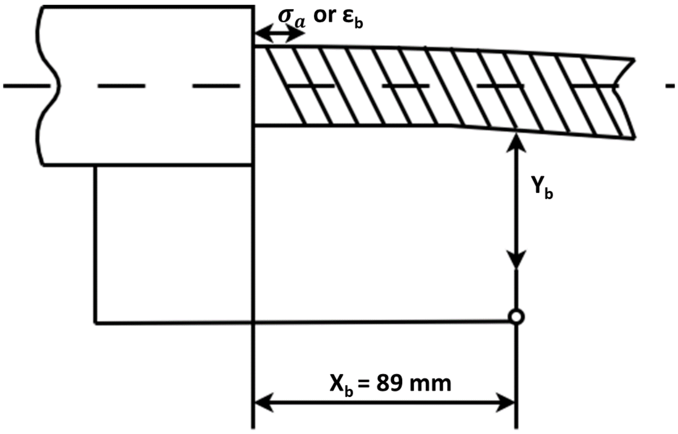

Figure 3.6: Explanation of the bending amplitude Y_b.

stress or strain in the conductor near the clamp [147, 153]. A linear correlation was established between bending amplitude and the strain measured on the conductor's surface adjacent to the clamp [104].

The bending behaviour of stranded conductors depends on the helical geometry, axial load, inter-wire friction, partial slip, and conductor–clamp boundary conditions. Theoretical models have represented no-slip, partial-slip, and full-slip behaviour using wire-bending equations, fibre effects, and bending-stiffness transitions from $B_{\max}$ to $B_{\min}$ [154–156]. Dynamic and static tests have related outer-wire strain, bending amplitude, equivalent stiffness, axial load, and boundary conditions, while finite-element and helicoidal models have shown that shear deformation and micro-slip reduce the effective flexural rigidity of the conductor [147, 157–162]. These studies provide the mechanical basis for interpreting vibration-induced strain and fatigue measurements, but further predictive modelling is still needed for practical conductor–clamp systems under field operating conditions [104, 163, 164].

3.4.4 OHL Conductor Bending Phenomenon

Aeolian vibration induces vertical oscillations in a tensioned conductor, resulting in cyclic bending near suspension clamps and other attachment points. Before this bending response is considered, the conductor is already subjected to an axial tensile load, which is distributed among the individual helical wires. Although this may appear to be a simple case of pure tension, the stress distribution in a stranded conductor is affected by wire material properties, lay angle, temperature, manufacturing history, and creep [165, 166]. For a simplified analysis, the tensile stress in an individual wire can be estimated using the approximate load-sharing relationship in Equation 3.15 [104, 165, 166].

$$\sigma_{T,w} = \frac{E_w \cos^2 \beta_l}{\sum_w E_w A_w \cos^3 \beta_l} T \tag{3.15}$$

where $\sigma_{T,w}$ is the tensile stress in wire w, E_w is the Young's modulus of the wire material, A_w is the cross-sectional area of wire w, β_l is the lay angle of the wire in layer l with respect to the conductor axis, T is the total axial tensile load applied to the conductor, and $\sum_w$ denotes summation over all wires in the conductor. The cosine terms account for the helical geometry of the wires and the projection of wire stiffness and force along the conductor axis. More detailed formulations may include Poisson effects and changes in wire curvature and torsion; however, these effects are generally secondary for the simplified stress estimate used here.

The tensile forces in the wires generate normal loads at the contact points between wires in adjacent layers, as shown in Figure 3.6. These loads contribute to contact stresses and influence the stick-slip behaviour of the wires during cyclic bending caused by aeolian vibrations [155]. When a conductor bends, the movement of its wires is initially restricted by friction forces, particularly between wires in adjacent layers. This situation is described by the equilibrium of axial forces within a differential wire element, as shown in Figure 3.7, where Z represents the tension in the wire, dZ is the tension differential along a differential length dx, dR is the friction force, and dN is the differential normal force at the crossover point with the underlying wire.

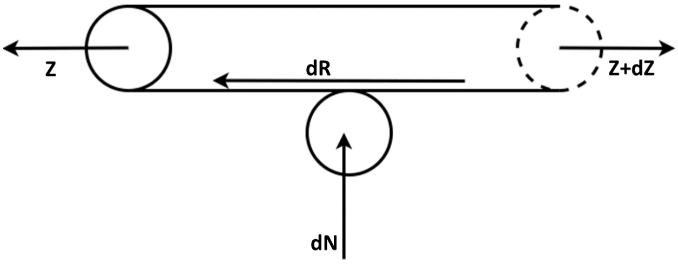

Figure 3.7: Equilibrium of axial forces in a differential wire segment.

This allows the wires to develop bending strain as if the conductor were a solid body with the wires adhering to each other. Beyond a certain curvature (or corresponding deflection), the interlayer friction forces become insufficient to prevent interwire movement, causing the wires to slip relative to each other. Their bending strain (and associated stress) then behaves as if they are bending around their neutral axis, while maintaining the maximum strain (and stress) value just before slipping, which is uniformly distributed across the wire cross-section, leading to secondary tensile stress. This process results in a variation in the conductor's bending stiffness during bending. The stiffness can be calculated at small bending amplitudes as if the wires are "welded" together, known as EI_{max}. At large bending amplitudes, the stiffness can be calculated as if the wires are completely loose, known as EI_{min}. Recent improvements to this model suggest that EI_{max} may never be fully reached [162]. Formulas for calculating EI_{max} and EI_{min} are provided in the equations 3.16 and 3.17 [104, 154, 155]. This variation in bending stiffness is also evident in the non-linear load-deflection curve of a conductor. It is a fundamental concept in the power dissipation mechanism of the messenger cable in Stockbridge dampers [104].

$$EI_{\text{min}} = \sum_{w} E_w \frac{\pi d_w^4}{64} \tag{3.16}$$

$$EI_{\text{max}} = EI_{\text{min}} + \sum_{l} \frac{n_l}{2} E_{w,l} A_{w,l} r_l^2 \cos^3 \beta_l \tag{3.17}$$

where $E_{w,l}$ and $A_{w,l}$ are the Young's modulus and cross-sectional area of the wires in layer l, respectively.

Due to the complexity of the bending process of a conductor under tension, as described above, a simplified model was developed in 1965 by Poffenberger and Swart [147]. This model has since been extensively used as a standard method for calculating "idealised" conductor stresses. These calculated stresses serve as a benchmark or "figure-of-merit" for comparing the vibration intensity of different conductors, as determined by bending amplitude measurements in the field. They also help assess these stresses against established safe or fatigue endurance limits, commonly represented by S/N (Wöhler) curves [153]. Such comparisons provide insights into the conductor's endurance capabilities.

The Poffenberger-Swart approach assumes that a vibrating conductor near the clamp behaves like a fixed cantilever beam under tension, with an imposed deflection (half the bending amplitude) at its free end. The bending stiffness of this beam is considered as the sum of the bending stiffnesses of the individual wires (assuming the wires are parallel and independent, with no interstrand friction), denoted as EI_{min}. Using the classic Bernoulli-Euler theory, the deflection curve near the fixed end (clamp) is calculated, which in turn allows for the calculation of the curvature at that point and the resulting stresses in the outer-layer wires. These wires are assumed to bend around their neutral axis, which coincides with their centre of gravity. The wire stress (or strain) formula derived from this method approximates the stress that would be obtained if the differential equation of a taut vibrating string with constant bending stiffness were used [152, 159]. The PS formula, which links measured bending amplitudes to calculated wire stresses in the outer conductor layer, is explained in equations 3.18 and 3.19.

$$\sigma_{PS} = \frac{E_a d_a p^2}{4\left(e^{-px_b} - 1 + px_b\right)} Y_b \tag{3.18}$$

$$p^2 = \frac{T}{EI_{min}} \tag{3.19}$$

Here, σ_{PS} denotes the dynamic bending stress amplitude estimated using the P-S formulation. E_a and d_a are, respectively, the Young's modulus and diameter of the outer-layer wire, Y_b is the measured bending amplitude, and x_b is the standard measurement distance from the last conductor-clamp contact point. The parameter p characterises the bending response of the tensioned conductor and is defined by Equation 3.19, where T is the axial conductor tension and EI_{min} is the minimum bending stiffness of the stranded conductor [104, 147].

The PS formula has been a cornerstone tool for assessing vibration severity in overhead line conductors for over 30 years. Its ease of application has led to its widespread adoption among researchers, becoming the de facto standard for calculating "nominal" conductor stress in the outer layer for a given measured bending amplitude. This standardisation has enabled valuable comparative analyses on the effects of certain vibration levels on the mechanical safety of a conductor, even if the results are not perfectly precise [104].

However, from the outset, there has been some unease regarding the ”universal” application of this formula without fully accounting for the approximations underlying its development. This concern is particularly relevant for small vibration amplitudes, which accumulate the highest number of cycles in the field and thus have a significant impact on conductor endurance. Even Poffenberger and Swart acknowledged in their seminal paper that there is a degree of uncertainty in this area [104].

The primary concern is that for small bending amplitudes, the individual strands of the conductor are expected to ”stick” together, causing the conductor to behave like a ”solid rod” with maximum bending stiffness. This would result in significantly higher stresses in the wires for small bending amplitudes than those predicted by the PS formula. As bending amplitudes increase, more wires slip, and the conductor’s bending stiffness approaches EI_{min}, making the PS formula a good approximation for outer layer wire stresses [104].

Various attempts have been made to address this issue, such as applying empirical factors to the bending stiffness, but none have gained widespread acceptance. Additionally, some studies [167] have presented strain measurement results on conductors that do not align well with the PS formula, but these findings have largely gone unnoticed. A notable discrepancy produced by the PS formula is that it results in different ”safe” vibration stress levels for multi-layer and single-layer conductors, differing by nearly a factor of three (8.5 MPa vs. 22.5 MPa) [152]. This suggests that the issue is related to wire contact conditions, which differ significantly between these two types of conductors [104].

Several reasons explain why the PS formula yields reasonable results when ”checked” in the laboratory through simultaneous bending amplitude and stress measurements, despite being based on crude approximations:

- The formula is often verified using conductors in commercial or custom-made suspension clamps, which deviate significantly from a fixed end, as assumed in the formula’s development. The measured stress, therefore, depends on the lateral distance of the strain gauge from the fixed end for the actual clamp, where the tangent to the deflection curve is horizontal. Even small deviations from this point can cause stress values to decline exponentially with distance, aligning more closely with the PS formula.

- The maximum stress in the wires may not occur at the wire top, where strain gauges are typically placed, because this stress depends on both the magnitude and direction change of the strand curvature vector. This results in measured values that tend to be lower than the actual maximum wire stress values, making them closer to those predicted by the PS formula.
- In short laboratory spans, compared to field conditions, tensile stresses in individual wires can differ by up to 100 %, even though the sum of these stresses over the conductor cross-section will match the external tensile load. Bending stresses, which depend on tensile stresses, may thus show much lower values in some wires closer to the PS stress values than expected by the stick-slip model.

These observations should not be seen as criticisms of the Poffenberger-Swart formula, which remains invaluable, but rather as an acknowledgement of the complexity of the issue, the limitations of the simplified conductor model, and potential areas for future research [104].

3.4.5 Bending amplitude measurement devices

The dynamic bending strain measured at the mouth of the suspension clamp is a critical parameter related to conductor fatigue, shown in Figure 3.8.

Early measurements of this strain involved placing strain gauges as close as possible to the points of maximum bending [168, 169]. While effective for laboratory tests, this method posed significant challenges when applied in the field [104].

In 1963, [170] introduced a more practical approach, proposing the use of a parameter directly related to the bending strain at the mouth of the suspension clamp, known as the bending amplitude Y_b. Ontario Hydro successfully used this method for 25 years, and [170]

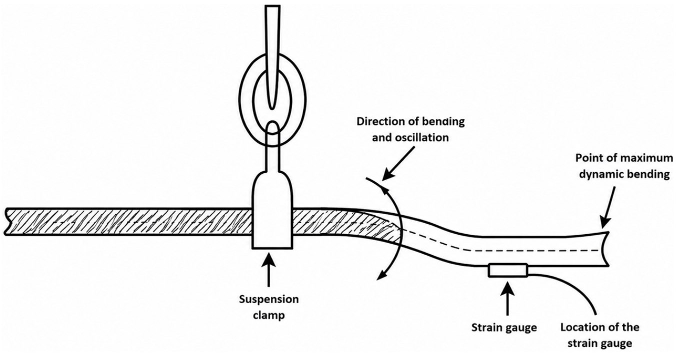

Figure 3.8: Schematic of dynamic bending strain measurement at a suspension clamp.

also developed the first live-line recorder designed to measure bending amplitude at the suspension clamp [104].

In 1966, the IEEE Task Force on the Standardisation of Conductor Vibration Measurements recommended the bending amplitude method as a practical means of assessing the fatigue exposure of overhead conductors in conventional suspension clamps [151]. They suggested an approximate equation to convert bending amplitude into bending strain and proposed evaluation criteria based on the maximum allowable bending strain [104].

The dynamic deflection field of a conductor near a fixed clamp was further developed to relate bending amplitude to dynamic curvature and bending stress in the outer-layer strands at the mouth of a conventional metal-to-metal suspension clamp [104, 147].

In 1981, an alternative method known as the inverse bending amplitude method was proposed, together with the associated Roctest TVM 90 measuring device. This recorder measured conductor motion directly above the last point of contact between the conductor and the clamp. In many cases, the inverse bending amplitude could be converted into bending amplitude or bending stress to align with IEEE standardisation. This development also supported improved data reduction for conductor vibration analysis, with results analysed in situ and recorded in a frequency–amplitude matrix [104, 162].

Bending-amplitude recorders can be categorised into analogue and digital devices. Analogue recorders, such as the Ontario Hydro Recorder and High Line Data Acquisition System (HILDA), provide time histories of conductor vibration, although they often require extensive data processing. Digital recorders, including the Pavica, Vibrec 400, Ribe LVR, Scolar III, and Eskom Vibration Recorder, offer more advanced capabilities, such as microprocessor-based processing, built-in memory storage, and direct connection to computers for data setup, retrieval, and analysis [104].

The standardisation of conductor vibration measurements has allowed the industry to compare results from different operating conditions. A method for estimating conductor lifetime under aeolian vibration was recommended using bending-amplitude measurements and Miner's rule to calculate the expected lifespan of conductors subjected to complex bending-strain spectra [146]. A comprehensive guide for performing vibration measurements on overhead conductors using bending-amplitude recorders was also provided [104, 153].

Bending amplitude recorders are typically mounted on the suspension clamp, except the Pavica recorder, which is designed for direct installation on the conductor itself. The "lever arm," or the distance between the sensor tip (or recorder position in the case of Pavica) and the last point of contact between the conductor and the suspension clamp, is ideally maintained at a standard distance of 89 mm. However, this may not always be feasible, such as with rubber-lined clamps with helical rod attachments or with long suspension clamps used in crossing spans [104].

When helical rods form a cage around the clamp, the sensor is positioned outside the cage area. The Pavica recorder has been applied along the helical rods, at their ends, and near the spacer damper clamps. If the lever arm is set at a distance other than 89 mm, the recorded amplitudes can be converted to the corresponding bending amplitude or bending strain values using the Poffenberger and Swart theory, taking into account the actual distance of the sensor tip from the suspension clamp [104].

Ontario Hydro and Alcoa provide correction curves for such cases, while other digital recorders can perform these conversions during data processing through their utility software. The IEEE suggests that the effect of a shift in lever arm distance can be approximately corrected by multiplying all recorded amplitudes by $(89/xb)^2$, where xb is the actual lever arm distance [104].

The 89 mm distance is chosen to ensure a measurable displacement while keeping the sensor tip in a conductor zone where the shape during vibration is governed by stiffness effects rather than by inertial forces in the vibration loops. Recorder manufacturers should provide recommendations for easily evaluating the maximum allowable distance between the sensor tip and the suspension clamp for each type of conductor and its relevant tensile loads [104].

3.4.6 Bending amplitude measurement at antinode position

Aeolian vibrations on OHLs can be monitored using various instruments such as vibration detectors, wireless vibration recorders, and optical monitoring devices, including FBG sensors for structural health monitoring. Measuring strain on the conductor's surface helps identify dynamic characteristics associated with vibration modes. While laboratory testing often employs high-resolution data acquisition platforms such as LabView with PXI hardware, field-deployable systems typically rely on embedded microcontrollers, industrial DAQs, or remote sensing units that are tailored for long-term, in-situ monitoring.

The fatigue of the conductor is assessed based on two approaches: the maximum bending amplitude and the maximum antinodal amplitude, as shown in Figure 3.9.

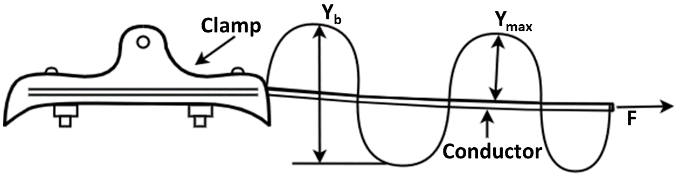

Figure 3.9: Depiction of bending amplitude and maximum antinode amplitude across the OHL span

The maximum strain occurs at the antinode locations, which can be calculated using the following formula in equation 3.20:

$$x = \frac{L(k - 1/2)}{n} \tag{3.20}$$

where k ranges from 1 to n.

Assume that the conductor is straight and vibrates in the form of standing waves. Additionally, assume that the supporting clamp is rigidly fixed and that the area near the clamp, where the conductor's shape deviates significantly from a sine-shaped loop, is relatively short compared to the loop's length. The conductor's axis, horizontal at the clamp, gradually aligns with the sine-shaped loop as the distance from the clamp increases. The bending moment at any cross-section is equal to the tension H multiplied by the deviation y_t of the conductor's axis from its line of action.

The curvature of the conductor is given by equation 3.21:

$$\frac{d^2 y_t}{dx^2} = \frac{M}{EI_{\text{min}}} \tag{3.21}$$

where M is the local bending moment and EI_{min} is the flexural rigidity. Since $M = H \times y_t$, equation 3.20 becomes as per equation 3.22:

$$\frac{d^2 y_t}{dx^2} = \frac{H}{EI_{\text{min}}} \times y_t \tag{3.22}$$

Thus, $y_t = A \times e^{\pm px}$.

The angle of the conductor axis relative to the tension's line of action is given in equation 3.23:

$$\frac{dy_t}{dx} = -pA \times e^{-px} \tag{3.23}$$

The slope at $x = 0$ (at the clamp, relative to the line of action) is equal to the angle and the curvature of the conductor as it emerges from the clamp is given in equation 3.24:

$$\left(\frac{d^2 y_t}{dx^2}\right)_{x=0} = p\beta = \beta\sqrt{\frac{H}{EI_{\text{min}}}} \tag{3.24}$$

The node angle corresponds to the maximum value of $\frac{dy}{dx}$, calculated as given in equation 3.25:

$$\beta = \frac{2\pi f y_{\text{max}}}{\sqrt{H/m}} \tag{3.25}$$

Therefore, the curvature and bending moment of the conductor at the clamp are given in equations 3.26 and 3.27:

$$\left(\frac{d^2 y_t}{dx^2}\right)_{x=0} = 2\pi\sqrt{\frac{m}{EI_{\text{min}}}} \times f \times y_{\text{max}} \tag{3.26}$$

$$M_0 = EI_{\text{min}} \times \left(\frac{d^2 y_t}{dx^2}\right)_{x=0} = 2\pi\sqrt{m \times EI_{\text{min}}} \times f \times y_{\text{max}} \tag{3.27}$$

The maximum bending amplitude is calculated during vibrations and uses the Poffenberger-Swart formula to estimate the fatigue stresses of the conductor. The maximum antinodal amplitude calculates the bending strain using wind-induced vibration frequency and the maximum antinodal amplitude to determine the conductor's fatigue in terms of bending stress, as follows: equations 3.28 and 3.29:

$$\varepsilon_b = \pi \times D \times \sqrt{\frac{m}{EI_{\text{min}}}} \times f \times Y_o \tag{3.28}$$

$$\sigma = \varepsilon_b \times E_{\text{Cu}} \tag{3.29}$$

where ε_b is the maximum bending strain of the conductor, D is the diameter of the conductor, Y_o is the maximum amplitude at the antinodal position, E_{Cu} is the modulus of elasticity of copper, and f is the vibration frequency.

The preceding discussion shows that fatigue assessment of OHL conductors requires accurate measurement of bending strain, vibration frequency, and conductor response near critical regions such as suspension clamps. Conventional vibration and bending-amplitude methods provide the mechanical basis for estimating fatigue stress, but their practical application in the field depends on the availability of robust sensors capable of capturing both quasi-static and dynamic conductor behaviour. Since the fatigue-related quantities described above can be related to strain, temperature, and vibration-induced dynamic strain, fibre-optic sensing provides a suitable route for obtaining these measurements in high-voltage environments. The following section therefore introduces fibre Bragg grating sensors, their operating principles, and their relevance to OHL sag, temperature, and vibration monitoring.

3.5 Introduction to fibre Bragg grating sensor

3.5.1 FBG principles and sensing mechanism

A fibre Bragg grating (FBG) is created within a germanium-doped single-mode optical fibre segment, where periodic modulation of the core refractive index is induced by exposing it to a spatial pattern of ultraviolet light, as depicted in Figure 3.10. This process takes advantage of the photorefractive effect in the germania oxygen vacancy defect band, first observed in Ge-doped optical fibres by [171]. FBGs typically range from 1 to 20 mm, and their reflectivity can reach 100 % [172].

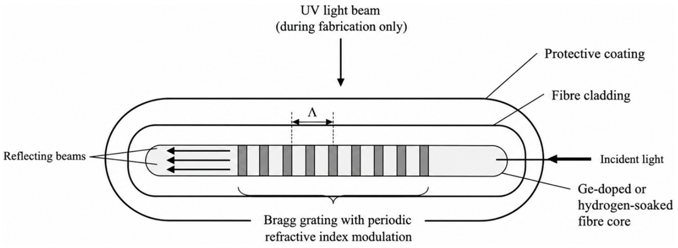

Figure 3.10: Schematic illustration of an in-fibre Bragg grating configuration.

When illuminated by a broadband light source, FBGs create multiple reflected beams from partially reflective planes formed by the periodic modulation of the core's refractive index. These beams interfere destructively unless they are all in phase, a condition described by Bragg's law. This law states that only one wavelength, known as the Bragg wavelength λ_B, is reflected, which is defined by the equation 3.30 [172]:

$$\lambda_B = 2n\Lambda \tag{3.30}$$

where n is the effective refractive index of the core and Λ is the period of index modulation.

The reflectivity at the Bragg wavelength is estimated using equation 3.31 [172]:

$$R = \tanh^2(\Omega L) \tag{3.31}$$

where $\Omega = \pi n(\frac{L}{\lambda_B})(\frac{\Delta n}{n})\eta(V)$.

This equation describes the peak reflectivity of a uniform FBG at the Bragg wavelength. It shows that the reflectivity increases with both the coupling coefficient, Ω, and the grating length, L. Physically, a larger coupling coefficient corresponds to a stronger refractive-index modulation, while a longer grating provides a longer interaction length for Bragg reflection. As ΩL increases, the reflectivity approaches unity, indicating that most of the incident optical power at the Bragg wavelength is reflected. Therefore, this relationship is important for FBG design because it links the required grating length and index modulation strength to the desired reflectivity.

The factor $\eta(V)$, approximated as $1 - 1/V^2$ for $V \geq 2.4$, represents the fraction of the fundamental-mode intensity confined within the fibre core, where V is the normalised frequency of the fibre. This factor is important because the Bragg grating is written primarily in the fibre core; therefore, only the part of the guided optical field overlapping with the core contributes strongly to Bragg coupling and reflection. The condition $V \geq 2.4$ is used because $V \approx 2.405$ corresponds to the cut-off value of the first higher-order mode in a step-index fibre. In this range, the optical mode is sufficiently confined within the core for the approximation to be applicable. The reflectivity increases with grating length L and the refractive-index perturbation $\Delta n/n$, which is influenced by the UV inscription conditions, including exposure power and exposure time [172].

The full width at half maximum (FWHM) bandwidth $\Delta\lambda$ of the grating can be approximated as defined in equation 3.32:

$$\Delta\lambda = \lambda_B s \sqrt{\left(\frac{\Delta n}{2n}\right)^2 + \left(\frac{1}{N}\right)^2} \tag{3.32}$$

where s is approximately 1 for strong gratings and 0.5 for weak gratings, and N is the number of grating planes. Because the index change is small, the modulation depth greatly affects the linewidth [172].

For example, Figure 3.11 illustrates the normalised reflectivity response of an FBG sensor under two conditions: its original state (blue solid curve) and a shifted condition (red dashed curve), typically due to external influences such as strain or temperature. The central wavelength of the original response is denoted as λB, while the shifted response is offset by a wavelength $\Delta\lambda$.

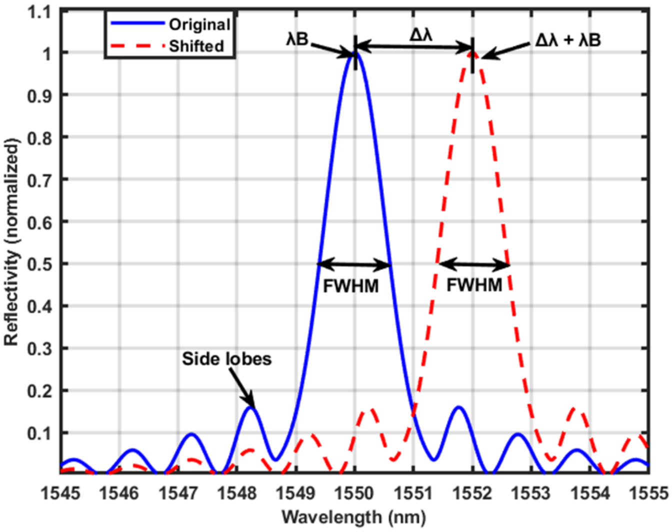

Figure 3.11: Simulated reflectivity response of a uniform FBG sensor calculated using a coupled-mode-theory-based spectral model under initial and perturbed conditions. The figure shows the shift in the central Bragg wavelength, the FWHM, and the side lobes around the main Bragg reflection peak.

The full width at half maximum is annotated for both peaks, highlighting the bandwidth of the reflected signals. Additionally, the figure marks the shifted Bragg wavelength, $\lambda_B + \Delta\lambda$. Side lobes are secondary peaks that appear adjacent to the main reflection peak in the reflectivity spectrum of an FBG. They arise due to abrupt transitions or uniform modulation of the refractive index along the grating length. In simple terms, when the grating structure has sharp start and end points, with no tapering or smoothing, these discontinuities introduce additional spatial-frequency components into the grating profile, which appear as side lobes in the reflected spectrum. While the main peak, corresponding to the Bragg wavelength λ_B, is used for sensing applications, side lobes can be undesirable because they reduce the dynamic range, increase crosstalk in multiplexed systems, and degrade signal quality in communication or sensing setups. To suppress side lobes, apodisation techniques are employed. Apodisation involves smoothly varying the strength of refractive-index modulation along the grating length. This tapering minimises abrupt transitions, thereby reducing the generation of side lobes. Common apodisation profiles include Gaussian, raised-cosine, hyperbolic tanh, sinc, and exponential profiles.

FBG sensors differ from many conventional fibre-optic interferometric sensors in their interrogation requirements. Interferometric sensors often measure phase changes and therefore commonly require highly coherent laser sources. In contrast, FBG sensors encode the measurand as a shift in the Bragg wavelength, so they are typically interrogated using either a broadband optical source with wavelength-selective detection or a tunable laser-based demodulation system. These systems track shifts in the Bragg wavelength caused by strain, temperature, or other measurands.

The achievable wavelength resolution is governed primarily by the interrogation method, wavelength sampling interval, detector noise, signal-to-noise ratio, and the spectral linewidth of the FBG reflection peak. The light source contributes indirectly: a sufficiently broad bandwidth defines the measurable wavelength range, while adequate optical power improves the signal-to-noise ratio and therefore enables more accurate determination of the Bragg wavelength. Common light sources used for FBG interrogation include edge-emitting light-emitting diodes (ELEDs), super-luminescent diodes (SLDs), super-fluorescent fibre sources (SFSs), and tunable fibre lasers (TFLs) [172].

Several types of fibre-optic sensors have been investigated for strain and temperature measurement, including Fabry–Perot interferometric (FP), two-mode fibre optic (TM), and polarimetric fibre optic (PM) sensors. FP sensors operate by measuring changes in the optical path length of a cavity formed between two partially reflecting surfaces; external perturbations such as strain or temperature change the cavity length and therefore the interference pattern [173–176]. TM sensors rely on interference between two propagating fibre modes, where the phase difference between the modes changes in response to the measurand [177, 178]. PM sensors exploit birefringence-induced phase changes between orthogonal polarisation states, which vary with strain or temperature and can therefore be used for sensing [179, 180].

Their operating principles are illustrated in Figure 3.12.

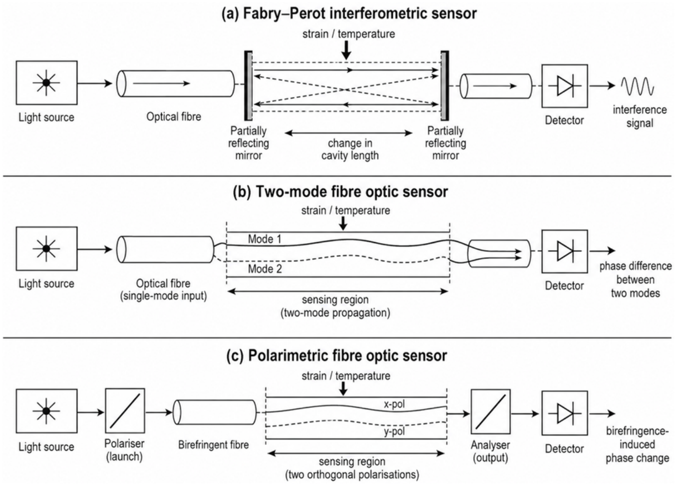

Figure 3.12: Schematic illustration of the operating principles of common fibre-optic sensor types: (a) Fabry–Perot interferometric sensor, in which the measurand changes the cavity length and hence the interference pattern; (b) two-mode fibre optic sensor, in which the measurand alters the phase difference between two propagating modes; and (c) polarimetric fibre optic sensor, in which the measurand changes the birefringence and hence the phase difference between orthogonal polarisation states.

Table 3.4 provides a comparison of FBG, FP, TM, and PM fibre-optic strain sensors.

Table 3.4: Comparison of various fibre-optic strain sensors.

Sensor Type	**Linear Response**	**Absolute Measurement**	**Range to Resolution**	**Sensor Gauge Length**	**Mechanical Strength**	**Multiplexing**	**Mass Production**	**Potential Cost**
FBG	Yes	Yes	High	Short	High	Yes	Yes	Low
FP	Yes	Yes	High	Short	Low	Yes	Yes	Low
TM	Yes	Yes	Low	Long	High	Yes	Yes	Low
PM	Yes	Yes	Low	Long	High	Yes	Yes	Low

FBG sensors can be used to measure several physical parameters, including strain, temperature, pressure, and dynamic magnetic fields. Their sensing mechanism is based on changes in the Bragg wavelength, which occur when the effective refractive index and/or the grating period are altered by an external perturbation. For mechanical and thermal measurements, strain changes the grating period and the refractive index through the photoelastic effect, while temperature changes them through thermal expansion and the thermo-optic effect. Pressure and magnetic-field effects can also modify the reflected Bragg response, although their sensitivities are generally lower in standard silica fibres. Since different measurands can contribute simultaneously to the measured wavelength shift, cross-sensitivity, particularly between strain and temperature, must be considered in practical FBG sensing systems.

3.5.2 Measurements with FBG Sensing

Strain Sensing

The wavelength shifts due to applied longitudinal strain, as shown in Figure 3.13, denoted as $\Delta\lambda_{BS}$, are expressed in equation 3.33 [172]:

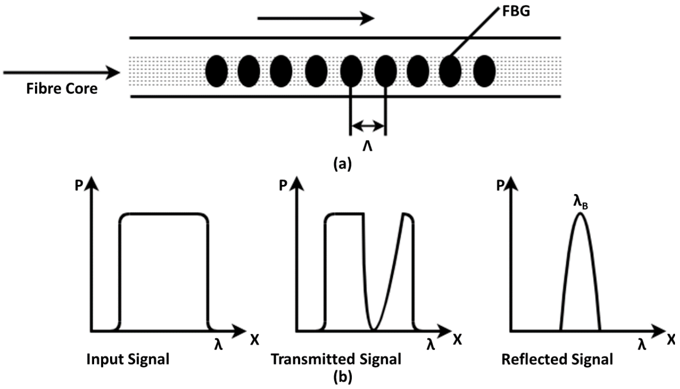

Figure 3.13: Illustration of FBG sensing principle: (a) periodic refractive-index modulation in the fibre core with grating period Λ*; and (b) broadband input spectrum, transmitted spectrum with attenuation at the Bragg wavelength, and reflected spectrum centred at the Bragg wavelength* λ_B*.*

$$\Delta\lambda_{BS} = \lambda_B(1 - p_e)\Delta\varepsilon \tag{3.33}$$

where p_e is the effective photoelastic coefficient of the fibre, given by:

$$p_e = \frac{n^2}{2}\left[p_{12} - \nu\left(p_{11} + p_{12}\right)\right] \tag{3.34}$$

Here, n is the effective refractive index of the fibre core, p_{11} and p_{12} are the photoelastic coefficients of silica, and ν is Poisson's ratio. For silica fibres, the wavelength-strain sensitivities of FBGs operating near 800 nm and 1.55 μm are approximately 0.64 pm/$\mu\varepsilon$ and 1.15 pm/$\mu\varepsilon$, respectively [181, 182]. Since acceleration, ultrasound, and force can be converted into strain through an appropriate transducer or mechanical structure, the same strain-response relationship can also be used for these measurements [172].

Temperature Sensing

For a change in temperature ΔT, the wavelength shift $\Delta\lambda_{BT}$ is given by equation 3.35:

$$\Delta\lambda_{BT} = \lambda_B(1+\xi)\Delta T \tag{3.35}$$

where ξ is the thermo-optic coefficient of the fibre. In silica fibres, the temperature sensitivities for FBGs at 800 nm and 1.55 μm are around $6.8\ \mathrm{pm}/^\circ\mathrm{C}$ and $13\ \mathrm{pm}\ ^\circ\mathrm{C}$, respectively. These values allow for accurate temperature monitoring [181–183].

Pressure Sensing

For pressure changes ΔP, the corresponding wavelength shift $\Delta\lambda_{BP}$ is described by equation 3.36:

$$\frac{\Delta\lambda_{BP}}{\lambda_B} = \left(\frac{1}{\Lambda}\frac{\partial\Lambda}{\partial P} + \frac{1}{n}\frac{\partial n}{\partial P}\right)\Delta P \tag{3.36}$$

In a weakly guided single-mode fibre, the primary contribution to this shift arises from the changes in refractive index and fibre length rather than diameter. Using Young's modulus E, the changes in length and refractive index due to pressure are the following equations 3.37 and 3.38 [184, 185]:

$$\frac{\Delta L}{L} = -\frac{(1-2\nu)P}{E} \tag{3.37}$$

$$\frac{\Delta n}{n} = \frac{n^2 P}{2E}(1-2\nu)(2\rho_{12}+\rho_{11}) \tag{3.38}$$

For a Ge-doped FBG at 1.55 μm, the wavelength pressure sensitivity is approximately -3 $\times$ 10^{-3} nm/MPa [186, 187].Typical ambient or operational pressure fluctuations, such as from 0 to 0.5 MPa (e.g., due to packaging, mounting, or environmental changes), would cause a Bragg wavelength shift of approximately 1.5 pm. Given that the typical strain sensitivity of an FBG is $\approx$ 1.2 pm/ $\mu\epsilon$ and the temperature sensitivity is $\approx$ 10 pm/°C, such a pressure-induced shift could correspond to a false strain reading of $\approx$ 1.25 $\mu\epsilon$ or a temperature error of $\approx$ 0.15 °C.

While small, this pressure-induced cross-sensitivity can introduce measurable errors in high-precision sensing applications, especially when pressure fluctuations are dynamic or unaccounted for. Therefore, in applications requiring sub-microstrain or sub- 0.1 °C accuracy, pressure compensation or environmental isolation may be necessary.

Dynamic Magnetic Field Detection

FBG sensors are commonly described as immune to electromagnetic interference (EMI) because the optical fibre is electrically insulating and the measurement is encoded as an optical wavelength shift rather than as an electrical voltage or current. Therefore, unlike conventional electrical sensors, standard FBG sensors are not significantly affected by induced currents, ground loops, or electromagnetic pickup. However, this does not imply that optical fibres have no physical interaction with magnetic fields. Magnetic fields can interact with light propagating in a fibre through the Faraday effect, which induces circular birefringence and produces a small difference in the refractive index experienced by left- and right-circularly polarised light, as shown in Figure 3.14 [172, 188].

The two circular polarisation components can therefore satisfy slightly different Bragg conditions:

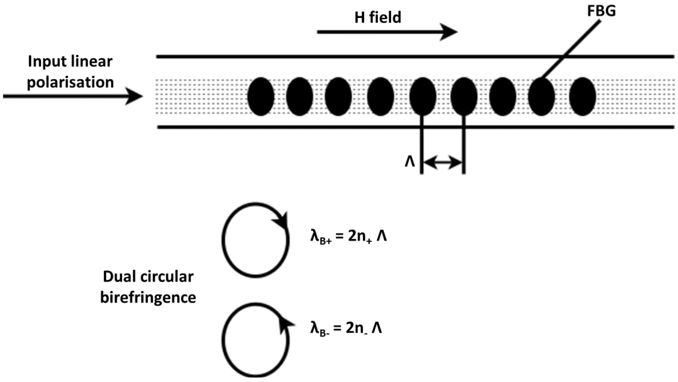

Figure 3.14: Bragg resonance splitting caused by circular birefringence induced by a magnetic field.

$$\lambda_{B+} = 2n_+\Lambda \tag{3.39}$$

$$\lambda_{B-} = 2n_-\Lambda \tag{3.40}$$

where n_+ and n_- are the effective refractive indices for the two circular polarisation states. In standard silica fibres, this effect is very weak because the Verdet constant is small. For example, the Verdet constant of standard silica fibre near 1550 nm is typically reported to be of the order of 0.5 - 0.8 $\mathrm{rad\,T^{-1}\,m^{-1}}$. As a result, magnetic-field-induced polarisation rotation or Bragg splitting is usually much smaller than the wavelength shifts caused by strain or temperature in conventional FBG sensing. Detection of this effect generally requires polarisation-sensitive or interferometric interrogation, long interaction lengths, or magnetically enhanced fibre structures.

Thus, the EMI immunity of FBG sensors should be understood in a practical instrumentation sense: standard FBG strain and temperature sensors are largely insensitive to electromagnetic noise and do not suffer from electrical pickup, but specialised optical configurations can intentionally exploit weak magneto-optic effects for magnetic-field sensing.

Simultaneous Strain and Temperature Measurements

An FBG sensor's strain and temperature influence the Bragg wavelength shift. The relationship between these factors is typically expressed as 3.41:

$$\Delta\lambda_B = K_\epsilon \cdot \Delta\epsilon + K_T \cdot \Delta T \tag{3.41}$$

This can be written in matrix form as 3.43:

$$\begin{bmatrix}\Delta\lambda_B\end{bmatrix} = \begin{bmatrix}K_\epsilon & K_T\end{bmatrix} \cdot \begin{bmatrix}\Delta\epsilon \\ \Delta T\end{bmatrix} \tag{3.42}$$

where, $\Delta\lambda_B$ is the change in Bragg wavelength, K_ϵ is the strain sensitivity coefficient, K_T is the temperature sensitivity coefficient, $\Delta\epsilon$ is the applied strain change, ΔT is the temperature change. The strain sensitivity K_ϵ is influenced by the photoelastic effect and the refractive index. The temperature sensitivity K_T arises from both the thermal expansion of the fibre and the thermo-optic effect, which alters the refractive index.

For standard silica FBGs operating near 1550 nm, the temperature sensitivity is typically around $10\text{–}13\ \mathrm{pm}\,{}^\circ\mathrm{C}^{-1}$, whereas the strain sensitivity is approximately $1.1\text{–}1.2\ \mathrm{pm}\,\mu\varepsilon^{-1}$. Therefore, a temperature change of $1\ {}^\circ\mathrm{C}$ can produce a wavelength shift comparable to approximately $8\text{–}12\ \mu\varepsilon$ of apparent strain. This shows that temperature compensation is important when FBGs are used for strain or sag measurements, especially in outdoor OHL applications where temperature variations can be significant.

To separate strain and temperature effects, FBG sensors often use a reference FBG that is only temperature-sensitive, allowing for compensation in practical applications. One common approach involves using a strain-free reference FBG, allowing the temperature effect to be compensated for by subtracting the temperature-induced wavelength shift from the total wavelength shift. Other methods, such as chirped FBGs, dual-wavelength superimposed FBGs, and combined FBGs with other sensors, have also been explored for more accurate simultaneous strain and temperature measurements [189].

These methods provide versatile solutions for detecting and compensating multiple external factors in various environments, making FBG sensors highly valuable in fields such as structural health monitoring, telecommunications, aerospace, and power-system monitoring [172]. Within the broader field of optical fibre sensing, FBG sensors are typically point or quasi-distributed sensors, whereas distributed optical fibre sensing (DOFS) methods based on Rayleigh, Raman, or Brillouin scattering provide spatially continuous strain or temperature measurements along the fibre. Although DOFS is highly relevant to large-scale infrastructure monitoring, this thesis focuses on FBG-based sensors because they offer high sensitivity, wavelength-encoded operation, multiplexing capability, and practical integration with compact transducers for OHL sag, strain, temperature, and vibration monitoring.

3.5.3 FBG fabrication techniques

Advanced techniques for fabricating FBGs are crucial to achieving high-quality, cost-effective sensors. The ideal fabrication method for FBG sensors should possess the following characteristics:

- **Flexibility:** The ability to produce FBGs with customisable reflectivities and central wavelengths to allow quasi-distributed sensing.
- **Cost-effective Mass Production:** The technique should support rapid and economical large-scale production of FBGs, keeping costs low.
- **High Physical and Optical Quality:** The mechanical strength of the FBG should remain robust after fabrication while maintaining a narrow spectral line width and low excess loss to ensure high-resolution measurements.
- **Repeatability:** Both the central wavelength and the reflectivity of the FBG should be consistent across batches, enabling reliable mass production and device interchangeability without the need for recalibration.

Given the demand for both telecommunication and sensing applications, significant research has been dedicated to the development of FBG fabrication techniques. The two conventional approaches are the two-beam interferometer method and the phase-mask method [172]. In addition to these methods, more recent fabrication approaches include point-by-point writing and femtosecond-laser direct writing. In point-by-point writing, individual refractive-index modifications are inscribed sequentially along the fibre to form the grating period, allowing flexible fabrication of complex or localised grating structures. Femtosecond-laser direct writing uses tightly focused ultrashort laser pulses to induce permanent refractive-index changes inside the fibre core or cladding, enabling FBG inscription in fibres that may be difficult to process using conventional UV photosensitivity methods [190, 191]. These emerging techniques provide additional flexibility for fabricating gratings in special fibres, high-temperature sensors, and harsh-environment sensing applications.

The FBG sensors used in this research were commercially manufactured T220 strain transducers supplied by Technica SA. The exact FBG inscription technique used by the manufacturer was not specified in the available documentation and was not part of the experimental work. Nevertheless, commercial FBG sensors are commonly fabricated using UV inscription methods, especially phase-mask-based techniques, owing to their repeatability, optical quality, and suitability for mass production. The fabrication methods reviewed here, therefore, provide relevant background to the sensors employed in this thesis.

Two-Beam Interferometer Technique

Initially, FBGs were written into germanium-doped fibres, demonstrated in 1978 [171]. More recently, the hydrogen ”loading” technique was introduced, which increases the fibre’s photosensitivity. In this process, the fibres are exposed to low temperature and high-pressure hydrogen, which diffuses into the fibre [192]. In germanium-doped optical fibres, exposure to ultraviolet (UV) light can induce a permanent change in the refractive index of the fibre core. Hydrogen loading is often used to enhance this photosensitivity by increasing the UV-induced modification at germanium-related defect sites, thereby enabling efficient inscription of the Bragg grating, as illustrated in Figure 3.15 [172].

However, hydrogen loading can also enhance photosensitivity in standard telecommunication fibres, such as SMF-28, whose cores are typically lightly germanium-doped. The presence

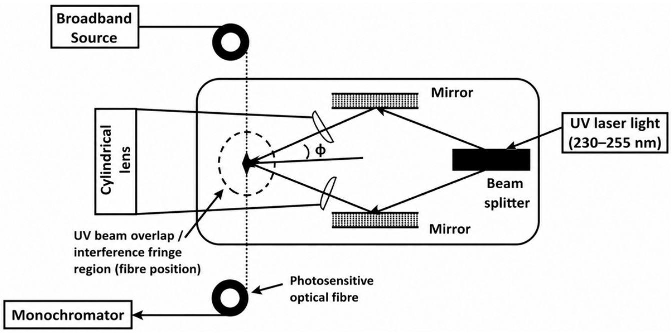

Figure 3.15: Diagram of the two-beam interferometer technique.

of hydrogen increases the UV-induced refractive-index change by modifying germanium-related defect centres and forming hydrogen-related species, thereby enabling efficient FBG inscription even in fibres with relatively low intrinsic photosensitivity. This approach is widely used to fabricate gratings in standard germanosilicate telecommunication fibres [172, 191].

- **Holographic Method:** The first practical method for the fabrication of FBG involved the use of a holographic interferometer to create an interference pattern in the fibre core perpendicular to the axis. By adjusting the angle between the writing beams and the fibre, it is possible to tune the Bragg wavelength of the FBGs. This method is highly flexible, as different Bragg wavelengths can be obtained by varying the writing angle or the UV source wavelength [193–196].

- **Source-tunable interferometer method:** This method uses a wavelength-tunable UV laser source together with a phase-mask-based interferometer, as shown in Figure 3.16. In this context, tuning the UV source means changing the emission wavelength of the UV writing laser. This changes the spacing of the interference fringes formed by the two UV beams, while adjustment of the beam-interference angle provides an additional means of controlling the grating period. Since the Bragg wavelength is determined by the grating period and the effective refractive index, this approach allows the central Bragg wavelength of the FBG to be selected during inscription. However, the method requires a relatively complex and highly coherent tunable UV laser system, together with accurate interferometer alignment. The achievable grating length is also limited by the coherence length of the UV source and the spatial overlap region of the interfering beams, with reported grating lengths of approximately 7 mm [197]. Although the method provides precise wavelength control, its optical complexity, alignment sensitivity, limited grating length, and higher system cost restrict its practical use compared with conventional phase-mask inscription techniques [197].

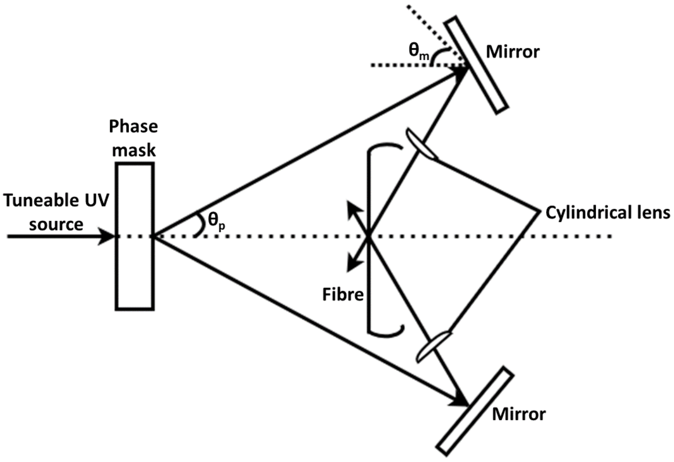

Figure 3.16: Diagram of the wavelength-tunable interferometer method.

Phase-Mask Technique

The phase-mask method is a widely adopted approach due to its practicality and cost-effectiveness. In this method, a phase mask, a diffractive optical element, generates a lateral interference pattern that imprints a refractive-index modulation on the photosensitive fibre behind the mask, as shown in Figure 3.17. Compared to the two-beam interferometer technique, the phase mask method offers several advantages [198, 199]:

- **Precision:** The Bragg wavelength is determined by the phase-mask pitch, making it independent of the UV laser's wavelength.
- **Mass Production Capability:** Phase masks can be produced with high precision using computer-controlled photolithography, making them ideal for mass production.

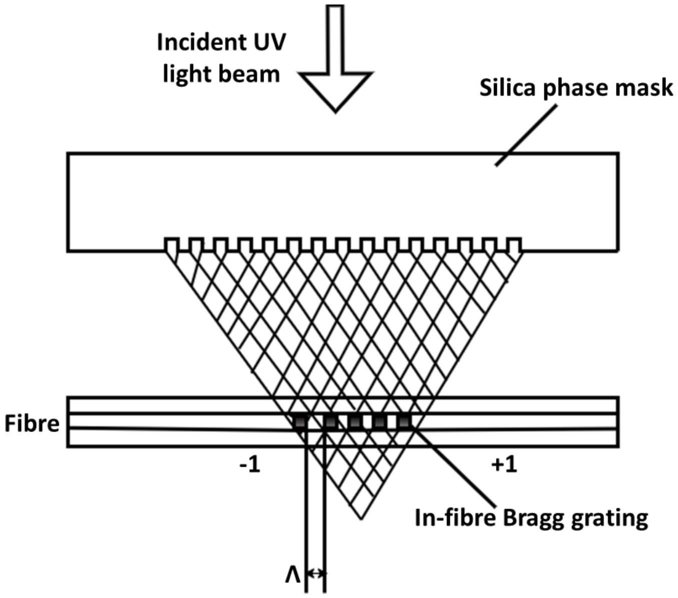

Figure 3.17: Diagram of the phase-mask writing technique.

- **Mechanical Stability:** This single-beam writing method offers greater mechanical stability, simplifying the fabrication process.

- **Reduced Coherence Requirements:** The phase mask technique requires less coherence from the UV laser, allowing the use of less expensive lasers than the two-beam interferometer method.

The phase mask technique has the following models [172]:

- **Modified Phase-Mask Method:** A modification of this technique allows tuning the Bragg wavelength using a diverging or converging wavefront incident on the phase mask, as shown in Figure 3.18. By adjusting the relative positions of the lens and the fibre, the pitch of the grating can be varied, providing a range of Bragg wavelengths [200–203].

- **Moving Fibre/Phase-Mask Scanning Method:** A novel approach, the moving fibre/phase mask scanning method, uses a moving fibre relative to a stationary phase mask while scanning the UV beam. This enables the production of FBGs with different wavelengths using a single-phase mask. This technique is promising for mass produc-

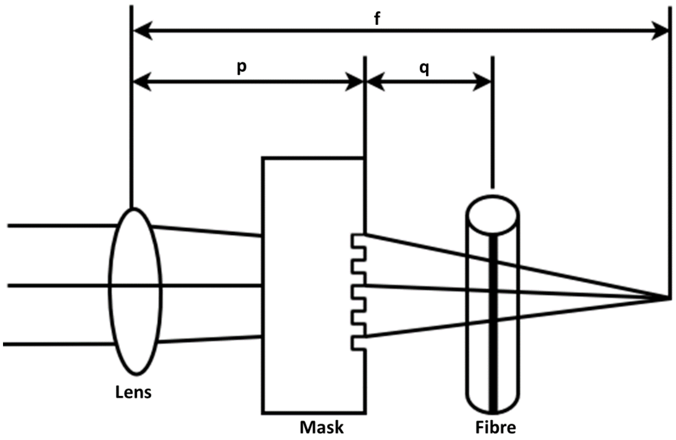

Figure 3.18: Diagram of the modified phase-mask method using a lens.

tion because of its ability to fabricate FBGs with high precision and tunable wavelength separations [201, 202, 204].

Advancements in FBG fabrication techniques, particularly the phase mask method and its variants, offer flexible, cost-effective solutions to produce high-quality FBG sensors in large volumes, meeting the growing demands of industries such as telecommunications and structural health monitoring [172].

3.6 FBG interrogation techniques

Accurate measurement of the wavelength shift in FBGs due to external influences is essential for optimal sensor performance. An effective interrogation method should ideally meet the following criteria.

- **High Resolution with a Wide Measurement Range:** Many applications require a wavelength shift detection resolution from subpicometers to a few picometers, with a range-to-resolution ratio between 10^3:1 and 10^5:1.

- **Cost-Effectiveness:** The interrogation system should be economically competitive with traditional optical and electrical sensors.

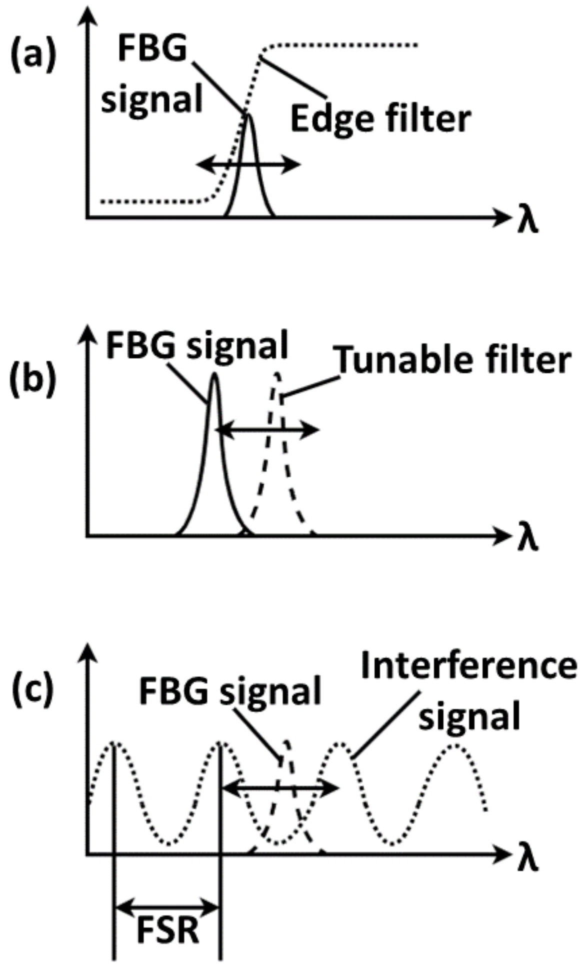

Figure 3.19: (a) Concept of the edge filter method. (b) Concept of the tunable filter method. (c) Concept of the interferometric scanning method.

- **Multiplexing Compatibility:** The method should support multiplexing configurations to make the entire sensing system more cost-efficient.

Conventional spectrometers, with a typical resolution of 0.1 nm, are generally used to evaluate the optical properties of FBG during fabrication rather than for the precise detection of wavelength shifts. Research into high-resolution interrogation methods has increased, leading to the development of several techniques for measuring wavelength shifts with greater accuracy. These techniques are classified based on their operational principles, including edge filters, tunable filters, interferometric scanning, and dual-cavity interferometric scanning.

3.6.1 Principles of Interrogation Methods

Edge Filter

This approach uses an edge filter, as shown in Figure 3.19(a), to convert the wavelength shift of the FBG into an intensity change. In practice, the reflected spectrum from the FBG is passed through an optical filter whose transmission varies approximately linearly over the wavelength range of interest. When the Bragg wavelength shifts due to strain or temperature, the reflected peak moves along the sloped transmission edge of the filter, producing a corresponding change in transmitted optical power. This power variation is measured using a photodiode and is then calibrated against wavelength shift or the measurand. Common implementations use thin-film filters, fibre Fabry–Perot filters, wavelength-division multiplexing filters, or other optical filters with a near-linear spectral edge. The method is simple and low cost, but its measurement range is limited to the linear region of the filter response, and the resolution depends strongly on the filter slope, source power stability, detector noise, and signal-to-noise ratio.

Tunable Filter

A tunable filter can detect FBG wavelength shifts by convolutionally combining its spectrum with that of the FBG, shown in Figure 3.19(b). A maximum output is achieved when the tunable filter spectrum aligns with the FBG. This method's resolution depends on the signal-to-noise ratio and the line widths of both the tunable filter and the FBG. This technique offers a high resolution and a broad measurement range.

Interferometric Scanning

In the interferometric scanning method, FBG wavelength shifts due to strain or temperature are detected through a scanning interferometer, shown in Figure 3.19(c). This technique is particularly useful for high-resolution dynamic and quasi-static strain measurements. The interference signal from the scanned interferometer (SI) can be expressed as:

$$\frac{I}{I_0} = 1 + B\cos\left(\Delta\Phi_B + \phi(t)\right) \tag{3.43}$$

where I_0 is the initial intensity, B is the visibility of the interference signal, and $\phi(t)$ represents phase drift caused by thermal effects. The SI functions as a wavelength scanner by modulating the optical path. The strain or temperature variation affecting the FBG changes the optical phase $\Delta\Phi_B$, expressed as:

$$\Delta\Phi_B = -\frac{2\pi\Delta L_{SI}}{\lambda_B^2}\Delta\lambda_B = -\frac{2\pi\Delta L_{SI}}{\lambda_B}\xi_g\Delta Y \tag{3.44}$$

This phase change is directly related to the optical path difference in the interferometer, where ΔY is the variation in strain or temperature applied to the FBG, ΔL_{SI} is the optical path difference, and ξ_g is the normalised sensitivity of the FBG for the measured parameter.

ΔY represents the change in strain or temperature applied to the FBG, and ΔL_{SI} denotes the optical path difference (OPD) in the scanned interferometer. The normalised sensitivity of the FBG for strain or temperature, ξ_g, is defined by:

$$\xi_g = \frac{1}{\lambda_B}\frac{\delta\lambda_B}{\delta Y} \tag{3.45}$$

Thus, the phase sensitivity to strain or temperature ($\Delta\Phi_B/\Delta Y$) is directly proportional to the OPD in the interferometer. By measuring $\Delta\Phi_B$ using a pseudo-heterodyne processing method, changes in strain or temperature can be accurately determined.

The operational range of the FBG is determined by the free spectral range (FSR) of the interferometer, given by the following:

$$FSR = \frac{\lambda_B^2}{\Delta L_{SI}} \tag{3.46}$$

This relationship shows that the operational range is inversely proportional to the OPD in the interferometer. Consequently, there is a balance between sensitivity and operational range, as the measurement range is limited by a phase shift 2π on the interferometer. To maintain stability in quasistatic or static measurements, a reference FBG can be used to offset thermal

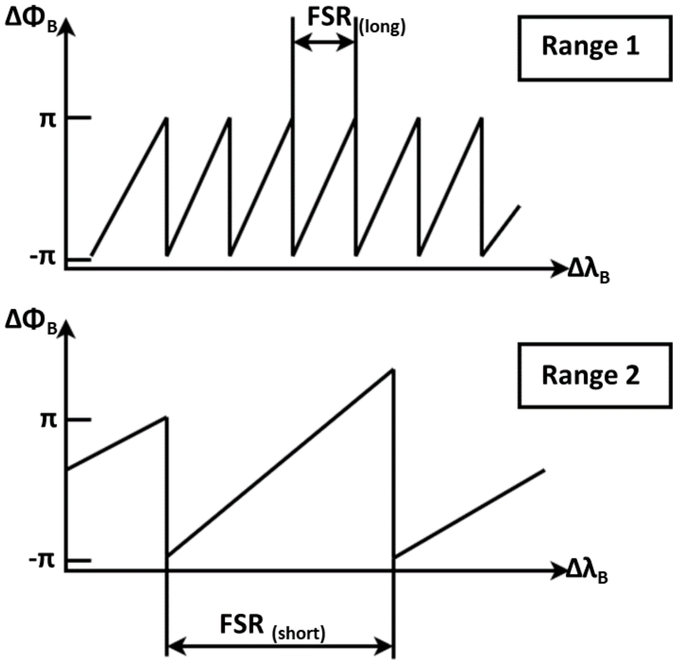

Figure 3.20: Concept of the dual-cavity interferometric scanning method.

drift by comparing the phase difference between the sensing FBG and the reference FBG.

3.6.2 Dual-Cavity Interferometric Scanning

A dual-cavity interferometric scanning technique has been introduced to extend the measurement range of interferometric scanning. This method uses two sets of interferometric fringes, switching from a longer cavity to a shorter one to expand the unambiguous measurement range, as shown in Figure 3.20. The phase output from the longer cavity provides high-resolution data, while the shorter cavity phase output helps count the number of fringes from the longer cavity. The total phase shift can be expressed as $\Delta\Phi_B + 2\pi N$, where N represents the number of fringes.

The enhancement factor, M, for the unambiguous range is determined by the ratio of the lengths of the two cavities:

$$M = \frac{FSR_{\text{short}}}{FSR_{\text{long}}} = \frac{L_{SI}}{L_{SI}^{0}} \tag{3.47}$$

where L_{SI} and L_{SI}^{0} are the lengths of the longer and shorter cavities, respectively. In principle, M can be quite large, as the cavity length in a well-collimated interferometer can vary from hundreds of microns to hundreds of millimetres, though in practice, M is typically chosen to fall between 10 and 100.

3.6.3 Relevance of FBG Sensing to OHL Sag, Temperature, and Vibration Monitoring

The preceding sections have shown that FBG sensors are well suited to measuring strain and temperature through shifts in the Bragg wavelength [172, 205]. These two measurands are directly relevant to overhead line (OHL) monitoring because conductor sag, tension, thermal expansion, and vibration all alter the mechanical and thermal state of the conductor [29, 47, 52]. When an FBG strain transducer is attached to a conductor through a suitable mechanical assembly, changes in conductor tension and bending are transferred to the optical fibre as strain-induced wavelength shifts [125, 126]. Similarly, temperature changes can be measured using either an integrated temperature FBG or a strain-isolated reference FBG, allowing thermal effects to be compensated or analysed separately [181, 183, 189].

For sag monitoring, the FBG does not measure sag directly. Instead, it measures strain or tension-related changes that can be related to conductor sag using calibration, span geometry, or a conductor mechanical model [29, 47, 125]. This makes the mechanical design of the sensor assembly important, because reliable strain transfer between the conductor, mounting plate, and FBG transducer is required for accurate sag estimation [126, 127]. In addition, because OHL conductors experience both mechanical loading and temperature variation, simultaneous strain and temperature measurement is needed to distinguish between load-induced and thermally induced wavelength shifts [172, 189].

FBG sensors are also suitable for vibration monitoring because dynamic conductor motion produces time-varying strain in the sensor [172, 205]. These dynamic wavelength changes can be processed to identify vibration amplitude, frequency content, and cyclic strain histories. Such information is important for assessing aeolian vibration, galloping, wake-induced oscillation, and fatigue-related conductor behaviour [52, 127, 206]. The ability to capture both quasi-static changes, such as sag and temperature variation, and dynamic strain changes makes FBG sensing particularly useful for structural health monitoring of OHL conductors [3, 47].

The relevance of FBG sensing to this thesis therefore lies in its ability to provide a dielectric, multiplexable, and remotely interrogated sensing platform for OHL condition monitoring [172, 205]. Its practical immunity to electromagnetic interference makes it suitable for high-voltage environments, while its sensitivity to strain and temperature enables the same sensing platform to support sag estimation, thermal monitoring, vibration detection, and fatigue assessment [125, 126, 207]. Building on this background, the following chapter focuses on the design, modelling, and laboratory characterisation of an FBG-based OHL sag sensor developed for monitoring conductor sag, temperature, and vibration under representative operating conditions.

3.7 Conclusion

This chapter reviewed the state of the art in monitoring overhead line (OHL) conductors for sag, dynamic line rating, and structural health assessment. Regular inspection and reliable condition assessment of conductor systems, joints, fittings, insulators, and support structures are essential for maintaining the integrity and reliability of overhead transmission lines. Effective condition monitoring enables early identification of degradation, supports timely maintenance, and reduces the likelihood of costly failures.

The chapter first examined established sag monitoring methods, including aerial, terrestrial, contact-based, electrical, RF, space-potential, PMU, carrier-signal, and optical approaches. These methods differ considerably in their measurement principle, installation requirements, sensitivity to environmental conditions, suitability for continuous monitoring, and compatibility with high-voltage environments. Optical and FBG-based methods are particularly relevant to this thesis because they provide a dielectric, multiplexable, and remotely interrogated sensing platform capable of measuring strain, temperature, and vibration-induced dynamic strain in OHL conductors.

Dynamic line rating was also reviewed to provide context for how conductor temperature, sag, clearance, and tension are used in real-time line operation. Although this thesis does not develop a complete DLR forecasting algorithm, it contributes to the mechanical-state monitoring route by providing direct optical measurements of conductor behaviour. The FBG-based sag sensor developed in this work can therefore complement DLR methods by supplying field measurements that support validation, condition monitoring, and operational confidence in real-time line-rating decisions.

The chapter further reviewed fatigue endurance in conductor-clamp systems. Existing fatigue assessment methods, including those based on the Poffenberger–Swart formulation, provide a strong engineering basis for estimating bending strain and fatigue damage in overhead line conductors. However, many of these approaches rely on simplified assumptions and laboratory-derived conditions. Further work is required to represent conductor vibration, fretting fatigue, contact mechanics, and fracture behaviour under realistic field conditions.

In addition to classical analytical and experimental approaches, emerging methods based on artificial intelligence, machine learning, and digital twins are becoming increasingly relevant for grid monitoring and asset management. These approaches can combine sensor measurements, environmental data, historical loading records, and physics-based models to support anomaly detection, remaining-life estimation, and predictive maintenance. Digital twins of OHL assets can also provide a framework for updating conductor condition models in real time as new field data become available. However, their reliability depends strongly on the quality, continuity, and physical relevance of the measured data used for model updating and validation.

Overall, this chapter has shown that accurate OHL condition assessment requires both robust sensing and appropriate interpretation of measured data. The limitations of snapshot inspections, indirect sag estimation methods, laboratory-based fatigue models, and simplified conductor assumptions highlight the need for field-deployable monitoring systems that can capture real operating conditions. The following chapters build on this review by presenting the design, modelling, laboratory characterisation, field deployment, and fatigue-assessment methodology of an FBG-based optical sag sensor for monitoring conductor sag, temperature, strain, and vibration.

References

[1] Abdeen Mustafa Omer. Energy, environment and sustainable development. *Renewable and Sustainable Energy Reviews*, 12(9):2265–2300, 2008.

[2] MT Bedialauneta, E Fernandez, I Albizu, AJ Mazon, and KJ Sagastabeitia. Factors that affect the sag-tension model of an overhead conductor. In *2013 IEEE Grenoble Conference*, pages 1–6. IEEE, 2013.

[3] Yunfei Chen and Xiaolin Ding. A survey of sag monitoring methods for power grid transmission lines. *IET Generation, Transmission & Distribution*, 17(7):1419–1441, 2023.

[4] Linnea Sjöholm. Computational Handbook for Power Line Engineers: Methodology for Design of Non-Standard Transmission Line Supports. Master's thesis, KTH Royal Institute of Technology, School of Engineering Sciences, Stockholm, Sweden, 2017.

[5] U.S. Department of Energy. Dynamic Line Rating: Report to Congress. Technical report, U.S. Department of Energy, Washington, DC, USA, June 2019.

[6] IEEE standard for calculating the current-temperature of bare overhead conductors. Ieee std., IEEE, 1993.

[7] CIGRE WG 22.12. The thermal behavior of overhead line conductors. Technical report, CIGRE, 1992.

[8] IEC. IEC: Standard TR 1597 Overhead Electrical Conductors - Calculation Methods for Stranded Bare Conductors. Technical report, IEC, 1985.

[9] Dávid Kalmár, Dávid Szabó, Gábor Göcsei, and Bálint Németh. Extension of dynamic line rating models with the effect of conductor aging. In *2022 8th International Youth Conference on Energy (IYCE)*, pages 1–5. IEEE, 2022.

[10] Elżbieta Pastucha, Edyta Puniach, Agnieszka Ścisłowicz, Paweł Ćwiakała, Witold Niewiem, and Paweł Wiacek. 3D reconstruction of power lines using UAV images to monitor corridor clearance. *Remote Sensing*, 12(22):3698, 2020.

[11] Shu-ichi Ashidate, Susumu Murashima, and Noritsuna Fujii. Development of a helicopter-mounted eye-safe laser radar system for distance measurement between power transmission lines and nearby trees. *IEEE Transactions on Power Delivery*, 17(2):644–648, 2002.

[12] Robert A McLaughlin. Extracting transmission lines from airborne LIDAR data. *IEEE Geoscience and Remote Sensing Letters*, 3(2):222–226, 2006.

[13] Siheon Jeong, Donggeun Kim, San Kim, Ji-Wan Ham, Jae-Kyung Lee, and Ki-Yong Oh. Real-time environmental cognition and sag estimation of transmission lines using UAV equipped with 3-D LiDAR system. *IEEE Transactions on Power Delivery*, 36(5):2658–2667, 2021.

[14] Zijie Zheng, Jianhua Liu, Bingyan Zhou, Yuwen Luo, Qi Ning, and Zipeng Zhou. Research on UAV sag measurement system based on 3D LiDAR. In *2020 5th International Conference on Automation, Control and Robotics Engineering (CACRE)*, pages 1–7. IEEE, 2020.

[15] Heng Wang, Shijia Han, Li-Jun Lv, and Li-Jun Jin. Transmission line sag measurement based on single aerial image. In *2017 24th International Conference on Mechatronics and Machine Vision in Practice (M2VIP)*, pages 1–5. IEEE, 2017.

[16] Elena Golinelli, Daniele Bartalesi, Gian Mario Ogliari, and Umberto Perini. A new IR laser sag meter prototype for remote on line monitoring of high voltage overhead line: A special application. In *2019 AEIT International Annual Conference (AEIT)*, pages 1–6. IEEE, 2019.

[17] Andrzej Kwinta, Karolina Ważydrag, and Mariusz Zygmunt. Analysis of power lines

span geometry based on tls measurements. In *E3S Web of Conferences*, volume 55, page 00013. EDP Sciences, 2018.

[18] P Greeshma Shivani, Somani Harshit, Ch Vamsi Varma, and R Mahalakshmi. Detection of icing and calculation of sag of transmission line through computer vision. In *2020 Third International Conference on Smart Systems and Inventive Technology (ICSSIT)*, pages 689–694. IEEE, 2020.

[19] Achref Abed, Martin Glass, Hafedh Trabelsi, and Faouzi Derbel. Sag monitoring of overhead power lines based on image processing. In *2021 18th International Multi-Conference on Systems, Signals & Devices (SSD)*, pages 142–146. IEEE, 2021.

[20] Michal Wydra, Pawel Kubaczynski, Katarzyna Mazur, and Bogdan Ksiezopolski. Time-aware monitoring of overhead transmission line sag and temperature with LoRa communication. *Energies*, 12(3):505, 2019.

[21] Aydın Tarık Zengin, Gökhan Erdemir, Tahir Cetin Akinci, and S. Serhat Seker. Measurement of power line sagging using sensor data of a power line inspection robot. *IEEE Access*, 8:99198–99204, 2020.

[22] Ajit Paul Abraham and S Ashok. Gyro-accelerometric sag analysis and online-monitoring of transmission lines using line recon robot. In *2012 Annual IEEE India Conference (INDICON)*, pages 1036–1040. IEEE, 2012.

[23] Chris Mensah-Bonsu, Ubaldo Fernandez Krekeler, Gerald Thomas Heydt, Yuri Hoverson, John Schilleci, and Baj L Agrawal. Application of the global positioning system to the measurement of overhead power transmission conductor sag. *IEEE Transactions on Power Delivery*, 17(1):273–278, 2002.

[24] Chris Mensah-Bonsu and Gerald Thomas Heydt. Real-time digital processing of GPS measurements for transmission engineering. *IEEE Transactions on Power Delivery*, 18(1):177–182, 2003.

[25] S Kamboj and R Dahiya. Evaluation of DTLR of power distribution line from sag measured using GPS. In *2011 International Conference on Energy, Automation and Signal*, pages 1–6. IEEE, 2011.

[26] Satish M Mahajan and Uma Mahesh Singareddy. A real-time conductor sag measurement system using a differential GPS. *IEEE Transactions on Power Delivery*, 27(2):475–480, 2012.

[27] Shalini Sushmitha Komaragiri and Satish M Mahajan. A sag monitoring device based on a cluster of code based GPS receivers. In *2009 IEEE Power & Energy Society General Meeting*, pages 1–7. IEEE, 2009.

[28] Poorani Ramachandran, Vijay Vittal, and Gerald Thomas Heydt. Mechanical state estimation for overhead transmission lines with level spans. *IEEE Transactions on Power Systems*, 23(3):908–915, 2008.

[29] Michal Wydra, Piotr Kisala, Damian Harasim, and Piotr Kacejko. Overhead transmission line sag estimation using a simple optomechanical system with chirped fiber Bragg gratings. Part 1: Preliminary measurements. *Sensors*, 18(1):309, 2018.

[30] HB Dwight. Sag calculations for transmission lines. *Transactions of the American Institute of Electrical Engineers*, 45:796–805, 1926.

[31] Pradeep Kumar and Asheesh K Singh. Optimal mechanical sag estimator for leveled span overhead transmission line conductor. *Measurement*, 137:691–699, 2019.

[32] Xia Xiao, Yan Xu, Jianghua Zhang, and Ken Xu. Research on sag online monitoring system for power transmission wire based on tilt measurement. *Int. J. Smart Grid Clean Energy*, 2(1):6–11, 2013.

[33] Sunita Malhara and Vijay Vittal. Mechanical state estimation of overhead transmission lines using tilt sensors. *IEEE Transactions on Power Systems*, 25(3):1282–1290, 2010.

[34] Xing Gong, Zhiming Wang, Wenping Xu, Hangfeng Li, Ke Wang, and Jian Guo. Research on online sag monitoring of transmission lines based on barometric pressure. In *IOP Conference Series: Earth and Environmental Science*, volume 791, page 012094. IOP Publishing, 2021.

[35] Danil Yaroslavsky, Marat Sadykov, Mikhail Goryachev, Dmitry Ivanov, Nikolay Andreev, et al. Determination of the conductor sag according to the period of own harmonic oscillations. In *E3S Web of Conferences*, volume 220, page 01036. EDP Sciences, 2020.

[36] Eric Cloet and Jean-Louis Lilien. Uprating transmission lines through the use of an innovative real-time monitoring system. In *2011 IEEE PES 12th international conference on transmission and distribution construction, operation and live-line maintenance (ESMO)*, pages 1–6. IEEE, 2011.

[37] Peter G Halverson, Steven J Syracuse, Roy Clark, and Frederick M Tesche. Non-contact sensor system for real-time high-accuracy monitoring of overhead transmission lines. In *Proc. epri conf. overhead trans. lines*, pages 1–13, 2008.

[38] Xinghua Sun, KS Lui, Kenneth KY Wong, WK Lee, Yunhe Hou, Qin Huang, and Philip WT Pong. Novel application of magnetoresistive sensors for high-voltage transmission-line monitoring. *IEEE Transactions on Magnetics*, 47(10):2608–2611, 2011.

[39] Arsalan Habib Khawaja, Qi Huang, Jian Li, and Zhenyuan Zhang. Estimation of current and sag in overhead power transmission lines with optimized magnetic field sensor array placement. *IEEE Transactions on Magnetics*, 53(5):1–10, 2017.

[40] Yuqing Ji and Jiaxin Yuan. Overhead transmission lines sag and voltage monitoring method based on electrostatic inverse calculation. *IEEE Transactions on Instrumentation and Measurement*, 71:1–12, 2022.

[41] Robert G Olsen and Kenneth S Edwards. A new method for real-time monitoring of high-voltage transmission-line conductor sag. *IEEE Transactions on Power Delivery*, 17(4):1142–1152, 2002.

[42] Ayman Uddin Mahin, Shama Naz Islam, and Md Farhad Hossain. Millimeter wave-based sag measurement using parabolic approximation for smart grid overhead transmission line monitoring. In *2019 IEEE International Conference on Communications, Control, and Computing Technologies for Smart Grids (SmartGridComm)*, pages 1–5. IEEE, 2019.

[43] Yan Du and Yuan Liao. Online estimation transmission parameters temperature sag. *North American Power Symposium*, pages 1–6, 2011.

[44] Irina Oleinikova, Anna Mutule, and Mairis Putnins. PMU measurements application for transmission line temperature and sag estimation algorithm development. In *2014 55th International Scientific Conference on Power and Electrical Engineering of Riga Technical University (RTUCON)*, pages 181–185. IEEE, 2014.

[45] Wernich De Villiers, Johannes Hendrik Cloete, L Martin Wedepohl, and Arthur Burger. Real-time sag monitoring system for high-voltage overhead transmission lines based on power-line carrier signal behavior. *IEEE Transactions on Power Delivery*, 23(1):389–395, 2007.

[46] Wernich De Villiers. *Real-time HV OHTL sag monitoring system based on Power Line Carrier signal behaviour*. PhD thesis, Stellenbosch: University of Stellenbosch, 2005.

[47] Krzysztof Skorupski, Damian Harasim, Patryk Panas, Sławomir Cieszczyk, Piotr Kisała, Piotr Kacejko, Janusz Mroczka, and Michał Wydra. Overhead transmission line sag estimation using the simple opto-mechanical system with fiber Bragg gratings–Part 2: Interrogation system. *Sensors*, 20(9):2652, 2020.

[48] Zhe-Wen Ding, Xu-Ping Zhang, Ning-Mu Zou, Fei Xiong, Jin-Yu Song, Xing Fang,

Feng Wang, and Yi-Xin Zhang. Phi-otdr based on-line monitoring of overhead power transmission line. *Journal of Lightwave Technology*, 39(15):5163–5169, 2021.

[49] Jie Huang and Rui Bo. Real-time overhead power line sag monitoring, June 2019.

[50] Sai Chang Zhang, Jun Zheng Liu, Zheng Niu, Shuai Gao, Hai Zhi Xu, and Jie Pei. Power line simulation for safety distance detection using point clouds. *IEEE Access*, 8:165409–165418, 2020.

[51] Xingyu Ma and Fei Hou. Research and application for transmission line sag measurement method based on aerial image sequence. *DEStech Transactions on Engineering and Technology Research*, 2016.

[52] CIGRE Working Group B2.36. Guide for Application of Direct Real-Time Monitoring Systems. Technical Brochure 498, CIGRE, 2012.

[53] Elena Golinelli, Umberto Perini, and Gianmario Ogliari. A new IR laser scanning system for power lines sag measurements. In *Proceedings of the 18th Italian National Conference on Photonic Technologies (Fotonica 2016)*, pages 225–228, Rome, Italy, June 2016. IET.

[54] E Golinelli, S Musazzi, U Perini, and F Barberis. Conductors sag monitoring by means of a laser based scanning measuring system: Experimental results. In *2012 IEEE Sensors Applications Symposium Proceedings*, pages 1–4. IEEE, 2012.

[55] Letizia De Maria, Elena Golinelli, and Umberto Perini. Innovative optical systems and sensors for on line monitoring of high voltage overhead lines and power components. In *2017 AEIT International Annual Conference*, pages 1–6. IEEE, 2017.

[56] Elena Golinelli, Sergio Musazzi, Umberto Perini, and Giovanni Pirovano. Laser based scanning system for high voltage power lines conductors monitoring. In *CIRED 2009-20th International Conference and Exhibition on Electricity Distribution-Part 1*, pages 1–3. IET, 2009.

[57] Elena Golinelli, Gian Mario Ogliari, and Daniele Bartalesi. New optical system for online, real time sag monitoring of high voltage overhead lines. In *2021 AEIT International Annual Conference (AEIT)*, pages 1–5. IEEE, 2021.

[58] Elena Golinelli, Gian Mario Ogliari, Daniele Bartalesi, and Umberto Perini. Prototype design and preliminary tests for on line, real time sag monitoring of high voltage overhead lines. In *2020 Italian Conference on Optics and Photonics (ICOP)*, pages 1–4. IEEE, 2020.

[59] Amir Molaei, Hamid D Taghirad, and Javad Dargahi. Extracting of sagging profile of overhead power transmission line via image processing. In *2018 IEEE Canadian Conference on Electrical & Computer Engineering (CCECE)*, pages 1–5. IEEE, 2018.

[60] Piotr Kohut, Krzysztof Holak, Ziemowit Dworakowski, and Krzysztof Mendrok. Vision-based measurement systems for static and dynamic characteristics of overhead lines. *Journal of Vibroengineering*, 18(4):2113–2122, 2016.

[61] Chris Mensah-Bonsu. *Instrumentation and Measurement of Overhead Conductor Sag Using the Differential Global Positioning Satellite System*. PhD thesis, Arizona State University, Tempe, Arizona, USA, August 2000.

[62] Chris Mensah-Bonsu and Gerald Thomas Heydt. Overhead transmission conductor sag: A novel measurement technique and the relation of sag to real-time circuit ratings. *Electric Power Components and Systems*, 31(1):61–69, 2003.

[63] Sangeeta Kamboj and Ratna Dahiya. Application of GPS for sag measurement of overhead power transmission line. *International Journal on Electrical Engineering and Informatics*, 3(3):268–277, 2011.

[64] S Kamboj and R Dahiya. Case study to estimate the sag in overhead conductors using GPS to observe the effect of span length. In *2014 IEEE PES T&D Conference and Exposition*, pages 1–4. IEEE, 2014.

[65] Satish M Mahajan and Uma Maheshwar Singareddy. Real time GPS data processing for sag measurement'on a transmission line. In *2008 Joint International Conference on Power System Technology and IEEE Power India Conference*, pages 1–6. IEEE, 2008.

[66] John R. Fanchi. Electric power generation and distribution. In *Energy: Technology and Directions for the Future*, pages 28–58. Academic Press, Burlington, MA, USA, 2004.

[67] Shelley L Chen, William Z Black, and Michael L Fancher. High-temperature sag model for overhead conductors. *IEEE Transactions on Power Delivery*, 18(1):183–188, 2003.

[68] Mehran Keshavarzian and Charles H Priebe. Sag and tension calculations for overhead transmission lines at high temperatures-modified ruling span method. *IEEE Transactions on Power Delivery*, 15(2):777–783, 2000.

[69] Konstantinos Kopsidas, Simon M Rowland, and Boud Boumecid. A holistic method for conductor ampacity and sag computation on an OHL structure. *IEEE Transactions on Power Delivery*, 27(3):1047–1054, 2012.

[70] FVB De Nazaré and MM Werneck. Development of a monitoring system to improve ampacity in 138kV transmission lines using photonic technology. In *IEEE PES T&D 2010*, pages 1–6. IEEE, 2010.

[71] Fabio Vieira Batista de Nazare and Marcelo Martins Werneck. Hybrid optoelectronic sensor for current and temperature monitoring in overhead transmission lines. *IEEE Sensors Journal*, 12(5):1193–1194, 2011.

[72] Alen Hatibovic. Derivation and analysis of the relation between conductor sags in inclined and levelled spans based on known data of the latter. In *CIGRÉ 2014 Session*, number B2-202, Paris, France, 2014. CIGRÉ.

[73] Liu Yongfu, Zhang Liguo, and Wang Jun. Computation of standard sag of overhead lines for power grid based on mathematical model of iterative technique. In *2010 2nd*

International Conference on Computer Engineering and Technology, volume 1, pages V1–445. IEEE, 2010.

[74] Dumitru Sacerdoţianu, Marcel Nicola, Claudiu-Ionel Nicola, and Florica Lăzărescu. Research on the continuous monitoring of the sag of overhead electricity transmission cables based on the measurement of their slope. In *2018 International Conference on Applied and Theoretical Electricity (ICATE)*, pages 1–5. IEEE, 2018.

[75] Ray M. Hayes and Ali Nourai. Power line sag monitor, March 2001.

[76] AV Mamishev, RD Nevels, and BD Russell. Effects of conductor sag on spatial distribution of power line magnetic field. *IEEE Transactions on Power Delivery*, 11(3):1571–1576, 1996.

[77] US Patent. Promethean devices LLC, sensor, method and system of monitoring transmission lines, February 10 2012. US Patent 8,280,652 B2.

[78] Arsalan Habib Khawaja and Qi Huang. Characteristic estimation of high voltage transmission line conductors with simultaneous magnetic field and current measurements. In *2016 IEEE international instrumentation and measurement technology conference proceedings*, pages 1–6. IEEE, 2016.

[79] Arsalan Habib Khawaja and Qi Huang. Estimating sag and wind-induced motion of overhead power lines with current and magnetic-flux density measurements. *IEEE Transactions on Instrumentation and Measurement*, 66(5):897–909, 2017.

[80] Qi Xu, Xuyang Liu, Ke Zhu, Philip WT Pong, and Chunhua Liu. Magnetic-field-sensing-based approach for current reconstruction, sag detection, and inclination detection for overhead transmission system. *IEEE Transactions on Magnetics*, 55(7):1–7, 2019.

[81] Haoyang Fan, Qi Huang, Zhenyuan Zhang, Shi Jing, Kaiji Liao, and Xin Yang. A novel non-contact measurement method for current positioning based on magnetic

sensors. In *2021 IEEE/IAS Industrial and Commercial Power System Asia (I&CPS Asia)*, pages 1518–1524. IEEE, 2021.

[82] Nemanja Kitić and Petar Matić. Approximate magnetic flux density model of overhead power lines for conductor sag estimation. *International Journal of Electrical Engineering and Computing*, 5(2):69–76, December 2021.

[83] Nemanja Kitić, Petar Matić, ore Lekić, Predrag Mršić, Bojan Erceg, Čedomir Zeljković, and Vanja Starčević. Real-time sag estimation of overhead power lines based on approximate magnetic field model. In *2022 21st International Symposium INFOTEH-JAHORINA (INFOTEH)*, pages 1–6. IEEE, 2022.

[84] Ayman Uddin Mahin, MD Farhad Hossain, Shama Naz Islam, Kumudu S Munasinghe, and Abbas Jamalipour. Millimeter wave-based real-time sag measurement and monitoring system of overhead transmission lines in a smart grid. *IEEE Access*, 8:100754–100767, 2020.

[85] Ayman Uddin Mahin. Design of millimeter wave based sag measurement and monitoring system for overhead transmission lines in a smart grid. Master's thesis, Bangladesh University of Engineering and Technology, Dhaka, Bangladesh, November 2019.

[86] Tlotlollo Sidwell Hlalele and Shengzhi Du. Radio technology frequency identification applied in high-voltage power transmission-line for sag measurement. *International Journal of Electrical and Computer Engineering*, 7(7):928–932, 2013.

[87] Tlotlollo Sidwell Hlalele. *Radio frequency identification for the measurement of overhead power transmission line conductor sag*. PhD thesis, University of South Africa, 2015.

[88] Joe-Air Jiang, Huan-Chieh Chiu, Yu-Cheng Yang, Jen-Cheng Wang, Chien-Hsing Lee, and Cheng-Ying Chou. On real-time detection of line sags in overhead power grids using an IoT-based monitoring system: theoretical basis, system implementation, and

long-term field verification. *IEEE Internet of Things Journal*, 9(15):13096–13112, 2022.

[89] Tsui Shan Hsu, Huan Chieh Chiu, Yu Cheng Yang, Ching Ya Tseng, Ming Jhou Lin, Jen Cheng Wang, and Joe Air Jiang. An IoT-based sag monitoring system for overhead transmission lines. In *2019 IEEE PES GTD Grand International Conference and Exposition Asia (GTD Asia)*, pages 515–519. IEEE, 2019.

[90] Monish Mukherjee, Robert G Olsen, and Zhi Li. Noncontact monitoring of overhead transmission lines using space potential phasor measurements. *IEEE Transactions on Instrumentation and Measurement*, 69(10):7494–7504, 2020.

[91] Adel Z El Dein, Mohamed AA Wahab, Mohamed M Hamada, and Tamer H Emmary. The effects of the span configurations and conductor sag on the electric-field distribution under overhead transmission lines. *IEEE Transactions on Power Delivery*, 25(4):2891–2902, 2010.

[92] Mohamed M Saied. On the sag monitoring for the dynamic rating of overhead power lines. In *proceedings international conference on condition monitoring and diagnosis, Changwon, South Korea*, pages 2–5, 2006.

[93] Yan Du and Yuan Liao. On-line estimation of transmission line parameters, temperature and sag using PMU measurements. *Electric Power Systems Research*, 93:39–45, December 2012.

[94] Tarun K Gangopadhyay, Mukul C Paul, and Leif Bjerkan. Fiber-optic sensor for real-time monitoring of temperature on high voltage (400kV) power transmission lines. In *20th International Conference on Optical Fibre Sensors*, volume 7503, pages 671–674. SPIE, 2009.

[95] RA Bush, WZ Black, TC Champion, and WR Byrd. Experimental verification of a real-time program for the determination of temperature and sag of overhead lines. *IEEE Transactions on Power Apparatus and Systems*, (7):2284–2288, 1983.

[96] Lijia Ren, Hong Li, and Yan Li. Online monitoring and prediction for transmission line sag. In *Proceedings of the 2012 IEEE International Conference on Condition Monitoring and Diagnosis (CMD)*, pages 813–817. IEEE, 2012.

[97] Dávid Balango, Bálint Németh, and Gábor Göcsei. Predicting conductor sag of power lines in a new model of dynamic line rating. In *2015 IEEE Electrical Insulation Conference (EIC)*, pages 41–44. IEEE, 2015.

[98] LIAO Ruchao, LIAO Jiandong, ZHANG Ying, LI Guoqiang, LI Xionggang, and WU Yunfa. Sag prediction of high-voltage transmission lines based on PSO-SVM. In *2020 35th Youth Academic Annual Conference of Chinese Association of Automation (YAC)*, pages 772–777. IEEE, 2020.

[99] X. Liao et al. Sag prediction of high-voltage transmission lines based on PSO-SVM. *Journal/Conference details to be verified*, 2020. Uses particle swarm optimisation to optimise support-vector-machine parameters for transmission-line sag prediction.

[100] S. Eckroad. Video sagometer application guide. Technical Report 1001921, Electric Power Research Institute (EPRI), Palo Alto, CA, USA, 2001.

[101] CIGRÉ Task Force B2.11.07. Fatigue endurance capability of conductor/clamp systems: Update of present knowledge. Technical Brochure 332, CIGRÉ, Paris, France, 2007.

[102] CIGRÉ Working Group 22.12. Joints on transmission line conductors: Field testing and replacement criteria. Technical Brochure 216, CIGRÉ, Paris, France, 2002.

[103] CIGRÉ Working Group B2.32. Evaluation of aged fittings. Technical Brochure 477, CIGRÉ, Paris, France, 2011.

[104] CIGRÉ Task Force B2.11.07. Fatigue endurance capability of conductor/clamp systems: Update of present knowledge. Technical Brochure 332, CIGRÉ, Paris, France, 2007.

[105] Eric Cloet, Jean-Louis Lilien, and Patrick Ferrières. Experiences of the belgian and

french tsos using the “ampacimon” real-time dynamic rating system. In *CIGRE 2010*, 2010.

[106] USi-Power Inc. Donut® line monitor. Online product information, 2022. Accessed 31 October 2022.

[107] USi-Power Inc. Power donut2 system for overhead transmission line monitoring: Product overview. Product brochure, 2006.

[108] Fred A. Brown. Apparatus and method of monitoring a power transmission line. U.S. Patent US6229451B1, May 2001. Issued 8 May 2001; priority date 20 February 1997; assignee: ECSI Corporation.

[109] The Valley Group Inc. CAT-1 transmission line monitoring system. Product brochure, 2006. Accessed 31 October 2022.

[110] EDM International, Inc. Sagometer: Product overview. Product brochure, 2022. Accessed 31 October 2022.

[111] IEEE Power and Energy Society Transmission and Distribution Committee. IEEE guide for the installation of overhead transmission line conductors. IEEE Std. 524-2016, IEEE, New York, NY, USA, 2016.

[112] CIGRÉ Task Force B2.12.3. Sag-tension calculation methods for overhead lines. Technical Brochure 324, CIGRÉ, Paris, France, April 2016. Revision of the first edition published in June 2007.

[113] Carl Johan Wallnerström, Patrik Hilber, Peter Söderström, Robert Saers, and Olle Hansson. Potential of dynamic rating in sweden. In *2014 International conference on probabilistic methods applied to power systems (PMAPS)*, pages 1–6. IEEE, 2014.

[114] Saifal Talpur, Carl Johan Wallnerstrom, Christer Flood, and Patrik Hilber. Implementation of dynamic line rating in a sub-transmission system for wind power integration. *Smart grid and renewable energy*, 6(8):233–249, 2015.

[115] Stephen D Foss and Robert A Maraio. Dynamic line rating in the operating environment. *IEEE Transactions on Power Delivery*, 5(2):1095–1105, 1990.

[116] E Fernandez, I Albizu, MT Bedialauneta, AJ Mazon, and Patricia T Leite. Review of dynamic line rating systems for wind power integration. *Renewable and Sustainable Energy Reviews*, 53:80–92, 2016.

[117] Andrea Michiorri, Huu-Minh Nguyen, Stefano Alessandrini, John Bjørnar Bremnes, Silke Dierer, Enrico Ferrero, Bjørn-Egil Nygaard, Pierre Pinson, Nikolaos Thomaidis, and Sanna Uski. Forecasting for dynamic line rating. *Renewable and Sustainable Energy Reviews*, 52:1713–1730, 2015.

[118] E Fernandez, I Albizu, MT Bedialauneta, AJ Mazon, and PT Leite. Dynamic line rating systems for wind power integration. In *IEEE Power and Energy Society Conference and Exposition in Africa: Intelligent Grid Integration of Renewable Energy Resources (PowerAfrica)*, pages 1–7. IEEE, 2012.

[119] Clifton R Black and William A Chisholm. Key considerations for the selection of dynamic thermal line rating systems. *IEEE Transactions on Power Delivery*, 30(5):2154–2162, 2014.

[120] Guido Coletta, Alfredo Vaccaro, and Domenico Villacci. A review of the enabling methodologies for PMUs-based dynamic thermal rating of power transmission lines. *Electric Power Systems Research*, 152:257–270, 2017.

[121] David L Alvarez, Javier A Rosero, F Faria Da Silva, Claus Leth Bak, and Enrique E Mombello. Dynamic line rating–technologies and challenges of PMU on overhead lines: A survey. In *2016 51st International Universities Power Engineering Conference (UPEC)*, pages 1–6. IEEE, 2016.

[122] Soheila Karimi, Petr Musilek, and Andrew M Knight. Dynamic thermal rating of transmission lines: A review. *Renewable and Sustainable Energy Reviews*, 91:600–612, 2018.

[123] Dale A. Douglass, Ian Grant, Jose Antonio Jardini, Robert Kluge, Paula Traynor, Cody Davis, Jake Gentle, Huu Minh Nguyen, William Chisholm, Charles Xu, Tip Goodwin, Hong Chen, Sarma Nuthalapati, and Neil Hurst. A review of dynamic thermal line rating methods with forecasting. *IEEE Transactions on Power Delivery*, 34(6):2100–2109, December 2019. Article no. 8782593.

[124] Jiashen Teh, Ching-Ming Lai, Nor Asiah Muhamad, Chia Ai Ooi, Yu-Huei Cheng, Muhammad Ammirrul Atiqi Mohd Zainuri, and Mohamad Khairi Ishak. Prospects of using the dynamic thermal rating system for reliable electrical networks: A review. *IEEE Access*, 6:26765–26778, 2018.

[125] Grzegorz Fusiek and Pawel Niewczas. Design of an optical sensor with varied sensitivities for overhead line sag, temperature, and vibration monitoring. In *2022 IEEE International Instrumentation and Measurement Technology Conference (I2MTC)*, pages 1–6. IEEE, 2022.

[126] Himanshi Singh, Grzegorz Fusiek, and Pawel Niewczas. Extended characterization of an optical sag sensor for high-temperature low-sag lines. *IEEE Sensors Letters*, 2023.

[127] Himanshi Singh, Grzegorz Fusiek, Pawel Niewczas, and Valerie Livina. Estimation of the fatigue life of a fiber bragg grating overhead line sag sensor. In *2024 IEEE International Instrumentation and Measurement Technology Conference (I2MTC)*, pages 1–6. IEEE, 2024.

[128] L. Staszewski and W. Rebizant. The differences between IEEE and CIGRÉ heat balance concepts for line ampacity considerations. In *Proceedings of the 2010 International Symposium on Modern Electric Power Systems (MEPS)*, Wroclaw, Poland.

[129] Jiao Fu, S Abbott, Brendan Fox, D John Morrow, and Sobhy Abdelkader. Wind cooling effect on dynamic overhead line ratings. In *45th International Universities Power Engineering Conference UPEC2010*, pages 1–6. IEEE, 2010.

[130] Rambabu Adapa and Dale A Douglass. Dynamic thermal ratings: monitors and calculation methods. In *2005 IEEE Power Engineering Society Inaugural Conference and exposition in Africa*, pages 163–167. IEEE, 2005.

[131] F Alvarez Gomez, JM Garcia De Maria, D Garcia Puertas, A Baïri, and R Granizo Arrabe. Numerical study of the thermal behavior of bare overhead conductors in electrical power lines. *Recent Res. Commun. Electr. Comput. Eng*, 1:149–153, 2011.

[132] Masaki Miura, Takuya Satoh, Shinichi Iwamoto, and Ikuo Kurihara. Application of dynamic rating to evaluation of atc with thermal constraints considering weather conditions. In *2006 IEEE Power Engineering Society General Meeting*, pages 6–pp. IEEE, 2006.

[133] S Islam and Foredul Islam. Impact of temperature, wind flow, solar radiation, skin effect and proximity effect on overhead conductor. *Glob. J. Res. Eng. Electr. Electron. Eng*, 12(1):1–5, 2012.

[134] Marija Bockarjova and Goran Andersson. Transmission line conductor temperature impact on state estimation accuracy. In *2007 IEEE Lausanne power tech*, pages 701–706. IEEE, 2007.

[135] Xiaolong Hu and Ian Cotton. Impact of climate change on overhead lines operated using dynamic rating in a smart gird. In *IEEE PES ISGT Europe 2013*, pages 1–5. IEEE, 2013.

[136] Stan M Kaplan. Electric power transmission: background and policy issues. Library of Congress, Congressional Research Service, 2009.

[137] Quan Chai, Yang Luo, Jing Ren, Jianzhong Zhang, Jun Yang, Libo Yuan, and Gang-Ding Peng. Review on fiber-optic sensing in health monitoring of power grids. *Optical Engineering*, 58(7):072007–072007, 2019.

[138] Leif Bjerkan. Application of fiber-optic bragg grating sensors in monitoring environmental loads of overhead power transmission lines. *Applied Optics*, 39(4):554–560, 2000.

[139] CIGRÉ Working Group 22.13. Management of existing overhead transmission lines. Technical Brochure 175, CIGRÉ, Paris, France, 2000.

[140] Konstantin O. Papailiou, editor. *Overhead Lines*. CIGRÉ Green Books. CIGRÉ / Springer, Paris, France, 2017.

[141] CIGRE Task Force B2.11.04. Overhead conductor safe design tension with respect to aeolian vibrations. Technical Brochure 273, CIGRE, Paris, France, June 2005.

[142] C. Dalpé, L. Cloutier, A. Cardou, and S. Goudreau. State of knowledge on the fretting behaviour in stranded conductors. Report SM-03-05, GREMCA, Laval University, Quebec, Canada, May 2003.

[143] William G. Fricke and Charles B. Rawlins. Importance of fretting in vibration failures of stranded conductors. *IEEE Transactions on Power Apparatus and Systems*, PAS-87(6):1381–1384, 1968.

[144] L. Moecks. Vibration damage on stranded conductors. *Bulletin of the Swiss Electrotechnical Association*, 61(5):223–227, 1970.

[145] P. W. Dulhunty. Some recent field experiences with vibration dampers. Working Group Document ISC22-71 WG04, CIGRÉ, May 1971.

[146] CIGRÉ Working Group 22.04. Recommendations for the evaluation of the lifetime of transmission line conductors. Electra ELT_063_3, CIGRÉ, Paris, France, 1979.

[147] JC Poffenberger and RL Swart. Differential displacement and dynamic conductor strain. *IEEE Transactions on Power Apparatus and Systems*, 84(4):281–289, 1965.

[148] Alain Cardou, Louis Cloutier, Michel St-Louis, and Andre Leblond. ACSR electrical conductor fretting fatigue at spacer clamps. In *Standardization of fretting fatigue test methods and equipment*. ASTM International, 1992.

[149] A. Cardou, A. Leblond, S. Goudreau, and L. Cloutier. Electrical conductor bending fatigue at suspension clamp: A fretting fatigue problem. In R. B. Waterhouse and T. C. Lindley, editors, *Fretting Fatigue*, ESIS 18, pages 257–266. Mechanical Engineering Publications, London, UK, 1994.

[150] L Cloutier, C Dalpé, A Cardou, C Hardy, and S Goudreau. Studies of conductor vibration fatigue tests, flexural stiffness and fretting behaviour. In *Proceedings of the Third International Symposium on Cable Dynamics, Trondheim, Norway*, pages 16–18, 1999.

[151] IEEE Committee Report. Standardization of conductor vibration measurements. *IEEE Transactions on Power Apparatus and Systems*, PAS-85(1):10–22, January 1966.

[152] CB Rawlins. Fatigue of overhead conductors. *Transmission Line Reference Book, Electrical Power Research Institute, Palo Alto CA*, pages 51–81, 1979.

[153] CIGRÉ Task Force 22.11.02. Guide to vibration measurements on overhead lines. Electra ELT_163_5, CIGRÉ, Paris, France, 1995.

[154] J. Lanteigne. Theoretical estimation of the response of helically armored cables to tension, torsion, and bending. *Journal of Applied Mechanics*, 52(2):423–432, June 1985.

[155] K. O. Papailiou. On the bending stiffness of transmission line conductors. *IEEE Transactions on Power Delivery*, 12(4):1576–1588, October 1997.

[156] S. Goudreau and A. Cardou. Flexural testing of an epoxy oversized strand model under traction. *Experimental Mechanics*, 33(4):300–307, 1993.

[157] Rodolfo Claren and Giorgio Diana. Dynamic strain distribution on loaded stranded cables. *IEEE Transactions on Power Apparatus and Systems*, PAS-88(11):1678–1690, November 1969.

[158] Rodolfo Claren and Giorgio Diana. Mathematical analysis of transmission line vibration. *IEEE Transactions on Power Apparatus and Systems*, PAS-88(12):1741–1771, December 1969.

[159] R. H. Scanlan and R. L. Swart. Bending stiffness and strain in stranded cables. In *IEEE Winter Power Meeting*, number 68 CP 43-PWR, New York, NY, USA, 1968.

[160] T. O. Seppa. Self-damping measurements and energy balance of ACSR drake. In *IEEE Winter Power Meeting*, number 71 CP 151-PWR, New York, NY, USA, 1971. Presented 31 January–5 February 1971.

[161] Kenneth G. McConnell and W. P. Zemke. The measurement of flexural stiffness of multistranded electrical conductors while under tension. *Experimental Mechanics*, 20(6):198–204, June 1980.

[162] C. Hardy and A. Leblond. On the dynamic flexural rigidity of taut stranded cables. In *Proceedings of the 5th International Symposium on Cable Dynamics*, pages 45–52, Santa Margherita Ligure, Italy, September 2003. Presented 15–18 September 2003.

[163] Alain Cardou and Claude Jolicoeur. Mechanical models of helical strands. *Applied Mechanics Reviews*, 50(1):1–14, January 1997.

[164] Alain Cardou. Taut helical strand bending stiffness. UFTscience technical note, UT 01-2006, 2006.

[165] Rolf Helms. Zur sicherheit der hochspannungsfreileitungen bei hoher mechanischer beanspruchung. *VDI-Forschungsheft*, 30(506):5–52, 1964.

[166] Josef Ziebs. Über das mechanische verhalten von aluminium-stahl-freileitungsseilen als

beispiel für verbundbauteile. Forschungsbericht 3, Bundesanstalt für Materialforschung und -prüfung (BAM), Berlin, Germany, 1970.

[167] J. Lanteigne, L. Cloutier, and A. Cardou. Fatigue life of aluminum wires in all-aluminum and ACSR conductors. CEA Report 131 T 241, Canadian Electrical Association, Montreal, Canada, July 1986.

[168] A. R. Hard. Studies of conductor vibration in laboratory span, outdoor test span, and actual transmission lines. Report 404, CIGRÉ, Paris, France, 1958.

[169] W. Buckner, H. Kerner, and W. Philipps. Stresses in transmission line conductors near the suspension clamp. Session Materials 23-07_1968, CIGRÉ, Paris, France, 1968.

[170] A. T. Edwards and J. M. Boyd. Ontario hydro live-line vibration recorder for transmission conductors. *IEEE Transactions on Power Apparatus and Systems*, PAS-82(66):269–273, 1963.

[171] Kenneth O Hill, Yoshihisa Fujii, Derwyn C Johnson, and Brian S Kawasaki. Photosensitivity in optical fiber waveguides: Application to reflection filter fabrication. *Applied Physics Letters*, 32(10):647–649, 1978.

[172] Yun-Jiang Rao. In-fibre bragg grating sensors. *Measurement Science and Technology*, 8(4):355, 1997.

[173] AD Kersey, DA Jackson, and M Corke. A simple fibre fabry-perot sensor. *Optics Communications*, 45(2):71–74, 1983.

[174] CE Lee, JJ Alcoz, Y Yeh, WN Gibler, RA Atkins, and Henry F Taylor. Optical fiber fabry-perot sensors for smart structures. *Smart Materials and Structures*, 1(2):123, 1992.

[175] Drope S Kist R and Wolfelschnelder H. Fibre-fabry–perot (ffp) thermometer for medical applications. *2nd Int.Conf. on Optical Fibre Sensors*, 1(2):165, 1984.

[176] Farhad Ansari. Applications of fiber optic sensors in engineering mechanics. American Society of Civil Engineers, 1993.

[177] James N Blake, Shang-Yuan Huang, Byoung Yoon Kim, and Herbert J Shaw. Strain effects on highly elliptical core two-mode fibers. *Optics Letters*, 12(9):732–734, 1987.

[178] Zhuo Jun Lu and Franz A Blaha. Application issues of fiber-optic sensors in aircraftt structures. In *Fiber Optic Smart Structures and Skins IV*, volume 1588, pages 276–281. SPIE, 1991.

[179] Malcolm P Varnham, DN Payne, AJ Barlow, and K Okamoto. Polarimetric strain gauges using high birefringence fibre. *Electronics Letters*, 19:699, 1983.

[180] Wojtek J Bock and Tomasz R Wolinski. Temperature-compensated fiber optic strain sensor based on polarization-rotated reflection. In *Fiber optic smart structures and skins III*, volume 1370, pages 189–196. SPIE, 1990.

[181] William W Morey, Gerald Meltz, and William H Glenn. Fiber optic bragg grating sensors. In *Fiber optic and laser sensors VII*, volume 1169, pages 98–107. SpIE, 1990.

[182] Yun Jiang Rao, AB Lobo Ribeiro, David A Jackson, Leishi Zhang, and Ian Bennion. Combined spatial-and time-division-multiplexing scheme for fiber grating sensors with drift-compensated phase-sensitive detection. *Optics letters*, 20(20):2149–2151, 1995.

[183] MG Xu, J-L Archambault, L Reekie, and JP Dakin. Discrimination between strain and temperature effects using dual-wavelength fibre grating sensors. *Electronics letters*, 30(13):1085–1087, 1994.

[184] GB Hocker. Fiber-optic sensing of pressure and temperature. *Applied optics*, 18(9):1445–1448, 1979.

[185] WW Morey. Evaluation of a fiber bragg grating hydrostatic pressure sensor. *Proc. OFS8, Moneterey, USA, Post-Deadline Session*, 1982.

[186] MG Xu, L Reekie, YT Chow, and J Pj Dakin. Optical in-fibre grating high pressure sensor. *Electronics letters*, 29(4):398–399, 1993.

[187] MG Xu, H Geiger, and JP Dakin. Fibre grating pressure sensor with enhanced sensitivity using a glass-bubble housing. *Electronics Letters*, 32(2):128–129, 1996.

[188] Alan D. Kersey and Michael J. Marrone. Fiber bragg grating high-magnetic-field probe. In *Tenth International Conference on Optical Fibre Sensors*, volume 2360 of *Proceedings of SPIE*, pages 53–56, 1994.

[189] Faramarz Farahi, David J Webb, Julian DC Jones, and David A Jackson. Simultaneous measurement of temperature and strain: cross-sensitivity considerations. *Journal of Lightwave Technology*, 8(2):138–142, 1990.

[190] A. Martinez, M. Dubov, I. Khrushchev, and I. Bennion. Direct writing of fibre bragg gratings by femtosecond laser. *Electronics Letters*, 40(19):1170–1172, 2004.

[191] Stephen J. Mihailov. Fiber bragg grating sensors for harsh environments. *Sensors*, 12(2):1898–1918, 2012.

[192] Paul J Lemaire, RM Atkins, V Mizrahi, and WA Reed. High pressure h2 loading as a technique for achieving ultrahigh uv photosensitivity and thermal sensitivity in geo2 doped optical fibres. *Electronics letters*, 29(13):1191–1193, 1993.

[193] Gerald Meltz, William W Morey, and William H Glenn. Formation of bragg gratings in optical fibers by a transverse holographic method. *Optics letters*, 14(15):823–825, 1989.

[194] R Kashyap, JR Armitage, R Wyatt, ST Davey, and DL Williams. All-fibre narrowband reflection gratings at 1500 nm. *Electronics Letters*, 26(11):730–732, 1990.

[195] CG Askins, T-E Tsai, GM Williams, MA Putnam, M Bashkansky, and EJ Friebele. Fiber bragg reflectors prepared by a single excimer pulse. *Optics Letters*, 17(11):833–835, 1992.

[196] J-L Archambault, L Reekie, and PJ Russell. High reflectivity and narrow bandwidth fibre gratings written by single excimer pulse. *Electronics Letters*, 29(1):28–29, 1993.

[197] Michael L Dockney, Stephen W James, and Ralph P Tatam. Fibre bragg gratings fabricated using a wavelength tuneable laser source and a phase mask based interferometer. *Measurement science and technology*, 7(4):445, 1996.

[198] Kenneth O Hill, B Malo, F Bilodeau, DC Johnson, and Jacques Albert. Bragg gratings fabricated in monomode photosensitive optical fiber by uv exposure through a phase mask. *Applied Physics Letters*, 62(10):1035–1037, 1993.

[199] DZ Anderson, V Mizrahi, T Erdogan, and AE White. Production of in-fibre gratings using a diffractive optical element. *Electronics Letters*, 29(6):566–568, 1993.

[200] JD Prohaska, E Snitzer, S Rishton, and V Boegli. Magnification of mask fabricated fibre bragg gratings. *Electronics Letters*, 29(18):1614–1615, 1993.

[201] J Martin and F Ouellette. Novel writing technique of long and highly reflective in-fibre gratings. *Electronics Letters*, 30(10):811–812, 1994.

[202] HN Rourke, SR Baker, KC Byron, RS Baulcomb, SM Ojha, and S Clements. Fabrication and characterization of long, narrowband fibre gratings by phase mask scanning. *Electronics Letters*, 30(16):1341–1342, 1994.

[203] Raman Kashyap, PF McKee, RJ Campbell, and DL Williams. Novel method of producing all fibre photoinduced chirped gratings. *Electronics Letters*, 30(12):996–998, 1994.

[204] MJ Cole, WH Loh, RI Laming, MN Zervas, and Sergio Barcelos. Moving fibre/phase mask-scanning beam technique for enhanced flexibility in producing fibre gratings with a uniform phase mask. *Electronics Letters*, 31(17):1488–1490, 1995.

[205] Alan D. Kersey, Michael A. Davis, Heather J. Patrick, Michel LeBlanc, K. P. Koo,

C. G. Askins, M. A. Putnam, and E. Joseph Friebele. Fiber grating sensors. *Journal of Lightwave Technology*, 15(8):1442–1463, 1997.

[206] Bertrand Godard, Suzanne Guérard, and Jean-Louis Lilien. Original real-time observations of aeolian vibrations on power-line conductors. *IEEE Transactions on Power Delivery*, 26(4):2111–2117, 2011.

[207] Himanshi Singh, Grzegorz Fusiek, and Pawel Niewczas. Methodological framework for conductor lifetime estimation using optical sag sensors. *IEEE Sensors Letters*, 8(7):1–4, 2024.

4

Design and Laboratory Characterisation of an FBG OHL Sensor

4.1 OHL sensor specifications and design

The principles of FBG sensing, fabrication, and interrogation have been reviewed in Chapter 3. Building on this background, the present chapter focuses on the design, modelling, and laboratory characterisation of the FBG-based overhead line sensor developed in this research.

4.1.1 Power Network Demonstration Centre (PNDC)

The conductor used in this work is composed of hard-drawn copper (HDC), a material known for its high strength and good conductivity, making it suitable for overhead line applications. The conductor has a circular cross-sectional area of 70 mm^2, which corresponds to an approximate diameter of 10.5 mm, as shown in Figure 4.1 [1].

For mechanical calculations, the weight of the conductor per unit length is considered to be 5.81 N/m, which reflects the gravitational load acting on the span. Additionally, the elastic modulus of the hard-drawn copper is taken as 120 GPa, indicating the material's resistance to elastic deformation under tensile loading [1].

Figure 4.1: HDC conductor used for OHL at PNDC with zoomed images showing 7 strands and cross section.

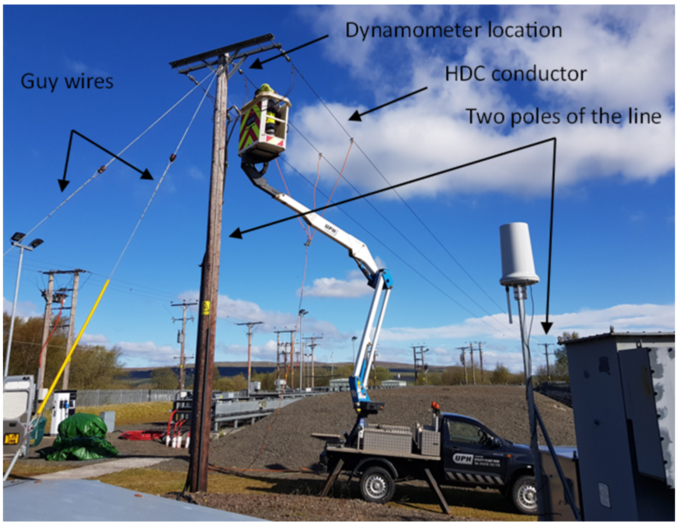

Figure 4.2: Overhead line at PNDC.

To reflect the actual physical conductor arrangement at PNDC, the modelled overhead line segment spans a total length of 80 m, with the conductor assumed to be securely anchored at both ends to the support structures (e.g., poles or towers) that are positioned at an equal elevation, shown in Figure 4.2, thereby simplifying the analysis by eliminating any vertical gradient in the setup [1].

Table 4.1 summarises the parameters of the HDC conductor considered for the research.

Table 4.1: HDC conductor parameters.

Parameter	**Value**
Material	Hard-drawn copper (HDC)
Cross-sectional area	70 mm^2

Continued on next page

Table 4.1: HDC conductor parameters continued.

Parameter	**Value**
Diameter	10.5 mm
Weight per unit length	5.81 Nm^{-1}
Number of strands	7
Elastic modulus	120 GPa

4.1.2 T220 FBG Strain Transducer

To measure strain, vibration, and sag in the HDC conductor, a sensor was designed and constructed, as described in the next section, using a commercially available T220 FBG strain transducer from Technica SA [2]. The transducer was required because a bare FBG is too fragile for direct installation on an overhead conductor and would not provide reliable strain transfer under mechanical loading, vibration, and temperature cycling. The packaged T220 transducer provides a mechanically robust interface between the conductor-mounted sensor assembly and the FBGs, enabling repeatable conversion of conductor deformation into measurable Bragg wavelength shifts.

The T220 transducer contains two FBGs: one bonded to measure strain and one isolated from mechanical strain to measure temperature. The temperature FBG is used to compensate the strain measurement by estimating the temperature-induced wavelength shift and subtracting it from the total wavelength shift measured by the strain FBG. In this way, the remaining wavelength shift is associated primarily with mechanical strain. The transducer is packaged in stainless steel (SS)316, secured at both ends with strain-relief buffers, and terminated with 3 mm armoured cables [3]. It is designed to operate up to 200 °C, making it suitable for HTLS applications. The supplier specifies an accuracy of <0.5 % full scale, including hysteresis, nonlinearity, and repeatability, and a strain range of ±2000 $\mu\varepsilon$. The specifications of the T220 transducer are provided in Table 4.2.

Table 4.2: General manufacturer specifications of the T220 FBG strain transducer [4].

Parameter	**Specification**
Nominal Bragg wavelength range	1459–1621 nm, with ±0.5 nm tolerance; 980 nm, 1060 nm, and 1310 nm options also available
Reflection bandwidth, $\Delta\lambda$ (FWHM)	0.1–2.0 nm
Reflectivity	75 % typical; 1–99 % available
Side-lobe suppression ratio (SLSR)	15 dB
Strain measurement range	±2000 $\mu\varepsilon$
Anchor spacing	105 mm, ±6 mm
Strain accuracy	<0.5 % full scale; <0.25 % full scale typical
Strain precision	<0.25 % full scale; <0.15 % full scale typical
Temperature compensation	Integrated within the sensor
Temperature accuracy	less than 1 % over the temperature range from -20 °C to +60 °C
Ingress protection rating	IP67
Sensor pigtail	1 m length, 3 mm diameter
Cable bend radius	Static: 30 mm; dynamic: 40 mm
Optical connector	FC/APC or custom
Housing material	SS316L
Dimensions	127×35×8.2 mm
Weight	170 g
Mounting method	Spot welding, screws, or glue

The sensor-specific baseline Bragg wavelength, λ_B, was taken as 1542.27 nm from the unloaded measurement at 20 °C as specified in Table 4.3. The reflection bandwidth, $\Delta\lambda$, was not measured in the experimental dataset; therefore, only the manufacturer-specified FWHM range of 0.1-2.0 nm is reported in Table 4.2.

Table 4.3: Sensor-specific Bragg wavelength of the T220 FBG strain transducer used in this work. The baseline Bragg wavelength was obtained from the unloaded measurement at 20 °C.

Sensor	Condition	Bragg wavelength, λ_B (nm)	Reflection bandwidth, $\Delta\lambda$ / FWHM (nm)
T220 FBG strain transducer	0 kN, 20 °C	1542.27	Not measured

4.1.3 Sag Sensor Construction

The proposed sag sensor assembly was developed by integrating a commercially available T220 FBG strain transducer with a custom-designed mechanical mounting structure for installation on an HDC conductor. The T220 transducer itself was not fabricated as part of this research; rather, the contribution of this work was the design, fabrication, and evaluation of the conductor-mounted sag sensor assembly that enables the transducer to measure sag-related strain, temperature, and vibration in an OHL environment.

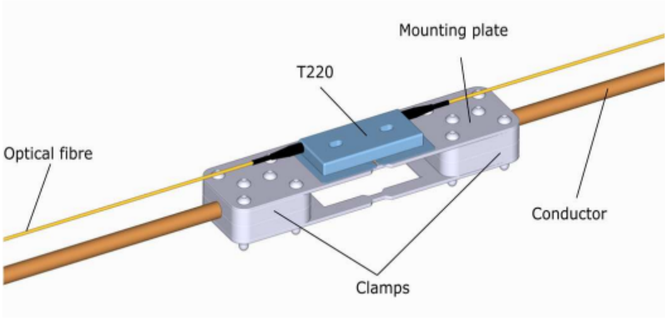

Figure 4.3: Schematic representation of the optical sag sensor assembly. The commercially available T220 FBG strain transducer contains the integrated FBG sensing elements and is spot-welded to a custom SS304 mounting plate, which is clamped to the conductor [4].

The conceptual representation of the proposed sag sensor assembly on a conductor is illustrated in Figure 4.3. The T220 strain transducer is spot-welded to a stainless steel SS304 mounting plate with a thickness of 2 mm. This plate is secured between two sets of SS304 metal clamps, which are fixed onto the conductor using M5 bolts. The clamps are positioned 100 mm apart along the conductor axis. To promote a symmetric strain distribution and reduce structural bending during operation, an identical mounting plate is placed on the opposite side of the conductor. The plates are located approximately 5 mm from the conductor surface [1].

The FBG sensing elements were supplied as part of the commercially available T220 strain transducer; therefore, no bare FBG insertion or packaging was carried out in this work. The contribution of this research was the integration of the packaged T220 transducer with the custom SS304 mounting plate and conductor-clamp assembly.

The mounting plate and custom sag sensor components were fabricated from SS304 according to the specified design. SS304 was selected because it provides good mechanical strength, corrosion resistance, and compatibility with the spot-welding process used to integrate the T220 strain transducer. Although the T220 transducer is packaged in SS316, SS304 was used for the fabricated mounting components because it offers suitable weldability and mechanical compatibility for the sensor assembly. Furthermore, SS304 has a coefficient of thermal expansion (CTE) reasonably close to that of the conductor, helping to reduce differential thermal strain during temperature fluctuations. This material compatibility also minimises galvanic potential differences, thereby decreasing the likelihood of galvanic corrosion [1]. To further safeguard the system from environmental degradation, such as moisture-induced corrosion, a protective anti-corona lacquer or conductive coating can be applied to the sensor assembly [1]. The strain transducer was prestrained before welding using a dedicated tool and then spot-welded to the SS304 mounting plate. The prestraining step ensured that the sensor operated within the desired strain measurement range of -1 mε to 3 mε. This adjustment was monitored in real time using an FBG interrogator to ensure that the required strain offset was achieved. Once the correct strain offset was obtained, the opposite end of the transducer was spot-welded, and the prestraining tool was removed [1].

To evaluate the strain transfer characteristics, five different mounting plate geometries were tested under identical axial load conditions. As depicted in Figure 4.4, one end of each design is subjected to a constant force (F), while the opposite end is held fixed.

The objective of this comparative analysis was to understand how variations in geometry influence the strain transfer efficiency, mechanical flexibility, and overall sensitivity of the sensor assembly. Among the tested configurations, the narrow and spring-section plate design was selected for further study due to its enhanced mechanical responsiveness and superior strain localisation. This design effectively isolates the sensing area from unwanted rigid-body motion and external mechanical disturbances, minimising the impact of parasitic strains. Its structure is particularly advantageous in low-force environments or applications that demand high-resolution strain measurements. The integrated spring-like features provide elastic resilience, enabling the sensor to endure cyclic loading without permanent deformation, thereby offering reliable performance and extended fatigue life.

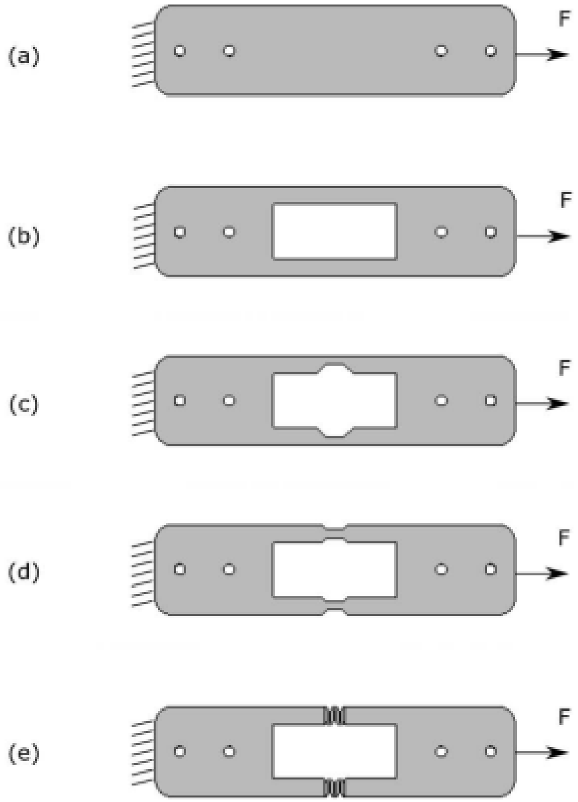

Figure 4.4: Different mounting plate designs used for stress analysis: (a) straight rectangular mounting plate; (b) tapered mounting plate; (c) curved mounting plate; (d) narrow mounting plate; and (e) spring mounting plate [4].

The performance of narrow plates has been simulated using COMSOL software; the results are discussed in the next section.

4.2 Finite element modelling of OHL sensor between -20 °C to 200 °C

4.2.1 Material properties of the conductor's geometry

This subsection outlines the temperature-dependent material properties used in the finite element analysis of the conductor system. The conductor assembly consists of two primary materials, i.e., stainless steel 304, which is used for structural components like clamps and mounting plates, and copper, which constitutes the hard-drawn copper (HDC) conductor. Each material exhibits unique thermomechanical behaviour, which is essential to account for during thermal stress analysis and deformation studies.

4.2.2 Properties of Stainless Steel 304

Stainless steel 304's thermal and mechanical properties for the simulations are considered temperature-dependent and have been modelled accordingly. The coefficient of thermal expansion is implemented using a temperature-sensitive expression that accounts for variation from a reference temperature (293 K), ensuring accurate thermal strain predictions.

The density calculated using equation 4.1, represented as a function of temperature $\rho(T)$, decreases with increasing temperature obtained from material property data within COMSOL Multiphysics, as shown in Figure 4.5.

$$\rho(T) = \rho_o[1 - \alpha(T - T_o)] \tag{4.1}$$

Similarly, the coefficient of thermal expansion (CTE) increases with temperature obtained from material property data within COMSOL Multiphysics, as depicted in Figure 4.6, indicating dimensional changes at higher thermal loads. The CTE has been calculated by using equation 4.2.

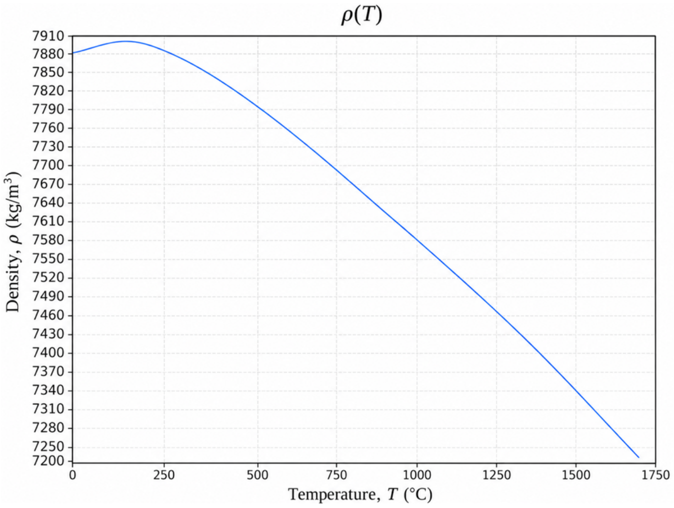

Figure 4.5: Variation in stainless steel density as a function of temperature.

$$CTE = \frac{\alpha(T) + (T_{\text{ref}} - 293)\begin{cases} \dfrac{\alpha(T) - \alpha(T_{\text{ref}})}{T - T_{\text{ref}}}, & |T - T_{\text{ref}}| > 10^{-3} \\ \dfrac{d\alpha(T)}{dT}, & |T - T_{\text{ref}}| \leq 10^{-3} \end{cases}}{1 + \alpha(T_{\text{ref}})(T_{\text{ref}} - 293)} \tag{4.2}$$

where CTE is the coefficient of thermal expansion at temperature T, $\alpha(T)$ is the temperature-dependent thermal strain function, T is the temperature at which the CTE is evaluated, T_{ref} is the reference temperature, and 293 K is the reference temperature used in the material model. The conditional term accounts for the slope of the thermal strain function between T and T_{ref}. When $|T - T_{\text{ref}}| > 10^{-3}$, the slope is calculated using the finite-difference term $(\alpha(T) - \alpha(T_{\text{ref}}))/(T - T_{\text{ref}})$. When T is very close to T_{ref}, the derivative $d\alpha(T)/dT$ is used instead to avoid numerical division by a very small temperature difference.

Young's modulus governs the stiffness of the material and decreases with increasing temperature. In this work, the temperature-dependent Young's modulus of SS304 was obtained from the material property data in COMSOL Multiphysics and implemented as an interpolation function:

$$E = E(T) \tag{4.3}$$

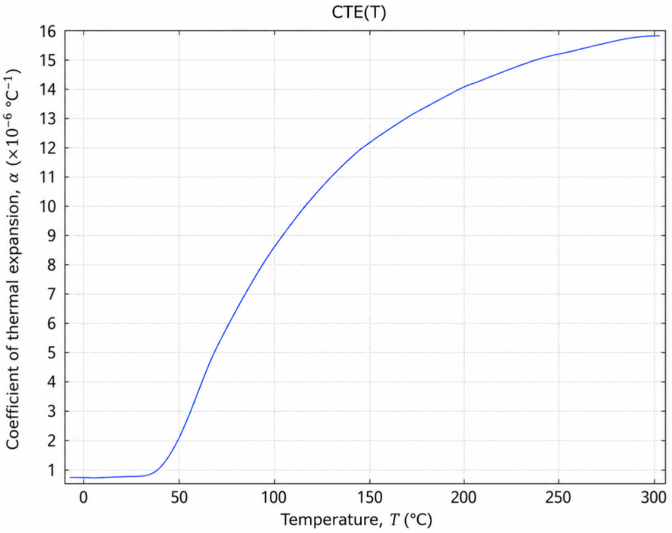

Figure 4.6: The graph illustrates the variation of the coefficient of thermal expansion (CTE) with temperature.

where $E(T)$ represents the Young's modulus evaluated at temperature T by interpolation of the tabulated material-property data. The resulting variation is shown in Figure 4.7. This temperature dependence was included in the finite element model to account for the reduction in material stiffness at elevated temperatures.

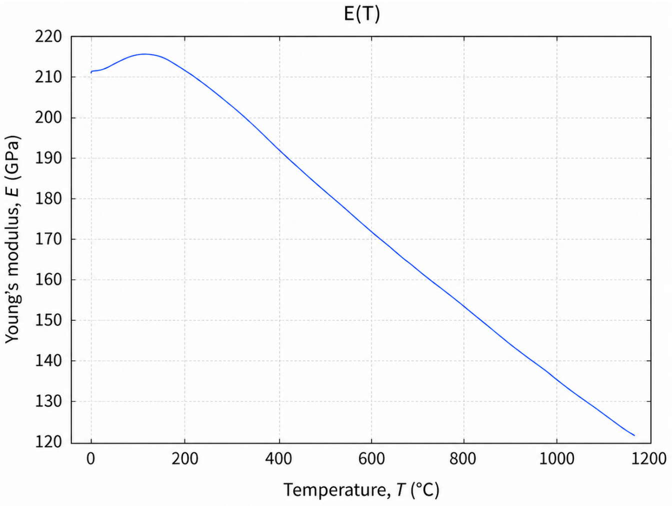

Figure 4.7: This graph displays the variation of Young's modulus as a function of temperature.

Lastly, Poisson's ratio, which reflects the tendency of the material to expand laterally when compressed, also varies slightly with the temperature obtained from the material property data within COMSOL Multiphysics, as illustrated in Figure 4.8. The example of the parameters mentioned above at 20 °C has been calculated using the above equations and is shown in Table 4.4.

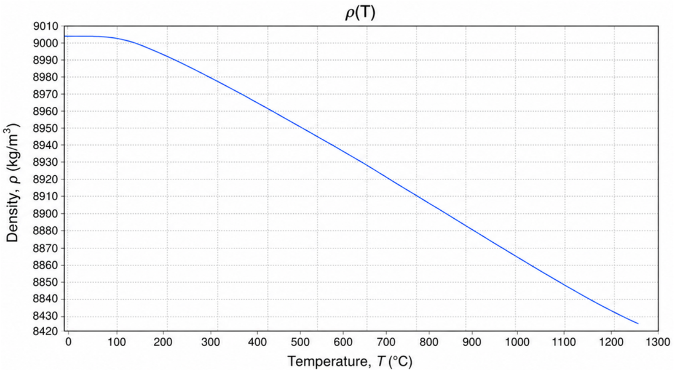

Figure 4.8: The plot illustrates the variation of Poisson's ratio with temperature.

Table 4.4: SS304 parameter values at 20 °C.

Name	**Value**	**Unit**
Coefficient of thermal expansion	17×10^{-6}	K^{-1}
Density	8000	kg/m^3
Young's modulus	193×10^9	Pa
Poisson's ratio	0.29	1

4.2.3 Properties of Copper

The material properties of copper assumed for the simulation are similar to those of stainless steel in that they are temperature dependent. The variation in density with temperature, obtained from material property data within COMSOL Multiphysics, is shown in Figure 4.9.

The coefficient of thermal expansion (CTE) of copper is also modelled as temperature-dependent. Figure 4.10 shows that the CTE increases with temperature, which contributes to increased thermal deformation at elevated temperatures.

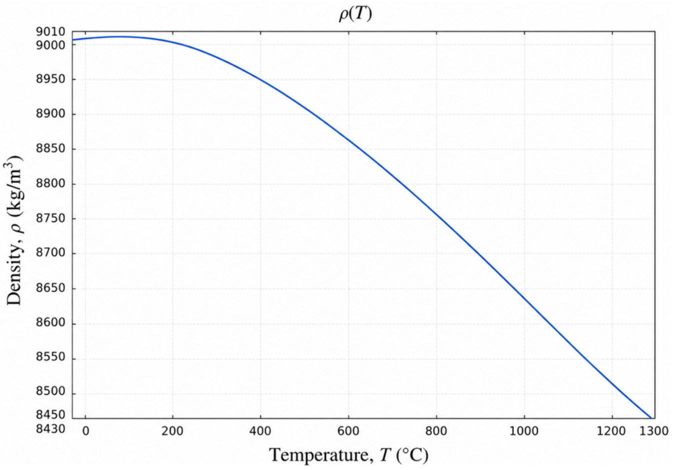

Figure 4.9: Variation of copper density as a function of temperature.

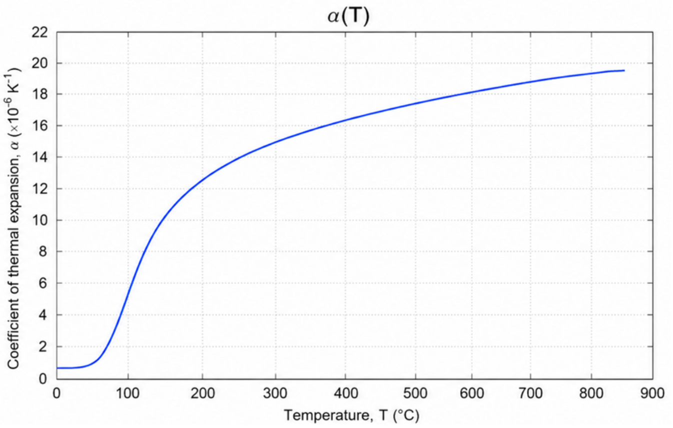

Figure 4.10: Variation of the coefficient of thermal expansion, α, for copper as a function of temperature.

The Young’s modulus of copper obtained from material property data within COMSOL Multiphysics is shown in Figure 4.11. The modulus decreases significantly as temperature increases, indicating reduced stiffness and mechanical resistance at elevated temperatures.

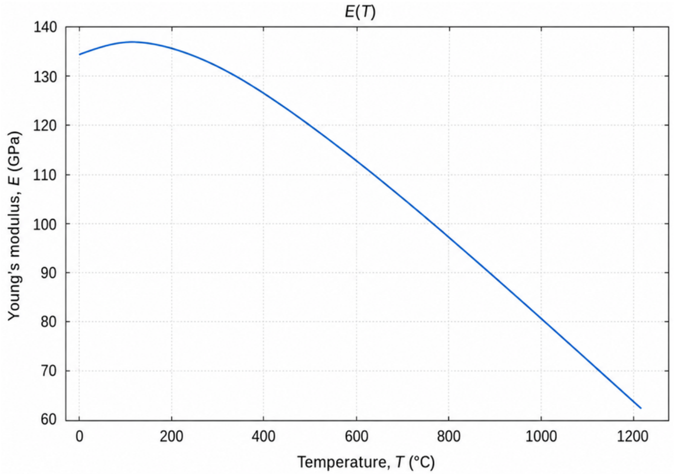

Figure 4.11: Variation of Young's modulus, E, for copper as a function of temperature.

Figure 4.12 shows the small but noticeable increase in Poisson's ratio with increasing temperature, obtained from material property data within COMSOL Multiphysics. This temperature-dependent variation can influence the stress distribution and structural response of copper under thermal loading.

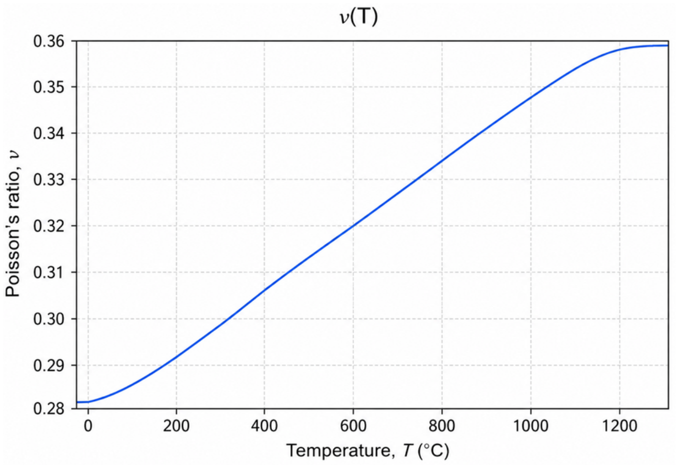

Figure 4.12: Variation of Poisson's ratio, ν, for copper as a function of temperature.

Representative values of the copper material parameters at 20 °C are given in Table 4.5.

Table 4.5: Copper material values at 20 °C.

Name	**Value**	**Unit**
Coefficient of thermal expansion	16.55×10^{-6}	K^{-1}
Density	8960	kg/m^3
Young's modulus	110×10^{9}	Pa
Poisson's ratio	0.34	1

4.2.4 COMSOL Modelling

The HDC was attached to the mounting plate and clamp system, as shown in Figure 4.13.

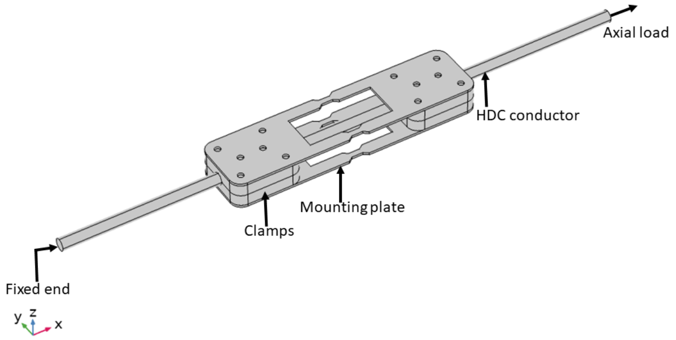

Figure 4.13: Boundary conditions considered for the FEM in COMSOL.

One end of the HDC conductor is modelled with a Fixed Constraint boundary condition. This condition completely restricts all degrees of freedom, including translations and rotations, by simulating a rigidly anchored end of the conductor, similar to being clamped to a utility pole or transmission tower. As a result, this end remains stationary and serves as a reference point for displacement and stress computations throughout the structure. On the other end of the conductor, the boundary condition accounts for the thermal expansion behaviour. The prescribed displacement enables the conductor to expand longitudinally in response to thermal loads, thus mimicking its behaviour under current-induced heating or ambient temperature variations. The contrast with the fixed left end introduces internal thermal stresses, essential for a realistic simulation of the stress development in the conductor body.

An axial load is applied at the other end of the conductor along the longitudinal x axis to simulate the effects of mechanical tension and thermal expansion. This boundary condition simulates temperature-induced strain and deformation. The mechanical response is then influenced by the material's coefficient of thermal expansion (CTE), which governs how much the conductor and structural components expand or contract with temperature variations.

In the simulation model, the sensor's strain response was analysed using a copper rod with two flat plates at both ends, representing a prototype HDC conductor with the same dimensions as the specimen used in the experiments discussed later in Section 4.3.2. The rod was subjected to axial loads ranging from 0 kN to 5 kN over a temperature range of 20 °C to 200 °C. One end of the rod was fixed, while the axial force was applied to the other end. The length of the HDC rod was set to 225 mm, with a sensor clamp spacing of 100 mm [3]. A stationary study was conducted, with temperature and force included as dependent variables.

This analysis did not include the stiffness of the T220 FBG strain transducer, as its contribution was assumed to be small compared with the stiffness of the SS304 mounting plates and the conductor replica. Therefore, the transducer was treated as a sensing element attached to the mounting structure rather than as a load-bearing component in the finite element model. The purpose of the simulation was to evaluate the strain distribution in the conductor-mounted structure under combined mechanical and thermal loading conditions. The strain distribution on the rod surface under a 1 kN axial load at 20 °C is illustrated in Figure 4.14 [3].

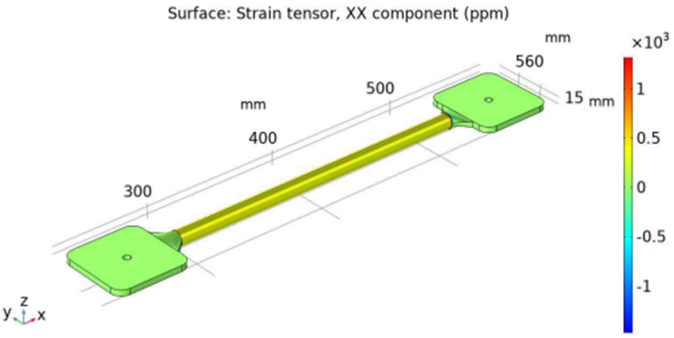

Figure 4.14: Strain distribution in the copper rod under a 1 kN load at 20 °C [3].

Several mounting plate geometries were evaluated before selecting the final sag sensor design. The purpose of this comparison was to identify a geometry that could provide sufficient strain transfer to the T220 FBG strain transducer while maintaining mechanical robustness under tensile and thermal loading. A straight plate provided a stiffer response, but its lower mechanical compliance reduced the strain transferred to the sensing region. In contrast, the narrow-section and spring-type designs introduced controlled flexibility into the mounting plate, which increased local strain concentration in the sensing region and improved the sensitivity of the sensor to conductor elongation [1].

The selected design was therefore chosen because it provided a suitable compromise between sensitivity and structural integrity. It enhanced the measurable strain response without causing excessive stress concentration or permanent deformation in the mounting plate. This made it more appropriate for monitoring small sag-related strain changes and vibration-induced dynamic strain in the conductor. FEA results for the selected sag sensor design under a 5 kN load at 200 °C, showing the surface strain distribution, are presented in Figure 4.15.

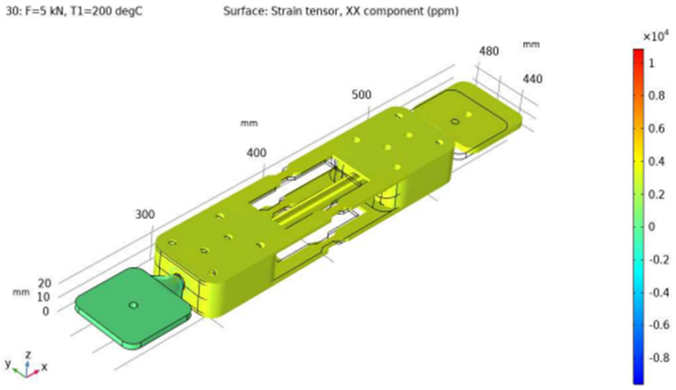

Figure 4.15: Strain in the conductor under a 5 kN load at 200 °C [3].

The correlation between applied force and the resulting strain in the rod, measured between the sensor clamps at various temperatures, is shown in Figure 4.16. As expected, mechanical strain increases with applied force, while thermal strain rises with temperature [3].

It is important to note that previous studies, such as [1], demonstrated that the strain in the rod between the clamps was approximately 40 % of the strain in the conductor outside the clamps for this sensor design. Additionally, the strain in the narrower sections of the

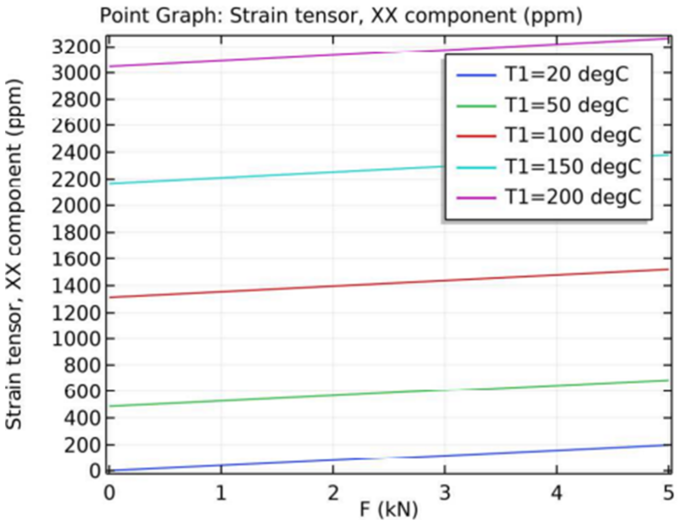

Figure 4.16: Relationship between strain and force in the conductor equipped with a sag sensor at various temperatures [3].

mounting plates was approximately 75 % of the strain in the conductor outside the clamps. This design advantage allows the strain transfer to the optical sensor to be tailored to specific applications by adjusting the width of the narrow sections in the mounting plate [3].

The results of both spring and narrow mounting plate simulations were verified with laboratory experiments using the tensioning machine by applying force up to 3 kN in the next section.

4.2.5 Experimental Objectives and Available Test Facilities

The experimental programme in this section aimed to characterise the sag sensor's response to mechanical force and temperature over a wide operating range (-20 °C to 180 °C), to evaluate its suitability for deployment on high-temperature low-sag (HTLS) conductors. The characterisation involved isolating and quantifying the sensor's sensitivity to strain and temperature, both independently and in combined conditions.

To achieve this, a series of experiments were conducted using a combination of electromechanical tensioning machines and environmental chambers located within the University of Strathclyde's research infrastructure, specifically:

- **Advanced Materials Research Laboratory (AMRL):** Equipped with a 50 kN Instron 5969 Series tensioning machine, offering precise control over load application (±0.5 % accuracy) and a wide range of displacement speeds. This facility was used for room temperature force characterisation.
- **Environmental Testing Laboratory:** Hosted a Thermotron 2800 environmental chamber, used for temperature-only characterisation (no force) in the range of -20 °C to 20 °C. This helped isolate the temperature response of the sensor without mechanical interference.
- **Advanced Sensor Laboratory:** Contained a 10 kN Testometric M350-10CT tensioning machine integrated with a dedicated temperature chamber, enabling force cycling at temperatures up to 180 °C. This facility was essential for combined force and temperature characterisation.

4.3 Sensor characterisation for force and temperature

The sag sensor was characterised by recording its response to force at room temperature and at temperatures between -20 °C and 180 °C by using tensioning machines in the AMRL laboratory, Advanced Sensor Laboratory, and environmental laboratory of the University of Strathclyde.

4.3.1 Initial force characterisation at room temperature

Experimental Setup

To assemble the initial sag sensor, the T220 strain sensor was first spot-welded at one end to the mounting plate with springs (Sensor 1). The strain offset was then adjusted to allow measurements of -1 mϵ to 3 mϵ. The strain sensor response was monitored in real-time using an FBG interrogator during this adjustment process. Subsequently, the other end of the sensor was secured to the mounting plate, and the pre-stressing tool was removed.

The sag sensor was then assembled and installed on a spare segment of a 70 mm^2 HDC conductor, as shown in Figure 4.17. The strain sensor was further protected with a steel strip to prevent any damage during installation.

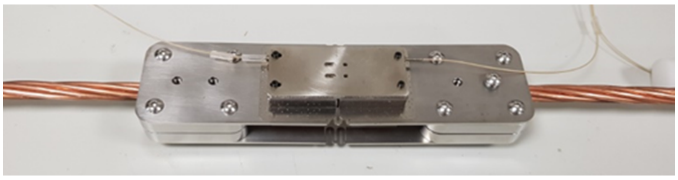

Figure 4.17: Sag Sensor installed on a 1 m long conductor sample.

Similarly, the other sensor, which was mounted on plates with narrow sections (Sensor 2), was assembled. Both sensors were then characterised by recording their responses to the force applied by a tensioning machine.

Force characterisation

To verify the response of each sag sensor to force, the sensors were assembled and installed on a 10.5 mm diameter, 1 m long HDC conductor. A mid-range 50 kN electromechanical 5969 Series Instron tensioning machine in the AMRL laboratory, which offers extensive control of loading rates (speed range of 0.001-3000 mm/min) and a load measurement accuracy of ± 0.5 % of the reading down to 1/1000 of the load cell capacity, was used to characterise the sensors. For this purpose, the HDC conductor with the attached sag sensors was secured in the machine clamps as shown in Figure 4.18.

The applied force was varied from 0 to 3 kN in 200 N increments. Each loading step was applied over approximately 1 min and then held constant for 20 s before the next force level was applied. Force readings from the test machine were logged at 10 Hz. The Bragg centre wavelength of each FBG channel was recorded using a high-speed FBG interrogator at an acquisition rate of 5 kHz. The interrogator model, wavelength range, wavelength resolution, number of optical channels, and maximum sampling rate are summarised in Table 4.6. Although a 5 kHz sampling rate is not required for the quasi-static force calibration itself, it was used to retain consistency with the dynamic measurement configuration and to ensure that any vibration-induced wavelength fluctuations during loading could be captured.

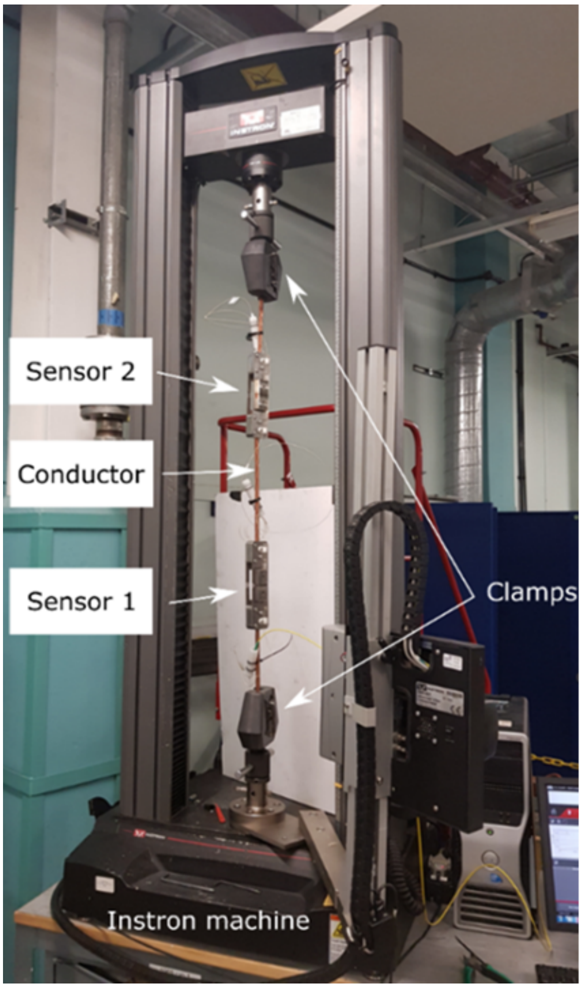

Figure 4.18: Sensors installed in Instron tensioning machine.

For the quasi-static force–wavelength calibration, the wavelength data recorded during the 20 s hold period at each force level were averaged before fitting. Both force and wavelength signals were timestamped to facilitate post-processing and synchronisation. The measurements were repeated three times at constant ambient temperature to assess repeatability.

The responses of the sag sensors to the applied force at room temperature are shown in Figures 4.19 and 4.20. The measured data points from the repeated loading tests are plotted together with the corresponding linear fit to show the repeatability and linearity of the force–wavelength response.

Table 4.6: FBG interrogator and data-acquisition specifications used for laboratory characterisation.

Parameter	**Specification**
Interrogator model	NI PXIe-4844 optical sensor interrogator
Wavelength range	1510–1590 nm
Wavelength accuracy	1 pm
Wavelength resolution / repeatability	1 pm
Number of optical channels	4
Force acquisition rate	10 Hz
FBG centre-wavelength acquisition rate	5 kHz
Recorded measurands	Force and FBG centre-wavelength shift, $\Delta\lambda_B$

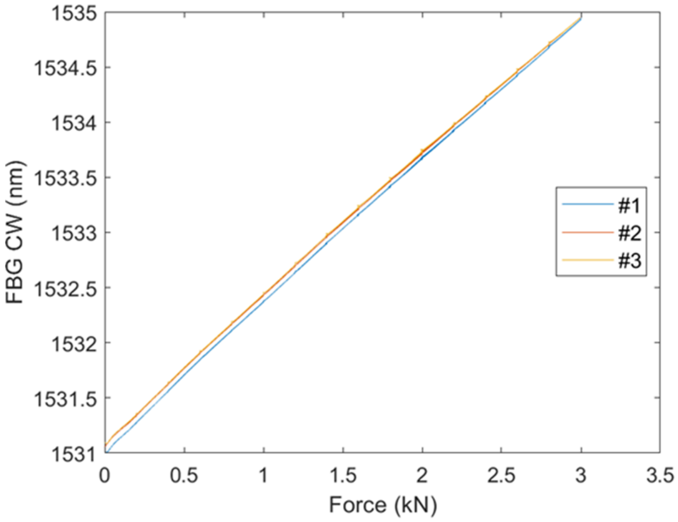

Figure 4.19: Force–wavelength response of the spring plate sensor, S1, at room temperature. The markers represent measured data points from repeated loading tests, and the line represents the linear fit used to determine the force sensitivity.

The wavelength shift of Sensor 1 (S1) was 4 nm at an applied force of 3 kN, while Sensor 2 (S2) exhibited a shift of nearly 300 pm under the same force, indicating a different strain transfer ratio. For the 70 mm^2 HDC conductor, a strain of approximately 360 $\mu\varepsilon$ is expected in the conductor at 3 kN. Given that the T220 strain sensor has a 1:1 strain transfer ratio

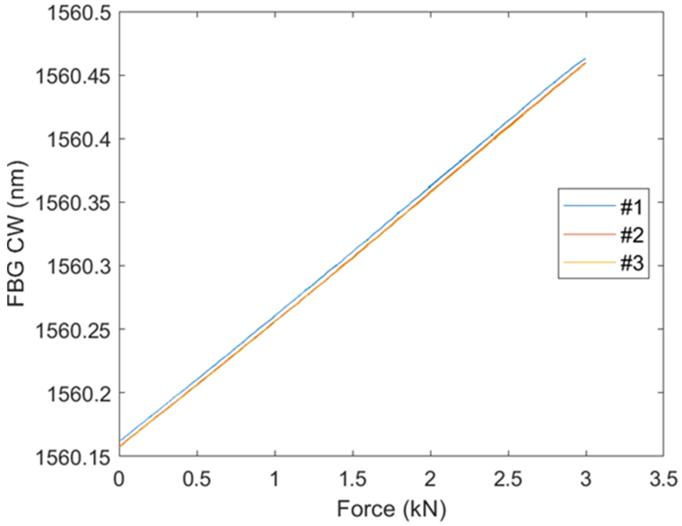

Figure 4.20: Force–wavelength response of the narrow plate sensor, S2, at room temperature. The markers represent measured data points from repeated loading tests, and the line represents the linear fit used to determine the force sensitivity.

from the substrate, it can be concluded that Sensor 1 provides over 8 times greater strain transfer, while Sensor 2 has a strain transfer ratio of around 75 %. The strain sensitivities can be estimated at 11 $\mathrm{pm}/\mu\varepsilon$ for Sensor 1 and 0.8 $\mathrm{pm}/\mu\varepsilon$ for Sensor 2.

The force sensitivity of Sensor 1 (S1) was approximately 1.3 nm/kN, while that of Sensor 2 (S2) was approximately 0.1 nm/kN. Using the manufacturer's calibration coefficient, as shown in Figure 4.21, an FBG wavelength shift of 4 nm would correspond to an apparent strain of approximately 3.4 mε. This value exceeds the nominal T220 strain range of ±2000 $\mu\varepsilon$ specified in Table 4.2; therefore, the calculated value should be interpreted as the effective strain in the sensor assembly under the applied loading condition rather than as operation within the nominal standalone transducer range.

This results in a strain amplification of approximately eight times relative to the conductor strain for the sag sensor with spring plates, Sensor 1. The sag sensor with narrow-section plates, Sensor 2, showed a lower strain transfer factor of approximately 0.7.

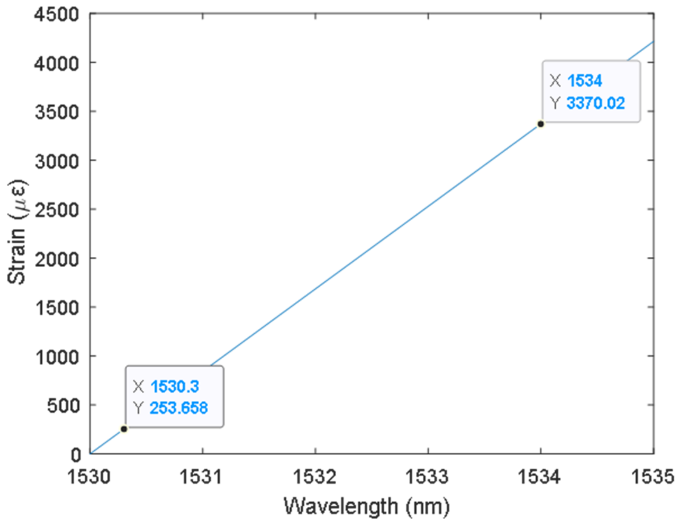

Figure 4.21: Strain sensor characteristics at a constant temperature, according to the manufacturer's calibration coefficients.

4.3.2 Temperature characterisation between -20 °C and 20 °C at no force

HDC conductor prototype and sag sensor design for experiments

Due to the size limitations of the tensioning machine with an environmental chamber, the sag sensor was assembled and installed with a 10.5 mm diameter copper rod, which replicates an HDC conductor, as shown in Figure 4.22. The rod was designed with two flat ends with holes for securing the conductor in the machine grips.

Experimental setup

The temperature in the chamber was controlled by the machine controller. For temperature monitoring, a 4-channel PT-104 temperature logger (Pico Technology) was used, paired with a PT100 platinum resistance thermocouple (PRT) that has a temperature range of -50 °C to +250 °C and an accuracy of ±0.03 %. The temperature of the machine was increased in 20 °C increments within the considered range at a rate of 1.2 °C per minute and stabilised for 2.5 hours at each level before force cycling commenced to ensure a stable temperature [5].

During the characterisation process, the optical sensor was interrogated at a sampling rate

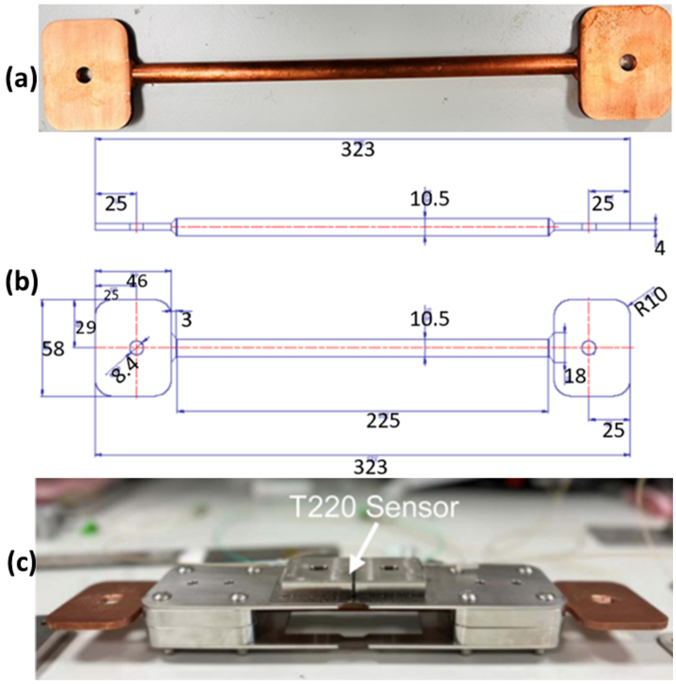

Figure 4.22: The prototype HDC conductor and sag sensor used for temperature characterisation from -20 °C to 180 °C: (a) HDC conductor rod; (b) measurements of HDC rod; and (c) sensor assembly prepared for thermal characterisation [5].

of 1 kHz, and the Bragg wavelengths of the FBGs were logged using an FBG interrogator. This sampling rate was lower than that used during the room-temperature strain testing because the force and temperature variations in this experiment were applied quasi-statically. The main objective was to characterise the sensor response to controlled force and temperature changes, rather than to capture high-frequency vibration. Therefore, 1 kHz provided sufficient temporal resolution for monitoring the wavelength response while reducing the volume of recorded data during long-duration temperature cycling. The setup enabled synchronised monitoring of wavelength, force, and temperature, allowing the sensor performance to be characterised under varying thermo-mechanical conditions [5].

In addition to the above-mentioned experiments, the sensor was further characterised within a temperature range of -20 °C to 20 °C in an environmental chamber (Thermotron 2800) in the laboratory conditions, with no applied force, as illustrated in Figure 4.23.

During these experiments, to ensure stable temperature conditions within the machine, a waiting period of 2 hours was observed before ramping up to the next temperature value. The

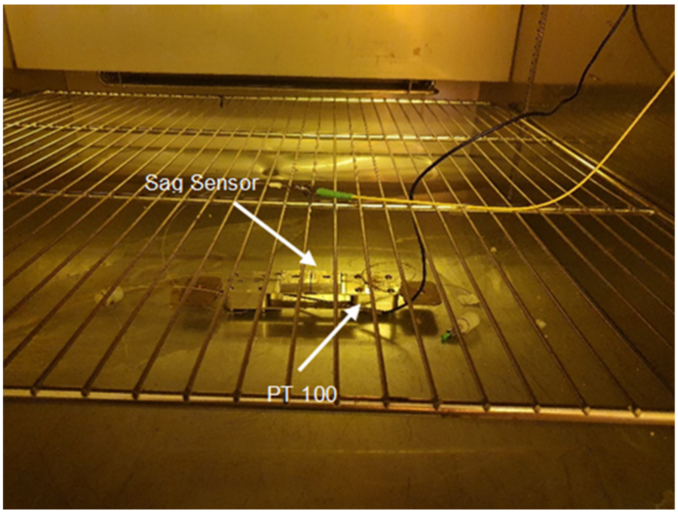

Figure 4.23: Environmental chamber (Thermotron 2800).

temperature was increased at a rate of 5 °C per hour [5].

4.3.3 Temperature characterisation between 20 °C and 180 °C

Experimental setup

High-temperature conductors are specifically designed to operate at elevated temperatures, above 100 °C, due to weather conditions and high ampacity requirements. HTLS conductors can sustain continuous operation at temperatures up to 180 °C and short-term operation up to 250 °C without a significant loss of tensile strength or increased sag [6–8].

A 10 kN Testometric tensioning machine (model M350-10CT), equipped with a dedicated temperature chamber, was used in the Advanced Sensor Laboratory to perform force characterisation of the sag sensor between 20 °C and 180 °C. As described previously, the sensor was mounted on a 10.5 mm diameter copper rod representative of the HDC conductor. The modified rod geometry enabled secure attachment within the machine grips during thermal and mechanical loading, as shown in Figure 4.24 [3, 5].

The force measurements were recorded using a load cell and the machine software. At each temperature level, the applied force was increased from 0 kN to 3 kN in 500 N increments, with a 1 min transition between consecutive force levels. The force was then held for 2 min at each

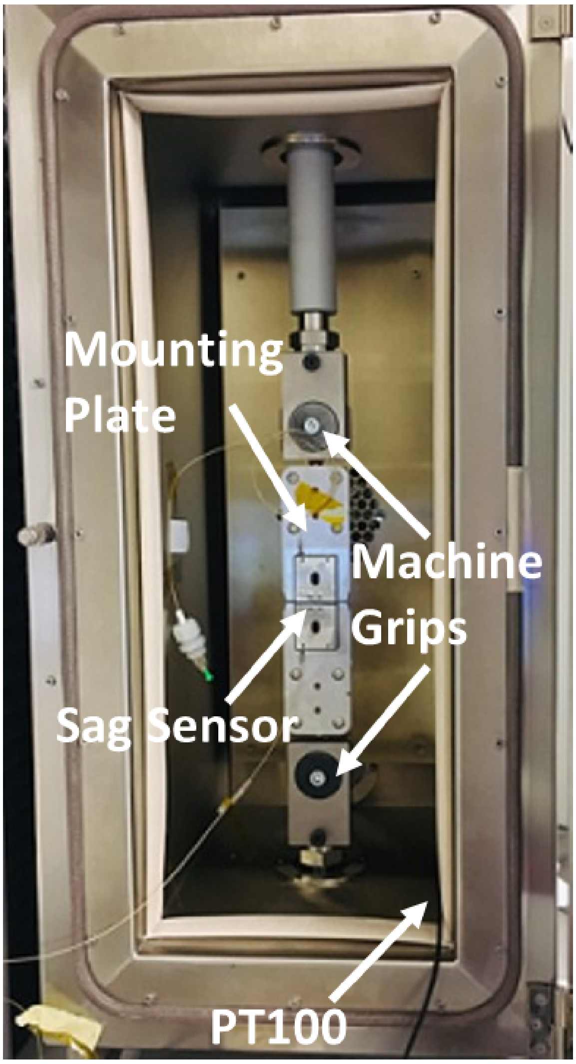

Figure 4.24: Sag Sensor installed in Testometric tensioning machine.

increment before being decreased in the same manner. This force cycling process was repeated three times at each temperature level. The measurements were performed at temperature steps of 20 °C, from 20 °C to 180 °C, i.e., at 20, 40, 60, 80, 100, 120, 140, 160, 180 °C [5].

During the force characterisation experiment between 20 °C and 180 °C, temperature and FBG wavelength data were recorded using separate acquisition systems. The temperature was monitored using a 4-channel PT-104 temperature logger (Pico Technology) connected to a PT100 platinum resistance thermometer (PRT). The PT-104 provides high-resolution temperature measurements, but its sampling rate is much lower than that of the optical interrogator; depending on the number of active channels and logger configuration, the temperature logging rate is at a logging interval of 1 sample/s per channel. The FBG wavelength data were acquired using an FBG interrogator at 1 kHz [5].

Force characterisation at temperatures between -20 °C and 180 °C

Examples of the applied force (ranging from 0 kN to 3 kN) and the corresponding strain FBG wavelength waveforms recorded at 20 °C over three continuous cycles are shown in Figure 4.25.

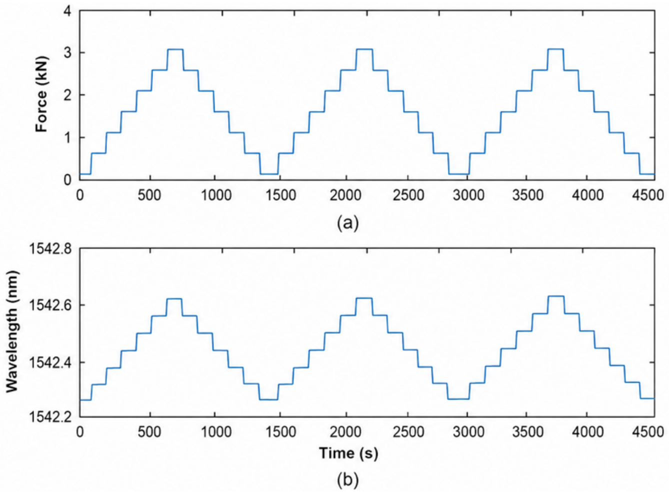

Figure 4.25: Cyclic loading response at 20 °C: (a) applied force waveform; and (b) corresponding FBG wavelength waveform [5].

As detailed in the experimental setup section, the force was incrementally increased and decreased in 500 N steps, with a hold time of 2 minutes at each step to ensure stable readings. This force application process was repeated for three consecutive cycles to accurately compare and characterise the sensor's performance. The multi-cycle approach allowed for assessing the sensor's repeatability and consistency under controlled conditions. Each cycle provided valuable data on how the sensor's strain response varied with the applied force, ensuring that any anomalies could be identified and addressed. The repeated application and removal of force helped determine the linearity of the sensor response and its ability to return to baseline readings after each cycle [5].

The force and wavelength data were averaged over the three cycles to plot the sag sensor characteristics. This averaging process focused on the stable portions of the hold time in each force step, ensuring that transient effects were minimised and the steady-state response of the sensor was accurately captured [5].

The response of the sag sensor to the applied force at various temperatures, ranging from 20 °C to 180 °C, is presented in Figure 4.26.

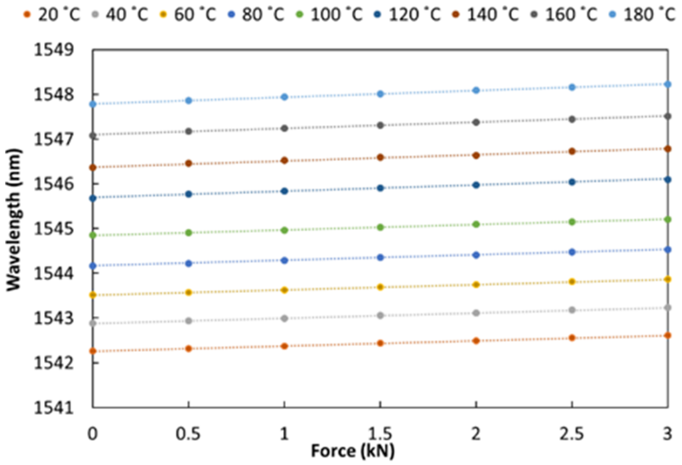

Figure 4.26: Sag sensor response to force at temperatures between 20 °C and 180 °C [5].

This comprehensive analysis demonstrated a linear relationship between the applied force and the corresponding wavelength shifts at each temperature step. By examining the sensor's behaviour across this temperature range, we could assess its performance under different thermal conditions, ensuring its reliability for real-world applications [5].

The observed linear change in the sag sensor response across the considered temperature steps indicates that the sensor maintains consistent sensitivity and accuracy, despite variations in the environmental conditions. This linearity is crucial for the sensor's application in monitoring and predicting mechanical stresses in overhead transmission lines, where both force and temperature can fluctuate significantly [5].

An example of the sensor's response to force at a constant temperature of 20 °C is presented in Figure 4.27.

The sensitivity was determined from the slope of the wavelength-force response during both ramp-up and ramp-down phases over three loading cycles. The reported value,

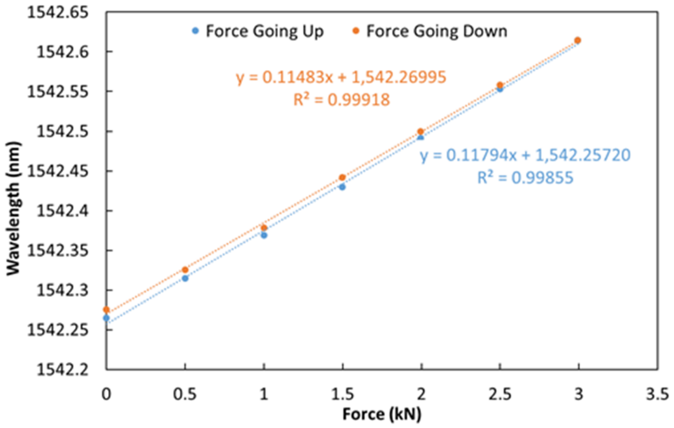

Figure 4.27: Sag sensor response to force at a temperature of 20 °C [5].

0.116 nm/kN, represents the average sensitivity obtained from the increasing and decreasing force responses, with a variation of approximately ±2 pm/kN [5].

The temperature sensitivities of approximately 30 pm/°C for both the strain and temperature FBG sensors within the -20 °C to 180 °C range are shown in Figure 4.28. This figure provides a detailed analysis of how the sensors respond to changes in temperature over this extensive range [5]. The 30 pm/°C sensitivity indicates that for every degree Celsius change in temperature, there is a corresponding shift of 30 picometers in the wavelength measured by the FBG sensors. This high level of sensitivity is crucial for accurately monitoring the thermal conditions of the conductor and the surrounding environment [5].

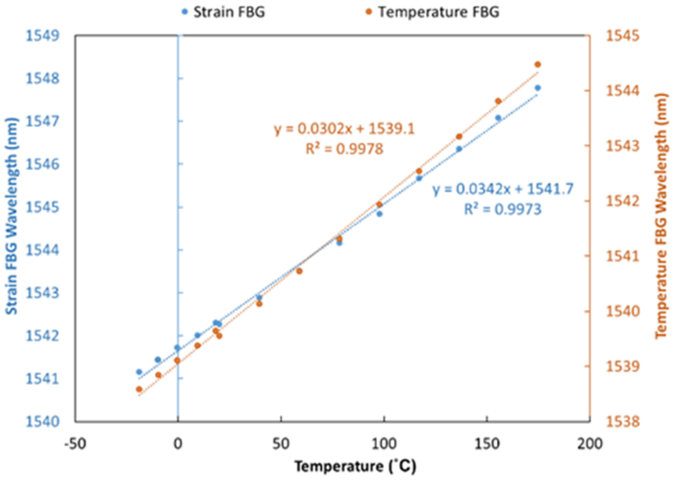

Figure 4.28: Sag sensor response to temperatures between -20 °C and 180 °C [5].

Figure 4.28 shows the linear response of the FBG sensors across the entire temperature spectrum, demonstrating their reliability and precision. The linearity ensures that the sensors provide consistent and predictable data, which is essential for applications where precise temperature measurements are necessary, such as in high-voltage transmission lines [5].

The change in the sag sensor's sensitivity to force is about 25 % across the considered temperature range, as depicted in Figure 4.29.

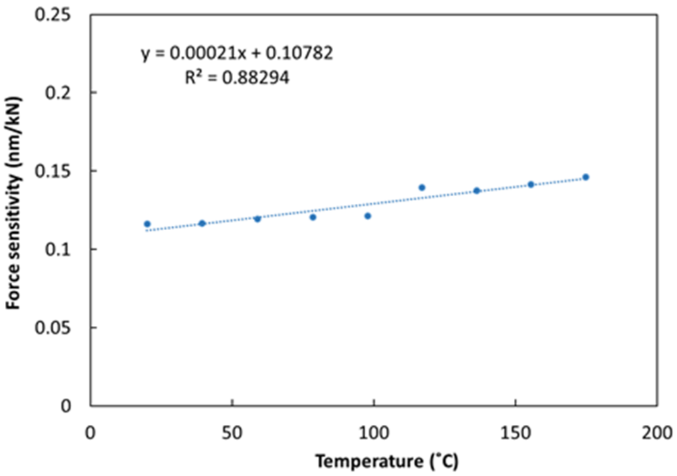

Figure 4.29: Change in the sag sensor sensitivity to force within the considered temperature range [5].

This figure illustrates how the sensor's response to applied force varies with temperature, highlighting the importance of accounting for thermal effects in practical applications. A 25 % variation indicates that the sensor's sensitivity to force is significantly influenced by temperature changes, which could impact its accuracy and reliability if not properly calibrated for these effects [5].

Similarly, the change in the sag sensor's sensitivity to temperature is around 2 % within the considered force range, as shown in Figure 4.30. This relatively minor variation indicates that while the sensor's response to temperature is affected by the applied force, the impact is much less significant compared to the influence of temperature on force sensitivity.

Figure 4.30 presents a detailed analysis of the temperature sensitivity under different force conditions, showing that the sensor remains largely stable in its temperature measurements even when subjected to varying mechanical loads. This stability is essential for ensuring

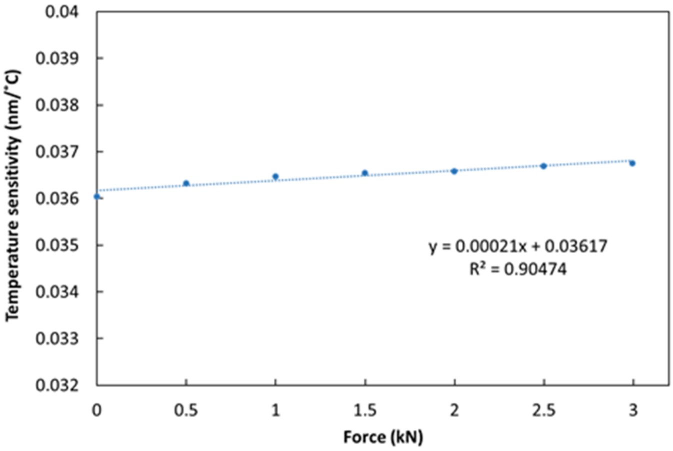

Figure 4.30: Change in the sag sensor sensitivity to temperature for the considered force range [5].

that the sensor provides reliable temperature data, which is critical for applications involving thermal monitoring and management. [5].

At each temperature T, the force sensitivity $K_F(T)$ is defined as the slope of the linear fit between the applied force F kN and the Bragg wavelength λ_B nm, as given in Equations Eq. (4.4) and Eq. (4.5):

$$\lambda_B(F,T) = a(T) + b(T)\,F \tag{4.4}$$

$$K_F(T) = \left.\frac{\partial \lambda_B}{\partial F}\right|_T = b(T) \quad [\mathrm{nm\,kN^{-1}}] \tag{4.5}$$

As mentioned earlier, the force was stepped (0 to 3 kN in 0.5 kN steps), held for 2 min per step, and repeated for three cycles. For each step, the wavelength was averaged over the stable hold portion (to suppress transients), then ordinary least squares (OLS) was applied to the (F,λ) data; repeating per cycle and per temperature and averaging the slopes yields the reported K_F = 0.116 nm/kN (116 pm/kN at 20 °C). The linearity visible in Figure 4.28 and 4.29 justifies the linear model and the use of a single slope.

At zero applied force, the temperature sensitivity K_T is obtained from the slope of $\lambda_B(T)$, as given in Equations Eq. (4.6) and Eq. (4.7):

$$\lambda_B(T) = c + dT \tag{4.6}$$

$$K_T = \left.\frac{\partial \lambda_B}{\partial T}\right|_{F=0} = d \quad [\mathrm{pm}\,^{\circ}\mathrm{C}^{-1}] \tag{4.7}$$

Using the same averaging over temperature holds at each temperature, OLS of (T,λ) gives K_T = 30 pm/°C across -20 °C to 180 °C. Figures 4.28 and 4.29 then quantify cross-sensitivities by regressing K_F versus T (25 % variation over the range) and K_T versus F (2 % variation over the tested force range).

Compared with commercial FBG strain sensors (strain resolution often < 1 $\mu\varepsilon$, i.e., 1 pm at 1550 nm), the proposed sensor achieves competitive practical resolution, with higher effective sensitivity in the spring-plate variant due to mechanical gain. While absolute accuracy is bounded by interrogator accuracy, thermal cross-sensitivity, and strain-transfer efficiency, the system provides reliable relative sag measurement over wide thermal cycles when appropriately compensated and calibrated.

4.4 Analysis of force and temperature measurement errors in the sag sensor

This section quantifies how measurement errors propagate to the final estimate of mid-span sag s (mm). A standards-based approach is used for the force measurements (BS EN ISO 7500-1), and all symbols used throughout are defined. The relevant performance terms of the optical interrogator (I-MON), including fit (wavelength) resolution, repeatability, linearity, and temperature drift as specified by the vendor, are then identified, and their contribution to the uncertainty budget under the operating conditions is discussed. A linear measurement model is derived to relate wavelength λ, force F, and temperature T to a chosen reference state. Uncertainties are subsequently propagated to F and T, and then to s, following the Guide to the Expression of Uncertainty in Measurement (GUM) [9]. Throughout, the "standard uncertainty" u(.) denotes an estimated standard deviation; independent contributions are combined by root-sum-of-squares (RSS), and, where helpful, we also report an expanded uncertainty $U \approx$ 2u (coverage $k =$ 2, 95 $\%$) [9].

4.4.1 Standards basis for the force chain (BS EN ISO 7500-1)

The M350-10CT machine used to test the sag sensor was equipped with a load cell (model LC1000), which had the force measurement accuracy complying with the 0.5 class requirements as defined by the BS EN ISO 7500-1 standard [10]. The class is determined by a prescribed calibration procedure (three full loading runs, measurements at defined points) that assesses accuracy, repeatability, zero behaviour, and resolution. The outcome is a maximum permissible error (MPE) as a percentage of the indicated reading across the machine's usable range.

Example: Class 0.5, MPE $\leq$ ±0.5 $\%$ of the force reading. The class specification is determined at a controlled temperature; temperature effects are not included in the class accuracy. Any temperature-induced load-cell errors must be added separately using the load-cell manufacturer's temperature coefficients (zero shift and span shift per °C).

I-MON wavelength measurement accuracy

- λ (pm or nm): FBG Bragg wavelength reported by the interrogator.
- F (N or kN): axial force applied during calibration.
- T (°C): conductor/sensor temperature.
- D mm: mid-span sag inferred from the measured force and temperature range from 20 °C to 180 °C.

Force-to-wavelength slope: $K_F = \partial\lambda/\partial F =$ 116 pm kN^{-1} Temperature-to-wavelength slope: $K_T = \partial\lambda/\partial T =$ 30 pm °C^{-1}.

These are partial derivatives evaluated at a specific operating point (F_0, T_0). They are local slopes of the function $\lambda(F, T)$. In general, K_F and K_T can vary with F and T (and with packaging/strain state).

Forward measurement model (what the interrogator sees).

Linearise $\lambda(F, T)$ around (F_0, T_0, λ_0), as shown in equation 4.8:

$$\lambda \; = \; \lambda_0 \; + \; K_F \, (F - F_0) \; + \; K_T \, (T - T_0) \; + \; \varepsilon_\lambda \tag{4.8}$$

where ε_λ is any residual (noise/drift not captured by the linear model), λ [pm or nm] is the FBG wavelength, F kN is the applied force (tension), T °C is the sensor/conductor temperature, $K_F = (\partial\lambda/\partial F)_{(F_0,T_0)}$ $[\text{pm kN}^{\text{-1}}]$ and $K_T = \left(\frac{\partial\lambda}{\partial T}\right)_{(F_0,T_0)}$ $[\text{pm °C}^{\text{-1}}]$ are the local sensitivities.

”Span” refers to the physical conductor segment between two supports. The span mapping is the mechanical relationship that relates the state of the span, primarily conductor tension and temperature, to the mid-span sag D. For a taut, level conductor, the catenary model gives D as a function of the horizontal tension H, conductor weight per unit length w, span length L, and temperature-dependent effects such as thermal expansion and creep. Linearising this mechanical relationship around the operating point (F_0, T_0) gives the sag-per-force factor:

$$\kappa_{DF} = \left(\frac{\partial D}{\partial F}\right)_{(F_0,T_0)} \qquad [\text{mm}\,\text{kN}^{-1}] \tag{4.9}$$

where D is the mid-span sag, F is the measured axial force, and T is the conductor temperature. For physical interpretation, the classical parabolic approximation of the catenary equation gives:

$$D \approx \frac{wL^2}{8H} \tag{4.10}$$

where w is the conductor weight per unit length, L is the span length, and H is the horizontal component of conductor tension. Differentiating this expression with respect to H gives:

$$\frac{\partial D}{\partial H} \approx -\frac{wL^2}{8H^2}. \tag{4.11}$$

Thus, if the measured axial force F is taken to approximate the horizontal tension H, κ_{DF} is negative, meaning that increasing tension reduces sag. In this thesis, the magnitude of this factor is used for the illustrative PNDC-like span, for example $|\kappa_{DF}| = 30\ \mathrm{mm\,kN^{-1}}$.

The parabolic approximation is accurate when the sag-to-span ratio is small, the span is approximately level, and the conductor is sufficiently tensioned so that the profile is shallow. These conditions are commonly satisfied for many overhead line spans under normal operating conditions. However, for long spans, large sag, unequal support heights, low-tension conditions, or significant ice/wind loading, the full catenary equation should be used instead.

Sag explicitly as a function of force and temperature

The sag–force–temperature relationship can be expressed using a local first-order approximation around a reference operating point (F_0, T_0, D_0), where F_0 is the reference conductor force, T_0 is the reference conductor temperature, and D_0 is the corresponding reference mid-span sag. In this thesis, D is used to denote mid-span sag, consistent with the sag definition introduced earlier. The local approximation is given by:

$$D(F,T) = D_0 + \kappa_{DF}\,(F - F_0) + \kappa_{DT}^{(\mathrm{cat})}\,(T - T_0) \tag{4.12}$$

where $\kappa_{DF} = (\partial D/\partial F)_{(F_0,T_0)}$ is the local force-to-sag sensitivity, and $\kappa_{DT}^{(\mathrm{cat})} = (\partial D/\partial T)_{(F_0,T_0)}$ is the direct thermal sag sensitivity obtained from the catenary or sag–tension model. This expression is derived by linearising the classical sag–tension relationship about the selected operating point. Therefore, it should be interpreted as a local approximation rather than a replacement for the full catenary model.

If the conductor force is inferred from the FBG wavelength response, temperature also affects the estimated force through the temperature sensitivity of the FBG. The optical force sensitivity is K_F, and the temperature sensitivity is K_T. Therefore, the temperature-induced wavelength shift can be expressed as an equivalent apparent force change, which produces an additional apparent sag contribution:

$$\left(\frac{\partial D}{\partial T}\right)_{\text{opt}} = \kappa_{DF}\frac{K_T}{K_F} \tag{4.13}$$

Combining the mechanical and optical temperature contributions gives the practical working model:

$$D(F,T) \approx D_0 + \kappa_{DF}(F - F_0) + \kappa_{DF}\frac{K_T}{K_F}(T - T_0) + \kappa_{DT}^{(\text{cat})}(T - T_0) \tag{4.14}$$

where D_0 is the reference sag at (F_0, T_0), κ_{DF} is the local force-to-sag sensitivity, K_F is the force sensitivity of the FBG sensor, and K_T is the temperature sensitivity of the FBG sensor. The third term represents the apparent sag contribution caused by the temperature dependence of the optical force measurement. The fourth term represents the direct thermal sag contribution from the conductor/span mechanics, including thermal expansion and temperature-dependent tension changes.

This model is a calibration-based local form of the classical model that is convenient for interpreting FBG sensor measurements near a defined operating point. Its accuracy depends on the validity of the first-order linearisation, the calibration of K_F, K_T, and κ_{DF}, and the accuracy of the reference sag D_0. The approximation assumes that the span is level or near-level, the conductor remains within the elastic range, the force F is representative of the horizontal conductor tension, the sag-to-span ratio is small, and external effects such as wind load, ice loading, support movement, and long-term creep are negligible over the measurement interval.

The reference sag D_0 should ideally be determined from an independent direct measurement at the reference condition (F_0, T_0), such as a total-station survey, laser range measurement, photogrammetry, or LiDAR-based clearance measurement. If such a measurement is unavailable, D_0 may be estimated from the classical catenary or parabolic sag–tension equation using the known span length, conductor weight per unit length, and measured tension. In that case, the model should be used primarily to estimate relative sag changes rather than as a fully validated absolute sag measurement. For final validation, the FBG-based sag estimate should be compared with an independent direct sag or clearance measurement, which serves as the reference or gold-standard measurement.

Wavelength uncertainty maps to sag ("sag-per-picometre").

The chain rule links the optical and mechanical routes, as shown in equation 4.15:

$$\kappa_{s\lambda} = \frac{\partial s}{\partial \lambda} = \frac{\partial s/\partial F}{\partial \lambda/\partial F} = \frac{\kappa_{sF}}{K_F} \left[\mathrm{mmpm}^{-1}\right]. \tag{4.15}$$

With $\kappa_{sF} = 30$ mm/kN and $KF = 116$ pm/kN, $\kappa_{s\lambda} = 30/116 = 0.2586$ mm/pm. This factor is what is multiplied by any wavelength standard uncertainty to get the corresponding sag standard uncertainty.

4.4.2 Optical interrogator wavelength measurement accuracy

The I-MON 512 is a spectrometer-based FBG interrogation monitor. In this approach, the reflected optical spectrum from the FBG sensors is spatially dispersed using a transmission grating and measured using a 512-pixel InGaAs detector array. The Bragg centre wavelength of each FBG is then determined by fitting the corresponding reflection peak. This interrogation method provides simultaneous full-spectrum monitoring of multiple FBG sensors over the 1510–1595 nm wavelength range, with a maximum measurement frequency of approximately 17–18 kHz [9].

The following parameters of the I-MON 512 interrogator are considered for the wavelength measurement error analysis purposes [9]:

- Wavelength fit resolution is defined as "the standard deviation of the fitted wavelength over a series of measurements with temperature and polarisation held constant", and is specified to be a maximum of 0.5 pm. For the uncertainty analysis purposes, the probability distribution is assumed to be normal.

- Repeatability is defined as "the peak-to-peak change in measured wavelength when the

> input polarisation is rotated through 360 ° at constant temperature; i.e., the polarisation-induced wavelength shift", and is specified to be 3 pm (max). Since there is no information on the probability distribution provided by the manufacturer, a uniform distribution (as the worst-case scenario) is assumed for uncertainty estimation purposes.

Wavelength linearity is defined as "deviation from the I-MON wavelength fit relative to a reference wave meter at the factory calibration temperature (25 °C)" and is specified to be 5 pm (max). It should be noted that this parameter is related to the absolute wavelength measurements across the whole I-MON wavelength range (1510-1595 nm). Since the sag sensor response to force and temperature was only within a fraction in % of that wavelength range and the sensor sensitivities were delivered from the wavelength changes rather than the absolute values, this error was not considered in the measurement uncertainty analysis.

Wavelength drift is defined as "wavelength shift per °C." Since the I-MON unit was kept during experiments in a controlled environment and at a constant room temperature of 21 °C with the I-MON temperature compensation active [10], no drift in the I-MON wavelength due to the thermal effects in the interrogator was observed. Therefore, this error was not included in the uncertainty budget calculations. Based on the above definitions, a maximum standard deviation (1 σ) of 0.5 pm was assumed for the standard uncertainty calculations due to the I-MON wavelength fit resolution, as shown in equation 4.16:

$$u_{\text{res}} = 0.5 \text{ pm}. \tag{4.16}$$

The repeatability is specified as a 3 pm (max) peak-to-peak change in wavelength (0-3 pm range) when the input polarisation is rotated through 360 ° at constant temperature. If the 3 pm value is interpreted as a full-width range, the half-width is 1.5 pm, and the standard uncertainty is shown in equation 4.17:

$$u_{\text{rep}} = \frac{1.5 \text{ pm}}{\sqrt{3}} \approx 0.87 \text{ pm}. \tag{4.17}$$

The combined standard uncertainty in wavelength for the I-MON is then given in equation 4.18.

$$u_\lambda^{\mathrm{IMON}} = \sqrt{u_{\mathrm{res}}^2 + u_{\mathrm{rep}}^2} = \sqrt{(0.5\ \mathrm{pm})^2 + \left(\frac{1.5\ \mathrm{pm}}{\sqrt{3}}\right)^2} \approx 1.0\ \mathrm{pm}. \tag{4.18}$$

This value is used in the numerical examples below. For a worst-case interpretation in which the specified 3 pm value is treated as a full half-width (3 pm), the repeatability term becomes as shown in equation 4.19:

$$\left(u_{rep} = 3/\sqrt{3} \approx 1.73\mathrm{pm}\right), \tag{4.19}$$

and the combined wavelength uncertainty increases to $\left(\mathrm{u}_\lambda^{\mathrm{IMON}} \approx\ 1.8\mathrm{pm}\right)$. All I-MON-driven uncertainty terms would scale accordingly; these worst-case figures are not used in the baseline budget but provide an upper bound.

4.4.3 Uncertainty in temperature measurements

For temperature measurements, a PT-104 platinum resistance data logger (accuracy ±0.01 °C, resolution 0.001 °C) and a Pico SE012 PT100 1/10 DIN probe (accuracy ± 0.03 °C at 0 °C, -50 to +250 °C range) were used [10, 11].

The combined standard uncertainty in temperature measurement, due to the temperature logger and probe, was estimated as shown in equation 4.20, equation 4.21 and equation 4.22:

$$u_{T,\mathrm{PT100}} = \frac{0.03}{\sqrt{3}} = 0.0173\,^\circ\mathrm{C}. \tag{4.20}$$

$$u_{T,\mathrm{PT104}} = \frac{0.01}{\sqrt{3}} = 0.0058\,^\circ\mathrm{C}. \tag{4.21}$$

resulting in the combined standard uncertainty:

$$u_{T,\mathrm{elec}} = \sqrt{0.0173^2 + 0.0058^2} = 0.0183\,^\circ\mathrm{C}, \qquad U_{T,\mathrm{elec}}(k=2) \approx 0.036\,^\circ\mathrm{C}. \tag{4.22}$$

In both cases, the probability distribution was assumed to be uniform. The temperature-measurement uncertainty arising from the FBG temperature sensor and the I-MON interrogator can be calculated using the following formula, as shown in equation 4.23:

$$u_{T,i}^{IMON} = \frac{u_{\lambda,i}}{K_{T,i}} \tag{4.23}$$

and the numerical sensitivity $K_{T,\text{temp}} = 30\text{ pm }{}^{\circ}\text{C}^{-1}$.

The combined standard uncertainty of the I-MON is taken as $u_{\lambda,IMON} = 1.0$ pm. The characteristic indicates a small difference between the two temperature sensitivities; however, this difference is minor compared with other uncertainty contributors and does not materially affect the propagated uncertainty. Accordingly, a single representative value is adopted: $K_{T,\text{temp}} = K_{T,\text{strain}} = 30\text{ pm}\,{}^{\circ}\text{C}^{-1}$, as in equation 4.24:

$$(u_{\lambda}^{(\text{IMON})} = 1.0\text{ pm}), \text{and} (K_{T,\text{temp}} = K_{T,\text{strain}} = 30\text{ pm }{}^{\circ}\text{C}^{-1}), \tag{4.24}$$

the interrogator-limited temperature standard uncertainty in each optical channel is shown in equation 4.25:

$$u_{T,temp}^{IMON} = u_{T,strain}^{IMON} = \frac{u_{lambda}^{IMON}}{K_T} = \frac{1.0}{30} \approx 0.033^{\circ}C. \tag{4.25}$$

Combining the two optical channels by RSS gives the following equation 4.26:

$$u_{T,opt} = \sqrt{\left(u_{T,temp}^{IMON}\right)^2 + \left(u_{T,strain}^{IMON}\right)^2} = \sqrt{2}\,\frac{1.0}{30} \approx 0.047\ {}^{\circ}C. \tag{4.26}$$

The logger–probe chain contributes $(u_{T,elec} = 0.0183$ °C, so the overall combined standard uncertainty in temperature measurement is shown in equation 4.27:

$$u_{T,sys} = \sqrt{u_{T,elec}^2 + u_{T,opt}^2} = \sqrt{(0.0183)^2 + (0.047)^2} \approx 0.051\ {}^{\circ}C, \tag{4.27}$$

and the corresponding expanded uncertainty in temperature, defined as equation 4.28

$$U_{T,sys} = k,\ u_{T,sys}, k = 2\ \left(\approx 95\% \text{ confidence level}\right), \tag{4.28}$$

is equation 4.29:

$$U_{T,\mathrm{sys}} \approx 0.10\,^{\circ}\mathrm{C}. \tag{4.29}$$

4.4.4 Uncertainty in force measurements

For force measurements, a 0.5 class load cell (model LC1000, Testometric) with an overall accuracy of 0.5 % of the reading, and its thermal drift specified by the manufacturer as less than 0.005 % per applied load per °C was used [11].

For a Class 0.5 load cell, the MPE is ±0.5 % of the reading. Assuming a rectangular distribution, the standard uncertainty in force measurements can be calculated for a given force reading, F, as follows in equation 4.30:

$$u_{F,\mathrm{class}} = \frac{0.005F}{\sqrt{3}}. \tag{4.30}$$

The corresponding expanded uncertainty in force, $(U_{F,\mathrm{comb}})$, defined as $U_{F,\mathrm{comb}} = ku_{F,\mathrm{comb}}$, k=2 ($\approx$ 95 % confidence level), is $U_{F,\mathrm{comb}} \approx 34.4$ N.

Assuming the sag sensor force sensitivity of 116 pm/kN, the standard uncertainty in force measurements due to the optical system is in equation 4.31:

$$u_F^{int} = \frac{u_\lambda^{IMON}}{K_F} = \frac{1.0\mathrm{pm}}{116\mathrm{pm\ kN}^{-1}} = 0.00862\ \mathrm{kN}\ \approx 8.6\ \mathrm{N}. \tag{4.31}$$

For the load-cell/machine path, using BS EN ISO 7500-1 Class 0.5 (MPE = ±0.5 % of reading) as a rectangular bound gives the class term, as shown in equation 4.32:

$$u_{F,\mathrm{class}} = \frac{0.005}{\sqrt{3}}\,[\mathrm{N}]\,, \tag{4.32}$$

and the manufacturer's temperature coefficients add (for a load-cell temperature rise ΔT_{cell} and rated load F_{rated}), as in equation 4.33:

$$u_{F0} = \frac{0.00005\ \Delta T_{\mathrm{cell}}\ F_{\mathrm{rated}}}{\sqrt{3}}, u_{F,\mathrm{span}} = \frac{0.00005\ \Delta T_{\mathrm{cell}}\ F}{\sqrt{3}}. \tag{4.33}$$

The machine-side standard uncertainty (no re-zero at temperature) is

$$u_{F,\mathrm{mach}} = \sqrt{u^2_{F,\mathrm{class}} + u^2_{F0} + u^2_{F,\mathrm{span}}} \tag{4.34}$$

Finally, the overall force uncertainty that includes the optical interrogator mapped to force is shown in equation 4.35:

$$u_{F,\mathrm{comb}} = \sqrt{\left(u_F^{(\mathrm{int})}\right)^2 + (u_{F,\mathrm{mach}})^2}. \tag{4.35}$$

Using existing machine-side terms at F = 3 kN, $U_{T,\mathrm{sys}} \approx 0.10$ °C, as in equation 4.36:

$$u_{F,mach} = 14.9\ \mathrm{N}\ \text{(unchanged)}, \tag{4.36}$$

Updated interrogator: $u_F^{int} \approx 8.6$ N. Then equation 4.37:

$$u_{F,comb} = \sqrt{u^2_{F,mach} + (u_F^{int})^2} = \sqrt{14.9^2 + 8.6^2} \approx 17.2\ \mathrm{N}, \tag{4.37}$$

giving an expanded force uncertainty ($U_{F,\mathrm{comb}} \approx\ 34.4\ \ \mathrm{N}$), as shown in equation 4.38:

$$U_{F,comb}\,(k = 2)\ \approx 34.4\ \mathrm{N}. \tag{4.38}$$

Numerical illustration at room temperature $\Delta T_{\mathrm{cell}}\ \approx 0$ °C:

For a representative load of F = 3 kN at approximately room temperature, $T_{\mathrm{cell}} \approx T_{\mathrm{cal}}$ so that $\Delta T_{\mathrm{cell}} = 0$ and the temperature–dependent zero- and span-shift terms vanish ($u_{F0} = u_{F,\mathrm{span}} = 0$).

The machine-side uncertainty therefore reduces to the class term, $u_{F,class} = \frac{0.005{,}F}{\sqrt{3}} = \frac{0.005\times3000}{\sqrt{3}} = 8.66\ \mathrm{N}$,

so that equation 4.39:

$$u_{F,mach} = u_{F,class} = 8.66\ \mathrm{N} \tag{4.39}$$

Using the combined I-MON wavelength standard uncertainty ($u_\lambda^{(\mathrm{IMON})}\ \approx\ 1.0$ pm) and

$K_F = 116\,\mathrm{pm\,kN}^{-1}$ gives an interrogator-limited force uncertainty, as shown in equation 4.40:

$$u_F^{(\mathrm{int})} = \frac{u_\lambda^{(\mathrm{IMON})}}{K_F} = \frac{1.0\,\mathrm{pm}}{116\,\mathrm{pm\,kN}^{-1}} = 0.00862\,\mathrm{kN} \approx 8.6\,\mathrm{N}. \tag{4.40}$$

The combined standard uncertainty in force at room temperature is then equation 4.41

$$u_{F,comb} = \sqrt{u_{F,mach}^2 + (u_F^{int})^2} = \sqrt{8.66^2 + 8.6^2} \approx 12.2\text{ N}, \tag{4.41}$$

and the corresponding expanded uncertainty in force, defined as $(U_{F,\mathrm{comb}} = k u_{F,\mathrm{comb}})$ with coverage factor $(k = 2)$ (approximately 95 % confidence level), is $U_{F,\mathrm{comb}} \approx$ 24.4 N.

At the 180 °C, worst-case extrapolation point, where $u_{F,mach} \approx$ 49 N, the updated combination becomes, equation 4.42:

$$u_{F,comb} \approx \sqrt{49^2 + 8.6^2} \approx 49.8\text{ N}, U_{F,comb} \approx 100\text{ N}. \tag{4.42}$$

4.4.5 Sag as a function of force and temperature

The sag of the conductor as a function of force and temperature can be expressed as follows, equation 4.43:

$$D = \frac{wS^2}{8F} + \frac{\alpha_s S^2}{8h}(T - T_0) \tag{4.43}$$

where, D is sag (m), w is weight per unit length of conductor (N/m), S is span length (m), F is defined as horizontal tension in the conductor (N), α_s is the coefficient of linear expansion of conductor (/ °C), h is initial horizontal tension (N), T is the conductor temperature (°C) and T_0 is the reference temperature (°C).

Using the law of uncertainty propagation [12], the combined standard uncertainty in sag measurement can be calculated as follows, equation 4.44:

$$u_D = \sqrt{(\frac{\partial D}{\partial F} u_F)^2 + (\frac{\partial D}{\partial T} u_T)^2} \tag{4.44}$$

To clarify the relationship with the practical working model introduced earlier, equation Eq. (4.45) represents the underlying physical sag–tension model for a level span. It estimates the absolute mid-span sag from conductor parameters, span length, horizontal tension, and temperature. By contrast, the practical working model in equation Eq. (4.14) is a local first-order approximation around a reference operating point, written in terms of measured changes in force and temperature from the FBG-based sensor system. Therefore, equation Eq. (4.45) provides the mechanical basis from which the local sag sensitivities, such as κ_{DF} and $\kappa_{DT}^{(\mathrm{cat})}$, can be obtained.

For a level span, the mid-span sag D can be approximated as 4.45:

$$D(F,T) = \underbrace{\frac{wS^2}{8F}}_{\text{mechanical catenary term}} + \underbrace{\frac{\alpha_s S^2}{8h}(T - T_0)}_{\text{thermal expansion term}} \tag{4.45}$$

where w is the conductor weight per unit length $\left(\mathrm{N\,m^{-1}}\right)$, S is the span length (m), F is the horizontal conductor tension (N), α_s is the conductor linear thermal expansion coefficient $\left(^\circ\mathrm{C}^{-1}\right)$, h is the reference horizontal tension used in the thermal term (N), T is the conductor temperature $(^\circ\mathrm{C})$, and T_0 is the reference temperature $(^\circ\mathrm{C})$.

The first term in equation Eq. (4.45) is the parabolic approximation of the catenary sag equation, where sag decreases as horizontal tension increases. The second term approximates the additional sag caused by thermal expansion of the conductor relative to the reference temperature. This model is not separate from the practical working model; rather, it provides the physical basis for determining the local coefficients used in that model. For example, around the reference condition (F_0, T_0), the force-to-sag sensitivity can be obtained by differentiating equation Eq. (4.45) with respect to F:

$$\kappa_{DF} = \left.\frac{\partial D}{\partial F}\right|_{(F_0,T_0)} = -\frac{wS^2}{8F_0^2}. \tag{4.46}$$

Similarly, the thermal sag sensitivity associated with the explicit thermal term is:

$$\kappa_{DT}^{(\mathrm{cat})} = \left.\frac{\partial D}{\partial T}\right|_{(F_0,T_0)} = \frac{\alpha_s S^2}{8h}. \tag{4.47}$$

Thus, Equation Eq. (4.45) estimates absolute sag from physical span parameters, whereas the practical working model estimates local sag changes from measured force and temperature variations. The practical model is more convenient for processing FBG sensor data, but it is not inherently more accurate than the classical sag–tension model. Its accuracy depends on calibration of the local coefficients and should be validated against an independent direct sag or clearance measurement, such as total-station, laser, photogrammetry, or LiDAR measurement.

The sensitivity (Jacobian) coefficients needed for uncertainty propagation are the partial derivatives, as shown in equation 4.48:

$$\frac{\partial D}{\partial F} = -\frac{wS^2}{8F^2} \text{ and } \frac{\partial D}{\partial T} = \frac{\alpha_s S^2}{8h}. \tag{4.48}$$

Let u_F denote the overall combined standard uncertainty in force (machine class load-cell temperature terms interrogator-mapped-to-force), and let u_T denote the overall combined standard uncertainty in temperature (PT100/PT104 electronics residual optical drift). Assuming F and T uncertainties are independent (GUM first-order law), the combined standard uncertainty in sag is defined as equation 4.49

$$u_D = \sqrt{\left(\frac{\partial D}{\partial F}u_F\right)^2 + \left(\frac{\partial D}{\partial T}u_T\right)^2} = \sqrt{\left(\frac{wS^2}{8F^2}u_F\right)^2 + \left(\frac{\alpha_s S^2}{8h}u_T\right)^2}. \tag{4.49}$$

Since F and T estimates are not independent (as they are both derived from the same optical chain), the covariance term is included in equation 4.50:

$$u_D = \left[\left(\frac{\partial D}{\partial F}u_F\right)^2 + \left(\frac{\partial D}{\partial T}u_T\right)^2 + 2\rho_{FT}\frac{\partial D}{\partial F}\frac{\partial D}{\partial T}u_F u_T\right]^{1/2}, \tag{4.50}$$

where ρ_{FT} is the correlation coefficient between F and T, in the baseline budget. The author has set ρ_{FT} =0 because u_F already includes the interrogator-to-force mapping and machine terms, while u_T is dominated by the electronics and residual optical drift after compensation.

Force term, as in equation 4.51:

$$\frac{\partial D}{\partial F}u_F = \left(3.0 \times 10^{-5}\,\mathrm{m/N}\right) \times 17.2\,\mathrm{N} \approx 5.16 \times 10^{-4}\,\mathrm{m} = 0.516\,\mathrm{mm}. \tag{4.51}$$

The temperature term is negligible ($\approx$ 0.0004 mm).

So, equation 4.52:

$$u_D \approx 0.52\,\mathrm{mm}, U_D\,(k = 2) \approx 1.0\,\mathrm{mm}. \tag{4.52}$$

Numerically, for the illustrative PNDC-like span ($D_0 \approx$ 90 mm at F_0 = 3 kN), the updated combined force and temperature uncertainties give a standard sag uncertainty of $u_D \approx$ 0.52 mm ($U_D \approx$ 1.0 mm, $k = 2$). The I-MON contribution alone corresponds to a sag standard uncertainty of $\kappa_{s\lambda} u_\lambda^{IMON} \approx$ 0.26 mm, i.e. roughly half of the total sag uncertainty in this operating regime.

4.5 Conclusion

This chapter presented the design and laboratory characterisation of a compact FBG-based sag sensor for OHL applications, along with finite element modelling to anticipate sensor–conductor interactions under combined mechanical and thermal loading. Two sensor configurations were investigated: Sensor 1, based on a spring-plate mounting design, and Sensor 2, based on a narrow-plate mounting design. Each configuration used a commercially available T220 FBG strain transducer integrated with a custom SS304 conductor-mounted assembly. Therefore, the work did not involve fabrication of the commercial FBG transducer itself, but rather the design, integration, modelling, and characterisation of the complete sag sensor assembly for OHL monitoring.

The mounting architecture was engineered to transfer axial conductor strain efficiently to the FBG transducer while remaining mechanically robust and suitable for field deployment. Finite element analyses showed close agreement with the intended strain-transfer behaviour: for the spring-plate configuration, the conductor strain measured between the clamps was

97 % of the outside-clamp strain at 20 °C and 5 kN; for the narrow-plate configuration, the inside-clamp strain was 43 % of the outside-clamp level, with local strain concentration in the narrowed section as designed. These results confirmed that the mounting plate geometry can be used to tune the mechanical gain and localisation of strain at the FBG location.

Comprehensive laboratory tests quantified the sensor response over load steps up to 3 kN and temperatures from -20 °C to 180 °C. The measured sensitivities were approximately 0.116 nm/kN to force and 30 pm $°C^{-1}$ to temperature. Cross-sensitivity trends were modest but non-negligible: the force sensitivity varied by 25 % over the thermal range, while the temperature sensitivity changed by 2 % over the tested force range. These behaviours are consistent with the modelled mechanics and materials and were subsequently addressed in the metrology strategy.

The metrology analysis distinguished resolution from accuracy in the optical readout and highlighted the importance of temperature compensation for reliable measurement. Using an I-MON interrogator with a wavelength fit resolution of <0.5 pm and absolute wavelength accuracy of 5 pm, together with the measured sensitivities, the instrument-limited resolution in force and temperature was on the order of a few newtons and a few hundredths of a degree Celsius, respectively. However, absolute accuracy remains bounded by the 5 pm wavelength accuracy unless external referencing is applied. In this context, a co-located unbonded FBG channel was used to compensate thermal drift. With compensation, steady-state residuals dominated the random uncertainty budget, while the interrogator noise floor was comparatively minor. Overall, after compensation, the practical sag error was reduced to approximately ±1–2 mm, which is within acceptable limits for conductor sag monitoring under HTLS-relevant conditions.

In relation to the distributed sensing theme of this thesis, the implementation should be understood as quasi-distributed FBG sensing. FBGs provide discrete, wavelength-encoded sensing points that can be multiplexed along a single optical fibre and interrogated simultaneously. In this work, two sensor assemblies were used to compare different strain-transfer designs and demonstrate the feasibility of multi-point OHL monitoring. This differs from fully distributed optical fibre sensing based on Rayleigh, Raman, or Brillouin scattering, where measurements are obtained continuously along the fibre length. Nevertheless, the FBG approach provides a practical route to distributed condition monitoring by placing multiple compact sensor assemblies at selected critical locations along an OHL span, such as high-sag regions, suspension points, or mechanically vulnerable fittings.

Taken together, the design, modelling, and laboratory evidence indicate that the proposed sensor can deliver operationally useful, millimetre-level sag measurements across wide thermal excursions and realistic mechanical loads, with predictable cross-sensitivities that can be calibrated and compensated. The spring-plate variant provides higher effective gain, while the narrow-plate variant offers mechanical simplicity and durability; both are viable options depending on deployment constraints. These outcomes validate the sensor as a practical building block for quasi-distributed OHL condition monitoring and motivate the next step: using measured time histories to assess fatigue-relevant behaviour of the line system under real environmental excitation, as developed in the following chapter.

References

[1] Grzegorz Fusiek and Pawel Niewczas. Design of an optical sensor with varied sensitivities for overhead line sag, temperature and vibration monitoring. In *2022 IEEE international instrumentation and measurement technology conference (I2MTC)*, pages 1–6. IEEE, 2022.

[2] Technica SA. T220 FBG surface strain sensor. Online product information, 2024. Accessed: 19 June 2024.

[3] Grzegorz Fusiek, Himanshi Singh, and Pawel Niewczas. Temperature and force characterization of an optical sag sensor for overhead line monitoring. In *2023 IEEE International Instrumentation and Measurement Technology Conference (I2MTC)*, pages 1–5. IEEE, 2023.

[4] Grzegorz Fusiek. Interim Report on Distributed Mechanical Sensor Designs. Deliverable

4.2, Innovate UK, Energy Catalyst Project: Yes to Energy Through Innovative Sensing, 2021.

[5] Himanshi Singh, Grzegorz Fusiek, and Pawel Niewczas. Extended characterization of an optical sag sensor for high-temperature low-sag lines. *IEEE Sensors Letters*, 7(9):1–4, 2023.

[6] Elsewedy Cables. High Temperature Low Sag Conductors. Online product information. Publication details to be verified.

[7] ZMS Cable. HTLS Conductor Cables. Online product information. Publication details to be verified.

[8] Sterlite Technologies. HTLS Conductor Technology. Online product information. Publication details to be verified.

[9] Ibsen Photonics A/S. *I-MON 512 USB Interrogation Monitor – Product Sheet*. Ibsen Photonics A/S, Farum, Denmark, n.d. Product sheet.

[10] Pico Technology. PT-104 platinum resistance data logger. `https://www.picotech.com/data-logger/pt-104/pt-104-platinum-resistance-data-logger`, n.d. Accessed: 18 November 2025.

[11] International Electrotechnical Commission. Iec 60751: Industrial platinum resistance thermometers and platinum temperature sensors. Technical Report IEC 60751, Geneva, 2008.

[12] Testometric Co. Ltd. Lc series load cells—LC1000 model: accuracy and temperature characteristics, n.d. Accessed: 18 November 2025; manufacturer data to be verified.

5

Fatigue assessment of OHLs using FBG sensor

5.1 Introduction

Fatigue failure of strands in overhead conductors is the most common damage caused by aeolian vibration. Aeolian vibration can lead to fatigue in other line components, such as armour rods, dampers, ties, insulators, and tower members. Conductor strand fatigue typically occurs at points where the conductor's motion is constrained against transverse vibration, particularly vertical motion due to aeolian vibration. These points include support locations, suspension clamps, clamp-top and pin insulators, goatheads, and dead ends, as well as damper and bundle conductor spacer clamps, hot-line taps, splices, and armour rod end clamps. Fatigue failures have been observed at each of these locations [1].

The likelihood of fatigue at these locations is directly related to the rigidity with which the conductor's motion is restricted. Most fatigued strands are found at tangent supports, where structural stiffness in the vertical direction is necessary to support the load associated with the weight span. Other locations, such as dead-ends and damper positions, also experience fatigue, often due to the resonances of the involved parts. For example, fatigue at dead ends is often linked to the resonance of the insulator string and jumper system. In contrast, fatigue at damper locations is usually associated with poorly-damped resonances of the damper or the segment of the conductor between the damper and the adjacent support [1].

Historically, real-time and experimental studies have documented fretting-induced failures in conductors [2–4]. Finite element modelling has been used to predict the lifetime of high-temperature low-sag (HTLS) conductors by homogenising the conductor's geometry [5]. Proposed solutions in [6] include increasing the voltage to reduce current and sag. Aeolian vibration fatigue has been addressed through the energy balance model (EBM). Introduced in the 1960s, the Everyday Tension (EDT) concept aimed to cap conductor tension within safe design limits, a practice that has evolved to incorporate vibrational considerations in transmission lines [7–10].

Condition monitoring of overhead transmission lines serves two distinct purposes:

- **DLR:** Real-time capacity assessment. Two common approaches are used to estimate allowable ampacity:
  - Model-based DLR: solves the thermal balance using meteorological inputs (ambient temperature, wind speed direction, solar irradiance) together with line current to estimate conductor temperature and dynamic rating.
  - Measurement-based DLR: relies on direct field measurements, such as conductor temperature, sag clearance, or tension, to estimate the conductor's real-time operating condition and calculate the corresponding safe current-carrying capacity.
- Asset health/integrity monitoring: Fatigue and damage prevention. This focuses on detecting conditions that can cause wear or failure, such as fretting fatigue at clamps and spacers. It relies on targeted measurements like vibration amplitude (aeolian, galloping, rain-wind), dynamic bending strain at the clamp mouth, and event counts/energy, with criteria set for damage accumulation, not for ampacity.

Overhead line conductors are subjected to repeated mechanical loading from wind-induced motion, fluctuating tension, thermal cycling, and environmental exposure. These effects can progressively reduce conductor service life, particularly near suspension clamps, spacers, and fittings where local bending and contact stresses are concentrated. Among these mechanisms, aeolian vibration is especially relevant to fatigue assessment because it produces repeated low-amplitude stress cycles that can initiate fretting fatigue and wire fracture over long operating periods [11, 12]. Larger-amplitude motions, such as galloping, may also impose significant cyclic stress under specific weather conditions, particularly when wind acts on ice-accreted conductors [13, 14]. Therefore, this chapter focuses on using measured FBG sensor data to quantify cyclic strain histories and estimate fatigue damage in the conductor system.

Despite these measures, failures have persisted, leading to the introduction of a new safe tension limit based on practical assessments. The rainflow counting algorithm, originally developed for mechanical engineering, is crucial in OHL fatigue analysis as it effectively quantifies cyclic loading effects. When combined with the stress-life (S-N) curves of the materials and Miner's rule for cumulative damage estimation, it can provide estimates of the material's remaining lifetime.

Although several OHL sag and vibration monitoring techniques have been reported in the literature, including electrical, wireless, optical, optoelectronic, and laser-based approaches [11, 15–20], this thesis focuses on compatibility with the optical sensing platform previously developed by the Advanced Sensors Team at Strathclyde [14, 21–23]. Existing CFBG- and FBG-based sag measurement methods have demonstrated the feasibility of optical sag monitoring [24–27]; however, a mechanically robust FBG-based sag sensor compatible with the team's wider optical monitoring architecture is still required. Developing such a sensor would enable sag, strain, temperature, and vibration measurements to be integrated within a unified platform for OHL condition monitoring, protection, and control. This requirement provides a key motivation for the work presented in this thesis.

This chapter presents the methodological framework developed in this thesis for estimating the lifetime of the FBG-based OHL sensors developed herein and of the overhead line conductor. The results of the OHL sag and vibration measurements obtained from sensors undergoing a field trial in a simulated power network environment are used to estimate their longevity. The maximum tension in the conductor, transmitted to the sensors, simulates the maximum stress in the plates used for the transfer of strain between the conductor and the

FBG sensors. Two different stainless-steel plate designs are considered, and the fatigue life is calculated on the basis of a finite element model of the OHL sensors and existing fatigue data for stainless steel samples from the literature. The highest vibration amplitude recorded by the sensor in the span is used to estimate the conductor's lifetime using the rainflow counting algorithm and the Miner rule for cumulative damage. A key advantage of the proposed FBG-based OHL sensors is their ability to be passively interrogated and multiplexed over long distances. The power network operator can use the data collected in the central sensor interrogator to make better-informed decisions, such as implementing improved dynamic line rating procedures. Additionally, these sensors are compatible with FBG-based current and voltage sensors, enabling the development of a comprehensive and cost-effective power grid condition monitoring and control system.

5.2 PNDC – Field Experiments and results

5.2.1 Practical Considerations from the PNDC Field Trial

Following laboratory verification, the PNDC field trial provided an opportunity to assess the practical deployment of the proposed FBG-based sag sensor under outdoor operating conditions. The main challenges were associated with mechanical installation, environmental exposure, signal stability, and data interpretation. Unlike the controlled laboratory setup, the field installation required reliable clamping of the sensor assembly to the conductor, protection of the optical fibre and connectors, and stable routing of the optical cable to the interrogator. Wind-induced motion, temperature fluctuations, and changing conductor tension introduced dynamic variations in the measured wavelength, which required careful separation of strain, temperature, and vibration-related components. In addition, the field environment introduced practical constraints such as access to the span, installation repeatability, protection against moisture and contamination, and ensuring that the sensor assembly did not alter the conductor behaviour significantly.

The scalability of the system for large transmission networks depends primarily on the multiplexing capability of FBG sensors and the deployment strategy. Since FBGs are wavelength-encoded, multiple sensors can be connected along a single optical fibre and interrogated using one optical interrogator, enabling quasi-distributed monitoring at selected critical locations. For large networks, sensors would not necessarily be required on every span. Instead, deployment could be prioritised at mechanically or thermally critical spans, such as long spans, river crossings, high-sag locations, areas exposed to strong wind, ageing fittings, or sections selected for dynamic line rating and uprating assessment. This targeted deployment approach improves scalability while limiting system complexity and cost.

In terms of cost–benefit, the proposed FBG-based system is expected to have a higher initial cost than simple visual inspection or isolated electrical sensors because it requires optical sensors, fibre routing, installation hardware, and an interrogator. However, it offers several potential benefits compared with conventional monitoring approaches, including immunity to electromagnetic interference, passive sensing at the conductor, multiplexing of several sensors along one fibre, simultaneous strain and temperature measurement, and the ability to capture dynamic strain histories for fatigue assessment. Compared with aerial inspection, LiDAR, or UAV-based methods, the FBG system can provide continuous or repeated measurements from fixed locations rather than only snapshot measurements during inspection campaigns. Therefore, the greatest benefit is expected in applications where continuous condition monitoring, early warning of abnormal sag or vibration, fatigue assessment, and improved asset utilisation can reduce inspection frequency, support predictive maintenance, and defer unnecessary line replacement or reinforcement.

5.2.2 Installation of Sensor at PNDC

The Power Networks Demonstration Centre (PNDC) is the University of Strathclyde’s utility-grade test facility that provides full-scale overhead line bays, controllable network conditions, and safe access for instrumented trials. It was chosen for sensor testing because it combines a representative outdoor environment (real spans, fittings, and weather exposure) with controlled set-ups (known geometry, verified tensions, supervised switching), allowing repeatable measurements, rapid reconfiguration, and compliance with utility safety procedures.

The PNDC conductor was tensioned to a lower level than specified in the stringing tables for 70 mm^2 HDC conductors [28]. This adjustment was necessary because stringing charts and tables generally apply to new conductors, whereas old or reused conductors should not be restrung to their initial values. As a general rule of thumb, the tension and sag of reused conductors should be set to approximately half of the initial values [28]. In addition, the lower tension was required because the guy wires at one of the poles were not installed at the standard 45 ° angle, which limited the maximum tension that could be safely applied to the conductor.

In total, two optical sag sensor assemblies, denoted as Sensor 1 (S1) and Sensor 2 (S2), were deployed on the middle conductor of the PNDC line. The sensors were installed approximately 2 m from the pole with non-ceramic strain insulators, as shown in Figure 5.1. The sensor location was selected to provide a mechanically accessible and controlled installation point close to the termination hardware, while still allowing the sensors to capture conductor strain and vibration response. The location of the sensors is important because the measured strain and vibration amplitudes depend on the local boundary conditions, including proximity to the pole, strain insulators, clamps, fittings, and the mode shape of conductor motion along the span. Therefore, the results from this deployment represent the local mechanical response at the selected sensor positions rather than the full-span sag profile.

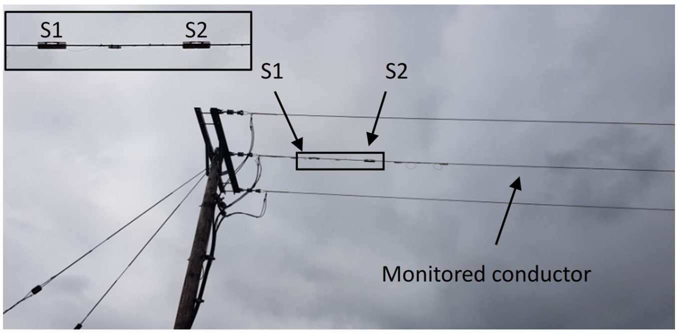

Figure 5.1: Two optical sag sensor assemblies, S1 and S2, installed on the middle conductor of the PNDC overhead line, approximately 2 m from the pole with non-ceramic strain insulators [29].

Although strain insulators provide the necessary support and help manage mechanical stresses, they introduce greater rigidity into the system than suspension insulators. This rigidity can lead to localised stress concentrations at attachment points, which may influence conductor fatigue life, particularly under temperature variations and wind-induced dynamic loading. The conductor tension was verified using a dynamometer attached between the conductor and the anchor point on the pole. The measured force was 3.45 kN, with an estimated uncertainty of ±50 N due to wind during the measurement. The ambient temperature during installation was 10 °C. For the subsequent thermal and mechanical analysis, the maximum allowable conductor temperature was taken as 75 °C. This value is consistent with the example line-rating condition used in [30], where a maximum conductor temperature of 75 °C is adopted for real-time thermal rating calculations, although CIGRE notes that the allowable temperature depends on conductor type and line-rating requirements [30]. The sensors were positioned along the conductor with an approximate spacing of 1 m. After installation, the optical sensors were connected to a dedicated FBG interrogator through an optical link. These installation constraints and verified boundary conditions define the reference state for the subsequent measurements and analysis.

The optical sag sensors developed in this work were shown to detect a range of wind-induced conductor motions, including aeolian vibration, galloping, and wake-induced oscillations [29]. Under long-term cyclic loading, the corresponding fatigue life of the conductor-sensor system can be estimated using the fatigue-assessment methodology developed in this thesis and reported in [7].

During the field trials, the sensors were interrogated at a frequency of 5 kHz, with signals logged by the interrogator for 1 minute every 4 hours. Given the distance between the sensors and the interrogator, distance compensation was applied to account for the time of flight (ToF). This ToF correction shifts the FBG peaks on the spectrum and can introduce errors in peak wavelength estimation, contributing to temperature and strain measurement inaccuracies. According to the manufacturer, the accuracy of the FBG temperature sensor is ±1 °C. It should be noted that the optical sag sensors were only characterised at room temperature, so their temperature response was unknown during the initial field trials. Strain estimation relied on the temperature compensation data provided by the manufacturer for the strain sensors.

In addition to the optical sensors, a weather station was installed near the monitored line to track weather conditions during field trials. Weather data, including temperature and wind speed, were recorded every 10 minutes [29].

5.2.3 Measurement Results

Although S1 was found to be more sensitive than S2 during laboratory characterisation, both sensors were installed at PNDC to compare the field performance of two different mounting-plate geometries. The spring-plate design of S1 provided higher mechanical gain for detecting small dynamic strain changes, while the narrow-plate design of S2 provided a lower-gain and mechanically simpler configuration. This comparison was important for assessing whether improved sensitivity justified the additional mechanical complexity of the spring-plate design under real outdoor operating conditions.

Examples of logged wavelength data from sensors S1 and S2 during monitoring of the HDC conductor at PNDC are shown in Figures 5.2 and 5.3 [29]. The data sample was recorded on 29 January 2022 at 10:50:58.75144 using ENLIGHT interrogator software version 1.18.8.0 with a Hyperion module. The hardware acquisition rate was 5000 Hz, the data save interval was 1 s, and the wavelength tracking range was 400 pm per acquisition.

Figures 5.2 and 5.3 present the time-domain wavelength responses of sensors S1 and S2. An example of the corresponding frequency-domain response of the S1 sensor signal, obtained using fast Fourier transform (FFT) analysis, is presented in Figure 5.4. Together, the time and frequency-domain results demonstrate that the FBG sensors can detect dynamic conductor motion, including vibration components associated with low-frequency conductor oscillations and higher-frequency aeolian-type vibrations [29].

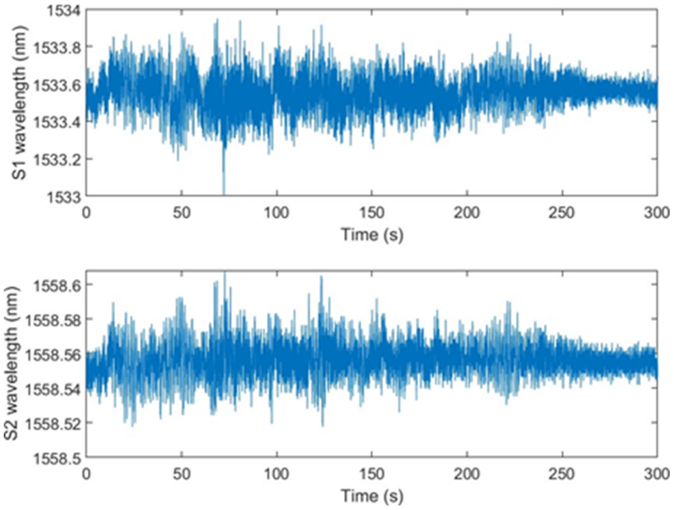

Figure 5.2: Recorded wavelength responses of sensors S1 and S2 during monitoring of the HDC conductor at PNDC [29].

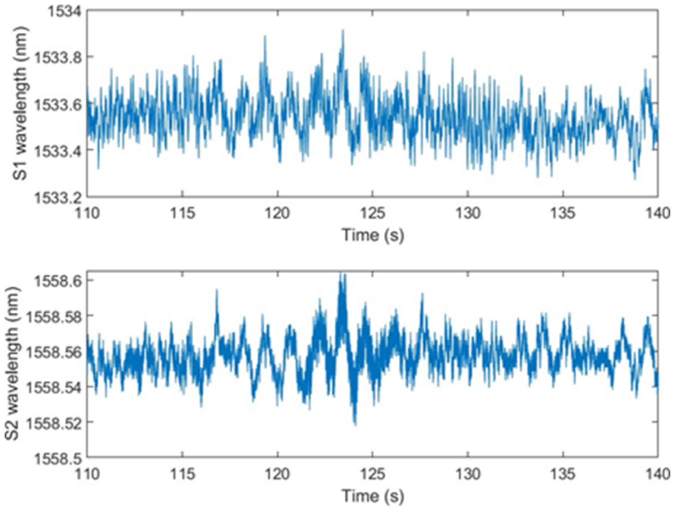

Figure 5.3: Zoomed view of the S1 and S2 wavelength signals shown in Figure 5.2 [29].

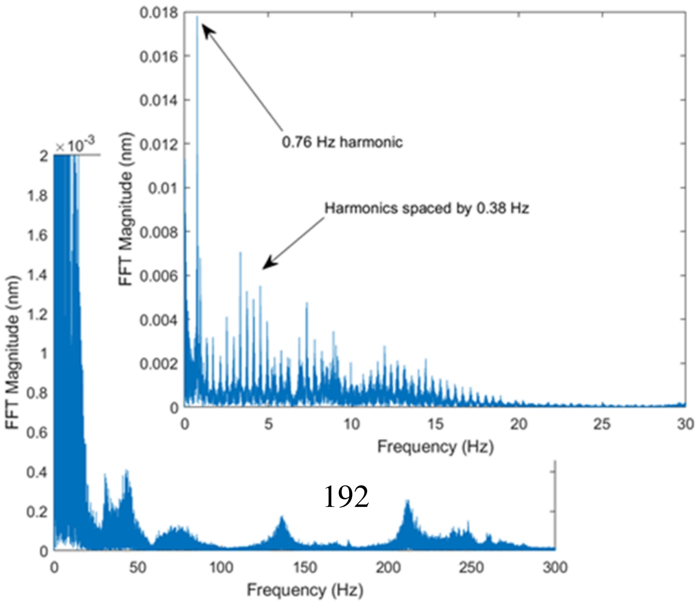

Figure 5.4: FFT analysis of the S1 sensor wavelength signal.

Based on the conductor and line specifications, the fundamental harmonic for vibrations in the considered conductor is 0.38 Hz. The FFT and power spectrum of the vibrations detected by the optical sensors clearly show the 2nd harmonic at 0.76 Hz, which aligns with the theoretical value. Higher harmonics are also visible in the spectra, though with smaller amplitudes. Since the S1 sensor is more sensitive to vibrations, harmonics from wind-induced vibrations are detectable in the spectra up to 400 Hz. No vibrations were detected above 500 Hz, which is consistent with the frequency range of aeolian vibrations [29].

5.3 Prediction of fatigue

In the context of this thesis, the data analytics contribution is the conversion of field-acquired FBG wavelength time histories into fatigue-relevant information for the conductor and sensor assembly. The processing workflow consists of:

- converting wavelength variations into strain or stress histories using the calibrated sensor response;
- extracting turning points from the stress signal;
- applying rainflow counting to identify stress cycles under variable-amplitude loading;
- mapping each counted cycle to the corresponding number of cycles to failure using an appropriate S–N curve;
- estimating cumulative fatigue damage using Miner's rule.

This workflow converts raw optical sensing data into an engineering indicator of fatigue damage and remaining life.

The primary cause of fatigue in conductors is the random cyclic stress induced by aeolian vibration, which results in fretting effects between the conductor strands. CIGRE has established criteria for conductor failure due to bending fatigue, defining failure as when either 3 strands or 10 % of the total number of strands in a conductor are broken, whichever is greater. The rainflow counting algorithm is essential in OHL fatigue analysis as it effectively quantifies cyclic loading effects. When used in conjunction with stress-life (S-N) curves of materials and Miner's rule for cumulative damage estimation, it can provide accurate estimates of the material's remaining lifetime. Conductor fatigue lifetime prediction is typically based on Wohler's curves (S-N curves), created during fatigue tests for a given conductor, which indicate the number of cycles required to break the material at a specific cyclic stress level. PNDC strain records were analysed using rainflow cycle counting to obtain the distribution of strain ranges and means. Each cycle was mapped to its expected life via the calibrated S–N relationship for the clamp–conductor interface, and Miner's cumulative damage rule was then applied to compute the damage rate and the corresponding fatigue life under the measured conditions.

5.3.1 Rainflow counting algorithm

Rainflow counting was selected because wind-induced conductor vibration produces irregular, variable-amplitude stress histories rather than constant-amplitude loading. Rainflow counting is widely used for fatigue analysis because it reduces a complex time-domain stress signal into an equivalent set of stress cycles defined by cycle range, mean stress, and cycle count. These cycle statistics can then be combined with material S–N data to estimate fatigue damage. Miner's rule was used because it provides a simple and widely accepted cumulative damage framework, allowing each counted stress cycle to contribute a damage fraction n_i/N_i, where n_i is the number of cycles observed at stress level i, and N_i is the corresponding number of cycles to failure from the S–N curve.

The rainflow counting algorithm, initially proposed by Matsuishi and Endo [31], employs a recursive approach to identify closed hysteresis loops in strain-stress plots, likened to the path of raindrops on a pagoda roof, as presented in Figure 5.5.

Later, a non-recursive form of the algorithm was developed [32], which is utilised in this chapter. Rainflow counting is essential for fatigue analysis as it identifies and counts stress cycles from a load signal, aiding in the assessment of material fatigue life under variable load

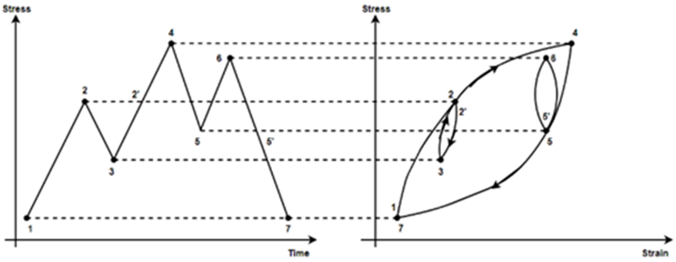

Figure 5.5: Principle of rainflow counting algorithm [7].

conditions. The principle of the rainflow counting algorithm is illustrated in Figure 5.6, with the following steps [31]:

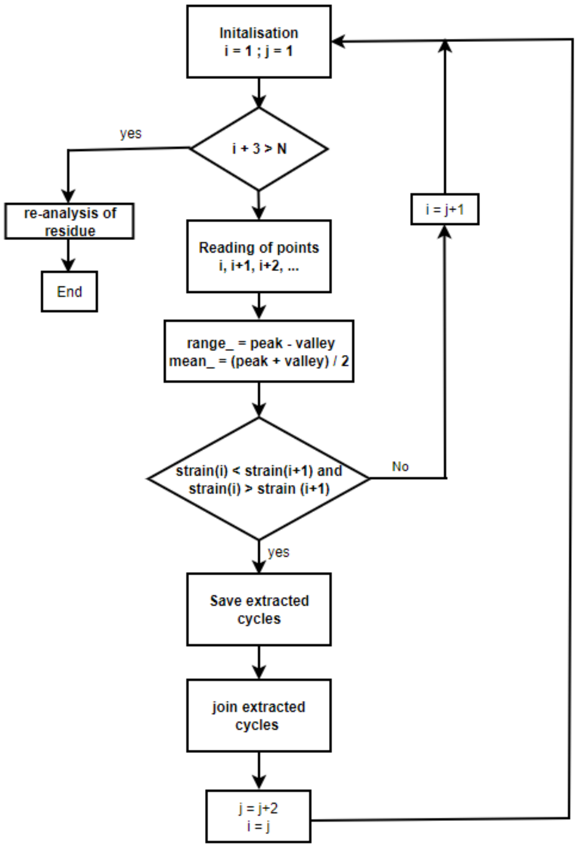

Figure 5.6: Rainflow counting algorithm flowchart.

- Identify turning points in a stress signal where the direction changes, either from increasing to decreasing (peak) or from decreasing to increasing (valley).
- Traverse the time history signal to pinpoint these turning points.

- Connect pairs of turning points to form closed loops, representing each cycle the material undergoes.
- For each cycle, calculate the range $\Delta\sigma$ and mean σ_{mean} values. The range is the stress difference between the peak and the valley, while the mean is the cycle's average stress.
- Count each unique range and mean pair. Remove the counted cycles from the original signal, leaving residuals for further analysis.
- Continue analysing the residuals until all cycles are accounted for.
- Compile the data into a matrix representing the load history. Each row corresponds to a different range-mean pair, with the matrix elements indicating the frequency of each pair.

These cycles are then utilised alongside fatigue analysis methods, such as the Palmgren-Miner rule, to estimate the material's fatigue life under varying loading conditions [7].

However, this approach has limitations. Rainflow counting identifies equivalent fatigue cycles but does not itself model the physical mechanisms of conductor fretting, strand interaction, or clamp-contact behaviour. Miner's rule assumes linear damage accumulation and does not account for load-sequence effects, mean-stress correction unless explicitly included, environmental degradation, corrosion, temperature-dependent material properties, or changes in boundary conditions over time. The accuracy of the fatigue estimate also depends strongly on the representativeness of the measured time window and the suitability of the selected S–N curve for the actual conductor, clamp, and fitting configuration. Therefore, the fatigue-life values obtained in this chapter should be interpreted as methodology-based estimates rather than absolute lifetime predictions unless validated using longer-term field data and independent inspection or failure observations.

The method can be extended towards more advanced predictive analytics by using longer-duration field datasets, environmental measurements, and statistical or machine-learning models to identify operating regimes associated with increased fatigue damage. Possible extensions include automated event detection, damage-rate trending, anomaly detection, probabilistic remaining-life estimation, and physics-informed models that combine measured FBG strain histories with weather, conductor temperature, wind speed, and line-loading data. Such approaches would allow the present rainflow–Miner workflow to evolve from an offline fatigue-assessment method into a predictive condition-monitoring tool for OHL asset management.

5.3.2 Miner's rule

In 1945, one of the pioneering papers published on predicting fatigue life, B. A. Miner, [33], introduced a criterion that has become widely known as Miner's rule. Treating fatigue as a deterministic phenomenon and employing concepts such as internal work and damage, Miner heuristically derived a rule for predicting fatigue life under repeated cyclic loadings with varying stresses. However, Miner's rule has persisted as a standard for comparison due to its simplicity and because it often produced results no worse than alternative methods. Calculations using extensive empirical data [34] demonstrated that, in many practical cases, Miner's rule provides approximately correct and conservative results, typically underestimating the true number of cycles to failure [35].

Consider standardised specimens of a material exposed to fluctuating stresses due to periodic loading. A load (or load oscillation) is defined as a continuous unimodal function over a unit interval, representing the stress imposed by the deflection of the material specimen at any given time. This load function includes all necessary information to determine parameters such as maximum stress, minimum stress, and average stress, which are typically used to define the loading oscillation.

The assumptions underlying Miner's rule are summarised as follows:

- The damage absorbed by the material in any one oscillation is determined solely by the load during that oscillation.
- Each specimen absorbs the same amount of damage, and failure occurs when that amount is reached.

- The total damage absorbed by the specimen under a sequence of load oscillations equals the sum of the damage absorbed in each oscillation during the sequence.

Using the notation, W is the total damage at failure, w is the amount of damage during one repetition of load oscillation, N is the number of oscillations to failure under repeated application of the same load l, and i is an index representing possible loads considered.

From the above-mentioned assumptions (a), (b), and (c), the derived equation 5.1 is:

$$W = Nw \text{ for each } i = 1, \ldots, k \tag{5.1}$$

If a sequence of different loads is applied until failure occurs after load l is applied in n_i oscillations, as shown in equation 5.2:

$$\sum_{i=1}^{k} n_i w = W \tag{5.2}$$

From this, failure is predicted when the cumulative damage reaches unity, as shown in equation 5.3:

$$D = \sum_{i=1}^{k} \frac{n_i}{N_i} \tag{5.3}$$

Failure is assumed to occur when:

$$D = 1 \tag{5.4}$$

which estimates the total life by determining the fraction of damage accrued during one cycle and using its reciprocal. In practice, N_i values are determined from a regression plot of the number of fixed oscillations until failure versus the maximum imposed stress per oscillation (S-N data), and n_i values are calculated from a typical loading spectrum during the cycle. This is then used to estimate N [35].

5.3.3 S-N Curve

An S-N Curve, sometimes referred to as an SN-Curve (also known as the Wöhler curve), is a graph that displays the relationship between the magnitude of an alternating stress and the number of cycles to failure for a specific material. Both the stress and the number of cycles are usually presented on logarithmic scales. Using a load time history and an S-N Curve, one can apply Miner's Rule to calculate the accumulated damage or estimate the fatigue life of a mechanical component [36].

5.3.4 Analysis of PNDC results for lifetime estimation of FBG-based sag sensor

As demonstrated in Section 5.2.2, when installed on a conductor, the sag sensors will experience dynamic loads transferred from the conductor at various frequencies and across its operating temperature range. Given that the sag sensor mounting and attachment structure is made of stainless steel 304, it is crucial to ensure that the sensor structure can withstand these dynamic loads and that its lifespan will exceed that of the conductor. To verify the expected endurance of the sag sensor mounting plate, the proposed mechanical structures' geometries were imported into COMSOL Multiphysics® software for FEA. This analysis did not take into account the stiffness of the T220 sensor, which was assumed to be significantly lower than that of the plates and the conductor, thus not significantly affecting the results [29].

In the initial study, the sensor structure made of SS304 was assumed to be attached to a hard-drawn copper conductor, and the stress in the mounting plates was analysed when the conductor was subjected to an axial load at its maximum operating temperature of 75 °C. As previously mentioned, the tension in the conductor at PNDC, measured at 10 °C, was 3.45 kN. The expected decrease in conductor tension at 75 °C was then estimated.

To calculate the expansion of the transmission line when heated to 75 °C, the following formula was used in equation 5.5:

$$\Delta L = CTE \times \Delta T \times L_0 \tag{5.5}$$

where CTE is the thermal expansion coefficient of the HDC conductor (17×10^{-6} 1/°C), (L_0) is the original length of the conductor, and (ΔL) is the change in conductor length.

The relationship between the conductor length, span, and horizontal tension is given in equation 5.6:

$$L = S\left(1 + \frac{S^2 \times w^2}{24 \times H^2}\right) \tag{5.6}$$

where L is the length of the conductor, S is the span, w is the weight of the conductor per unit length, and H is the tension of the conductor.

Using this equation, the initial conductor length was calculated at 10 °C with a tension of 3.45 kN. The length at 75 °C was then determined by combining the above equations 5.1 and 5.2. By rearranging the tension equation 5.2, the new tension in the conductor at 75 °C was found to be 2.38 kN. This value was applied axially to the conductor and sensor structure model in COMSOL to determine the maximum stress in the sag sensor mounting plates. The FEA results for the mounting plates with springs (sensor S1) and for the plates with narrow sections (sensor S2) are shown in Figures 5.7 and 5.8, respectively [29].

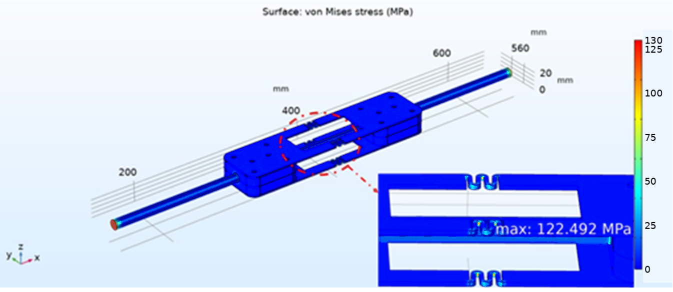

Figure 5.7: Stress in sensor S1 with a load of 2.38 kN at 75 °C [29].

As indicated in Figures 5.7 and 5.8, the maximum stress concentration occurs in the regions with springs and narrow sections of the respective plates. The stress at 75 °C on the spring plate is approximately 122.5 MPa, while the stress in the narrow section plate is 74.6 MPa. In both cases, the maximum stress experienced by the sensor plates under these

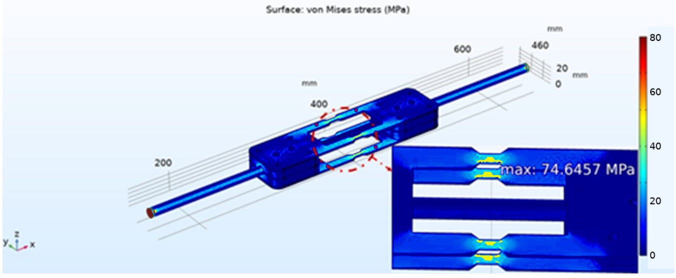

Figure 5.8: Stress in sensor S2 with a load of 2.38 kN at 75 °C [29].

conditions is well below the yield tensile strength (YTS, 215 MPa) and the ultimate tensile strength (UTS, 505 MPa) of 304 stainless steel [37, 38].

The next study involved modelling the dynamic stress in the conductor based on the logged data in the PNDC and determining the expected maximum stress in the mounting plates of the sensors. As seen in Figure 5.4, the second harmonic at 0.76 Hz has a much higher amplitude than the higher harmonics and was therefore used to estimate the maximum stress amplitude transferred to the sensor structure. The ambient temperature was assumed to be 10 °C for these considerations.

For the FEM analysis, the force in the conductor was estimated from the sensitivities of the sensors to force, assumed to be 1.3 nm/kN for sensor S1 and 0.1 nm/kN for sensor S2. The estimated force was then applied to the conductor and structure model in COMSOL in a frequency domain study. The results of this investigation, showing the maximum stress in the plates, are presented in Figures 5.9 and 5.10 [29].

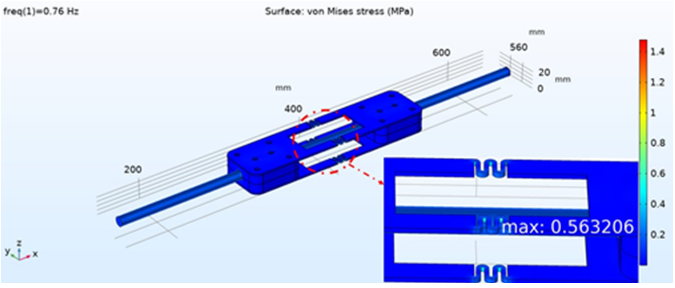

Figure 5.9: Stress in Sensor S1 at a Load with a Second Harmonic Frequency of 0.76 Hz [29].

As illustrated in Figures 5.9 and 5.10, the dynamic stress level on both plates is significantly lower than at 75 °C. The maximum stress concentration occurs in the regions with springs and

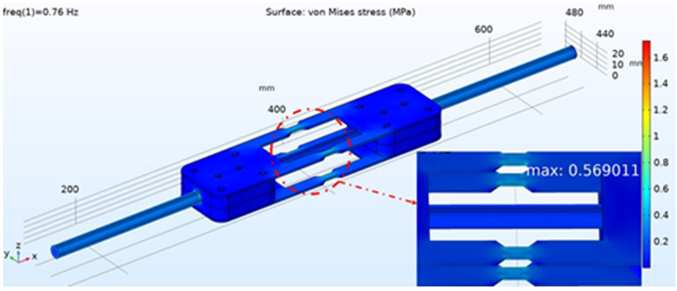

Figure 5.10: Stress in Sensor S2 at a Load with a Second Harmonic Frequency of 0.76 Hz [29].

narrow sections of the respective plates. The stress in both plates is approximately 0.5 MPa, which is more than two orders of magnitude below the endurance limit of 200-240 MPa for stainless steel 304. Given that the measured stress amplitude ($\approx$0.5 MPa) is $>$400× lower than the reference fatigue strength of SS304 ($\approx$200–240 MPa at 10^7 cycles), the mounting plates are not expected to accumulate measurable fatigue damage under the observed vibration spectrum (refer to Figure 5.11) [39, 40].

Predicting the fatigue lifetime of a conductor typically relies on the S-N (Wohler) curve, which is derived from fatigue tests and indicates the number of cycles required to fail the material at different cyclic stress levels. To estimate the dynamic bending stress in a conductor, the Poffenberger-Swart formula is often employed. This formula relates the dynamic bending stress to the vibration amplitude of a conductor at a specific distance from the last point of contact with a suspension clamp.

The S-N curve for the fatigue life of a conductor can be represented as equation 5.7:

$$\sigma_a = A \cdot N_i^B \tag{5.7}$$

where σ_a is the stress amplitude in MPa, N_i is the number of cycles to failure at each stress level, and A and B are constants derived from experimental fatigue data.

The Poffenberger-Swart formula is expressed as in equation 5.8:

$$\sigma_{PS} = K \cdot Y_b \tag{5.8}$$

where σ_{PS} is the stress amplitude (zero-to-peak), Y_b is the peak-to-peak vibration amplitude measured vertically from the last point of contact of the conductor with the suspension clamp, and K is the Poffenberger constant.

The Miner rule is widely used in fatigue analysis to estimate the total fatigue life of a material under various loading conditions. The rule is mathematically described in equation 5.3.

The remaining lifetime of the sample under test can be calculated using the following equation 5.9:

$$V = \frac{1}{D} \tag{5.9}$$

where D represents the cumulative damage, and V denotes the remaining life in cycles [7].

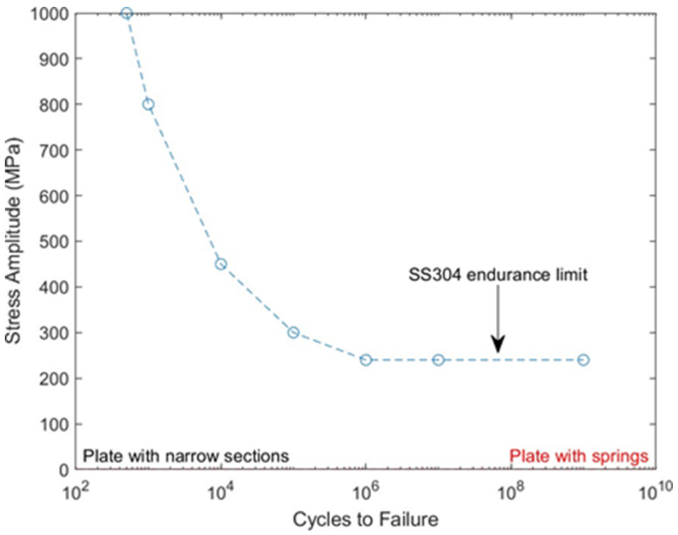

Figure 5.11: Standard SS304 S–N curve with the maximum stress values estimated for the two sag sensor mounting plate designs under PNDC vibration loading. Sensor S1 corresponds to the spring-plate design, which provides higher strain sensitivity but higher local stress concentration, while Sensor S2 corresponds to the narrow-section plate design, which provides lower sensitivity but a larger mechanical margin [29].

A comparison of the maximum stress levels on the two SS304 mounting plate designs, derived from the vibration monitoring data of the conductor at PNDC, with the standard ASTM S–N curves for stainless steel is illustrated in Figure 5.11. The two designs considered were the spring-plate configuration used for Sensor S1 and the narrow-section plate configuration used for Sensor S2. The spring-plate design was included because it provides higher strain transfer and vibration sensitivity, while the narrow-section design was considered a mechanically simpler and lower-stress alternative. The comparison shows that the stress levels estimated for both plate designs are well below the fatigue-critical region of the SS304 S–N curve. Therefore, both mounting plate designs are expected to have sufficient fatigue margin under the measured PNDC vibration conditions, although S1 provides higher sensitivity at the cost of higher local stress concentration.

5.3.5 Analysis of PNDC results for lifetime estimation of HDC conductor

Reliable operation of overhead lines depends on controlling mechanical behaviour, tension, sag, and vibration, because wind-induced motions (aeolian, galloping, wake-induced) drive cumulative fatigue at clamps and fittings. Monitoring these mechanical parameters is therefore essential for both safety and asset life management. Previous work [29] shows that the proposed optical sag sensors can resolve the full range of relevant vibration phenomena. When such vibrations act over extended periods, the line's fatigue life can be quantified by processing the measured strain/vibration records and applying standard fatigue analysis (cycle counting and S-N/Miner formulations) [7].

An example of a 5-minute continuous record of vibration detected by the optical sag sensor S1 in the HDC conductor monitored at PNDC is shown in Figure 5.12. The wavelength changes in sensor S1 shown in Figure 5.12(a) were obtained by removing the mean component from the optical signal [29]. Using the sensor characteristics and conductor specifications [41], the maximum dynamic stress detected in the conductor during this measurement window was estimated to be approximately 10 MPa peak-to-peak, as shown in Figure 5.12(b). This stress range is over three times lower than the endurance limit of HDC conductors (35 MPa) [42], indicating that the monitored conductor operated within the endurance strength region of the material S-N curve under these particular environmental conditions. Because the available field dataset did not contain vibration amplitudes high enough to generate fatigue-relevant stresses, a uniform ×10 scaling was applied to the measured stress time series solely to

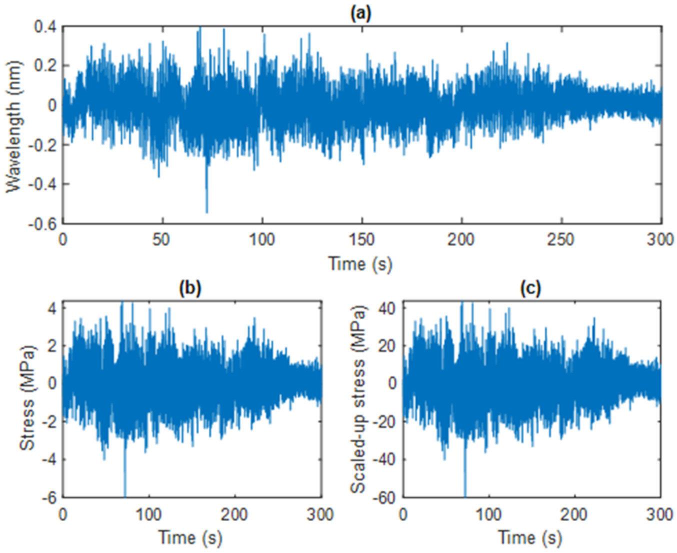

Figure 5.12: Wavelength change in sensor S1 monitoring the HDC conductor at PNDC [29]: (a) converted to stress in the conductor, (b) and stress scaled up for fatigue analysis purposes (c) [7].

demonstrate the analysis workflow. The scaled signal is used to illustrate cycle counting and Miner damage calculations; all quantitative life results from the scaled example are presented as illustrative rather than design values. Consequently, the stress range was increased to 116 MPa, as depicted in Figure 5.12(c).

To predict the remaining lifetime of the monitored conductor, the scaled-up stress data were analysed using the rainflow counting algorithm combined with cumulative damage estimation. For the analysis, modified MATLAB rainflow counting functions based on previously proposed algorithms [43] were used.

A 5-second window of the scaled stress signal is shown in Figure 5.13, together with the turning points identified by the rainflow pre-processing step. These turning points define the stress reversals from which full and half fatigue cycles are extracted.

The detection of load reversal points can be adjusted by setting a stress threshold, which in this case was set at 5 % of the maximum stress range detected (116 MPa) [44]. This setting helps to filter out stress levels that do not significantly contribute to material fatigue and can be ignored [7, 45].

In this analysis, a fatigue cycle is defined using the rainflow counting procedure rather than by a fixed time period. The stress time history is first reduced to a sequence of turning points, corresponding to local maxima and minima in the stress signal. A counted cycle is then identified when a pair of turning points forms a closed stress reversal according to the rainflow counting rules. Each counted cycle is characterised by its stress range, $\Delta\sigma$, stress amplitude, $\sigma_a = \Delta\sigma/2$, mean stress, σ_{mean}, and number of occurrences. Full cycles are assigned a count of 1, while residual half-cycles are assigned a count of 0.5. These counted cycles are then used with the S–N curve and Miner's rule to estimate cumulative fatigue damage.

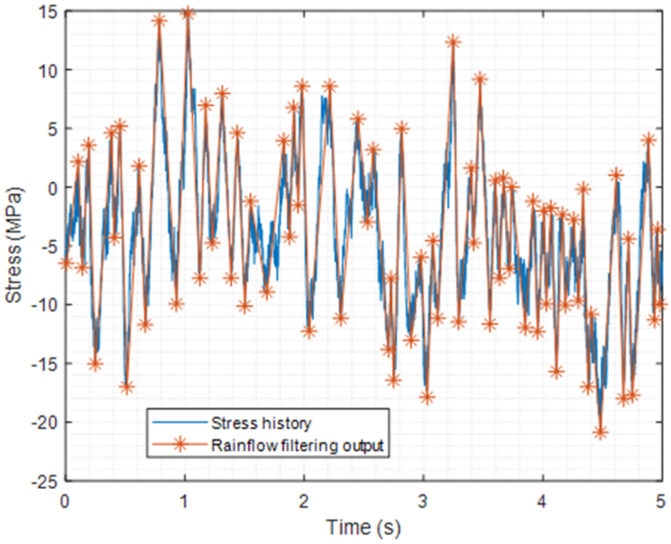

Figure 5.13: Turning points identified by the rainflow counting algorithm [7].

The rainflow counting output, which illustrates the load reversals over time and the distribution of cycles as a function of the detected stress range and mean value (rainflow matrix histogram), is shown in Figure 5.14.

The results from the rainflow counting were then compared to the S-N curve of hard-drawn copper [46] to determine the number of cycles to failure at each stress level, as shown in Figure 5.15.

Subsequently, cumulative damage and remaining lifetime were calculated using Miner's rule according to equations 5.8 and 5.9, respectively [7]. Based on the analysis procedure described above, the cumulative damage was estimated to be 1.1×10^{-6}, indicating that the conductor should not sustain damage under such a stress profile. The estimated lifetime of

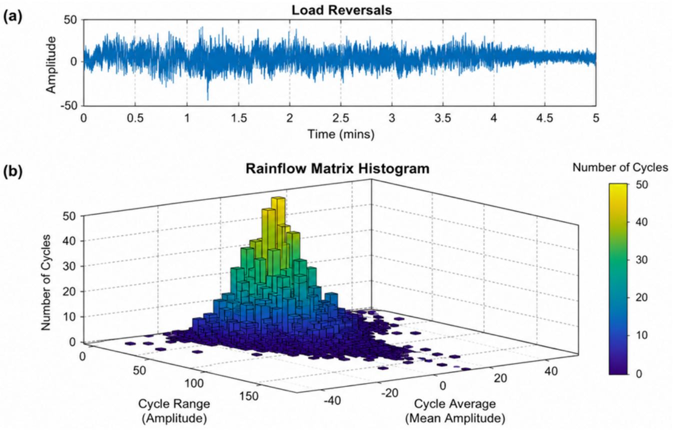

Figure 5.14: Rainflow cycle-counting results for the scaled stress signal: (a) time history of identified load reversals over a 5-minute interval; and (b) rainflow matrix showing the counted cycles as a function of stress range and mean stress. Each cycle is defined by a pair of stress reversals identified from the turning points of the stress time history. The colour scale indicates the number of counted cycles in each range–mean bin [29].

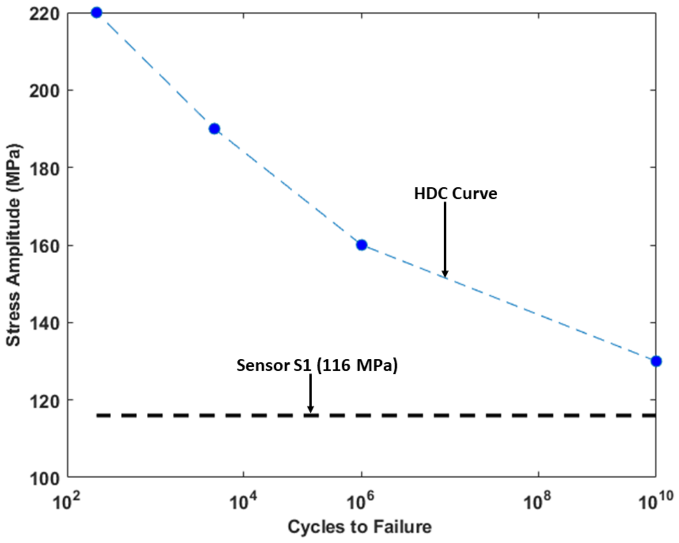

Figure 5.15: Sensor S1 stress value in standard S-N curve for HDC conductor.

the conductor was calculated to be 9.2×10^5 cycles [7].

5.4 Conclusion

This chapter discusses the results from an initial field trial of two optical sag sensors designed for OHL monitoring. It details the construction of the sensors and their laboratory characterisation before installation. Experimental results showed good agreement with theoretical predictions based on the conductor's assumed parameters. The vibration signals detected by the sensors matched theoretical estimations due to wind load and other line parameters, and temperature readings from the optical sensors were consistent with weather station data.

The initial field trials suggest that these sensors could be valuable for assessing key mechanical parameters of overhead lines, aiding in dynamic rating and structural health monitoring. Additionally, the fatigue life of FBG sag sensors was estimated using data from the field trial. The study simulated the maximum stress in the plates used for strain transfer between the conductor and the FBG sensors, considering two distinct stainless steel plate designs. The fatigue life was calculated using a finite element model and existing literature on fatigue data for stainless steel. Results indicated that the maximum stress levels in the sensor mounting plates are well below the endurance limit of SS304, theoretically ensuring the infinite lifetime of the sensor structure.

Moreover, a methodological framework for estimating the fatigue life of overhead conductors due to aeolian vibration was implemented using the rainflow counting algorithm and Miner's rule. This algorithm, based on data from the FBG-based sag sensors, helps understand the cyclic loading history of overhead line conductors and predict fatigue. It analyses stress cycles and assesses the structural integrity of the conductor under different loads over time. Each cycle's damage factor depends on material properties, conductor geometry, and load cycle amplitude. The cumulative damage at the considered stress range was estimated to be 1.1×10^{-6}, indicating that the conductor will endure 9.2×10^5 cycles of operation.

References

[1] John Chan, Dave Havard, Chuck Rawlins, Giorgio Diana, Louis Cloutier, Jean-Louis Lilien, Claude Hardy, Jeff Wang, and Anand Goel. EPRI transmission line reference book: wind-induced conductor motion. *EPRI, N*°1018554, 2009.

[2] RB Kalombo, JA Araújo, JLA Ferreira, CRM Da Silva, R Alencar, and AR Capra. Assessment of the fatigue failure of an all aluminium alloy cable (AAAC) for a 230 kV transmission line in the center-west of brazil. *Engineering Failure Analysis*, 61:77–87, 2016.

[3] CRF Azevedo and T Cescon. Failure analysis of aluminum cable steel reinforced (ACSR) conductor of the transmission line crossing the parana river. *Engineering Failure Analysis*, 9(6):645–664, 2002.

[4] B Ouaki, S Goudreau, A Cardou, and M Fiset. Fretting fatigue analysis of aluminium conductor wires near the suspension clamp: Metallurgical and fracture mechanics analysis. *The Journal of Strain Analysis for Engineering Design*, 38(2):133–147, 2003.

[5] Mohammed A Al Aqil and Konstantinos Kopsidas. Predicting the end-of-life for OHL conductors. In *2020 IEEE/PES Transmission and Distribution Conference and Exposition (T&D)*, pages 1–5. IEEE, 2020.

[6] K Kopsidas and SM Rowland. Evaluating opportunities for increasing power capacity of existing overhead line systems. *IET generation, transmission & distribution*, 5(1):1–10, 2011.

[7] Himanshi Singh, Grzegorz Fusiek, and Pawel Niewczas. Methodological framework for conductor lifetime estimation using optical sag sensors. *IEEE Sensors Letters*, 8(7):1–4, 2024.

[8] International Electrotechnical Commission. Overhead lines – requirements and tests for stockbridge type aeolian vibration dampers. Standard IEC 61897, International Electrotechnical Commission, 1998.

[9] CIGRÉ SC22 WG11. Safe design tension with respect to aeolian vibrations, part 2: Damped single conductors. Technical brochure, CIGRÉ, 2001.

[10] CIGRÉ SC B2 WG B2.25. Assessment of aeolian vibrations severity. Technical brochure, CIGRÉ, 2009.

[11] CIGRÉ. Fatigue endurance capability of conductor/clamp systems: Update of present knowledge. Technical Brochure 332, CIGRÉ, 2007.

[12] Bertrand Godard, Suzanne Guérard, and Jean-Louis Lilien. Original real-time observations of aeolian vibrations on power-line conductors. *IEEE Transactions on Power Delivery*, 26(4):2111–2117, 2011.

[13] CIGRE WG 04 SC 22-02. Recommendations for the evaluation of the lifetime of transmission line conductors. Technical report, CIGRE, 1979.

[14] Grzegorz Fusiek and Pawel Niewczas. Design of an optical sensor with varied sensitivities for overhead line sag, temperature and vibration monitoring. In *2022 IEEE International Instrumentation and Measurement Technology Conference (I2MTC)*, pages 1–6. IEEE, 2022.

[15] Arsalan Habib Khawaja, Qi Huang, and Zeashan Hameed Khan. Monitoring of overhead transmission lines: a review from the perspective of contactless technologies. *Sensing and Imaging*, 18:1–18, 2017.

[16] Eric Cloet and Jean-Louis Lilien. Uprating transmission lines through the use of an innovative real-time monitoring system. In *2011 IEEE PES 12th international conference on transmission and distribution construction, operation and live-line maintenance (ESMO)*, pages 1–6. IEEE, 2011.

[17] Federico Zanelli, Marco Mauri, Francesco Castelli-Dezza, Davide Tarsitano, Alessandra Manenti, and Giorgio Diana. Analysis of wind-induced vibrations on HVTL conductors using wireless sensors. *Sensors*, 22(21):8165, 2022.

[18] Elena Golinelli, Umberto Perini, and Gianmario Ogliari. A new ir laser scanning system for power lines sag measurements. 2016.

[19] Heng Wang, Shijia Han, Li-Jun Lv, and Li-Jun Jin. Transmission line sag measurement based on single aerial image. In *2017 24th International Conference on Mechatronics and Machine Vision in Practice (M2VIP)*, pages 1–5. IEEE, 2017.

[20] Yunfei Chen and Xiaolin Ding. A survey of sag monitoring methods for power grid transmission lines. *IET Generation, Transmission & Distribution*, 17(7):1419–1441, 2023.

[21] John Nelson, Grzegorz Fusiek, Lloyd Clayburn, Paweł Niewczas, Campbell Booth, Philip Orr, and Neil Gordon. Development and testing of optically-interrogated current sensors. In *2016 IEEE International Workshop on Applied Measurements for Power Systems (AMPS)*, pages 1–5. IEEE, 2016.

[22] Grzegorz Fusiek, John Nelson, Pawel Niewczas, Jussi Havunen, Esa-Pekka Suomalainen, and Jari Hällström. Optical voltage sensor for MV networks. In *2017 IEEE SENSORS*, pages 1–3. IEEE, 2017.

[23] Grzegorz Fusiek, Himanshi Singh, and Pawel Niewczas. Temperature and force characterization of an optical sag sensor for overhead line monitoring. In *2023 IEEE International Instrumentation and Measurement Technology Conference (I2MTC)*, pages 1–5. IEEE, 2023.

[24] Krzysztof Skorupski, Damian Harasim, Patryk Panas, Sławomir Cieszczyk, Piotr Kisała, Piotr Kacejko, Janusz Mroczka, and Michał Wydra. Overhead transmission line sag estimation using the simple opto-mechanical system with fiber bragg gratings–part 2: Interrogation system. *Sensors*, 20(9):2652, 2020.

[25] Michal Wydra, Piotr Kisala, Damian Harasim, and Piotr Kacejko. Overhead transmission line sag estimation using a simple optomechanical system with chirped fiber Bragg gratings. part 1: Preliminary measurements. *Sensors*, 18(1):309, 2018.

[26] Leif Bjerkan. Application of fiber-optic bragg grating sensors in monitoring environmental loads of overhead power transmission lines. *Applied Optics*, 39(4):554–560, 2000.

[27] Guo-Ming Ma, Cheng-Rong Li, Jian Jiang, Jun-Yu Liang, Ying-Ting Luo, and Yang-Chun Cheng. A passive optical fiber anemometer for wind speed measurement on

high-voltage overhead transmission lines. *IEEE Transactions on Instrumentation and Measurement*, 61(2):539–544, 2011.

[28] M Chapman. *The Design of Single Circuit High Voltage Overhead Lines on Wood Poles at 11 kV and 33 kV*. 2019.

[29] Himanshi Singh, Grzegorz Fusiek, Pawel Niewczas, and Valerie Livina. Estimation of the fatigue life of a fiber Bragg grating overhead line sag sensor. In *2024 IEEE International Instrumentation and Measurement Technology Conference (I2MTC)*, pages 1–6. IEEE, 2024.

[30] CIGRE Working Group B2.36. Guide for Application of Direct Real-Time Monitoring Systems. Technical Brochure 498, CIGRE, 2012.

[31] M. Matsuishi and T. Endo. Fatigue of metals subjected to varying stress. *Japan Soc. Mech. Eng. Fukuoka*, 68(2):37–40, 1968.

[32] Igor Rychlik. Fatigue and stochastic loads. *Scandinavian Journal of Statistics*, pages 387–404, 1996.

[33] Milton A Miner. Cumulative damage in fatigue. *Journal of Applied Mechanics*, 12(3):A159–A164, 1945.

[34] WJ Crichlow, AJ McCulloch, L Young, and MA Melcon. *An engineering evaluation of methods for the prediction of fatigue life in airframe structures*. Flight Dynamics Laboratory, Aeronautical Systems Division, Air Force Systems . . . , 1962.

[35] ZW Birnbaum and Sam C Saunders. A probabilistic interpretation of miner's rule. *SIAM Journal on Applied Mathematics*, 16(3):637–652, 1968.

[36] Siemens. What is an S–N curve? Online resource.

[37] ASTM International. Standard test method for measurement of fracture toughness. Technical report, ASTM International, 2011.

[38] Jambeswar Sahu and Sushil Mishra. Size effect on mechanical behaviour of SS304. In *Advances in Material Forming and Joining: 5th International and 26th All India Manufacturing Technology, Design and Research Conference, AIMTDR 2014*, pages 193–201. Springer, 2015.

[39] British Stainless Steel Association. Fatigue properties and endurance limits of stainless steels. Technical report, British Stainless Steel Association, 2018.

[40] OK Chopra and WJ Shack. Review of the margins for asme code fatigue design curve-effects of surface roughness and material variability. Technical report, Argonne National Laboratory, 2003.

[41] Himanshi Singh, Grzegorz Fusiek, and Pawel Niewczas. Extended characterization of an optical sag sensor for high-temperature low-sag lines. *IEEE Sensors Letters*, 7(9):1–4, 2023.

[42] Denis Benasciutti, ROBERTO Tovo, et al. On fatigue damage computation in random loadings with threshold level and mean value influence. *Structural Durability and Health Monitoring*, 2(3):149–164, 2006.

[43] Igor Rychlik. Simulation of load sequences from rainflow matrices: Markov method. *International Journal of Fatigue*, 18(7):429–438, 1996.

[44] Pär Johannesson. Extrapolation of load histories and spectra. *Fatigue & Fracture of Engineering Materials & Structures*, 29(3):209–217, 2006.

[45] Carlo Concari and Giada Bettini. Embedded implementation of rainflow-counting for on-line predictive maintenance. In *2020 IEEE Energy Conversion Congress and Exposition (ECCE)*, pages 981–988. IEEE, 2020.

[46] Fachri P Nasution, Svein Sævik, and Janne KØ Gjøsteen. Study of fatigue strength of copper conductor considering irregularities surfaces by experimental testings and fe-analysis. In *International Conference on Offshore Mechanics and Arctic Engineering*, volume 44908, pages 269–275. American Society of Mechanical Engineers, 2012.

6

General Conclusions and Future Work

6.1 Principal Results and Contributions

This thesis conceives, builds, and rigorously validates a fibre-optic sensing strategy for overhead transmission conductors, focused on high-fidelity sag/strain measurement and vibration metrics directly relevant to fatigue.

The research integrates three pillars:

- laboratory development and metrology of conductor-mounted FBG sensor assemblies, including calibration, temperature compensation, and a full uncertainty budget that separates resolution from absolute accuracy;
- mechanics and system modelling (catenary/tension relationships and finite-element corroboration of sensor hardware) to establish traceable mappings from wavelength to force, strain, and sag; and
- a field-oriented methodology for deploying sensors on live spans at a University test site, PNDC, with documented boundary conditions and quality control of acquired time series.

This research culminates in an end-to-end fatigue-assessment workflow comprising signal conditioning, rainflow cycle counting, S–N curve mapping, and Miner's damage accumulation that converts routine optical measurements into defensible integrity indicators for operational overhead lines.

6.1.1 Research problem and objectives

Contemporary transmission networks operate closer to their physical limits than ever before. Higher thermal loading driven by uprating strategies such as HTLS operation and increased ampacity pushes conductors to elevated temperatures where clearance, creep, and relaxation become critical. At the same time, wind-induced motions (aeolian vibration, galloping, and rain-wind excitation) act over wide time scales and directly influence fatigue at clamps and fittings. Existing monitoring options, including periodic patrols, camera or lidar systems, electromechanical sag meters, and multi-sensor packages, tend to be intrusive, costly to deploy at scale, prone to cyber-attacks, or difficult to maintain in harsh environments. Moreover, many approaches provide indirect indicators that are hard to translate transparently into strain, sag, or fatigue damage with quantified uncertainty.

Against this backdrop, the thesis addresses the need for a compact, conductor-mounted distributed sensing solution that produces traceable, high-resolution measurements and integrates naturally with structural-integrity assessment workflows. The specific objectives were to:

- Design and realise a practical FBG-based sensor system for direct installation on conductors, with mounting architectures that balance strain-transfer efficiency, robustness, and ease of installation.
- Quantify metrological performance across relevant operating envelopes, including linearity, repeatability, and cross-sensitivities to temperature and load. This includes a clear separation of resolution versus absolute accuracy, an uncertainty budget that accounts for interrogator behaviour, load-frame and load-cell characteristics, and temperature compensation, and validated mappings from wavelength to strain, force, and sag.

- Demonstrate an end-to-end, traceable route from measurements to fatigue-life estimates, using accepted methods (signal conditioning, rainflow cycle counting, S–N relationships, and Miner's rule), so that routine time-series data from operational spans can be converted into actionable integrity metrics.

6.1.2 Sensor design and laboratory characterisation

Two conductor-mounted FBG sensor architectures were designed, built, and evaluated under controlled mechanical and thermal conditions:

Sensor S1: spring-plate design (high mechanical gain).

Sensor S1 uses a compliant spring plate to amplify strain transfer from the conductor to the FBG. In quasi-static tests, the force-to-wavelength sensitivity was $K_F = 1.3$ nm/kN, corresponding to an effective strain amplification of approximately 9 times relative to the local conductor strain. The temperature sensitivity K_T was 30 pm /°C. FEA under a representative "hot" static state (conductor 75 °C, axial load 2.38 kN) predicted peak von Mises stresses of 122.5 MPa in the plate, comfortably below the yield and ultimate strengths of 304 stainless steel (yield = 215 MPa; ultimate = 505 MPa).

Sensor S2: narrow-plate design (robust, lower gain).

Sensor S2 trades mechanical gain for robustness and simpler packaging. Its measured force sensitivity was $K_F = 0.116\ \mathrm{nm/kN}\ (116\ \mathrm{pm/kN})$, with a strain-transfer ratio of about 75 %. The temperature sensitivity was again $K_T = 30\ \mathrm{pm/°C}$. FEA for the hot static case yielded peak plate stresses of $74.6\ \mathrm{MPa}$, also well below the material limits.

The cross-sensitivities and linearity of the sensor response were further assessed over the tested temperature and force ranges. Across 20 °C to 180 °C, the force sensitivity K_F varied by approximately 25 % with temperature, while the temperature sensitivity K_T varied by about 2 % across the tested force range. At each temperature step, the force–wavelength relationship remained linear, enabling simple slope-based calibration. These quantified cross-sensitivities were included in the compensation model used for data reduction.

6.1.3 Metrology and measurement uncertainty

Rather than quoting only nominal resolution and accuracy, the sag sensor was assigned a full, GUM-style uncertainty budget. Independent contributions were combined by RSS, and an expanded uncertainty $U = k\,u$ with coverage factor k=2 (approximately 95 % confidence level) is reported alongside the standard uncertainty $u(\cdot)$.

I-MON 512 wavelength uncertainty.

The I-MON 512 interrogator contributes two main random terms:

- Wavelength fit resolution: specified as a maximum standard deviation of 0.5 pm when temperature and polarisation are held constant. This is treated directly as a 1 σ standard uncertainty.
- Repeatability: a 3 pm (max) peak-to-peak polarisation-induced shift over a full 360 ° rotation. As stated earlier in section 4.4.2, the 3 pm value is interpreted as full width with half width 1.5 pm and standard uncertainty is 0.87 pm.

From these, a combined I-MON wavelength standard uncertainty $u_\lambda^{\mathrm{IMON}}$ is formed by RSS and used consistently in all numerical examples. A conservative baseline on this work gives $u_\lambda^{\mathrm{IMON}} \approx$ 1.0 pm, with a documented worst-case variant in which $u_\lambda^{\mathrm{IMON}}$ is increased by treating the 3 pm figure as a full half-width as $\approx$ 1.73 pm.

Temperature uncertainty (PT-104, PT100, and optical chain).

The electronic temperature channel uses a PT-104 platinum-resistance data logger and a Pico SE012 1/10 DIN PT100 probe. The logger has an accuracy of ± 0.01 °C and 0.001 °C resolution, while the probe has an accuracy of ± 0.03 °C at 0 °C over a -50 °C to +250 °C range. Both are modelled as rectangular distributions over their specified accuracy bands, giving logger and probe side standard uncertainties of order 10^{-2} °C and an RSS-combined logger probe standard uncertainty $u_{T,\text{elec}}$ of about 0.036 °C.

On the optical side, the temperature sensitivity of both the bonded and reference FBGs is $K_T = 30$ pm/°C. With $u_\lambda^{\text{IMON}} \approx 1$ pm, the interrogator-limited temperature standard uncertainty in each FBG channel is ≈ 0.033 °C.

Combining the two optical channels by RSS and then combining that result with the logger–probe chain gives an overall temperature standard uncertainty of order $u_{T,\text{sys}} \approx$ 0.051 °C, $U_{T,\text{sys}}(k = 2) \approx$ 0.10 °C.

Thus, both the electronics and the I-MON contribute at the few-hundredths-of-a-degree level, and the overall temperature error remains well below 0.1 °C (k = 2).

Force uncertainty (load cell, temperature coefficients, and I-MON).

Force is measured through a BS EN ISO 7500-1 Class 0.5 LC1000 load cell and, in the optical path, via the FBG force sensitivity $K_F = 116$ pm/kN.

- The class term is modelled as a rectangular distribution with an accuracy of ± 0.5 % of reading, giving $u_{F,\text{class}} = 0.005F/\sqrt{3}$. At F = 3 kN, this is ≈ 8.6 N.
- Manufacturer-supplied thermal coefficients (zero shift and span shift, each 0.005 %/ °C) add temperature-dependent terms that are negligible at room temperature but become important when the cell operates at elevated temperatures.
- The I-MON-limited force standard uncertainty is found by mapping wavelength noise through the measured sensitivity: $u_F^{(\text{int})} = \frac{u_\lambda^{\text{IMON}}}{K_F} \approx \frac{1.0 \text{ pm}}{116 \text{ pm/kN}} \approx$ 8.6 N at $F = 3$ kN

At room temperature, where the thermal zero- and span-shift terms vanish, the machine-side uncertainty reduces to $u_{F,\text{mach}} \approx u_{F,\text{class}}$. Combining with the interrogator term by RSS gives ≈ 12.2 N. So, the expanded force uncertainty is $U_{F,\text{comb}}(k = 2) \approx$ 24.4 N, corresponding to a relative uncertainty of about 1.1 % on a 3 kN reading.

For a worst-case high-temperature extrapolation (load cell ≈ 180 °C, the thermal zero- and span-shift terms dominate and the machine-side standard uncertainty grows to ≈ 49 N;

the same RSS combination then yields $U_{F,\mathrm{comb}}(k = 2) \approx$ 100 N, still below 0.6 % of full-scale at 3 kN.

Sag uncertainty and practical performance.

For an 80 m PNDC-like span with nominal mid-span sag $D_0 \approx$ 90 mm at $F_0 = 3$ kN, propagating the combined force and temperature uncertainties through the GUM law yields a sag standard uncertainty $u_D \approx$ 0.52 mm, and an expanded sag uncertainty $U_D(k = 2) \approx$ 1.0 mm.

The force term is dominant, and temperature contributes only at the level of a few tenths of a millimetre under the tested conditions. The chain-rule mapping $\kappa_{s\lambda} \approx$ 0.26 mm/pm shows that 1 pm of wavelength noise corresponds to about 0.26 mm of sag noise, so the I-MON alone contributes a sub-millimetre component to the overall sag budget.

In practice, isothermal holds in the laboratory showed residual wavelength excursions of 5–8 pm after temperature compensation. These observed values are consistent with the formal uncertainty budget and, crucially, remain well below the tens-of-millimetres sag changes associated with realistic thermal and mechanical loading.

6.1.4 Field installation and operating conditions (PNDC trial)

A full-scale deployment was carried out on a representative span at the PNDC test site under utility-grade safety procedures (permits-to-work, isolation, and live-line exclusion). The objective was to reproduce realistic installation and operating conditions while preserving traceability back to the laboratory calibration. To that end, all boundary conditions that materially influence strain transfer and sag were recorded and, where possible, independently verified:

- Conductor and stringing condition: The span used a reused conductor; its construction, diameter, mass per unit length, and prior service history were logged. Because reused conductors can deviate from handbook tables (creep, strand fretting, residual set), the as-installed stringing tension was taken from dynamometer measurements rather than nominal charts.

- Tension and temperature state: Initial tension was established with a calibrated dynamometer and rechecked after thermal stabilisation. Ambient air temperature, solar loading, and wind conditions at installation were recorded to anchor the catenary measured tension under operating temperature (2.38 kN, tensile).
- Geometry and layout: Span length, sag at mid-span, attachment heights, insulator type, and guy-wire orientation were measured. These details affect local stiffness and boundary restraint and were therefore included in the analysis notes to avoid implicit assumptions from idealised tower geometries.
- Sensor placement and orientation: For each FBG sensor, the arc-length from the clamp mouth, circumferential orientation, bonding length, and adhesive cure were documented. This enables reconstruction of the strain-transfer ratio used during laboratory calibration and supports comparison between nominal and installed sensitivities.
- Instrumentation and sampling: Interrogator model, wavelength fit resolution and absolute accuracy, sampling rate, fibre routing, connector count, and any reference (unbonded) FBG positions were logged so that temperature compensation and wavelength-to-force mappings used on the bench could be applied on-span without modification.

These measured boundary conditions were then propagated into the finite-element checks and tension models. Specifically, the FE models were driven by the measured hot-state tensile load of 2.38 kN; this avoids the common modelling error of translating a temperature-driven reduction in axial tension into an artificial compressive load on the plate assembly. Plate stresses predicted under this tensile boundary condition remained comfortably below material limits, consistent with laboratory results. Finally, the complete set of field notes (tension, temperature, geometry, sensor orientation, and interrogator settings) provides the audit trail necessary to transfer laboratory calibration slopes to the field data, apply temperature compensation, and quantify on-span uncertainty in a manner that is transparent and repeatable.

6.1.5 Fatigue-assessment methodology

To turn field measurements into integrity-relevant metrics, a practical workflow was implemented and demonstrated:

- Signal preparation: Bonded FBG signals were temperature-compensated using a co-located unbonded reference FBG, then linearly detrended. For vibration analysis, the signals were band-limited to the aeolian range to suppress low-frequency sag drift and high-frequency noise.
- Cycle extraction: Rainflow counting was applied to the compensated strain (or equivalent stress) time histories to obtain cycle amplitudes and mean values, forming histograms suitable for fatigue evaluation.
- Stress–life mapping: Cycles were mapped to stress using the measured strain-transfer and section properties of the clamp–conductor region (the life-critical detail). Appropriate S–N data and mean-stress adjustments were selected based on material and environment.
- Damage accumulation: Miner's rule was used to compute cumulative damage and to infer indicative life at the observed operating condition.

During the PNDC campaign, the wind environment was benign, and measured dynamic plate stresses were approximately 0.5 MPa, more than two orders of magnitude below typical 10^7 cycle endurance levels for 304 stainless steel. Consequently, sensor-plate fatigue damage is negligible, and attention correctly centres on the conductor–clamp interface. To illustrate reporting, a uniformly scaled stress history (factor 10) was used solely as a pedagogical example; all such results are clearly tagged as illustrative rather than site-specific predictions.

6.2 Future Work

- Extended field validation: It is desirable to deploy the sensor on a small number of contrasting sites, for example, coastal and inland locations, for at least one annual cycle.

The aim is to confirm that millimetre-level sag resolution and stable temperature compensation are maintained under different wind and temperature regimes, and to capture representative vibration events, including aeolian vibration, rain–wind excitation, and occasional galloping.

- Independent cross-checks: On selected spans, independent reference measurements should be added, such as periodic video-based sag measurements, laser rangefinder measurements, photogrammetry, LiDAR, or total-station surveys. A low-cost accelerometer could also be installed to compare vibration trends. These measurements would not replace the FBG system, but would provide reference data for assessing bias, uncertainty, and long-term drift in the FBG-derived sag and vibration estimates.
- Sensor packaging and installation details: Further work is required to document how adhesive coverage, protective packaging, plate thickness, clamp spacing, and mounting position around the conductor affect strain transfer and thermal bias, particularly under changing wind and temperature conditions. The goal is to develop practical installation rules that preserve sensitivity without introducing significant stiffness, thermal error, or local mechanical disturbance.
- Fatigue workflow and uncertainty bands: The rainflow → S–N → Miner workflow should be retained as an interpretable baseline fatigue-assessment method, but future work should present fatigue results as uncertainty or sensitivity bands rather than as a single lifetime value. This would account for uncertainty in stress conversion, S–N curve selection, mean-stress effects, installation conditions, and environmental variability. The fatigue workflow should be applied when vibration amplitudes are sufficiently large to be fatigue-relevant.
- Advanced predictive analytics: Future work should use long-duration FBG time-series data to develop predictive analytics for OHL condition monitoring. Possible extensions include automatic event detection, classification of vibration regimes, anomaly detection, damage-rate trending, probabilistic remaining useful life estimation, and

physics-informed machine-learning models. These approaches could combine FBG-derived strain, sag, temperature, and vibration features with weather data, conductor current, wind speed, and asset information. This would allow the system to progress from offline fatigue assessment towards real-time predictive maintenance and decision support.

- System considerations: As the system moves towards wider deployment, practical operational requirements should be addressed, including ruggedisation, optical connector protection, interrogator placement, power supply, data storage, secure data transfer, periodic sensor health checks, and compatibility with utility IT and asset-management systems.
- Broader implications: The platform provides two immediate benefits: sag tracking precise enough to support dynamic line rating and clearance management after temperature compensation, and vibration records that can be converted into transparent fatigue metrics when required. Together, these capabilities can help operators use existing corridors more effectively while monitoring mechanical integrity. Further multi-season deployments will be needed to assess robustness across different climates, conductor types, and installation practices.

6.3 Final Remarks

This thesis demonstrates that compact, conductor-mounted FBG sensors can provide reliable, in-situ measurements of sag and strain across temperatures relevant to high-temperature, low-sag (HTLS) operation, and that these measurements can be translated into fatigue-life estimates using a transparent, standards-aligned procedure. The work combined controlled laboratory characterisation, finite-element verification under realistic tensile and thermal states, and a field-oriented setup with explicitly documented boundary conditions. Together, these elements show that, once temperature compensation is applied, the sensing chain achieves millimetre-level sag resolution, with clearly stated accuracy limits and traceable uncertainty contributions from the interrogator, load-cell calibration, and residual thermal effects. Dynamic analyses further indicate that the sensor hardware itself operates with large safety margins relative to yield and high-cycle fatigue thresholds; mechanical risk remains concentrated at the conductor–clamp interface, where the method focuses its integrity assessment.

Beyond proving feasibility, the results establish a practical route from wavelength time series to actionable integrity metrics: temperature-compensated signals feed directly into rainflow counting, S–N mapping, and Miner's rule to produce damage rates that can inform inspection intervals and risk-based maintenance. In combination with span geometry, verified tension, and local weather, the platform can support both operational objectives (dynamic rating, clearance management) and long-term asset integrity (fatigue tracking at fittings). With extended field datasets, refined thermal compensation and packaging, and full uncertainty propagation integrated into reporting, the approach is well positioned to mature into a deployable, interoperable condition-monitoring tool for modern power networks.